

Resedimented Nile Silty Clay (RNSC): Characterization and Soil Behavior Comparison

A thesis submitted by

Mark Zablocki

In partial fulfillment of the requirements for the degree of

Master of Science

In

Civil and Environmental Engineering

Tufts University

August 2018

Addviser: John T. Germaine

ABSTRACT

A geotechnical laboratory test program was performed to evaluate the engineering properties of resedimented Nile Silty Clay. A bulk sample of Nile Silty Clay was collected from a construction site in Cairo, Egypt and shipped to Tufts University in Somerville, Massachusetts. The sample was characterized by index property tests and prepared for the resedimentation specimen reconstitution method.

Three Constant Rate of Strain (CRS) tests were conducted to observe the compression behavior of RNSC. Sixteen triaxial tests were performed to determine the stress-strength-strain behavior of RNSC. From the testing program the compression ratio, effective friction angle, undrained shear strength, lateral stress ratio and undrained secant Young's modulus for at low stress (<1 Mpa) was quantified.

The observed material behavior of RNSC was then compared to the material behavior of Resedimented Boston Blue Clay and Resedimented Gulf of Mexico Eugene Island Clay.

ACKNOWLEDGEMENTS

I wish to thank the following people who assisted me with this work:

Dr. John T. Germaine, my thesis and faculty adviser, whose patience, temperament and guidance made academics enjoyable. I feel honored to have been one of his students his knowledge on soil, soil mechanics and laboratory testing methods is truly legendary as is his patience. I thank him for his guidance within the soil laboratory and outside of it.

Dr. Peter Flemmings, Dr. Maria-Aikaterini Nikolinakou and the rest of the UT GeoFluids group. I am extremely thankful for them in allowing me to participate in their consortium and present in their annual meeting. This experience is worth the price of tuition a hundred times over. Dr. Flemmings' and Dr. Nikolinakou guidance although tough was excellent preparation for my future career.

Dr. Richard Plumb whose guidance helped me see what was important in my research and whose love of geology is a true inspiration.

My friends within Tufts University, I would like to thank the countless people at Tufts who made this experience so memorable. Whether I was working in the lab with them or winning a softball championship there was nowhere else I would rather be.

Matt Zablocki and Siobhan Nguyen for support over the last two years.

My Parents Ed and Valerie Zablocki, who provided love and encouragement throughout my time at Tufts, they are exceptional people and I am lucky to have them.

To Julia Bel, whose unconditional support and love kept me going.

Contents

ABSTRACT	ii
ACKNOWLEDGEMENTS	iii
Chapter 1	1
INTRODUCTION	1
1.1 BACKGROUND	1
1.2 RATIONALE FOR CHARACTERIZATION OF CLAY SOILS ORIGINATING FROM THE NILE RIVER	2
1.3 RESEARCH OBJECTIVES AND SCOPE	3
1.4 ORGANIZATION OF THE THESIS	3
Chapter 2	6
Cairo and the Nile History and Geology	6
2.1 INTRODUCTION	6
2.2 SAMPLE LOCATION	7
2.2.1 Geography	7
2.2.2 Cairo Topography	7
2.2.3 Location of Bulk Sample Collection	8
2.2.4 Cairo Quaternary Soils	8
2.3 NILE RIVER ALLUVIAL DEPOSITS	9
2.3.1 Nile Alluvial Deposits	9
2.3.2 Index Properties of the Nile Alluvial Sediments	9
2.3.3 Source of the Nile River	10
2.3.4 Source of the Nile Alluvial Sediments	11
2.3.5 Source Rocks of the Ethiopian Highlands	13
2.3.6 Source Rocks of the Egyptian Wadis	13
2.3.7 Source Rocks of the White Nile	14
2.3.8 Source of the Aeolian Dust	15
2.3.9 Nile Sediment Deposition Rates	15
2.3.10 Nile Silty Clay Summary	16
Chapter 3	21
Specimen Preparation and Scope of Testing Program	21
3.1 INTRODUCTION	21

3.2	SPECIMEN RECONSTITUTION	22
3.2.1	Intact Specimens	22
3.2.2	Introduction to Resedimentation (Slurry Sedimentation)	23
3.2.3	Resedimentation (Slurry Sedimentation) Process.....	24
3.3	LABORATORY TESTING EQUIPMENT	26
3.3.1	Introduction.....	26
3.3.2	Automated Stress Path Triaxial Cell	27
3.3.3	Automated Constant Rate of Strain Test Apparatus	29
3.3.4	Electronic Laboratory Instrumentation	30
3.3.4.1.	Linear Variable Displacement Transducers (LVDT)	30
3.3.4.2.	Load Cells.....	31
3.3.4.3.	Pressure Transducers	31
3.3.4.4.	Pressure-Volume Actuators (PVA).....	32
3.3.4.5.	Central Data Acquisition System (DAQ)	32
3.3.4.6.	Computer Control System	33
3.4	LABORATORY TESTING METHODS.....	35
3.4.1.	Introduction.....	35
3.4.2.	Index Property Tests.....	36
3.4.2.1.	Particle Size Distribution.....	37
3.4.2.2.	Atterberg Limits.....	37
3.4.2.3.	Calcite Equivalency	38
3.4.2.4.	Organics Content	39
3.4.2.5.	Specific Gravity	39
3.4.2.6.	Salt Content	40
3.4.2.7.	Mineralogy by X-Ray Powdered Diffraction (XRPD)	41
3.4.2.8.	Scanning Electron Microscopy.....	42
3.4.3.	Constant Rate of Strain (CRS) Tests.....	44
3.4.4.	Triaxial Test Methods	46
Chapter 4	64
TESTING RESULTS; CHARACTERIZATION, CONSOLIDATION AND STRENGTH	64
4.1	INTRODUCTION	64
4.2	CHARACTERIZATION	66

3.2.4	Introduction.....	66
3.2.5	Grain Size Distribution.....	66
3.2.6	Atterberg Limits.....	67
3.2.7	Organics Content and Calcite Equivalency.....	68
3.2.8	Scanning Electron Microscopy.....	68
3.2.9	X-Ray Powder Diffraction.....	70
3.2.10	Specific Gravity and Natural Salt Content.....	71
4.3	CONSOLIDATION.....	71
4.3.1.	Introduction.....	71
4.3.2.	CRS Consolidation Results.....	72
4.3.3.	Triaxial Consolidation Results.....	73
4.3.4.	Comparison of Consolidation Behavior by Testing Method and Series.....	75
4.4	Permeability.....	76
4.4.1.	Introduction.....	76
4.4.2.	CRS Permeability Results.....	78
4.5	Stress-Strain-Strength.....	79
4.5.1.	Introduction.....	79
4.5.2.	CK ₀ UC Triaxial Tests.....	80
4.5.3.	CIUC Triaxial Tests.....	82
4.5.4.	CI/K ₀ DC Triaxial Tests.....	83
4.5.5.	CK ₀ UE Triaxial Tests.....	84
4.5.6.	High OCR Triaxial Tests.....	86
4.5.7.	Critical State Friction Angle.....	88
4.5.8.	Undrained Shear Strength.....	88
4.5.9.	Lateral Stress Coefficient K ₀	89
4.5.10.	Undrained Secant Young's Modulus E ₀	89
Chapter 5	137
RNSC Comparison to Established Clay Behaviors	137
5.1	INTRODUCTION.....	137
5.2	INDEX PROPERTY AND CHARACTERISATION TESTS.....	138
3.2.11	Introduction.....	138
3.2.12	Grain Size Distribution and Specific Gravity.....	138

3.2.13	Atterberg Limits.....	139
3.2.14	Bulk Mineralogy an Mineralogy of Clay Fraction	139
5.3	COMPRESSION AND PERMEABILITY BEHAVIOR	141
5.3.1.	Introduction.....	141
5.3.2.	Compressibility	141
5.3.3.	Permeability.....	143
5.4	STRESS-STRENGTH-STRAIN.....	144
5.4.1.	Introduction.....	144
5.4.2.	Undrained Shear Strength.....	144
5.4.3.	Effective Friction Angle.....	146
5.4.4.	Lateral Stress Ratio, K_0	147
Chapter 6	161
CONCLUSIONS AND RECOMMENDATIONS	161
6.1	CONCLUSIONS	161
6.1.1	Introduction.....	161
6.1.2	Nile Silty Clay	161
6.1.3	Resedimentation	162
6.1.4	Successful Testing Procedures.....	162
6.1.5	Laboratory Testing.....	162
6.1.5.1.	Index Properties and Characterization Tests.....	162
6.1.5.2.	Compressibility	163
6.1.5.3.	Permeability.....	164
6.1.5.4.	Stress-Strength Response.....	164
6.1.6	Comparison to Other Soils.....	164
6.2	Recommendations for Future Research.....	165
6.2.1	Introduction.....	165
6.2.2	Triaxial Testing.....	165
6.2.3	CRS Testing	165
6.2.4	Salinity	166
6.2.5	Liquefaction	166
6.2.6	Evolution of Microstructure	166
Bibliography	167

Tables

Table 3- 1: Triaxial Station 01	54
Table 3- 2 Triaxial Station 02	54
Table 3- 3: Triaxial Station 08	54
Table 4- 1: Summary of RNSC Index Properties	92
Table 4- 2: Summary of CRS Phase Relations and Compression Parameters	92
Table 4- 3: Summary of RNSC Triaxial Test Phase Relations and Consolidation Phase Compression Parameters	93
Table 4- 4: Summary of RNSC Triaxial Test Shearing Phase Engineering Parameters	94
Table 5- 1: Index Properties of RNSC, RBBC, and RGoM_EI	150
Table 5- 2: Compression Properties of RNSC, RBBC, and RGoM_EI.....	151
Table 5- 3: Summary of Triaxial Tests Used to Compare RNSC, RBBC, and RGoM_EI	151

Figures

Figure 2-1:Location of the Country Egypt Bordered in Red (Background Map from Google Maps 2018).....	17
Figure 2- 2: Location of Bulk Sample Collection Within Cairo and Nile River Delta (Background Map from Google Maps 2018)	18
Figure 2- 3: Major tributaries of the Nile River from (Woodward, et al., 2015)	19
Figure 2- 4 African tectonic plate boundaries in Ethiopia from (USGS, 2014)	20
Figure 2- 5: Location of Aswan Dam in Southern Egypt (Background Map from Google Maps 2018).....	20
Figure 4- 1: Grain size Distribution from Sedimentation Testing on Series I	95
Figure 4- 2: Grain size Distribution from Sedimentation Testing on Series II	95
Figure 4- 3: Atterberg Limit Testing Performed on Series I Material	96
Figure 4- 4: Results of Atterberg Limit Testing on Series II and Series III Material	96
Figure 4- 5: Calcite Equivalency Pressure Curves (Series II)	97
Figure 4- 6: Ion Milled Cross Section at Low Magnification in in TX1316 (Series II)	97
Figure 4- 7: Cracking in the fabric of TX1316 (Series II).....	98
Figure 4- 8: Ion Milled Minerals within the Clay Matrix of TX1316 (Series II).....	98
Figure 4- 9: Intra-particle Porosity within TX1316 (Series II)	99
Figure 4- 10: Typical Mineral Grain within TX1316 (Series II)	99
Figure 4- 11: Ion Milled Cross Section of TX1379 (Series III).....	100
Figure 4- 12: Typical Crystalline Mineral Grains within TX1379 (Series III).....	100
Figure 4- 13: Typical Pore Space Observed within TX1379 (Series III)	101
Figure 4- 14: Typical Microscopic Pore Space Observed within TX1379 (Series III).....	101
Figure 4- 15: >#200 Sieve Grains Potentially Clay Cemented Aggregates	102
Figure 4- 16: >#200 Sieve Grains Potentially Clay Cemented Aggregates	102

Figure 4- 17: >#200 Sieve Grain Potentially Clay Cemented Aggregates	103
Figure 4- 18: >#200 Sieve Grain Crystalline Mineral	103
Figure 4- 19: >#200 Sieve Grain Crystalline Mineral	104
Figure 4- 20 >#200 Sieve Grain Crystalline Mineral	104
Figure 4- 21: >#200 Sieve Grain Crystalline Mineral	105
Figure 4- 22: Bulk XRPD Pattern with Main Non-Clay Phases	105
Figure 4- 23: XRPD Results of Clay Fraction (<2 μ m particle size) of RNSC.....	106
Figure 4- 24: CRS Test Results as plotting in Log Effective Stress by Axial Strain.....	107
Figure 4- 25: CRS Test Results as plotting in Log Effective Stress by Void Ratio	108
Figure 4- 26: ϵ - Log σ , Triaxial Consolidation Curves for Select RNSC Tests	109
Figure 4- 27: e -Log σ , Triaxial Consolidation Curves for Select Tests.....	110
Figure 4- 28: e - Log σ , Average Compression Curve for RNSC.....	111
Figure 4- 29: ϵ -Log σ , Consolidation Curves by RNSC Series for triaxial and CRS Tests	112
Figure 4- 30: e -Log σ , Consolidation Curves by RNSC Series for triaxial and CRS Tests	113
Figure 4- 31: ϵ - Log σ , Compression curves of the Three RNSC Series.....	114
Figure 4- 32: e - Log σ , Compression Curves of the Three RNSC Series	115
Figure 4- 33: Permeability by Void Ratio Calculated from RNSC CRS Tests	116
Figure 4- 34: Stress-Strain Curves from CK ₀ UC Triaxial Tests.....	117
Figure 4- 35: Normalized Stress-Strain Curves from CK ₀ UC Triaxial Tests	117
Figure 4- 36: Maximum Shear Stress by Consolidation Stress from NC CK ₀ UC Triaxial Tests.....	118
Figure 4- 37: Effective Steady State Friction Angle by Consolidation Stress from NC CK ₀ UC Triaxial Tests.....	118
Figure 4- 38: Shearing Stress Paths from CK ₀ UC Triaxial Tests in MIT p-q Space.....	119
Figure 4- 39: Normalized Shearing Stress Paths from CK ₀ UC Triaxial Tests in MIT p-q Space ...	119
Figure 4- 40: Sheared Induced Pore Pressure by Axial Strain in CK ₀ UC Triaxial Tests.....	120
Figure 4- 41: Stress Strain Curves from CIUC Triaxial Tests.....	120
Figure 4- 42: Normalized Stress Strain Curves from CIUC Triaxial Tests	121
Figure 4- 43: Normalized Stress Strain Curves from CIUC and CK ₀ UC Triaxial Tests	121
Figure 4- 44: CIUC Triaxial Test Shear Stress Paths in MIT p-q Space	122
Figure 4- 45: Normalized Shear Stress Paths from CIUC Triaxial Tests	122
Figure 4- 46: Sheared Induced Pore Pressure by Axial Strain in CIUC Triaxial Tests.....	123
Figure 4- 47: Shear Stress by Axial Strain from Drained Triaxial Tests.....	123
Figure 4- 48: Normalized Shear Stress by Axial Strain from Drained Triaxial Tests	124
Figure 4- 49: Volumetric Strain by Axial Strain from Drained Triaxial Tests	124
Figure 4- 50: Shear Stress by Axial Strain from Shear Phase of CK ₀ UE Triaxial Tests.....	125
Figure 4- 51: Normalized Shear Stress by Axial Strain from Shear Phase of CK ₀ UE Triaxial Tests	125
Figure 4- 52:CK ₀ UE Triaxial Test Shear Stress Paths in MIT p-q Space	126
Figure 4- 53: Normalized Shear Stress Paths from CK ₀ UE Triaxial Tests	126
Figure 4- 54: Normalized Shear Induced Pore Pressure by Axial Strain from CK ₀ UE Triaxial Tests	127
Figure 4- 55: ϵ - Log σ Consolidation Curves for High OCR CK ₀ UC Triaxial Tests	128

Figure 4- 56: e- $\log\sigma$ Consolidation Curves for High OCR CK0UC Triaxial Tests.....	129
Figure 4- 57: Stress Strain Curves from High OCR CK ₀ UC Triaxial Tests	130
Figure 4- 58: Normalized Stress Strain Curves from High OCR CK0UC Triaxial Tests	130
Figure 4- 59: Shear Stress Paths from <i>High OCR Triaxial Tests in MIT p-q Space</i>	131
Figure 4- 60: Normalized Shear Stress Paths from High OCR Triaxial Tests in MIT p-q Space	131
Figure 4- 61: Normalized Shear Induced Pore Pressure by Axial Strain from High OCR Triaxial Tests.....	132
Figure 4- 62: Variation in Critical Friction Angle by Vertical Consolidation test for RNSC Triaxial Tests.....	132
Figure 4- 63: Variation in Critical Friction Angle by Average Stress at Failure for RNSC Triaxial Extension Tests.....	133
Figure 4- 64: Maximum Shear Stress by Maximum Consolidation Stress for Compression Triaxial Tests.....	133
Figure 4- 65: Compression and Tension Stress Strain Curves at 150 KPa (TX1283 & TX1375) ...	134
Figure 4- 66: K_0 by Maximum Vertical Consolidation Stress for K_0 Consolidated Triaxial Tests .	135
Figure 4- 67: Example Calculation of E_{sec} for Undrained Triaxial Tests	135
Figure 4- 68: Elastic Modulus by Maximum Consolidation Pressure at 0.01% and 0.1% Strain During Shearing of Normally Consolidated Triaxial Compression Tests	136
Figure 4- 69 Normalized Elastic Modulus by Maximum Consolidation Pressure at 0.01% and 0.1% Strain During Shearing of Normally Consolidated Triaxial Compression Tests.....	136
Figure 5- 1: Constituent Minerals of Clay Fraction (<2 μ m) of NSC, BBC and GoM_EI	152
Figure 5- 2: Atterberg Limits of RNSC, RBBC and RGoM_EI	152
Figure 5- 3: Particle Size Distribution by Sedimentation Testing for RSC, RBBC and RGoM_EI..	153
Figure 5- 4: Virgin Compression Behavior from CRS tests for RNSC, RBBC and RGoM_EI in ε - $\log\sigma'_{vc}$ space	154
Figure 5- 5: Virgin Compression Behavior from CRS tests for RNSC, RBBC and RGoM_EI in e- $\log\sigma'_{vc}$ space.....	155
Figure 5- 6: Consolidation Curves of Bentonite Mixtures from (Marcial, Delage, & Yu Jun, 2001)	156
Figure 5- 7: Variations in RBBC Consolidation with Variations of Clay Concentration from (Schneider, 2011)	156
Figure 5- 8: Change in Permeability by Porosity for RNSC, RBBC and RGoM_EI from CRS Testing	157
Figure 5- 9: Maximum Shear Stress by Horizontal Confining Stress of the Three study Soils	157
Figure 5- 10: Normalized Maximum Shear Stress by Maximum Consolidation Stress for RNSC, RBBC and RGoM_EI	158
Figure 5- 11: Critical State Friction Angle by Maximum Consolidation Stress for RNSC, RBBC and RGoM_EI.....	158
Figure 5- 12: Coefficient of Lateral Earth Pressure K_0 by Maximum Consolidation Stress for RNSC, RBBC, and RGoM_EI	159
Figure 5- 13: K_0 by Normalized Shear Strength for RNSC, RBBC, and RGoM_EI.....	159

Figure 5- 14: Critical state Friction Angle by Lateral Stress Ratio with Comparison to Jaky1948 for RNSC, RBBC, and RGoM_EI..... 160

Chapter 1

INTRODUCTION

1.1 BACKGROUND

Since the advent of the Stress History and Normalized Soil Engineering Properties method Ladd & Foote (1974), which provided a strong framework in which to evaluate and compare the properties of clay, an effort has been made in the engineering community to characterize clay soils around the world by their normalized engineering properties

In geographic locations where reliable geotechnical laboratories are not available, or when soils are prone to extreme sample disturbance, reconstituted specimens have been found to be an appropriate alternative to intact samples. Reconstituted soil samples have been found to give general trends in material behavior for a given soil that carry into the natural soil deposits Varallyay (1964) and Betts (2014).

When running a laboratory testing program on soil it is important to account for sample disturbance, during the collection of the soil sample as well as the transportation of the sample to the laboratory. In some cases, the soil may be too sensitive or the distance to the laboratory may be too great such that it would be an impossible task to provide an intact sample. In these cases reconstituted samples would serve as an acceptable substitute. Several reconstitution techniques have been developed throughout the years but the new resedimentation technique Abdulhadi (2009) as will be discussed further provides an excellent sample for reconstituted clays.

The material source for this study comes from Cairo Egypt. The city is located in northern Egypt along the banks of the Nile River. Cairo is located 100 miles south of the Mediterranean Sea and 75 Miles West of the Gulf of Suez. Cairo is situated at the head of the Nile River delta into the Mediterranean. The clay material was mined from a shallow construction site excavation within Cairo and as discussed further is material that was deposited by the Nile. The material was provided by Dr. Sherif Akl of the University of Cairo.

1.2 RATIONALE FOR CHARACTERIZATION OF CLAY SOILS ORIGINATING FROM THE NILE RIVER

The rationale in creating a laboratory program to characterize the Nile Silty Clay is to further the understanding of the geotechnical community on clays. Through systematic study of the geologic source, classification and laboratory testing of the Nile Silty Clay, a comprehensive understanding of the soil and its behaviors can be gained. These data will be available, to the geotechnical community for use in designing engineered systems within the Nile Silty Clays or as inputs in a geo-mechanical model. Additionally, the measured behaviors of Nile Silty Clay will be compared to “benchmark” clay soil data sets such as Boston Blue Clay and Gulf of Mexico Eugen Island.

The laboratory testing program performed on Nile Silty clay consisted of Constant Rate of Strain (CRS) compression tests as well as consolidated undrained triaxial tests. From this testing program the friction angle, cohesion, undrained shear strength, at rest lateral stress ratio, coefficient of consolidation, coefficient of secondary consolidation, and permeability were quantified for Nile Silty Clay. These parameters are fundamental to designing engineered systems within a soil and can be adapted to a geo-mechanical model. The strength anisotropy

of Nile Silty Clay was explored through comparison of extension and compression triaxial tests and will be presented as a part of the laboratory testing results.

Furthermore, the Nile Silty Clay soil behavior will be compared to published high quality data sets of well-studied clay soils such as Boston Blue Clay and Gulf of Mexico Eugen Island Clay in order to provide a larger view of clay behavior. The clay soils will be compared by their mineralogy, geologic sources and engineering parameters. Differences observed within the Nile Silty Clays will be highlighted and a possible explanation will be provided when possible.

1.3 RESEARCH OBJECTIVES AND SCOPE

The objectives and scope of the research presented herein are listed as follows.

- 1) Conduct a detailed literature review of the geologic source of the Nile Silty Clay sediments.
- 2) Process the bulk soil sample for testing (performed by others).
- 3) Characterize the material through the use of index property tests
- 4) Characterize the engineering properties of Resedimented Nile Silty Clay. Using resedimented test specimens and a combination of CRS and Triaxial tests.
- 5) Measure and quantify the friction angle, undrained shear strength, at rest lateral stress ratio, compression behavior and permeability.
- 6) Evaluate strength anisotropy within Nile Silty Clay.
- 7) Compare the behavior of RNSC to the behavior of Resedimented Boston Blue Clay and Resedimented Gulf of Mexico Eugene Island.

1.4 ORGANIZATION OF THE THESIS

This thesis is organized into 6 chapters to present a complete understanding of the Nile Silty Clays.

Chapter two provides a review of the location of bulk sample collection, and a literature review on the geology of the Nile silty Clay. As the source material for this study is a natural soil deposited by the Nile River, it is important to understand the source rocks, method of deposition and mineralogy of the Nile Silty Clay. This will be done by first presenting the geography of northeast Africa and then a description of the Nile Silty Clays which will include the extents and thickness of the deposit. The variations in deposition history of Nile Silty Clay by changes of the Nile River and climate of Egypt will also be explained. Finally this section will provide information on the parent rocks for the Nile Silty clays and the likely process in which the parent rocks were transformed into the soil.

Chapter three will present the equipment and testing procedure used for the laboratory program. The first section will discuss the specimen reconstitution method of resedimentation as it was the method used within this study. The resedimentation method was employed as intact samples could not be transported from Cairo, Egypt to the Tufts laboratory without significant sampling disturbance. This will provide a context for the tests performed during the laboratory program. The third section of this chapter will discuss the laboratory testing equipment used during the testing program. This section will detail the control system hardware, software, measurement instrumentation and any modifications necessary to run the tests. The fourth section will detail the procedures used for each test within the laboratory program.

Chapter four presents the results of the laboratory testing program. The first section is an introductory note on nomenclature for Nile Silty Clay material preparation. Section 2 is on the

characterization of the Clays through index property tests. The index properties include Atterberg Limits, grain sized distribution, specific gravity, organic content, calcite equivalency and x-ray powder diffraction for mineralogy. Section three presents the compression characteristics of Resedimented Nile Silty Clays. The compression characteristics were measured through a combination of Constant Rate of Strain (CRS) and consolidated triaxial test. The final section of chapter four will discuss the undrained triaxial tests performed on the Nile Clays. This section will cover the stress-strain-strength behavior and strength anisotropy measured within the Nile Silty Clays. This section will look at the strength behavior over a range of consolidation stresses within the typical ranges of geotechnical construction projects (<1MPa).

Chapter five summarizes the most important results from the research and presents the best estimates of properties and other correlations for the Nile Silty Clays as compared to other clays. Section one provides an introduction and reasoning on why the comparison clays were chosen. Section two describes variations in the comparison clay index properties. Section three details observed variations in the compression and permeability behaviors between the comparison clays. The permeability data for the comparison clays are calculated from the measured hydraulic conductivity from CRS tests. Section four details observed variations of stress-strain-strength data from consolidated undrained tests.

Chapter six provides a section of conclusions on the behavior of Nile Silty Clay. Chapter six concludes the thesis with recommendations for future research as it pertains to Nile Silty Clay.

Chapter 2

Cairo and the Nile History and Geology

2.1 INTRODUCTION

The source material for this study is a natural soil deposited by the Nile River within Egypt. Egypt is a country located in Northeast Africa as shown in Figure 2-1. The climate of the country is hyper arid; a significant portion of the country is located within the Sahara Desert. It is important to understand the geology, and geologic evolution of the Nile River to understand the composition and texture of the Nile River Sediments. Through review of the parent rocks and deposition one can get a first approximation of the properties and stratigraphy of a soil. This chapter describes the location of soil collection for this study, a description of the alluvial sediment transport method and a description of the modern geology of the Nile River Flood Plain.

Section 2.2 will describe the location of soil collection within Cairo, Egypt. The city is situated at the head of the Nile River delta as it starts to fan out northwards where the River meets the Mediterranean Sea. A significant portion of the city is founded within the modern alluvium Nile sediments. The soil sample that is the subject of this research was collected from a construction site within the city of Cairo.

Section 2.3 will discuss the city of Cairo, specifically the geography, topography, and significant surficial geology. Two detailed descriptions on the geology of Cairo and the geology of Egypt as a whole are provided within "Geology of Cairo, Egypt (Shata)" and "The Geology of Egypt Said R (1990)." This section is an interpretation of the earlier work.

Section 2.4 will discuss the Nile River as it relates to the alluvial soil deposits such as visual identification, source, notable geologic characteristics, significant periods of deposition, and estimated yearly sediment discharge. This section will also discuss the construction of the Aswan Dam which has limited the deposition of the alluvial soils since its completion in 1970.

2.2 SAMPLE LOCATION

2.2.1 Geography

Cairo is in northern Egypt; the city is situated 150 miles south of the Mediterranean Sea and 120 miles west of the Suez Canal. The city is located at the southernmost point of the opening delta fan of the Nile and Mediterranean Sea. The location of Cairo within the Nile River Delta is shown on Figure 2-2. The metropolitan area extends into the Libyan Desert to the west and the Arabian Desert to the east.

2.2.2 Cairo Topography

The topography of Cairo is one of a flat river basin with elevated plateaus on either side. A larger and more energetic prehistoric Nile variation cut the channel in which the modern City of Cairo sits. The city is underlain by Tertiary sedimentary rocks and Quaternary soils.

The Nile River flood plain at Cairo is relatively flat varying from 17 to 21 m above sea level. The flood plain slopes south to north at a relative slope of 0.2 m/km as the River drains to the Mediterranean Sea. The city was constructed within the floodplain of the Nile and has a structural plateau and escarpment on either side. The structural plateau on the east side of Cairo rises to an elevation of 150 m above sea level and is underlain by Limestone. To the west the structural plateau rises to a 500 m elevation above sea level and is underlain by sandstone.

2.2.3 Location of Bulk Sample Collection

The bulk soil sample for this laboratory program was collected in a shallow construction excavation within the city of Cairo. The sample was collected approximately 7.8 kilometers north of the Great pyramids and approximately 10 kilometers west of the Nile River. Figure 2-2 shows the location of bulk sample collection within Cairo. Dr. Sherif Akl of the University of Cairo provided to bulk sample to the Tufts Advance Geomaterials Laboratory in summer 2016. The depth of the sample when collected is not known but estimated to be between 10 and 15 ft (typical excavation depth for a single below ground level).

2.2.4 Cairo Quaternary Soils

The general stratigraphic succession of the Cairo geology within the Nile River flood plain consists of the following units from ground surface down: a Quaternary soil unit, a Pliocene soils unit, a Miocene soils unit, a Cretaceous rock layer and a Jurassic rock layer. The Quaternary unit within Cairo consists of naturally deposited soils as well as relic fill soils. The relic fill soils generally consisting of historic building debris will not be discussed within this thesis. The Quaternary soils which constitute the natural top of the Nile flood plain are a Holocene Silt-Clay unit. This unit is the successive accumulation the deposits from the Nile during the flood seasons. This unit has an average thickness of 10 m but can be as large as 40 m. This soil deposit is the youngest of the Neogene period deposits, the subject of this investigation, and are the famed fertile soil of the Nile River. These soils have been deposited by the Nile River as its course shifted in Egypt. The estimated start of Holocene clay-silt deposit was 8000 years before present, the mechanism of deposition will be discussed in section 2.3.

2.3 NILE RIVER ALLUVIAL DEPOSITS

2.3.1 Nile Alluvial Deposits

The geological definition of alluvium is loose soil or sediments which have been eroded, reshaped by water and redeposited in a non-marine setting. The subject of the research presented herein is the Alluvial soil from the Nile River within the city of Cairo. Consisting of a dark brown predominantly clay and silt mix, the alluvial soils are deposited during yearly periods of flooding from the Nile River. The source of the sediments varies with both the climate of the region and over time as discussed in section 2.3.4.

2.3.2 Index Properties of the Nile Alluvial Sediments

A detailed analysis of the physical properties and mineral composition of the onshore and offshore Nile clays was performed in 1975 by the Rothamsted Experimental station in cooperation with the University of Cairo (Weir, Ormerod, & El Mansey, 1975). Offshore clays denote the samples collected from the Mediterranean Sea floor. Tests were performed to determine the grain size distribution, the calcium carbonate content, the total organics content and the mineralogy of soils. The clay fraction by grain size (<2 μm) of onshore clay samples was found to range between 17.5% and 60.8%. Offshore the clay fraction was found to range between 3.4% to 51.9%. The silt content by grain size (2 to 63 μm) of onshore samples was found to range between 36.3% to 53%. Offshore the silt fraction was between 4.7% and 50.9%. The sand content by grain size (63 to 2000 μm) of onshore samples was found to range between 0.4% and 35.5%. Offshore the sand content ranged between 2.9% and 91.5%. For both onshore and offshore samples the largest particle size measured was 8 mm. The calcium carbonate content for both onshore and offshore samples was found to range between 0% and 6% and was found to be 2% in most samples. The carbonate fraction is mainly molluscan fragments of various sizes; thought to be the result mollusk intrusion caused by periodical flooding from high

sea level in the Mediterranean (Dawood & Abd El-Naby, 2012). The total organics content for both onshore and offshore samples was found to range between 0.1 and 3.5% with the majority of samples having less than 1% organic content.

The mineral composition of the clay size particles was determined by X-Ray Powder Diffraction (XRPD). The dominant minerals were found to be: Smectite 39% to 52%, Kaolinite 15% to 23%, Illite 7% to 17% and Vermiculite 8% to 12% with traces of Iron, chlorite, quartz and feldspar.

2.3.3 Source of the Nile River

The Nile River flows south to north from the hills of central Africa to the Mediterranean Sea. The Nile is fed by two major sources that meet in Khartoum, Sudan. The two major sources are three rivers from the Ethiopian Highlands, the Atbara, Blue Nile and Sobat; and the White Nile sourced from Lake Victoria. The catchments of the Nile River tributaries, except for the Sobat River is shown on Figure 2-3.

The three Ethiopian rivers are source from the highlands at elevations ranging from 2000 to 3000 m above sea level. The Ethiopian highlands tilt west to east. Geologic evidence shows that the three rivers originally flowed from the highlands to the Indian Ocean. When the Great African Rift Valley formed, to the east of the Ethiopian highlands, the three Nile tributaries began flowing west. This change in flow direction connected the tributaries of the Ethiopian highlands to the Nile River. The northern most of the three tributaries, the Atbara, is a highly seasonal river which itself is fed from smaller mountain runoff tributaries. During the dry season of March and May in Ethiopia the Atbara typically ceases to flow. The water producing portion of the Atbara is found between latitudes 12 and 15 degrees north and longitudes 36 and 40 degrees east. The Blue Nile, the largest tributary of the Nile is primarily sourced from Lake

Tana, Ethiopia, but has several significant basin tributaries along its route. The Blue Nile does not cease flowing in the dry season. The Blue Nile drops elevation rapidly as it approaches the South Sudan border as the grade significantly flattens. The water producing portion of the Blue Nile is found between latitudes 9 and 12 degrees north and west of longitude 40 in Ethiopia. The southernmost Ethiopian tributary is the Sobat. The Sobat is fed by two major tributaries from the Ethiopian highlands, the Baro and the Pibor. The Sobat is found almost entirely in South Sudan and is a relatively new river forming with the start of the rift valley. The water producing portion of the Sobat River can be found between latitudes 8 and 9 degrees north and longitudes 31 and 33 degrees east.

The White Nile is the general name of the continuous stretch of river from Lake Victoria in Uganda up to its meeting point with the Blue Nile at Khartoum, Sudan. Khartoum is the official start of the Nile River. The White Nile is sourced by three of the African Great Lakes in Uganda, Lake Victoria, Lake Edward, and Lake Albert. Lake Albert and Lake Edward have thought to have been closed lakes to the White Nile, until 25,000 to 28,000 years ago. Periods of high rains at that time were thought to have connected the lakes to the White Nile.

2.3.4 Source of the Nile Alluvial Sediments

Historically there have been four major sources for the sediments of the Nile River; the individual contribution of each of the sources has varied with changes in climate and tectonics. Nile Holocene silt-clay deposits have remained relatively homogenous irrespective to the changes in the source of the sediments. In 2015, a very detailed strontium isotope survey was performed to trace Nile River sediments to their parent rocks (Woodward, et al., 2015). The study found that the quantifiable suspended sediment load within the modern Nile River was approximately 61% from the Blue Nile, 35% from the Atbara, and 3% from the White Nile. An

unquantifiable amount of the suspended sediments were found to be from aeolian transport from the deserts of Sudan and Egypt. Although it is currently unquantifiable the windblown material collected in the Nile should not be considered negligible as studies of the Mediterranean Sea floor have found that windblown dust could make up to 90% of the sediments. One last historic source of Nile Alluvial sediments was Egypt's wadis, a wadi being a drainage channel that is dry until the rainy season.

The 2015 study measured the ratio of Strontium isotopes within the Nile Alluvial deposits in forty excavations along the Nile River. The Strontium isotope ratios were found to be unique to the four major sources of sediment, the wadi muds, the White Nile, Ethiopian highlands as well as the aeolian dusts from the Sahara Desert. The excavations were dated through archaeological records which were used to estimate the contributions of the four sediment contributors over time. The timeline was as follows, 8500 years before present the constituents of the Nile deposits were sourced 55% by the Ethiopian highlands, 45% from the desert wadis with negligible input from the White Nile. During this time, the climate in Egypt was thought to be humid with significant precipitation which was why the wadis were such a large contributor to the overall sediments in the Nile. An estimated 4600 years before present the climate changed to be more arid and the wadis ceased to flow on a regular basis and the Nile Channel systems contracted, at this time the Nile deposits were estimated to be sourced 60% by the Ethiopian highlands, 40% from the desert wadis with negligible input from the White Nile. As the climate continued to become more arid to a hyper-arid condition the wadis slowly stopped contributing to the Nile sediments until the contribution was negligible. The current sediment contributions are estimated to be 96% from the Ethiopian highlands, 3% from the White Nile and the remainder sourced through the Wadis and aeolian dust.

2.3.5 Source Rocks of the Ethiopian Highlands

The Ethiopian highlands are a rugged mountainous area within Ethiopia and extending to the North into Eritrea. The region is the result of magma from the Earth's mantle uplifting a broad dome of the Arabian Nubian Shield. The Arabian Nubian Shield is an exposure of Precambrian crystalline rocks on the flanks of the Red Sea. The highlands are thought to have begun rising 75 million years ago and 30 million years ago the African Nubian plate began separating from the Arabian and African Somali plates creating the Great Rift Valley. Figure 2-4 shows the tectonic boundaries of the three plates. Continued rifting lead to an initial energetic period of volcanos and magma flows that lasted for roughly 1 million years, during this 1-million-year period the upheaved dome was turned into a vast volcanic plateau. After the initial energetic period a number of alkaline basalt shield volcanoes were formed and volcanism was confined to rift areas. In general it is the soft basalts formed during the rifting that is eroded and carried by the Rivers of the Ethiopian Highlands to the Nile River. The basalts are relatively uniform, most are aphyric to sparsely phyric, and contain phenocrysts of plagioclase and clinopyroxene with or without olivine. Most of the basalts have tholeiitic to transitional compositions (Kieffer, et al., 2004). Weathering of plagioclase forms dioctahedral smectite (Eggleton, Foudoulis, & Varkevisser, 1987) which is the dominant clay mineral of the Nile Holocene silt-clay unit. The Ethiopian tributary rivers drop in elevation, to the north of the Highlands. As the rivers drop the basalt rocks give way to sedimentary sequences consisting of dolomites, clays, and quartz (Mogessie, et al., 2002). The erosion of these sequences might be the major contributor of these minerals to the Nile Silty Clay.

2.3.6 Source Rocks of the Egyptian Wadis

Although currently considered negligible, historically the wadis of southern and central Egypt were a large source of sediments to the Nile River. The wadis are typically carved in

Nubian sandstone. The sandstone was deposited during the Jurassic period to the upper Cretaceous period primarily through cycles of deposition through fluvial, deltaic and lacustrine means. The deposition was controlled by periods of marine transgressions and regressions (Embabi, 2018). In general the Nubian Sandstone composed mainly of cemented Quartz, ferruginous sandstone and siltstone beds with occasional conglomerate bands. The sandstone and ferruginous sandstone beds are varicolored (yellowish brown to reddish brown), medium to very coarse-grained with granules and pebbles. Most of the sandstone beds are rich in iron oxides that give them a yellowish-brown to dark-reddish brown color and sometimes form nodules within the formation. The siltstone beds are varicolored (dark gray to violet), hard and sometimes alternate with thin sandstone beds (Aggour, Korany, Mosaad, & Kehew, 2012). Of the small amount of clay minerals within the Nubian sandstone the predominant mineral is Kaolinite with traces of Smectite.

2.3.7 Source Rocks of the White Nile

The White Nile starts at Lake Victoria and travels North through the Sudd, a large swampland in center of South Sudan. The Sudd acts as a catchment basin for the majority of the White Nile sediments collected from the headwaters. Due to the Sudd, the sediment brought from the White Nile into the Nile River is sourced from the portion of the river north of the Sudd and is in general a very small contribution to the overall sediments of the Nile River. Mineralogical and isotopic signatures of the White Nile sediments show them to be derived respectively from Archean gneisses of Uganda and Neoproterozoic basements of Ethiopia. The sediments become gradually homogenized and enriched in quartz, and remain unchanged past Khartoum to deposition along the Nile banks (Garzanti, Ando, Vezzoli, Megid, & El Kammar, 2006).

2.3.8 Source of the Aeolian Dust

The Nile River is exposed to 3000 Km of the sandy dunes of the Sahara desert as the river winds its way north from Khartoum to the Mediterranean Sea. An unquantifiable amount of the sand is blown into the river. This material is then deposited as a portion of the Nile River Alluvial soils. The Sahara sands are predominately composed of the following minerals, quartz, dolomite, calcite, smectite, halite and kaolinite, where the clay minerals have been formed through weathering. The windblown dust has an average particle size ranging from 4 μm to 32 μm . (va der Does, Korte, Munday, Brummer, & Stut, 2016). The dust particle size is dependent on the season, with coarser particles being generated during the summer and finer particles in the winter. Aeolian dust has become a major contributor to the Nile River sediments since the completion of the Aswan Dam in 1970.

2.3.9 Nile Sediment Deposition Rates

Just like the depth of the Nile alluvial sediments varies in the flood plain, the deposition rate of the sediments has varied over time and at different locations. The rate of deposition is thought to be most closely related to the level of the Mediterranean Sea. The deposition rate near Cairo had been periodically measured and was found to be about 21 cm a century from 1330 to 1630 and 8 cm a century from 1630 to 1841. The period of 1330 to 1630 was found to correspond to high sea level in the Mediterranean Sea and the period of 1630 to 1840 corresponds to low Mediterranean Sea level due to the little Ice age of Europe (Said R. , 1993). The last known effort to estimate the rate of sediment accumulation in the Nile River was performed by John Ball in 1939. He estimated that out of 110 million tons of sediments carried by the Nile annually 52 million tons settled out before the Mediterranean. This would correspond to a deposition rate of 10 cm per century. Diversion of the Nile River for irrigation, complicates the estimation of deposition making similar studies no longer feasible. Due to the

impoundment of sediments by the Aswan Dam and areal changes due to land subsidence, the Nile Delta is being eroded by the Mediterranean Sea. With the current deposition rate not sustainable for delta growth.

2.3.10 Nile Silty Clay Summary

Nile silty clay is an alluvial deposit found along the banks of the Nile River from Khartoum in Sudan, North to the Nile River Delta in Egypt. The soils is a mix of clays, silts and sands. The source of the sediments has been found to vary with time and climate. In general the dominant clay mineral, dioctahedral smectite is thought to originate from the weathering of Basalts in the Ethiopian highlands. The coarse mineral grain fraction are thought to be historically predominantly from Egyptian wadis during times of rain within Egypt. As the climate became more arid and the wadis were dry for longer periods, Aeolian dusts from the Sahara desert supplanted the wadis as the mineral grain source. Both of the wadis and Aeolian dust have the same parent rock Nubian sandstones. As such the major variation in the change in transport is average particle size with larger particles coming from the wadis. Nile silty clay has mollusk fragments that may contribute to cementation of the soil. The sample provided to the Tufts Advanced Geomaterials laboratory came from a shallow construction excavation within Cairo. The depth of the excavation is not known, but is estimated to be between 10 and 15 ft. Well below where the effects of the sediment impoundment from the Aswan Dam would be observed.



Figure 2-1: Location of the Country Egypt Bordered in Red (Background Map from Google Maps 2018)

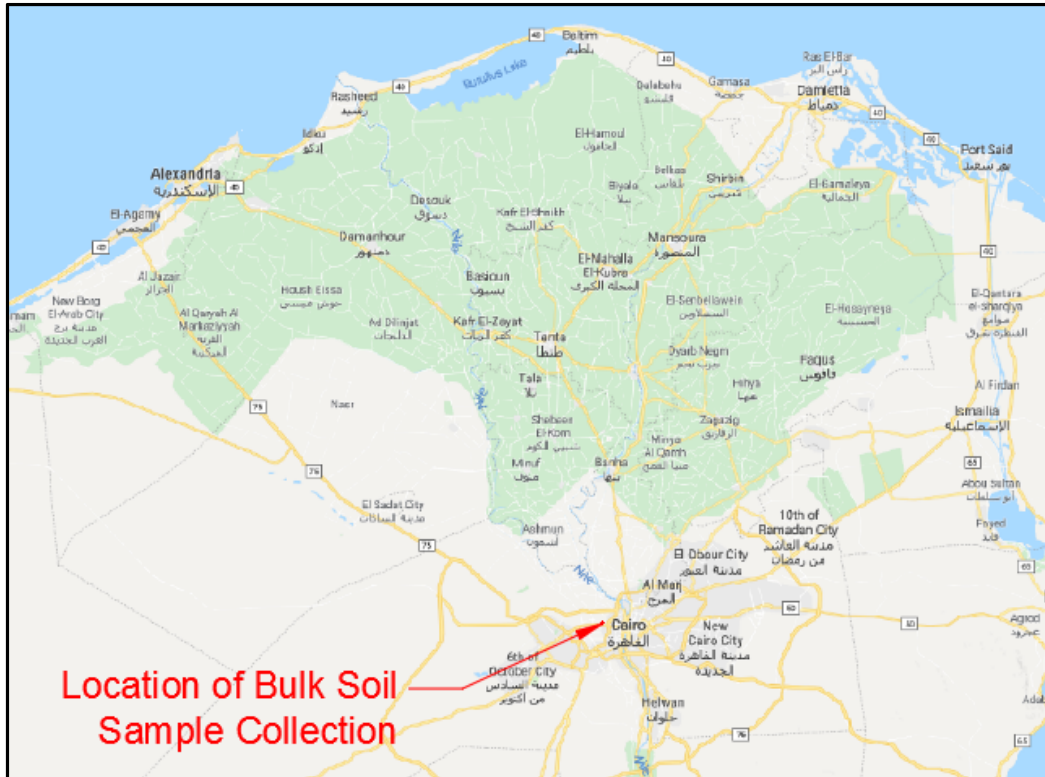


Figure 2- 2: Location of Bulk Sample Collection Within Cairo and Nile River Delta (Background Map from Google Maps 2018)

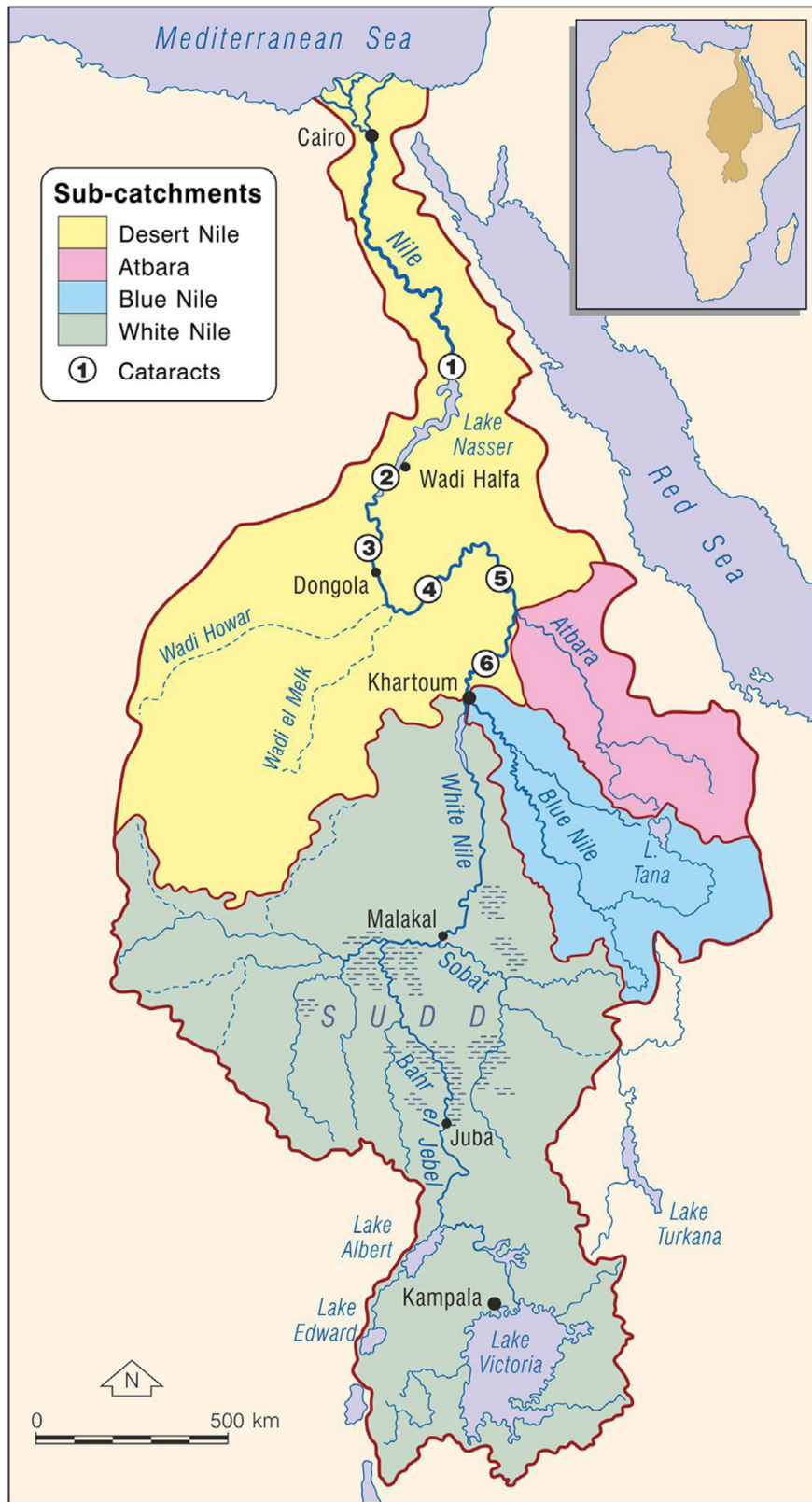


Figure 2- 3: Major tributaries of the Nile River from (Woodward, et al., 2015)

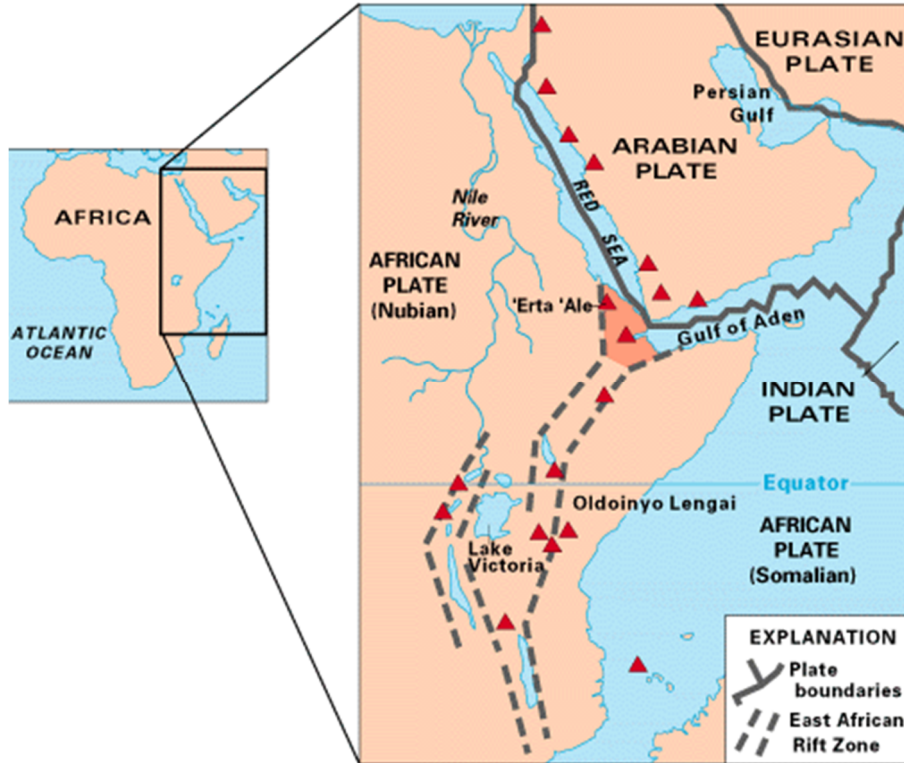


Figure 2- 4 African tectonic plate boundaries in Ethiopia from (USGS, 2014)

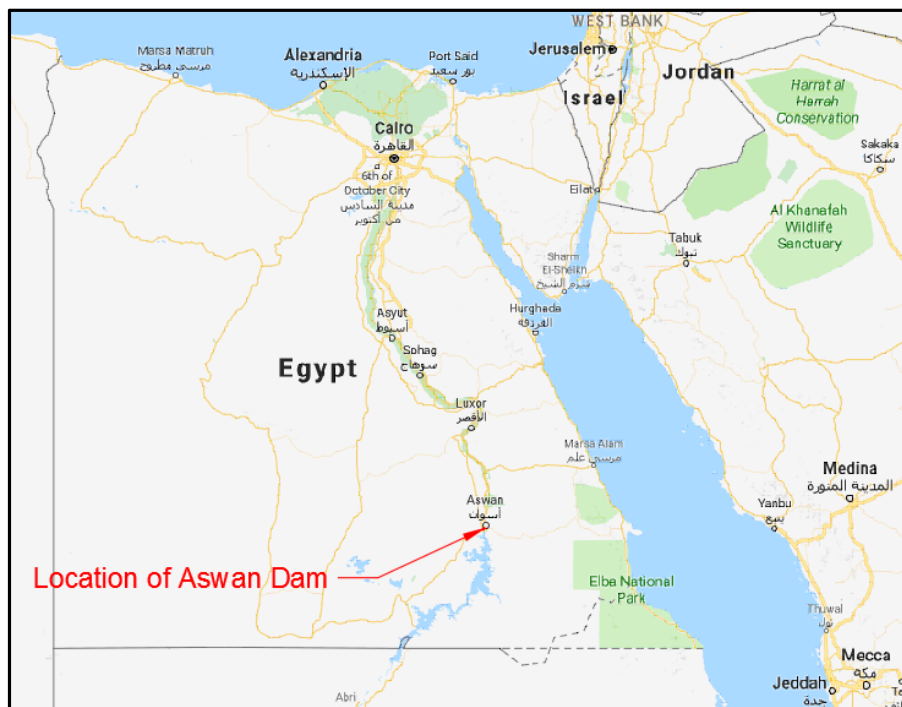


Figure 2- 5: Location of Aswan Dam in Southern Egypt (Background Map from Google Maps 2018)

Chapter 3

Specimen Preparation and Scope of Testing Program

3.1 INTRODUCTION

The behavior of fine grained soils can be quantified through three distinct testing categories. Index property tests can be used to classify the material by physical properties for field identification. Compression tests can be used to measure the compressibility and permeability of the soil. Triaxial shear tests can be used to measure the shear strength and Mohr Coulomb failure envelope of a fine grained soil. A thorough fine grained soil testing program should include a description for field identification and the estimation of engineering parameters for appropriate use in design. This chapter reviews the specimen preparation, and laboratory testing methods used for the classification and estimation of engineering parameters of Nile Silty Clay.

Section 3.2 describes the specimen preparation methods for reconstituted fine grained soil specimens. When intact specimens are not available for a variety of reasons reconstituted specimens can be a suitable alternative. Reconstituted clay specimens were created through the resedimentation procedure of incrementally loading a clay slurry in a rigid wall consolidometer. Resedimentation has been found to provide very consistent test specimens. The procedure has evolved from the earliest methods detailed within Ladd & Varrallyay (1965) through a refinement detailed within Germaine (1982) and finally to the current practice detailed within Abdulhadi (2009).

Section 3.3 describes the Tufts Advanced Geo-Materials (TAG) Laboratories automated testing equipment, electronic instrumentation, and data acquisition system used for the laboratory program presented herein. Section 3.3 presents the required electronics and equipment and protocols to operate the Tufts automated triaxial cell and automated constant rate of strain testing apparatus.

Section 3.4 details the laboratory testing methods used for soil identification and the estimation of engineering parameters for Nile Silty Clay. This section presents a detailed description of the index property tests, procedures for Constant Rate of Strain (CRS) compression testing, and triaxial shear testing.

3.2 SPECIMEN RECONSTITUTION

3.2.1 Intact Specimens

Intact clay samples collected from a thin walled metal sampling tube under the weight of a drilling fluid is considered to be the gold standard in sample collection. But there are issues with this procedure. It is costly, time consuming, there is no control on variability between specimens, and the samples are prone to disturbance both during insitu sample collection and during transportation. Reconstituted specimens allows for a systematic study of behavior as a function of material density, void ratio, grain size distribution and other observable factors. However, the fabric of a reconstituted material is thought to differ from a naturally deposited material as such the prediction of insitu behavior based on reconstituted specimens is uncertain. Reconstituted specimens can be used to observe and identify behaviors within a soil, while acknowledging there may be slight variations when transferred to the natural condition.

There are several different reconstitution methods for creating soil samples. This research will focus on the evolution of the clay slurry sedimentation method. The slurry sedimentation

technique was used due to the reproducibility in specimen creation and degree of control over the specimens stress history.

3.2.2 Introduction to Resedimentation (Slurry Sedimentation)

This method involves the one dimensional incremental consolidation of a dilute soil slurry in a rigid wall cylindrical container (consolidometer). Earlier methods Ladd & Varrallyay (1965) produced samples that were partially saturated and required the application of back pressure to achieve full saturation. Germaine improved upon the process (Germaine, 1982) which then produced fully saturated samples with a pore fluid salt concentration of 16 g/l. The next major evolution in the process was the addition of instrumentation to improve the uniformity and provide continuous monitoring of the process (Seah, 1990). These methods form the foundations of the resedimentation procedure that we know today. The consolidometer used at this time was 30 cm in diameter and the resultant product was a large soil cake that would be trimmed down for several different tests. Due to the large surface area, the loads required to consolidate the slurry were significant and considered inefficient. The large diameter was originally used due to concerns of sidewall friction causing nonconformities within the specimens.

An updated resedimentation procedure was developed in order to create individual test specimens (Abdulhadi, 2009). The updated procedure reduced the rigid wall cylinder diameter to an internal diameter of 7.6 cm. The reduction in the diameter of the specimen reduced the cross sectional area for the slurry which has greatly reduced the required load for each load increment. This reduction of the consolidometer diameter did introduce the effects of sidewall friction during specimen creation. The effects were found to be manageable if the bottom of the rigid walled consolidometer was elevated during consolidation, allowing the sample to strain

from both the top and bottom (Casey B. , 2014). The specimens reconstituted in small diameter consolidometers have been found to vary in density through the sediment column. This has been attributed to the applied stress acting fully on the top and bottom of the sediment column. In between the top and bottom of the sediment column the stress is reduced by sidewall friction proportional to the distance from the top of the column at low stresses (<0.1 MPa) or from either end at higher stresses (>0.1 MPa). In general the variance between sample densities, from large and small diameter consolidometers, is largest at low stresses and decreases as stress increases. Also from Casey B (2014) if a triaxial specimen is k_0 consolidated prior to shearing, the k_0 consolidation phase will largely eliminate density nonconformities due to sidewall friction.

3.2.3 Resedimentation (Slurry Sedimentation) Process

The resedimentation process starts with a bulk clay powder as shown in Figure 3-1. The clay powder is the result of a bulk sample collected in the field, air dried, and ground. Three different bulk powders were stored for Nile Silty Clay. The powders are labeled by series designation as Series I, Series II, and Series III. Each series had a different grain size distribution as described further in Chapter 4. The air dried powder is blended until thoroughly homogenous. This blending process greatly increases the reproducibility in the specimen creation process. The blended bulk powder is then mixed with a saline solution of 1 gram of sea salt per liter of water. The 1 g/L of sea salt to water does not account for the natural salt content of Nile Silty Clay which was found to be low as discussed in Chapter 4. The clay powder and saline water are mixed in controlled mass amounts and thoroughly blended with a stand mixer until a resultant homogenous stable clay slurry is formed as shown in Figure 3-2. The slurry is considered stable when there is no free water on its surface after a 24 hour period. The mixed slurry is allowed to temper in a confined container for a minimum of 12 hours. During tempering, the clay minerals are hydrated with the saline solution. After tempering the clay

slurry is evacuated through the use of a vacuum pump and a pressure chamber as shown in Figure 3-3. The evacuation of the clay slurry ensures saturation of the specimen and removes trapped air that would result in voids within the sample during resedimentation. The evacuated slurry is then tremied into a thick walled consolidometer shown in Figure 3-4 with the use of a funnel and tube to place the slurry from the bottom upwards. This method of placement limits the amount of trapped air within the specimen. Prior to the slurry being placed in the thick walled consolidometer cylinder, the interior of the cylinder is cleaned with silicon oil to reduce friction during the consolidation process. Porous stones and filter paper sandwich the slurry column to allow for drainage during consolidation. The porous stones are approximately the same diameter as the interior of the rigid walled cylinder to limit extrusion of the slurry around the porous stone during loading. Filter paper is used to separate the porous stone from the slurry column to limit clay particles from migrating into the porous stones. The soils are consolidated through a load that is applied to a piston at the top of the slurry column. A photograph of a thick walled consolidometer is shown in Figure 3-5.

The soil slurry is incrementally loaded by applying a load to a piston at the top of the slurry column with a load increment ratio $\frac{\Delta\sigma_v}{\sigma_v} = 1$. The slurry is loaded to a prescribed maximum vertical effective stress then unloaded to an overconsolidation ratio (OCR) of 4. At an OCR=4, the effective stress state of the sample is close to hydrostatic as such the shear stresses induced during extrusion and trimming of the sample are minimal as confirmed by Santagata (1994). The load is typically applied using dead weights hung from a hanging centralizer to ensure that the point of loading is at the center of the slurry column. During consolidation a single displacement transducer (LVDT) may be used to measure the vertical deformation. From the LVDT data the time to end of primary consolidation is determined using Cassagrande's log time

method (Germaine & Germaine, 2009). For RNSC the time to the end of primary consolidation was typically 48 hours. Each load increment is held until the end of primary consolidation, and the maximum load increment is held until the end of 1 log cycle of secondary consolidation typically 48 hours. In general due to the low stresses RNSC was tested at; resedimenting a specimen took two to three weeks in total.

After consolidation is complete, the soil specimen is then extruded from the consolidometer and prepared for the testing apparatus. The sample is extruded by using a piston to push the sample while carefully holding the consolidometer. A hydraulic jack can be used if the resistance does not allow for extrusion by hand. The sample is trimmed using a trimming stand, a wire saw, and a razor. A photo of the triaxial test trimming setup is shown in Figure 3-6. For the CRS, test the sample is trimmed with a trimming stand, a cutting shoe that is integral to the CRS apparatus and a specialty tool to remove excess material from the cutting shoe. A photo of the typical CRS trimming setup is shown in Figure 3-7. During both trimming processes, the excess material is used to determine a water content of the material prior to testing.

3.3 LABORATORY TESTING EQUIPMENT

3.3.1 Introduction

This section describes the testing equipment that has been automated by computer control. The triaxial testing methods and systems described herein are based on previous technology that was developed at MIT (Sheahan & Germaine, 1992). The Constant Rate of Strain (CRS) testing methods and equipment is based on previous technology that was developed at MIT (Wissa, Christian, Davis, & Heiberg, 1971).

Automation brought finer control over the test process combining the existing test equipment (load frame, triaxial cell, etc.) with electronic components (motors, transducers,

analog-to-digital converters, etc.) The inclusion of the electronics within the existing test equipment allowed for a computer to monitor and maintain stress states or strains within a specimen. The addition of electronic instrumentation, an analog-to-digital converter, and a data acquisition system provided a higher degree of accuracy to the computerized tests. The following sections describe how computerized automation was incorporated in to a triaxial test cell and CRS test equipment.

3.3.2 Automated Stress Path Triaxial Cell

The triaxial tests reported herein were carried out in a low capacity pressure cell developed at MIT and explained in significant detail within Sheahan & Germaine (1992). The major components of testing equipment and the incorporation of the automation will be described within this section.

The triaxial testing apparatus consists of an acrylic cell, internal posts, base and top pedestals, base and top drainage lines, internal load cell, a movable top piston, a fixed top cap and all necessary rubber O-ring seals to maintain pressure within the cell. The soil specimen is separated from the chamber fluid through the use of two thin impermeable rubber membranes, typically unlubricated Trojan brand latex condoms. The thin membranes are sealed against the base and top pedestals by rubber O-rings. The top cap is connected by a threaded rod connection to a compact shear beam load cell (500 lb., 2.2KN capacity) within the triaxial cell. The internal load cell eliminates the effect of piston friction on the loading measurement. The electronics for the load cell are wired through the base of the triaxial cell. The load cell is connected to the base of a piston centered in the triaxial cell, aligned by an O-ring seal and linear bearing within the top of the triaxial cell. The Piston movement is monitored by an externally mounted LVDT.

The triaxial cell is filled with Dow-corning “200 fluid,” 20 centistokes silicone oil. This silicone oil has a low viscosity under a wide range of temperatures which makes it ideal for triaxial testing. The oil is also transparent and does not degrade the rubber O-ring seals or membranes. The oil is also non-conductive which allows for the use internal electronics such as the internal load cell without the need of a sealed connection.

The triaxial cell is set in a ½ ton Wykeham Ferrance screw driven load frame with adjustable gear ratios. The screw driven load frame consists of a base with a gear driven piston, two vertical columns, and an adjustable crossbar connecting the two vertical columns. The triaxial cell base is placed on the top of the screw driven load frame, and adjustable crossbar is set so that it restricts the vertical movement of the triaxial piston with a spherical moment break between the top of the piston and load frame crossbar. The load frame is powered by a computer controlled DC-servo electric motor. The cell fluid and pore fluid are controlled through the use of a MIT-designed Pressure-Volume Actuator (PVA). PVAs are screw actuated pistons that are powered by computer controlled DC-servo electric motors. Both the cell fluid and pore fluid pressures are monitored with 200 psi (1.4 MPa) diaphragm type pressure transducers. The pressure transducers are located on the base of the triaxial cell to limit the amount of piping necessary. This helps to reduce system compliance issues. A diagram of a typical automated triaxial test setup is shown in Figure 3-8 and a photograph of a typical Tufts University triaxial apparatus is shown in Figure 3-9.

For tests run in the compression mode, the soil is loaded by the load frame piston pushing the triaxial cell upwards and the triaxial piston remaining in a constant position. For soils load in the extension mode, the triaxial cell base is clamped to the load frame piston and

the triaxial cell piston is bolted to the load frame cross bar. During the test the load frame piston is retracted and the triaxial piston is held in the same location.

The entire triaxial test apparatus is in a temperature controlled space within the climate controlled laboratory.

3.3.3 Automated Constant Rate of Strain Test Apparatus

The CRS tests reported herein were performed with a Trautwein brand C200000 CRS apparatus. The apparatus consists of a rigid cell made of steel or plastic, a steel base with drainage ports, a steel top with linear piston bearing, rubber O-rings seals and bolts to connect the three parts. A soil sample is trimmed into a fixed rigid ring and then sandwiched between layers of nylon fabric filter paper and porous stones. The fixed boundary conditions force one dimensional deformation. Prior to loading, the specimen is incrementally back pressured to ensure saturation and the pore fluid pressure is controlled by a PVA. During the constant rate of strain test, the sample is initially loaded slowly, as the computer controller increases the load continuously up to a predetermined constant rate of strain. The strain rate is measured by a pair of external LVDTs. The excess pore pressure generated during loading at the bottom of the sample is measured by a 200 psi (1.4 MPa) diaphragm type pressure transducer.

The CRS apparatus is set in a Wykeham Ferrance screw driven load frame with 1,000 lbs. capacity, and adjustable gear ratios. The screw driven load frame consists of a base with a gear driven piston, two vertical columns, and an adjustable crossbar connecting the two vertical columns. The CRS base is placed on the top of the screw driven load frame piston and the adjustable cross bar is set such that a load cell mounted on the crossbar is in contact with the top of the CRS piston through a spherical moment and shear break. The CRS test uses an external load cell to make load measurements on the specimen. The load frame is powered by a

computer controlled electronic motor. A diagram of a standard Trautwein CRS apparatus can be found in Figure 3-10 and a photograph of a typical Tufts University CRS setup can be found in Figure 3-11.

3.3.4 Electronic Laboratory Instrumentation

Accurate and timely measurements of force, distance, and pressure are required to run triaxial and CRS tests on soil. Electronic instrumentation was used for the tests performed reported herein. Electronic instrumentation was used, to run tests semi-autonomously, to provide high reading frequency, and to ensure high accuracy in the measurements made. Through the use of multiplexers the electronic instrumentation can be read and stored within a central data acquisition system. A localized power supply provides the power for an individual test setup which is typically around 5.5 volts Direct Current (DC). The input voltage is recorded with the measurements, as each of the electronic instrumentation is normalized to the input voltage to reduce sensitivity to changes in the input voltage. The electronic instrumentation is calibrated with the measured voltage normalized to the input voltage for this same reason. A typical calibration factor is then unit of measurement per volts per volts. The instrumentation can be separated into distinct categories of Linear Variable Displacement Transducers (LVDTs), load cells, diaphragm type pressure transducers, and Pressure-Volume Actuators (PVAs). The following sections describe the instrumentation used and Table 3-1, 3-2, 3-3, and 3-4 provide the device name, calibration factor, resolution, and transducer stability for each of the Tufts University testing devices used within this experimental program.

3.3.4.1 Linear Variable Displacement Transducers (LVDT)

Trans-tek (series 240) LVDTs were the standard LVDT used to measure displacement during resedimentation, triaxial tests and CRS tests. These transducers have a linear working

range of 2.5 cm with an additional 1.3 cm non-linear zone. In general only the linear range was used for measurement purposes. The LVDT consists of two parts; a ferrous rod core, and cylindrical body that is a faraday cage enveloping two coils of wire. The ferrous core is inserted into the body and an input voltage is run through one of the wire coils. The resulting magnetic field is sensitive to the position of the ferrous core and the output voltage from the non-electrified coil is directly proportional to the location of the ferrous core. The ferrous core is typically spring loaded to ensure a smooth and consistent measurement.

3.3.4.2. Load Cells

The load cells used were dependent on the test apparatus. A Data Instruments (model JP-500) 500 lbs (2.2 kN) capacity load cell is used to measure load for triaxial tests with internal load measurements. CRS tests used a CAS Corporation (model SBA-2.5KLB-I) 2,500 lbs. (11.1 kN) capacity load cell. Both load cells use an s-shaped steel section instrumented with strain gauges to measure load. During loading the input and output voltages are monitored; changes of voltage are proportional to the elastic deformation of the steel section.

3.3.4.3. Pressure Transducers

Pressure transducers are used to measure the pore pressure and cell pressure during a triaxial test as well as the generated pore pressure during a CRS test. Data Instruments AB/HP diaphragm type pressure transducers with 200 psi (1.4 MPa) capacities are used for both test set ups. The pressure transducer consists of a steel diaphragm with two strain gauges. Similar to the load cell, during loading the input and output voltages are monitored; changes of voltage are proportional to the elastic deformation of the diaphragm.

3.3.4.4. Pressure-Volume Actuators (PVA)

A computer controlled pressure volume actuator is used to control fluid pressures during testing, for both triaxial and CRS testing apparatuses. A PVA is also used to monitor volume changes of pore fluids in triaxial tests. A typical Tufts PVA was designed at MIT and consists of a piston in a sealed tube; a computer controlled electric motor to actuate the piston, a fluid reservoir connected by a valve to the tube and a LVDT to measure to position of the piston. The PVA piston has a known area so the displacement within the hollow tube is proportional to a pressure. The computer controlled motor will move the piston which creates the desired pressure in a feedback loop from the computer controller to the pressure transducer. The reservoir is used to fill the hollow tube with fluid when necessary. The piston position is measured with either a Trans-tek (series 240) LVDT with 10 cm working range or a Celesco (SP1) linear position transducer (string pot) with a 30 cm working range.

3.3.4.5. Central Data Acquisition System (DAQ)

The TAG Laboratory is equipped with a central data acquisition system (DAQ). This allows for the cost-efficient and accurate collection of a large volume of electronic instrumentation measurements. The system is flexible and allows for changes in data collection timing and instrumentation. The system consists of four components, the first being the laboratory box which contains the power supply, junction box, voltmeter, and ground. Second, a laboratory wide multiplexer allows the DAQ system to switch between instrumentation channels. Third the analog to digital converter; the TAG lab DAQ includes a Hewlett Packard HP3497A 5-1/2 digit integrating analog to digital (A/D) converter. The HP3497A A/D converter is capable of monitoring 1000 analog channels simultaneously. The HP3497A A/D converter is sensitive enough to resolve 1 microvolt signals and has auto range matching over four voltage scales (0.1, 1, 10 & 100 Volts). The fourth component is a computer to store the data and

perform the administrative scheduling tasks for the A/D converter. The TAG lab A/D converter, once scheduled, runs independent of the instrumentation at the testing apparatus. It only reads the instrumentation channel in accordance with the programmed testing schedule. Figure 3-12 shows a photograph of the TAG lab DAQ system.

3.3.4.6. Computer Control System

The initial automation of a triaxial control system was performed at MIT (Sheahan, 1991). The addition of electronic instrumentation, a computer control program, and a localized A/D converter to a traditional triaxial cell allowed for increased quality control and increased testing flexibility. Automation allows for much greater control in the testing process and reduces the possibility of human error.

Testing automation protocols are controlled through a feedback loop for the driving system of the apparatus. For example, during the undrained shearing portion of an undrained triaxial test, the strain rate of shearing is computer controlled and the end of undrained shearing is determined by a strain or stress limit. During this phase, the feedback loop is driven primarily through the LVDT. The electric motor on the load frame loads the specimen in accordance to the voltage sent to it by the computer controller. The LVDT measures the deformation of the specimen, while the computer controller monitors the LVDT through the localized A/D converter. The computer controller calculates the strain rate and varies the voltage sent to the electric motor on the load frame to maintain the strain rate set during the start of undrained shearing. When the predetermined axial stress or maximum strain is hit then the computer control stops shearing the specimen. The computer controller runs a second feedback loop, to keep cell pressure constant during undrained shearing. This loop is controlled through measurements by the cell pressure transducer.

The computer control equipment used to run a Tufts University automated triaxial cell is one with a disk operating system (DOS) environment, an A/D converter, a multiplexer and a digital motor encoder or a D/A converter. The Tufts University CRS and Triaxial computer controllers, depend on programming written in quick basic (QB) within the DOS environment. A few of the triaxial tests reported herein were run on a Windows 98 computer in the DOSBox simulated DOS environment. As these computers no longer support Industry Standard Architecture (ISA) ports, an ISA to Universal Serial Bus (USB) converter was required. The ISA to USB converter used was manufactured by ARS Technologies. The ARS converter works by inputting a series of hexadecimal bits within the computer memory to allocate the input/output channels as the ISA channels. Older model computers had to dedicate memory for ISA peripherals; modern computers no longer allocate dedicated memory as it is not necessary for USB peripherals. The ARS computer chip allows the user to provide dedicated input/output channels for an ISA peripheral on a modern computer.

The multiplexer for a typical triaxial test setup has eight separate channels. There are six dedicated channels for the LVDT, load cell, pore pressure transducer, cell pressure transducer, PVA, and input voltage. This leaves two channels available for additional instrumentation. The multiplexer connects to the computer controller and the voltages from each channel are converted to digital signals through an Analog Devices AD1170 A/D converter. The analog devices A/D converter is a minimum 22 bit resolution device. The very high resolution in the local A/D converter is required for very precise control in the testing apparatus. This equipment and terminology is discussed in greater detail within Sheahan & Germaine (1992).

After the computer controller reads the instrumentation, the QB program then compares the measured values to the target values. The program determines corrective action (minimizing the difference between the measured value and target value) using either intermittent proportional or continuous proportional integral differentiation (PID) control to generate a digital signal. The computer controller sends this digital signal through a Strawberry Tree Inc. D/A converter with a 12 bit resolution and ± 5 volt range. The Strawberry tree converts the digital signal to an analog voltage for the Electro-craft variable voltage motors.

An update to the control system has been made within Casey B (2014) as the Electro-craft motors had become obsolete and were updated with Maxon brand electric motors. The Maxon brand motors are controlled by Escon 50/5 servo controllers. The Escon controllers take the analog signal from the Strawberry Tree card and drive the Maxon band motor at a rotation rate that is proportional to the control voltage. Power for the motors is provided by a 50 volt DC power supply. The Escon 50/5s servo controllers can run the relic Electro craft motors if the input voltage from the tachometer is split such that 1/3 of the total voltage is used for feedback control. When required the voltage was split by wiring resistors into the motors wiring harness.

3.4 LABORATORY TESTING METHODS

3.4.1. Introduction

The laboratory testing methods utilized within this research are common practice within the geotechnical community and can be parsed into three distinct groups. First, there are the index property tests. These tests are used to classify the material and its constituents and to determine if there will be any non-standard behaviors present due to cementation or organic content within the soil. The second distinct category of tests is consolidation tests, which for this research will be limited to CRS tests. CRS tests measure compression behavior and

hydraulic conductivity of the soil. The final category of tests performed on RNSC is triaxial shear type tests. Strength anisotropy was explored within RNSC through the use of triaxial compression and extension tests. The effects of over-consolidation were explored by swelling test specimens within the triaxial cell prior to shearing. The following sections provide detailed information on the testing procedures.

3.4.2. Index Property Tests

Index properties are measurable values that help classify a soil. The classification of soils by geotechnical engineers is typically performed through a measurement of the constituent particles sizes, behavior at various water contents, and organic material content. For RNSC, the sedimentation method was used to determine the grain size distribution. Materials with an appreciable content of finer grains (>5% smaller than 0.075 mm) are classified by index values. These tests are known as the Atterberg Limit tests and they are used to measure the liquid limit and plastic limit of the soil. These tests are required to classify the soil by the Unified Soil Classification System (USCS), the most widely used soil classification system within the Geotechnical community. To ensure that the USCS classification for RNSC was accurate, the material was tested for organics content and calcite equivalency. The specific gravity and natural salt content of RNSC, was measured to support calculation in other tests. A RNSC sample was sent out to have the mineralogy determined through X-Ray Powder Diffraction (XRPD). Also a study on the fabric of oven dried RNSC was performed through the use of a JEOL Cross Section Polisher (ion mill) and a ZEISS Scanning Electron Microscope.

An important note on terminology within this research , about the usage of the term clay; clay will refer to a particle that is less than 0.002 mm (Germaine & Germaine, 2009) in size and not clay classified by mineralogy.

3.4.2.1. Particle Size Distribution

The particle size distribution of RNSC was determined through a sedimentation test. A sedimentation test measures the distribution of particle sizes by measuring the change in specific gravity of a column of fluid due to soil particles settling out over time. Stokes Law is the controlling theory behind sedimentation. Through Stokes law the terminal velocity of a falling particle can be related to the density difference between the particles and fluid. By knowing that the terminal velocity is proportional the square of the particle diameter the settling particles are able to be separated by size, time and position within the column of fluid (Germaine & Germaine, 2009). A full description of the procedure is available with ASTM-D7928 Particle Size Analysis of Soils. 5 grams of Sodium Hexametaphosphate is added to the soil to help break up clay floccs. A temperature reading is also performed at the same time as a specific gravity reading in order to compute the fluid density and viscosity.

3.4.2.2. Atterberg Limits

The Atterberg limits are determined for fine grained soils (>5% smaller than 0.075 mm). The limits are conceptual boundaries between various states of material behavior involving changes in water content. The liquid limit test determines the water content that separates the material behavior of a soil from a solid to a viscous liquid. The test is fully described in ASTM D4318. In general, the soil is placed in a testing apparatus known as a Cassagrande cup and a vertical groove is cut in to the soil. The test is performed by measuring how many drops (blows) of the cup are required to close ½ in. of the vertical groove. This test is performed for a minimum of five readings, with blows between 10 and 50. The soil is typically allowed to dry to change the blows recorded during the test. The water content of the soil is determined for each blow number. A plot of the water content by blows is created. The liquid limit of a soil is the water content that corresponds to 25 blows on a linear best fit line through the recorded data

(Germaine & Germaine, 2009). Figure 3-13 shows a photograph of the Cassagrande cup used for the liquid limit test.

The plastic limit is the water content that separates a semi-solid material behavior from the plastic material behavior. The test is fully described in ASTM D4318. In general, the soil is rolled into a thread on a glass plate to a 1/8 in. diameter. When the thread crumbles at exactly a 1/8 in. diameter the soil has hit the plastic limit. The plasticity index is the average water content for a minimum of three threads that crumble at 1/8 in. diameter (Germaine & Germaine, 2009).

The difference between the liquid limit and plastic limit is the plasticity index. A plot of liquid limit by plasticity index is used to classify the behavior of fine grained materials within the USCS.

3.4.2.3. Calcite Equivalency

Carbonate cemented soils behave differently than non-cemented soils. Calcite equivalency tests approximate the amount of carbonate within an unknown material (Germaine & Germaine, 2009). The test is fully described in ASTM D4373. The first step is to calibrate the measuring apparatus with pure calcium carbonate. A mass of pure calcium carbonate (0-1 gm) is placed within a sealed chamber of known volume and connected to a pressure transducer. A vial of a 1 normal solution of hydrochloric acid is also placed within the sealed container. When the chamber is sealed, the vial is tipped over and allowed to react with the calcium carbonate; the reaction is assisted with mixing by a wrist shaking action. The resulting gas pressure is recorded for minimum of 1 hour. The calibration for the chamber is found through the maximum pressure in terms of grams of calcium carbonate. The same process is recreated with 1 gm of the soil of unknown calcium content. The final change in pressure within the container

from the reaction with the unknown material compared to the pure reaction can be used to estimate the amount of carbonate ions in the material. This test is known as a calcite equivalency test due to calcium carbonate being the reference reaction. There are several carbonate containing minerals that are not calcium carbonate which will also off gas during this test. Figure 3-14 shows a photograph of the typical setup for the calcite equivalency test. Figure 3-15 shows the calibration curve developed for the pressure vessel used for calcite equivalency testing within this research.

3.4.2.4. Organics Content

Appreciable organic matter can significantly vary the behavior of soils, due to their compressibility, potential for degradation, and capacity for water storage. Organic content is determined through a loss on ignition testing. The test is fully described in ASTM D2974. In general a small sample of the soil at known water content is placed in a muffle furnace set to 400°C overnight. From the resulting change in mass the organics content can be approximated. This is an approximate measure as the water associated with the clay particles is also removed during this test.

3.4.2.5. Specific Gravity

The specific gravity of a soil is the ratio of its density to the standard which is typically pure water at 20 degrees Celsius in the geotechnical community. Several testing procedures and phase relationship calculations are reliant on accurate specific gravity measurements of the soil. The procedure is fully described in ASTM D854. In general, a sample of soil is submerged in distilled water inside a flask of known volume. The mass of the flask and submerged soil is measured several times under controlled temperature conditions. The flask is also measured containing distilled water only. From these two sets of measurements, a relationship of the

water displaced and the mass of the solids can be made to determine the specific gravity of the soil. The temperature is closely monitored to correct for variations in water density.

3.4.2.6. Salt Content

The chemical composition of the pore fluid of a fine grained soil is significant to the engineering properties of the soil as the strength for a fine grained soil is derived through long distance chemical forces (Mitchell, 1976). Salt concentration can affect the creation of clay floccs and in turn affect the specimen during the resedimentation process. Salt concentrations are also accounted for in phase relationship calculations during laboratory testing. The amount of dried salts is considered in the amount of dry mass at the end of the oven drying portion, of a laboratory test.

The salt content of the bulk powder is the amount of salt found within a set mass of bulk clay powder and is usually presented as grams of salt per kilogram of clay powder. There is no standard test procedure for measuring the salt content of soil. Instead a procedure which measures the conductivity of the supernatant liquid from a test tube in which the soil and distilled water is spun in a centrifuge is used as recommended in Martin (1982) and detailed within Germaine & Germaine (2009). The procedure is as follows:

1. The mass of the centrifuge test tube and cap are measured to 0.01 g.
2. Approximately 15 g of the wet soil is added to the centrifuge test tube.
3. The mass of the centrifuge test tube, test tube cap, and soil are measured to 0.01 g.
4. Approximately 15 g of distilled water is added to the test tube.
5. The mass of the test tube, test tube cap, wet soil, and distilled water is measured to 0.01 g.

6. Small glass beads are added to the test tube. The test tube is shaken vigorously for 30 seconds. The test tube is allowed to sit post shaking for 20 minutes to equilibrate and then shaken again for 30 seconds.
7. The test tube is then placed in the centrifuge and spun at 5000rpm for 10 to 20 minutes.
8. The resultant supernatant liquid post centrifuge is decanted into a small glass beaker.
9. The conductance of a reference salt solution is measured with a conductance probe.
10. The probe is cleaned with distilled water.
11. The supernatant liquid from the test tube is measured with the conductance probe.
12. The probe is cleaned and stored.
13. The conductivity reading of the supernatant liquid is normalized to the conductivity of the reference salt solution and the free salts are calculated from a calibration curve of the normalized conductivity by salt concentration previously established for the conductivity probe.

Figure 3-16 shows the calibration curve for the conductance probe used for this research. The conductivity measurements are normalized to a standard solution to help alleviate conductance fluctuation due to temperature variations.

3.4.2.7. Mineralogy by X-Ray Powdered Diffraction (XRPD)

A sample of the bulk powder was sent to the James Hutton Limited Institute in Craigiebuckler, Scotland for qualification of the mineralogy by X-Ray Powder Diffraction (XRPD).

X-Ray powder diffraction consists of bombarding a representative fraction of the sample with electrons and recording the response spectra. Each crystalline material has different response spectra which can be used to determine the minerals present within the sample and their approximate concentrations. The clay minerals were identified as both a part of the total sample and as a percentage of the <.002 mm fraction to provide an indication of which minerals dominated the clay domain.

The clay samples used for x-ray diffraction are prepared differently depending on whether the bulk mineralogy of the samples is being determined or if the clay mineralogy is being determined. For the bulk mineralogy the total samples is used; the sample is dried and milled, a randomly selected representative portion is mounted on a glass slide for XRPD testing. To determine the mineralogy of the clay fraction of the soil sample timed sedimentation is used to separate the clay particles from the silt and sand particles. The clay slurry from the timed sedimentation test is then dried and mounted on a glass slide for XRPD testing.

The XRPD results and interpretations performed on RNSC by the James Hutton Limited Institute can be found in Appendix A.

3.4.2.8. Scanning Electron Microscopy

A study of the microstructure of RNSC was performed through the use of a scanning electron microscope (SEM). The samples viewed were oven dried and prepared in accordance to the methodology set forth in Derieh (2016). The clay samples were cut from oven dried triaxial specimens using a saw. The resulting sample blocks had rough dimensions of 1 cm x 1cm x 0.5 cm. In preparation of ion milling, two perpendicular faces of the block were polished. They were polished, using variable grit sand paper starting with an average grit size of 66 µm

and working down to an average grit size of 3 μm . Hand polishing the two sides limits curtaining artifacts from the milling procedure.

After polishing, the clay sample was mounted using Crystalbond adhesive and a hotplate set at 100 °C to a brass mount designed for use within the JEOL Cross Section Polisher. The sample was loaded into the cross sectional polisher's variable position slide and a steel mask was positioned so that 50-100 μm of the sample were protruding from the mask. Using a microscope with 200 times magnification the mask and sample were aligned within the cross section polisher such that the broad argon ion beam will have its midpoint directly on the mask edge. The 50-100 μm protruding from the steel mask will be removed by the argon ion beam and the material being covered by the mask will remain creating a perfectly flat surface in which to view the samples structure. In general, it takes 8 hours of milling to provide a 1 mm wide flat surface approximately 1/3 mm deep on the edge of the sample.

The samples viewed under SEM were cut from near the midpoint of the triaxial specimen. The SEM samples edge closest to the center of the triaxial specimen was polished within the JEOL Cross Section Polisher. The SEM specimen was aligned within the Cross Section Polisher such that the argon ion beam was applied parallel to the height of the triaxial specimen and perpendicular to the triaxial specimen's diameter.

After the samples are milled they were loaded into a Zeiss Supra55VP SEM. Within the SEM the samples are viewed using the secondary electron (SE) mode at a scanning voltage of 1-2 KV and a working distance of 3-5 mm. This work was performed at the Center for Nanoscale Systems at Harvard University.

3.4.3. Constant Rate of Strain (CRS) Tests

The Constant Rate of Strain test (CRS) methodology was developed in 1969 by Smith and Wahls (Smith & Wahls, 1969). The equipment developed by Smith and Wahls was improved upon by Wissa by adding the ability to back pressure saturate a sample prior to the compression (Wissa, Christian, Davis, & Heiberg, 1971). A commercially available Trautwein CRS device was used for this research. The procedure for a CRS test is outline in ASTM standard D4186.

A CRS test begins by applying a light film of vacuum grease to the specimen cutting ring of the CRS apparatus. Then the specimen cutting ring is mounted on the CRS trimming stand and lowered gently to make contact with the top of a specimen. The sample from the consolidometers should be slightly larger in diameter than the specimen cutting ring. The specimen is trimmed by lightly removing the excess material restricting the front of the cutting edge on the specimen cutting ring. This is done using a tapered dental tool. The weight of the cutting ring and trimming stand will drive the cutting ring down as the excess material is removed creating a very tight seal between the soil specimen and ring sidewalls. The top and bottom of the specimen is trimmed by using a razor and the cutting ring as a guide. After trimming is complete the initial height of the specimen is measure within the cutting ring. The initial mass of the specimen, cutting ring, porous stones and filter paper is measured prior to installing the cutting ring into the CRS apparatus. The drainage lines are connected and the specimen is back pressure saturated for a minimum of 24 hours. After back pressure saturation, the specimen is loaded at a constant rate of strain. The bottom drain line is closed during loading. The strain rate is determined by the average of two LVDTs mounted to the piston to monitor the deformation within the specimen and a computer controller using a PID feedback loop. Taking the average of two LVDTs provides a stable and constant strain rate during loading even if the piston is slightly eccentric.

During loading, the base of the CRS apparatus is attached to a pressure transducer, which measures excess pore pressure. The measured excess pore pressure provides the effective stress within the specimen as well as the hydraulic conductivity of the specimen for a given stress level. The hydraulic conductivity of a soil sample during a constant rate of strain test is calculated by the computer controller from the following equations.

$$\sigma'_{a,n} = \left(\sigma_{a,n} - \frac{2}{3} u_{m,n} \right) \quad \text{Equation (3.1)}$$

Where:

$\sigma'_{a,n}$ = Axial effective stress at time n.

$\sigma_{a,n}$ = Total axial stress at time n.

$u_{m,n}$ = Base pressure at time n.

$$k_n = \frac{1}{2} \frac{\varepsilon_n^\circ H_n H_0 \gamma_w}{u_{m,n}} \quad \text{Equation (3.2)}$$

Where:

k_n = Hydraulic Conductivity at time n

ε_n° = Strain Rate at time n

H_0 = Initial Drainage Height in the sample

H_n = Drainage Height in the sample at time n

γ_w = Unit weight of water

$u_{m,n}$ = Base pressure at time n.

The drainage height at time n is calculated through Equation 3.2.

$$H_n = H_0 - \Delta H_n \quad \text{Equation (3.3)}$$

- a. The change in height of the specimen is calculated by Equation 3.4 which incorporates corrections due to apparatus compressibility and uplift forces.

$$\Delta H_n = \delta_n - \delta_{af,n} - \delta_{ap,n} \quad \text{Equation (3.4)}$$

Where:

δ_n = Axial Deformation

$\delta_{af,n}$ = Apparatus compressibility correction due to loading

$\delta_{ap,n}$ = Apparatus compressibility correction due to cell uplift forces

The total axial stress at any time step during the test is calculated by Equation 3.4.

$$\sigma_{a,n} = \frac{f_{a,n}}{A} \quad \text{Equation (3.5)}$$

Where:

$f_{a,n}$ = The net force

A = Specimen area

A data reduction converts the recorded instrumentation readings to the measured strain, cell pressure, pore pressure, void ratio, hydraulic conductivity and effective and total stresses using Equations 3.1 to 3.4.

3.4.4. Triaxial Test Methods

Triaxial tests performed on RNSC, were performed with a Tufts University automated triaxial cell. Each test had the same initial steps. ASTM D4767 was the standard procedure

typically followed for triaxial testing of RNSC. A triaxial specimen was trimmed from the soil extruded out of a resedimentation consolidometer. Each specimen consisted of a cylinder with general dimensions of 8 cm tall and 3.5 cm in diameter. The specimen was sandwiched between pairs of moist porous stones, nylon fabric, and the pedestals of a triaxial cell. The specimen was then fully enveloped in two thin rubber membranes (Durex brand unlubricated condoms) which are sealed against the top and bottom pedestals with three rubber O-ring seals. The drain line to the top and bottom pedestals were previously filled with water prior to the sample being installed within the triaxial cell.

Once the specimen is sealed, the triaxial cell is assembled and the cell is filled with silicon oil. The cell oil is initially pressurized to a level that is equal to one fourth of the maximum stress from resedimentation. This is known as pressuring up the specimen. The pressure up step puts the specimen in an isostatic stress state and generates a slight positive pore pressure which provides a record of the sampling effective stress. After a minimum of 12 hours of pressure up the specimen is back pressure saturated at a constant effective stress. Back pressure saturation is achieved by slowly incrementing the cell pressure and the pore pressure in small steps to increase the pore pressure while leaving the samples effective stress generally constant. Back pressure saturation both drives water into the sample and any trapped air bubbles into the pore fluid. A minimum pore pressure of 0.2 MPa is typically used as the final pressure increment for back pressure saturation. The specimen saturation is of critical importance as soil stresses are dependent on an Effective Stress Principle, which states that the total stress on the specimen is the sum of the effective stress on the soil skeleton and the pore pressure within the sample. If the specimen is not fully saturated than the effective stress cannot be accurately calculated. The specimen is back pressure saturated for a minimum of 24 hours and until the Skempton B value is larger than 0.96. The Skempton B value is an

experimental parameter defined as the change in pore pressure due to an incremental change in total octahedral stress that provides a way to approximate specimen saturation. It is described in great detail within Skempton (1954). The B value is measured at the end of the back pressure saturation step.

After initial pressure up and back pressure saturation the specimen was consolidated to a predetermined stress state. Consolidation of a specimen allows for control of the stress state within a triaxial cell prior to shearing.

Consolidation of the specimen ensures that it is normally consolidated. A resedimented specimen is typically over consolidated at the end of the resedimentation process due to the unloading of the specimen prior to extrusion. The consolidation phase forces the stress within the sample past the maximum stress applied during resedimentation and back to the virgin compression line where it can be sheared to determine normally consolidated behavior. Three different consolidation techniques were used during the testing of RNSC. These will be described as Isostatic consolidation, K_0 consolidation, and stress path consolidation. Isostatic consolidation within a triaxial cell is performed by compressing the specimen axially at a set rate and adjusting the cell fluid pressure to equal the axial stress. The compressive strain rate is selected to be slow enough to allow for the dissipation of generated excess pore pressure within the specimen. K_0 consolidation is performed similarly to isostatic consolidation compressing the specimen axially at a set rate and adjusting the cell fluid pressure to maintain a constant specimen cross sectional area. The height and volume of the specimen is reduced During K_0 consolidation. This is thought to be a much more realistic analog to the stress state within naturally deposited soils. The third method of consolidation is called stress path consolidation. This method uses a computer controller to consolidate the specimen to a predetermined stress

state along a linear stress path at a predetermined strain rate. A user of the stress path consolidation needs to input the ending stress and the desired axial strain rate, the computer controller will then perform the consolidation by calculating a slope from the current stress state to the desired ending state. This consolidation method was used to swell specimens during the exploration of the effects of overconsolidation on RNSC. The final stress state at the end of consolidation no matter the method of consolidation was held for a minimum of 48 hours to allow for one log cycle of secondary compression. At the end of the consolidation phase, the drainage lines are closed and the pore fluid pressure is measured for a minimum of 5 minutes to ensure no leaks are present prior to shearing.

After consolidation, the specimens were sheared within the triaxial cell. The shearing is computer controlled by setting the strain rate for the load frame. The samples were sheared in either compression or extension in a drained or undrained condition. In a compression, test the axial strain is increased while the cell stress remains constant. During an extension test the axial strain is decreased while the cell stress remains constant. These two different shearing modes were used to explore strength anisotropy within RNSC. During drained tests, the loading strain rate is set slow enough so that generated excess pore pressures are allowed to dissipate through open drainage lines. During an undrained test, a faster strain rate is allowed (typically 0.5% per hour for RNSC) because the generated excess pore pressures are measured and the effective stress within the specimen is known. A drained test is not typically performed due to the length of time required for the completion of the test but provides a very good verification on the friction angle of a soil as determined by undrained tests Drained test on RNSC were performed at a strain rate of 0.15% per hour.

Triaxial tests require several calculations during the test and during data post processing to ensure accurate results. Measurements must be made to determine the specimen's initial height, diameter, and mass. These measurements are used to determine the initial density of the specimen and are the basis for measured changes in density. The height of the sample post consolidation is calculated using Equation 3.6.

$$H_c = H_0 - \Delta H_0 \quad \text{Equation (3.6)}$$

Where:

H_c = Height of the specimen at the end of consolidation

H_0 = Initial specimen height

ΔH_0 = Change in the height of the specimen during consolidation

The cross sectional area of the specimen, at the end of consolidation can be calculated by two different methods either one or an average of the two is acceptable. The first method is presented in Equation 3.7.

$$A_c = (V_0 - \Delta V_{sat} - \Delta V_c) / H_c \quad \text{Equation (3.7)}$$

Where:

V_0 = Initial specimen volume

ΔV_{sat} = Change in specimen volume during saturation

ΔV_c = Change in specimen volume during consolidation

The second acceptable method to calculate the specimen cross sectional area at the end of consolidation is provided in equation 3.8.

$$A_c = (V_{wf} + V_s) / H_c \quad \text{Equation (3.8)}$$

Where:

V_{wf} = Final volume of water based on final water content

V_s = Volume of solids by phase relations = $M_s / (G_s \rho_w)$

Where:

M_s = Specimen dry mass

G_s = Specific gravity of solids

ρ_w = Density of water corrected for temperature

The cross sectional area for an applied load if a right cylinder shape is assumed during deformation is calculated by Equation 3.9. A right cylinder shape deformation is assumed during consolidation and shear in extension for this research.

$$A = A_c / (1 - \epsilon) \quad \text{Equation (3.9)}$$

Where:

A_c = Specimen cross sectional area at the end of consolidation

ϵ = Axial strain

The cross sectional area for specimens during and after shear in compression is calculated using a parabolic area correction. Equation 3.10 provides the parabolic area correction as detailed within (Germaine & Ladd, 1988).

$$A_{parabolic} = A_c \left(-0.25 + \frac{\sqrt{25 - 20\varepsilon - 5\varepsilon^2}}{4(1 - \varepsilon)} \right)^2 \quad \text{Equation (3.10)}$$

Where:

A_c = Specimen cross sectional area at the end of consolidation

ε = Axial strain

During the test the principle stress difference needs to be corrected for the effect of the rubber membrane. This correction is provided in Equation 3.11

$$\Delta(\sigma_1 - \sigma_3)_m = (4E_m t_m \varepsilon) / D_c \quad \text{Equation (3.11)}$$

Where:

$\Delta(\sigma_1 - \sigma_3)_m$ = Membrane correction to be subtracted from the principle stress difference

E_m = Young's modulus of membrane material

t_m = Thickness of membrane

ε = Axial strain

D_c = Diameter of specimen at the end of consolidation

Lastly the corrected principle stress difference can be calculated with equation 3.12.

$$(\sigma_1 - \sigma_3)_c = \frac{P}{A} - (\sigma_1 - \sigma_3)_m \quad \text{Equation (3.12)}$$

Where:

$(\sigma_1 - \sigma_3)_c$ = Corrected principle stress difference

P = Applied Force

A = Corrected specimen area

$\Delta(\sigma_1 - \sigma_3)_m$ = Membrane correction to be subtracted from the principle stress difference

Due to the large variability in consolidation and loading scenarios in a triaxial test, the following standard abbreviations for triaxial tests are used herein:

CIUC = Isotatically Consolidated Undrained Compression Test

CK₀UC = K₀ Consolidated Undrained Compression Test

CK₀UE = K₀ Consolidated Undrained Extension Test

CK₀DC = K₀ Consolidated Drained Compression Test

Table 3- 1: Triaxial Station 01

Measurement	Device	Calibration Factor	Range	Resolution	Stability
Axial Deformation	External LVDT	2.51444 cm/V/V	2.5 cm	±0.0006% (0.1 mV)	±0.006% (1 mV)
Axial Force	Internal Load Cell	6844.62 kN/V/V	2.2 kN	0.01 kN (0.001 mV)	0.1 kN (0.01 mV)
Cell Pressure	Pressure Transducer	709.63 kPa/V/V	1400 kPa	0.01 kPa (0.001 mV)	0.1 kPa (0.01 mV)
Pore Pressure	Pressure Transducer	-704.47 kPa/V/V	1400 kPa	0.01 kPa (0.001 mV)	0.1 kPa (0.01 mV)
Specimen Volume	Pressure Volume Actuator	23.44 cm ³ /V/V	45 cm ³	±0.0005% (0.1 mV)	±0.005% (1 mV)

Table 3- 2 Triaxial Station 02

Measurement	Device	Calibration Factor	Range	Resolution	Stability
Axial Deformation	External LVDT	2.084297 cm/V/V	2.5 cm	±0.0006% (0.1 mV)	±0.006% (1 mV)
Axial Force	Internal Load Cell	7038.18 kN/V/V	2.2 kN	0.01 kN (0.001 mV)	0.1 kN (0.01 mV)
Cell Pressure	Pressure Transducer	-700.251719 kPa/V/V	1400 kPa	0.01 kPa (0.001 mV)	0.1 kPa (0.01 mV)
Pore Pressure	Pressure Transducer	-706.924501 kPa/V/V	1400 kPa	0.01 kPa (0.001 mV)	0.1 kPa (0.01 mV)
Specimen Volume	Pressure Volume Actuator	-22.7268 cm ³ /V/V	45 cm ³	±0.0005% (0.1 mV)	±0.005% (1 mV)

Table 3- 3: Triaxial Station 08

Measurement	Device	Calibration Factor	Range	Resolution	Stability
Axial Deformation	External LVDT	2.48 cm/V/V	2.5 cm	±0.0006% (0.1 mV)	±0.006% (1 mV)
Axial Force	Internal Load Cell	6486.7 kN/V/V	2.2 kN	0.01 kN (0.001 mV)	0.1 kN (0.01 mV)
Cell Pressure	Pressure Transducer	-700.932164 kPa/V/V	1400 kPa	0.01 kPa (0.001 mV)	0.1 kPa (0.01 mV)
Pore Pressure	Pressure Transducer	704.68 kPa/V/V	1400 kPa	0.01 kPa (0.001 mV)	0.1 kPa (0.01 mV)
Specimen Volume	Pressure Volume Actuator	96.1276688 cm ³ /V/V	45 cm ³	±0.0005% (0.1 mV)	±0.005% (1 mV)



Figure 3- 1: Homogenized Bulk Nile Clay Powder



Figure 3- 2: Using a stand Mixer to Blend the Clay and Saline Solution for Resedimentation

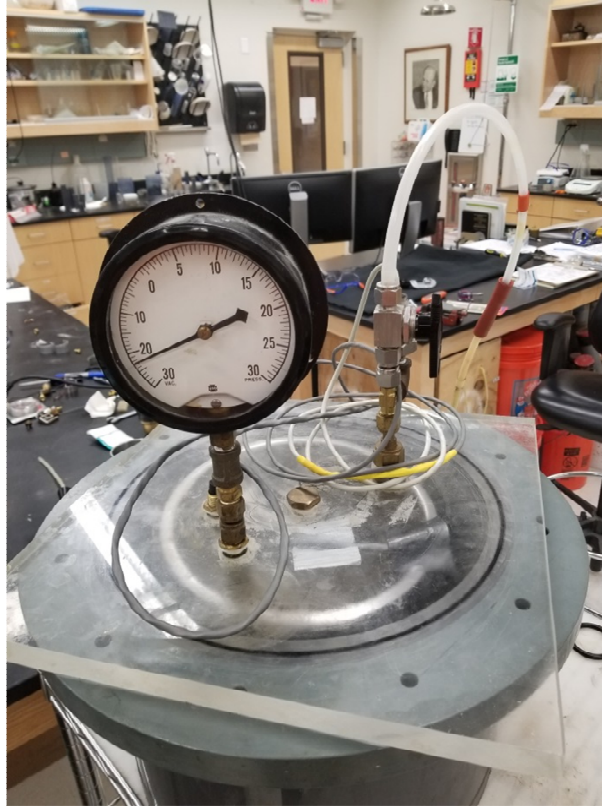


Figure 3- 3: Evacuating the Clay Slurry in a Pressure Chamber



Figure 3- 4: Tremieing the Clay Slurry into a Consolidometer



Figure 3- 5: Typical Consolidometer used for Resedimentation



Figure 3- 6: Triaxial Test Specimen Trimming Equipment

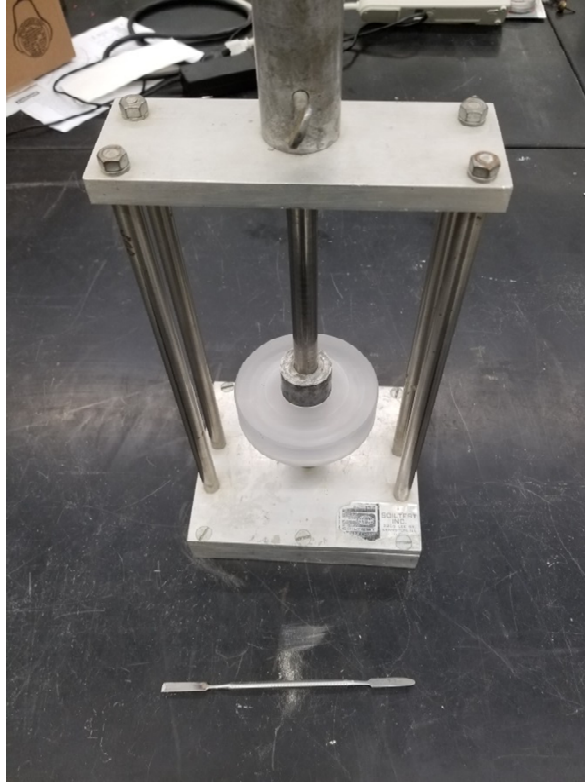
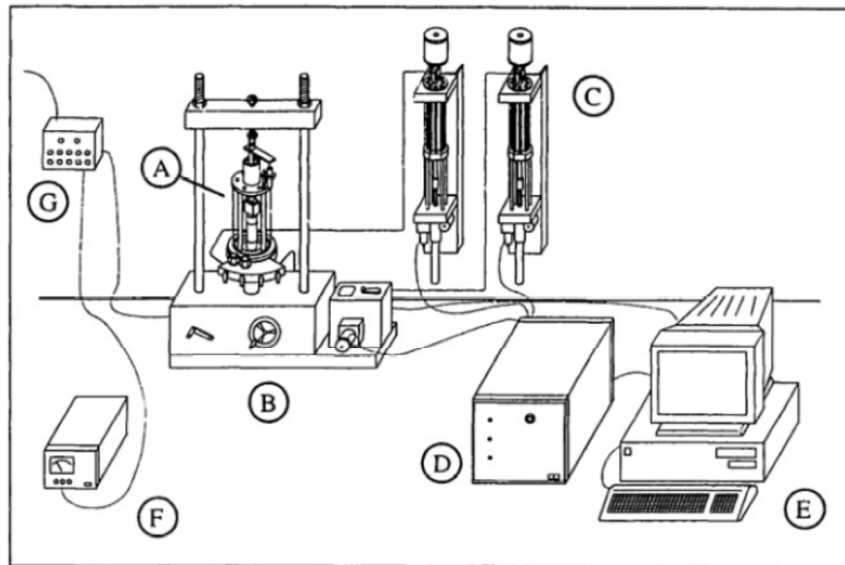


Figure 3- 7: CRS Test Specimen Trimming Equipment



- | | |
|---------------------------------|-------------------------------|
| A - Triaxial Cell | E - Personal Computer |
| B - Load Frame | F - DC Power Supply |
| C - Pressure/Volume Controllers | G - Data Acquisition Channels |
| D - Motor Control Box | |

Figure 3- 8: Schematic Diagram of Components for a Typical Tufts Automated Triaxial Test Apparatus from (Santagata, 1998)



Figure 3- 9: Photograph of Typical Tufts Automated Triaxial Testing Apparatus

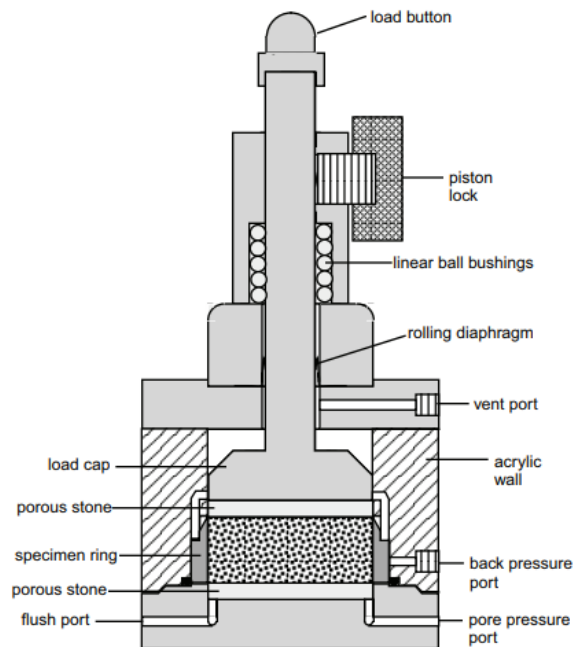


Figure 3- 10: Schematic Diagram of Trautwein C200000 Back Pressure Consolidation Cell from Trautwein Literature



Figure 3- 11: Photograph of Typical Tufts Automated CRS Testing Apparatus

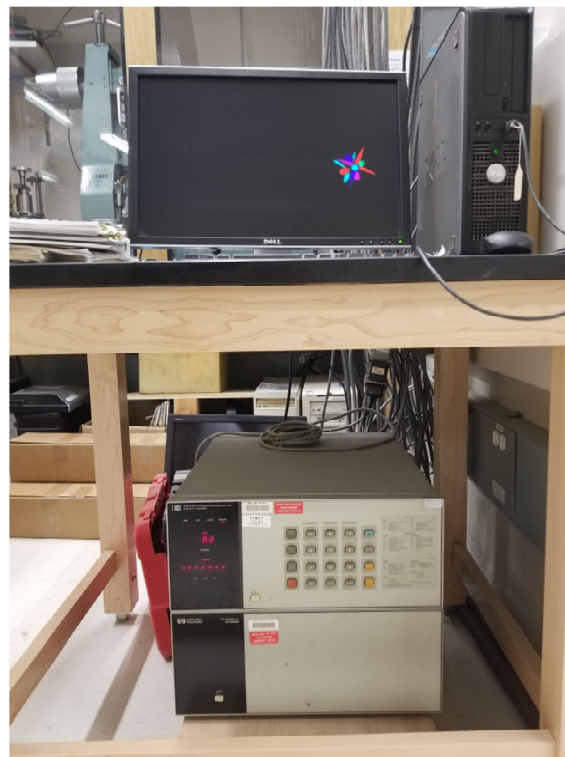


Figure 3- 12: Photograph of Tufts Central Data Acquisition System



Figure 3- 13: Cassagrande Cup used for Liquid Limit Testing

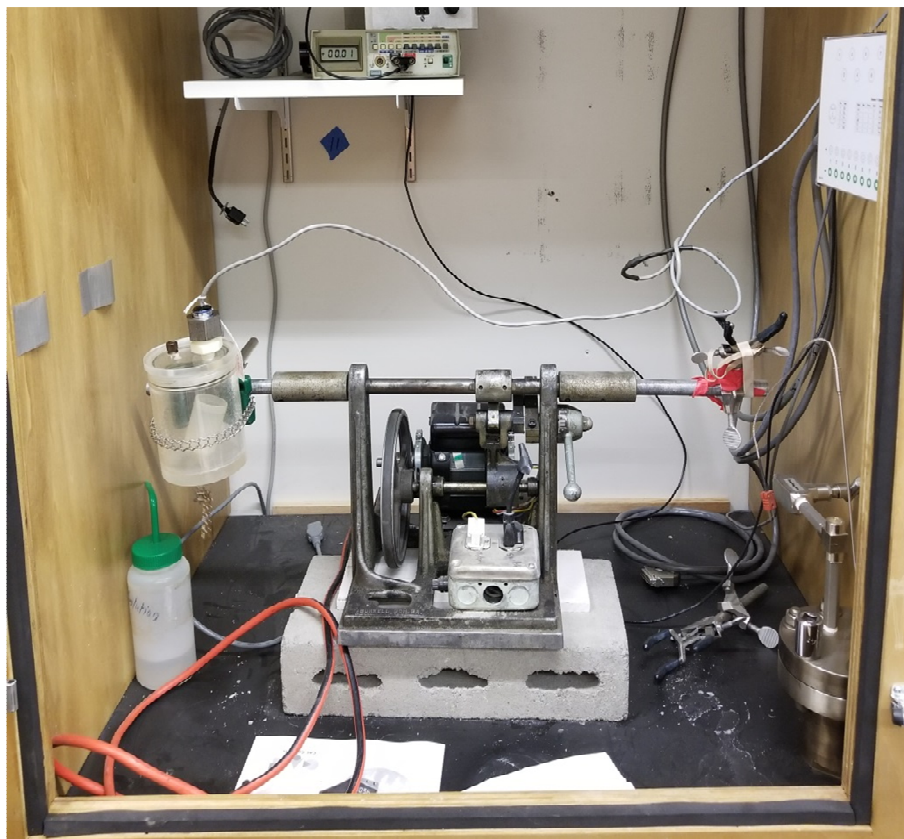


Figure 3- 14: Test Setup for Calcite Equivalency Testing

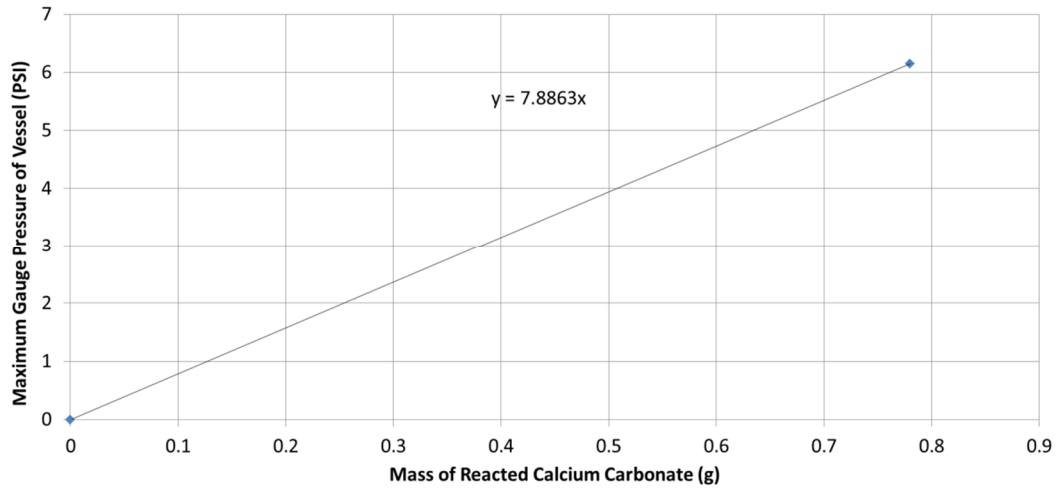


Figure 3- 15: Pressure Vessel Calibration Curve for Calcite Equivalence Testing

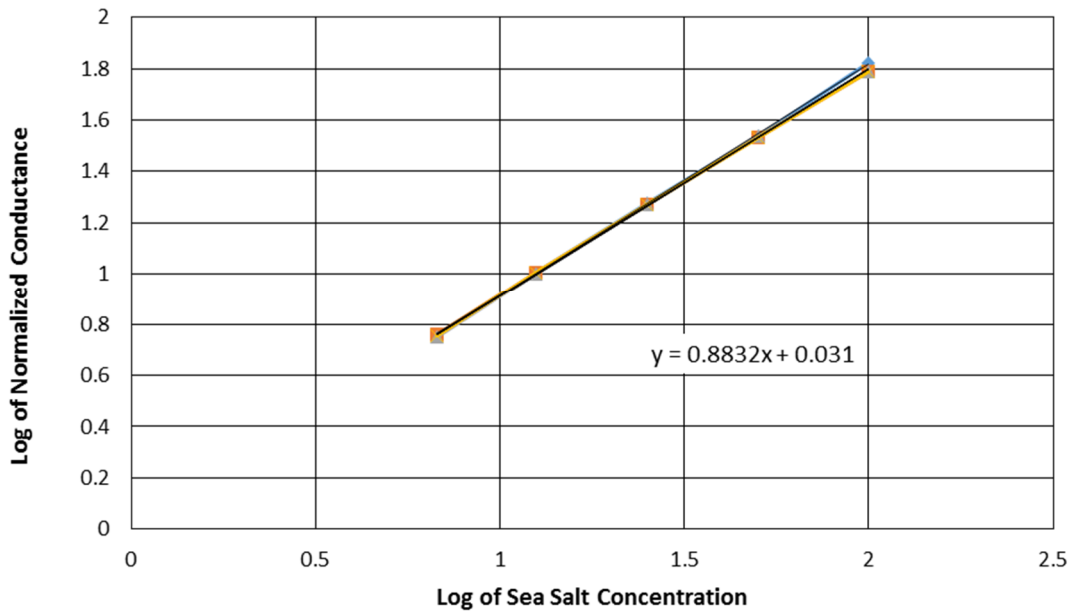


Figure 3- 16: Conductance Probe Calibration Curve for Salinity Measurements

Chapter 4

TESTING RESULTS; CHARACTERIZATION, CONSOLIDATION AND STRENGTH

4.1 INTRODUCTION

An extensive testing program was performed on Resedimented Silty Nile Clay (RNSC) to provide information on the characterization, consolidation, and strength properties of the material. The results of the testing program are provided within this chapter. The clay soil tested was provided by Dr. Sherif Akl from the University of Cairo, Egypt. An initial 3 kg of the soil was mailed to the TAG lab in the summer of 2016. This material had been sieved over the #100 sieve and the larger fraction had been removed prior to shipping. A separate bulk sample of around 50 kg was sent to the TAG lab in late summer of 2016. This material had not been sieved and was air dried, ground, and blended to create the bulk homogenous powder. To simplify the source of the material used for each the varieties of RNSC were categorized by series. Test samples created from the initial soil shipped; where the plus #100 sieve material was removed will be referred to as Series I samples. Samples created from the air dried and blended bulk powder of the second larger shipment will be referred to as Series II samples. Series II samples are the least manipulated and most analogous to the natural Nile Silty Clay material. Series III samples refers to a small amount of series II material in which the coarse fraction (particle size greater than #200 sieve) was removed from the fine fraction (particle size less than #200 sieve) through mechanical sieving with the TAG lab.

Section 4.2 provides the results for the characterization tests. Section 4.2 is split into two parts: characterization tests used to classify the soil via the Unified Soil Classification

System, and characterization tests performed in support of future testing methods.

Classification tests were performed on the various RNSC series as denoted herein. Table 4-1 provides a quick reference summary of the index property test results by material series. This section also summarizes the results of Scanning Electron Microscopy imaging performed to study the RNSC soil microstructure. As well as the X-Ray Powder Diffraction performed to determine the Mineralogy of RNSC.

Section 4.3 presents the consolidation behavior of RNSC. This was explored through Constant Rate of Strain testing and consolidated triaxial tests. Three CRS tests were performed to an ultimate effective stress level of 10 MPa. One CRS test had a series of unloading and reloading cycles to observe the swelling and reloading behavior of the soil. The material behavior during the consolidation portion of the triaxial testing is compared to the CRS tests to provide a broader understanding of the normally consolidated behavior of RNSC.

In section 4.4 the effect of stress on the permeability of RNSC is explored through the hydraulic conductivities measured during CRS tests.

In Section 4.5 the shear behavior of RNSC is presented based on the triaxial testing results. The strength anisotropy of RNSC is explored by varying the direction of shear during testing. The Stress History and Normalized Engineering Parameters (SHANSEP) for RNSC are explored through triaxial tests of over consolidated materials. The engineering parameters measured in the laboratory program are presented and the stress sensitivity of RNSC is explored through variation of maximum consolidation stress.

4.2 CHARACTERIZATION

3.2.4 Introduction

The following tests were performed on RNSC for the purpose of characterizing RNSC; grain size distribution through sedimentation, Atterberg limit tests, calcite equivalency and organics testing. The specific gravity of RNSC and the natural salt concentration was measured to support calculations for other laboratory tests and the resedimentation process. A study of the microstructure of RNSC was performed using Scanning Electron Microscopy. The study observed the structure of RNSC by comparing two oven dried samples. One sample consisted of the standard RNSC bulk powder (series II) and the other sample had the sand fraction removed prior to resedimentation (series III). Both samples were sheared in a CK₀UC triaxial prior to imaging. The coarse fraction of RNSC (>#200 Sieve) was also examined using SEM to determine if the sand was a solid mineral or a conglomerate of cemented clay particles. Lastly the mineralogy results provided by the James Hutton Limited Institute XRPD testing gives an estimated constituent mineralogy for RNSC.

3.2.5 Grain Size Distribution

The results several grain size distribution curves as measured through the sedimentation procedure for RNSC is provided in Figure 4-1. These tests were performed on Series I samples by Dr. Sherif Akl at the University of Cairo. Figure 4-2 shows the results of sedimentation testing performed on series II samples in the TAG lab. The samples in Figure 4-2 are identified by the date of the sedimentation test. There is minor variance between the two curves showing that the bulk Series II powder is fairly homogenous. Series I RNSC was found to be 70% silt and 30% clay by particle size. Series II RNSC was found to be 24% sand, 30% silt and 46% clay by particle size. The particle size distribution indicates that this is a fine grained material by USCS classification as more than 50% of the soil passed the #200 sieve.

A mechanical sieve analysis was performed on the Series II material to measure the grain size distribution, as verification to the sedimentation analysis. A discrepancy between the coarse fraction (>#200 sieve) was found during a mechanical sieving test and sedimentation testing on RNSC. The mechanical sieve measured the coarse fraction (>#200 sieve) to be 60% which is double the measurement from sedimentation. Furthermore, three samples of the removed coarse fraction were saturated in order to determine their maximum water contents. The soil samples were saturated by adding water to the sample powder with a pipette. The water was added and the bulk sample was stirred until free water was found to collect on the sample surface. The free water was blotted off and the water content was measured. The samples were found to have an average maximum water content of 76.3% indicating that they were likely to be clay cemented aggregates rather than crystalline mineral grains.

3.2.6 Atterberg Limits

The Atterberg limits for RNSC were determined for all series of RNSC. The Atterberg limit results for Series I are presented in Figure 4-3, as provided by Dr. Sherif Akl at the University of Cairo. The results for all three Series are presented in Figure 4-4. For Series I the average liquid limit was found to be 61.5% and the plastic limit was found to be 24.5%. For Series II the liquid limit was found to be 62.12% and the plastic limit was found to be 23.44%. For Series III the liquid limit was found to be 66.28% and the plastic limit was found to be 29.96%. For all series, the Atterberg limits plot above the A-line and above 50% water liquid limit on the Plasticity chart indicating the soil is classified as high plasticity clay (CH) by the Unified Soil Classification System.

The Atterberg limit results for RNSC indicate that the >#100 sieve material has a negligible effect on the plasticity behavior of RNSC. Series I and series II had very similar

Atterberg Limits. Removing the >#200 sieve material had an appreciable effect as series III had a higher Liquid Limit and a higher plastic limit, moving the point towards the A line. The A line being the demarcation of the plasticity behavior for Clays and Silts on the Atterberg limit plot.

3.2.7 Organics Content and Calcite Equivalency

The organic content of the Series II bulk NSC powder was found to be a maximum of 2% by mass, making the soil largely inorganic. The 2% value includes the loss of water from clay particles during the heating portion of the test; as such it is an upper limit to organics content of the soil. The organic content is not expected to affect the behavior of this soil.

Figure 4-5 shows the pressure curves from the calcite equivalency testing. The curves show an average calcite equivalency of 4.4% calcite by mass. The rate of the reaction indicates that the mineral reacting in RNSC is likely Dolomite. This small amount of calcium cementation is not likely to affect the material behavior of RNSC, but may be a contributor to the creation of the aggregate particles within the coarse fraction.

3.2.8 Scanning Electron Microscopy

Scanning Electron Microscopy (SEM) imaging was performed on RNSC to observe variations in the soil fabric and to observe the nature of the coarse grains (> #200 sieve). The fabric study was performed on two oven dried specimens post triaxial shearing. The specimens were prepared in accordance with the oven dried specimen preparation method detailed within Derieh (2016). One specimen was taken from triaxial test TX1316; a series II test in which the specimen was consolidated to a vertical consolidation stress of 585 kPa. The second sample imaged was from triaxial specimen TX1379 which was a series III (>#200 sieve material removed) specimen that was consolidated to a vertical consolidation stress of 141kPa. Both samples were

ion milled in a JEOL Cross section polisher for a minimum of 8 ½ hours and imaged using a Zeiss Supra55 SEM.

Figures 4-6 through 4-10 are images of triaxial specimen TX1316. The vertical lines within the images are artifacts of the milling process. Figure 4-6 shows the milled section of TX1316 at a magnification of 450 times. Figure 4-7 shows a milled section of TX1316 at a magnification of 1000 times. In Figure 4-7 long cracks are shown traversing the clay surface. These cracks are likely shrinkage cracks from the oven drying process. Figure 4-8 shows a milled section of TX1316 at 1000 times magnification that has several crystalline minerals within it. Figure 4-9 shows the intra-particle porosity within a mineral suspended in the clay matrix of TX1316. Figure 4-10 shows a mineral suspended within the clay matrix of TX1316 in an area of the specimen that was not ion milled. For Figures 4-6 to 4-9 the top of the milled section corresponds to the top edge of the figure. In general the Series II microstructure had the following characteristics.

1. No large particles in any of the micrographs.
2. A few grains in the 20 µm size.
3. The clay particles are too small to observe.
4. Shrinkage cracking.

Figures 4-11 to 4-14 are images of triaxial specimen TX1379. Figure 4-11 shows the ion milled cross section of TX1379. Figure 4-12 shows an ion milled section of TX1379 at 1500 times magnification containing crystalline minerals. Figure 4-13 shows the typical porosity of an ion milled section of TX1379 at 8,400 times magnification. Figure 4-14 shows the microscopic porosity of an ion milled section of TX1379 at 11,700 times magnification. For Figures 4-11 to 4-

14 the top of the milled section corresponds to the right edge of the figure. In general the Series III microstructure had the following characteristics.

1. No large particles in any of the micrographs.
2. A few grains in the 10 μm size.
3. The clay particles are too small to observe.
4. Shrinkage cracking.

To understand the coarse grained (> #200 Sieve) particles within RNSC, a sample of particles was imaged using a Zeiss Supra55 SEM. Figures 4-15 to 4-17 shows coarse RNSC particles that are likely clay cemented aggregates, the shape and texture of the particles do not indicate singular crystalline structures. Figures 4-18 to 4-21 shows crystalline mineral grains observed within the coarse RNSC grains. Anecdotally, the coarse grained material seemed to primarily consist of clay cemented aggregates but no quantitative studies have been performed on the coarse fraction.

3.2.9 X-Ray Powder Diffraction

The X-Ray Powder Diffraction results performed by the James Hutton Limited Institute are presented in Figure 4-22 and Figure 4-23. Figure 4-20 shows intensity versus two theta for Cu K-alpha Radiation from 2 to 75 of the bulk sample. The peaks represent the various crystalline mineral elements within RNSC. Figure 4-23 shows intensity versus two theta for Cu K-alpha radiation from 2 to 45 for the clay fraction (<2 μm particle size) of RNSC as separated through timed sedimentation. The XRPD test found bulk RNSC to be predominantly Quartz (24%), Plagioclase (14%) and K-feldspar (5%) with some calcium cementation in the form of Calcite (3.3%) and Dolomite (0.3%). The clay fraction of RNSC (<2 μm particle size) was found to consist of Smectite (93%), Kaolinite (4%) and trace Chlorite

and Illite. The full XRPD report from the James Hutton Limited Institute is provided in Appendix A.

The calcite equivalency and XRPD results indicate an agreement on the concentration of calcium cementation minerals contained within RNSC. The two test methods indicate different dominant cementitious minerals. The calcite equivalency testing rate of reaction indicates that Dolomite was likely the dominant cementitious mineral while XRPD indicates that calcite is likely dominant cementitious mineral.

3.2.10 Specific Gravity and Natural Salt Content

The specific gravity of Series II RNSC was found to be 2.816 with a standard deviation of 0.003. Five total determinations were performed during the specific gravity test.

The natural salt content of RNSC was found to be 0.02 grams of salt per kilograms of soil. This is a low but reasonable salt content as the soils were deposited by a freshwater source. To maintain the clay structure a minimum salinity of 1 gram of salt per liter of water was used as the pore fluid during resedimentation.

4.3 CONSOLIDATION

4.3.1 Introduction

RNSC was subjected to one dimensional consolidation tests using a Constant Rate of Strain (CRS) testing apparatus. The initial specimen densities were carefully calculated from measurements of the mass and dimensions of the specimen in order to calculate the test results and to check the consistency of the measurements. Three CRS tests were performed in total, 2 on series I material and 1 on series II material.

Prior to undrained shear all triaxial tests performed on RNSC had a consolidation phase. Most of the tests were K_0 consolidated using a computer to ensure that there was no radial deformation.

This section presents the consolidation results from all tests on RNSC. Table 4-2 summarizes the phase relations and consolidation characteristics from the CRS tests. Table 4-3 summarizes the phase relations, consolidation type and consolidation characteristics from consolidation during triaxial testing.

4.3.2. CRS Consolidation Results

In total, three Constant Rate of Strain tests were performed on RNSC. Figure 4-24 shows a plot of the results of the three tests in ϵ_a -Log σ'_v space. Figure 4-25 shows a plot of the results of the tests in e -Log σ'_v space. Figure 4-24 shows a very strong agreement on the behavior and location of the virgin compression line. The material has a curved virgin compression line that indicates the materials compression behavior stiffens at increasing stresses. Figure 4-25 shows an offset of the virgin compression line between CRS tests 1493 and 1494 to CRS test 1504. This is likely due to an error in measuring the initial dimensions of the specimen. Table 4-2 summarizes the phase relations and compression parameters measured during the CRS tests. In general, at low stresses 0.1 to 1 MPa RNSC has an average Compression Ratio (CR) of 0.213. The CR of a material is the change in axial strain by the change in logarithmic effective stress. At higher stress of 1 to 10 MPa RNSC has an average CR of 0.176. At the end of each of the tests the material was allowed to swell to determine its Swelling Ratio (SR), which is the change in axial strain by the change in logarithmic stress during an unloading portion of the test. RNSC had an average SR 0.054 when measured from the maximum effective stress to an OCR of 4. CRS 1504 had unloading/reloading cycles one of which was performed

the maximum stress during the test. This may have inflated the SR for RNSC. CRS tests 1493 and 1494 both had a measured SR of 0.014.

CRS test 1504 had three unload and reload cycles to help determine the loading response of RNSC. The first cycle was performed at very low stresses 0.01 to 0.15 MPa and the CRS piston lifted off of the specimen leading to free swelling. The RR is the change in axial strain by the change in logarithmic effective stress when the soil is being subjected to a stress state that is less than the maximum past pressure. The maximum past pressure is the largest stress the soil has ever been subjected to. The second cycle was performed at a stress range of .07 to 1.5 MPa. This unload reload cycle was found to have a RR of 0.062. The final unload and reload cycle was performed at a stress range of 0.7 to 8 MPa. This unload/reload cycle was found to have a RR of 0.052. These two cycles show a stiffening of RNS at higher stress levels as the RR is reduced indicating a smaller change in strain. This is very similar to the behavior observed in the CR of RNSC indicating that the compression behavior of RNSC is very sensitive to stress level. The ratio of RR/CR for each unload/reload cycle was consistent. For the second unload/reload cycle the value of RR/CR was 0.284 and for the final unload/reload cycle the value of RR/CR was 0.288.

4.3.3. Triaxial Consolidation Results

A total of 18 consolidated triaxial tests were performed on RNSC, 4 of the tests performed on Series I material and 14 of the tests performed on Series II material. Table 4-3 summarizes the phase relations and Compression Ratio (CR) measured during the consolidation portion of the triaxial tests. CR was computed for each consolidation test as the slope of the virgin compression line starting at a point after recompression and ending at the first point of final stress level. Each sample was consolidated at a rate of 0.15% strain per hour. This slow

rate ensured the dissipation of excess pore pressures and accuracy in the computer controller's K_0 consolidation algorithm.

Figure 4-26 shows the consolidation phase results of select tests in a logarithmic vertical effective stress by axial strain plot. Between the consolidation curves in Figure 4-26, there is a general agreement in the Compression Ratio of RNSC, which the average for these select tests was of 0.218. These tests were consolidated at a stress range of 0.1 to 0.35 MPa. This is very consistent with the CR from CRS testing at a stress range of 0.1 to 1 MPa which was found to be 0.213. The average CR for a stress range of 0.1 to 1 MPa from all consolidation testing was 0.190.

Figure 4-27 shows the same select consolidation phase results from K_0 consolidated triaxial testing in a vertical effective stress by void ratio space. The change from the strain space to the void ratio space allows for the ease of density based observations of the natural materials. Engineers tend to use the strain based testing for ease of calculations. RNSC was found to have an approximate $\pm 13.5\%$ variance within the void ratio at a given stress level from the select triaxial tests shown in Figure 4-27. This variance is likely due to errors in measurement for use in calculating the phase relations of the sample a start of the tests.

Two samples (TX1338 and TX1344) were isotropically consolidated, which was found to greatly reduce the CR value. The average CR of the isotropically consolidated samples at a stress range of 0.1 to 1 MPa was 0.054 which is approximately one third of the average value from all triaxial tests of 0.190.

The relatively high CR values indicate that RNSC is a “soft” material and would be expected to undergo extensive consolidation during loading. The CRS curves indicated that the

material stiffens in a curved fashion at higher stresses (>10 MPa). This phenomenon has been observed in fine grained material and detailed within Casey B (2014).

4.3.4. Comparison of Consolidation Behavior by Testing Method and Series

Figure 4-28 provides an average compression curve in e - $\log\sigma$ space for RNSC over the 0.1 to 10 MPa stress range. The curve was created by averaging the void ratio for given stress from the CRS tests and consolidation phase of the triaxial tests. The average compression curve was found to have a CR of 0.214 between 0.1 and 1 MPa, a CR of 0.144 between 1 and 10 MPa, and a CR of 0.176 between 0.1 and 10 MPa. The evolution of CR within RNSC shows the material becomes less compressible at higher stresses.

The compression behavior of the three RNSC series compared to the average compression curve from both CRS and triaxial consolidation phase is shown in Figure 4-29 in ϵ - $\log\sigma$ space. The primary consolidation (straight line portion) of the curves is very consistent in slope between each other and the average compression curve. The deviation in the location of the curve in ϵ - $\log\sigma$ space is a result of resedimenting the specimens to different maximum stresses. A higher maximum stress during resedimentation will shift the consolidation curve to higher stress as primary consolidation will only occur after the maximum past pressure (maximum stress from resedimentation). Figure 4-30 shows the same consolidation curves from figure 4-29 compared to the average compression curve in e - $\log\sigma$ space. Within this space the stress sensitivity of the density of RNSC can be observed. The void ratio is the ratio of the volume of voids to the volume of solids, and is an index of the dry density of soil. The curves in Figure 4-30 show that the test specimens initial void ratios ranged from 1.11 to 1.37. This is a range in initial dry densities of 74.1 to 82.3 lbs./ft³. Even with an 11% variance on the initial densities of the specimens the consolidation behavior is very similar for the three series and two

test methods. RNSC has a very consistent primary consolidation behavior (slope of the straight line portion). Variations in the location of the consolidation curve in $e\text{-log}\sigma$ are due to the variance in initial specimen densities as well as the variance in the maximum stress applied to the specimen during resedimentation.

Figure 4-31 shows consolidation curves from the consolidation phase of three triaxial tests performed on the three RNSC series, compared to the average compression curve in $\epsilon\text{-log}\sigma$ space. The three tests used for the comparison TX1283, TX1375, and TX1379, were chosen for their similarity in maximum stress during resedimentation (0.01 MPa) and their maximum stress at the end of consolidation (0.15 MPa). The three curves show very consistent compression behavior in $\epsilon\text{-log}\sigma$ space. Figure 4-32 shows the consolidation curves from Figure 4-31 in $e\text{-log}\sigma$ space. In this space there is an observation that the Series II initial density is higher (void ratio of 2.33, dry density of 74.1 lbs./ft³) than Series I or Series III which are generally the same (void ratio of 1.37, dry density of 75.4 lbs./ft³). At the maximum consolidation stress the triaxial test specimens had different void ratios indicating the three series had different microstructure changes with stress. At 0.15 MPa prior to any secondary compression occurring, TX1283 the Series I test had a void ratio of 1.14, which corresponds to a dry density of 82.1 lbs./ft³. TX1375, the Series II test had a void ratio of 1.14, which corresponds to a dry density of 82.9 lbs./ft³. TX1379, the Series III test had a void ratio of 1.18, which corresponds to a dry density of 80.6 lbs./ft³.

4.4 Permeability

4.4.1 Introduction

The permeability of a fine grained soil is has been found to depend on many factors including mean particle size, clay mineralogy, and size of the pores between particles. The

permeability dependence on particle size was studied in depth by Yang & Aplin (2010) in which they found that as the mean particle size decreases the permeability of a soil decreases. For a continuous homogenous soil deposit such as RNSC variations in permeability due to variations in particle size should be negligible as the method of deposition is consistent throughout the test specimens.

The clay mineralogy affects size of the double layer aspect ratio of potential bonded water with particles. The double layer refers to the layer of water that is chemically attracted to the surface of the clay particles. The size of the bonded water is dependent on the shape and electrostatic charge of the clay particle. Studied in depth by Van Olphen (1963) the size of the double layer has been found to vary with clay mineralogy. The size of the double layer affects the permeability of a soil in two distinct ways. The double layer size dictates the initial clay fabric during deposition. The structuring of the initial fabric is sensitive to available free ions within the pore fluid and is in general thought to have a relatively small impact on the permeability of a soil as discussed within Horan (2012). The second effect of the double layer on permeability is a reduction in the “effective porosity” available for flow by trapped water bound within the double layer. The mechanism of which is not understood but it has long been thought that water in the double layer is chemically trapped and does not contribute to flow through the soil. As such clay minerals with larger double layer sizes would expect to have smaller permeability’s due to the larger amount of “trapped” water blocking available pore space for flow. Similar to the mean particle size effects on permeability, within a consistent deposition of soil, the double layer effects are assumed to be fairly consistent.

Since the particle size and clay mineralogy effects are expected to be fairly consistent within the bulk clay powder; the major influence on the permeability of RNSC would be the

stress dependence of the permeability. In general as the stress level is increased the soil contracts and the void space within the soil decreases, which leads to less available pore space for flow. The change in permeability with stress level indicates a pressure dependence of permeability which can be measured through CRS testing.

4.4.2. CRS Permeability Results

Figure 4-33 shows the results of the measured permeability's from the CRS tests performed on RNSC. The permeability curves are calculated from the measured hydraulic conductivities recorded during the CRS test. The permeability's presented within this research were calculated from hydraulic conductivity measurements during virgin compression of the soil. This was done to remove any affects over consolidation may have on the hydraulic conductivity measurement. The permeability shows a log linear trend of decreasing permeability with decreasing void ratio. This trend is expected and is discussed in detail within Casey B. (2014) who documented a similar trend of decreasing permeability with decreasing porosity.

CRS 1504 (Series II) shows a large variation in permeability from CRS tests 1493 and 1494 (Series I) for a given void ratio. The variation is thought to be caused by variation grain size distribution between the Series I and Series II test specimens as well as the expansible nature of Smectite. CRS test 1504 has a lower permeability at the same void ratio with a larger sand fraction. A similar trend was observed within Mollins, Stewart, & Cousens (1995) in which Bentonite sand mixtures were found to have lower permeability's than pure Bentonite at a the same stress level. The theory presented within Mollins, Stewart, & Cousens (1995) argued that at low stress the expansive clays can separate the sand particles and achieve void ratios similar to pure Bentonite. As the stress level on the soil increases the work required to separate the

sand particles increases until it crosses a threshold stress after which the clay particles cannot separate the sand particles. The clay particles still expand but into the pore spaces between the sand particles sealing the available pore space for flow.

4.5 Stress-Strain-Strength

4.5.1 Introduction

This section presents results on the shear testing of RNSC performed within a triaxial testing apparatus. This section will discuss the variations in triaxial testing performed on RNSC. A total of seventeen triaxial tests were performed on RNSC. Thirteen of the tests were performed as compression tests and five were performed as extension tests. Three of the compression tests were sheared in an over consolidated (OC) stress state to observe the effects of over consolidation on RNSC. Two of the three over consolidated triaxial tests were sheared from an isotropic stress state. Table 4-4 provides a summary of the consolidation conditions and strength parameters for the seventeen triaxial tests performed on RNSC.

The stress-strain behavior will be discussed first through the results of normally consolidated (NC) CK_0UC tests. These tests are K_0 consolidated undrained compression tests, the results of which provide a basic understanding of the natural compressive failure of RNSC. As a part of the basic understanding of RNSC the material's sensitivity to stress is presented herein through shear results over various confining stresses. CIUC triaxial data is presented following the CK_0UC test data. During a CIUC test the specimen is isotopically consolidated in lieu of K_0 consolidation. Isotropic consolidation is performed by incrementing both the axial stress and the radial stress by the same amount to keep them equal. Following CIUC testing the strength Anisotropy of RNSC is presented through the results of the extension tests. Lastly a

basic understanding of the stress normalization for RNSC is provided through the results of compression triaxial tests performed on specimens with high Over Consolidation Ratios.

The later portion of this section will discuss measured engineering parameters of RNSC. Specifically the effective friction angle, undrained shear strength (including strength anisotropy), lateral stress coefficient, and material stiffness.

4.5.2. CK_0UC Triaxial Tests

Figure 4-34 shows the stress-strain response for 6 NC CK_0UC Triaxial tests performed on RNSC. In general the curves show that increasing the consolidation stress increases the maximum shear stress and that RNSC generally reaches a maximum shear stress at a relatively low strain (<0.5). Triaxial test TX1327 is the exception by having a strain at failure of 3.81%. RNSC also exhibits significant strain softening behavior after reaching maximum shear stress. Figure 4-35 shows the stress-strain curves normalized to the maximum consolidation stress from the consolidation phase of the triaxial test. These curves show that in a normalized space as the consolidation stress increases then the normalized shear strength decreases. This is an expected trend for clay dominated fine grained soil as detailed within Abdulhadi (2009) and expanded within Casey B. (2014). Other notable trends in the normalized stress space are the general decrease in strain to failure and the decrease in stress at large strains.

Figure 4-36 emphasizes the stress dependence of shear strength by plotting the maximum shear stress by consolidation stress. This clearly shows the significant trend of increasing in shear strength with increasing consolidation pressure. Figure 4-37 shows critical state friction angle by the vertical consolidation stress. For RNSC the critical state friction angle decreases as the consolidation stress increases. This was a trend detailed within Casey B. (2014) that found clays with higher liquid limits (>50%) tended to have a more rapid decrease in the

critical state friction angle with an increase in consolidation stress. Within RNSC this was found to be a decrease of around 10 degrees with an increase in the consolidation stress of around 430 KPa.

Figure 4-38 shows the shearing stress paths for the 6 NC CK₀UC triaxial tests in MIT p-q space. Where q is the shear stress and p is the average effective stress. The stress paths generally show a curved failure envelope for RNSC at higher stress levels. This is a general trend as TX1330 does not fit within a smooth curve failure envelope. Triaxial tests TX1316 and TX1327 indicate that the failure envelope may curve towards the hydrostatic axis at stresses higher than 400 KPa. There are not enough triaxial tests on RNSC to determine the non-linearity of the failure envelope definitively.

Figure 4-39 is a plot of the shearing stress paths from the CK₀UC triaxial tests normalized the maximum vertical consolidation pressure. The undrained shear stress path from CK₀UC tests are a good approximation of the yield surface for fine grained materials as detailed within Hanley (2017). Observed within Figures 4-38 and 4-39 is a significant rotation of the yield surface towards the hydrostatic axis with an increase in effective stress.

Figure 4-40 is a plot of the normalized shear induced pore pressure by axial strain from the shearing phase of the 6 NC CK₀UC triaxial tests. The shear induced pore pressure is the difference between the measured excess pore pressures within the specimen during shearing and a calculated constant octahedral stress state. Shear induce pore pressure is used to help identify material behavior during undrained shear tests. The shear induced pore pressure provides an index of the contraction or dilation potential of a specimen. A positive shear induced pore pressure is indicative of a contractive behavior within the specimen and a negative shear induced pore pressure is indicative of dilative behavior within a specimen. A constant

shear induced pore pressure indicates that the specimen is at its critical state. RNSC shows contractive behavior during the entire undrained shear phase which is consistent with the clay behaviors detailed within Ladd (1964). The continued increase in pore pressure generation indicates that RNSC has not reached its critical state limits for any of the 6 NC CK₀UC tests. The specimens that had higher consolidation stresses also had normalized shear induced pore pressures.

4.5.3. CIUC Triaxial Tests

Prior to the advent of computer controlled triaxial equipment, the laboratory standard was to isotropically consolidate triaxial specimens. This was the standard due to the ease in loading as well as the simplicity in determining the specimen's state of stress. Only two isotropic tests were performed as K_0 consolidation is considered to be a better analog to the natural soil behavior. During K_0 consolidation the specimen experiences shear stress, at a level that does not exceed the failure envelope. During isotropic consolidation the specimen does not experience any shear stress. When sheared an isotropically consolidated specimen experiences the shear stress that would have been already applied at the pre-shear stress state from k_0 consolidation. The structure of the soil develops during consolidation and the effects of the different structures from different consolidation techniques are observed during shear. There is a strong argument that the yield surface for the soil is different within isotropically consolidated tests and K_0 consolidated tests due to the change in soil structure.

Two CIUC tests were performed on RNSC, Test TX1338 and TX1346 which were consolidated to a consolidation stress of 0.39 MPa and 0.13 MPa respectively. Figure 4-41 shows the stress strain curves from the shear portion of the two CIUC tests. The CIUC tests have a much more rounded shape to the stress strain curve and a larger strain to failure. Strain

softening post failure within the CIUC test was fairly insignificant when compared to K_0 consolidated tests. Similar to the K_0 consolidated tests, the maximum shear strength increased with increases in consolidation stress. Figure 4-42 shows the stress-strain curves from CIUC testing where the shear stress is normalized to the maximum consolidation stress. Similar to the results from CK_0UC testing as the maximum consolidation stress increases the normalized shear stress decreases. Figure 4-43 shows select stress-strain curves from CIUC and CK_0UC testing where the shear stress is normalized to the maximum consolidation stress. Figure 4-43 shows the differences in strain to failure, strain softening and the shape of the stress strain curves between the two test methods.

Figure 4-44 shows a plot of the shear stress paths from the CIUC test in MIT p-q space. Which some interpret as the slope of the yield surface. Figure 4-45 shows the CIUC shear stress path in MIT p-q space normalized to the maximum consolidation stress. The critical state friction angle for TX1338 was found to be 23.4° and in 34.2° in TX1346. Figure 4-46 is a plot of the normalized shear induced pore pressure by axial strain from the CIUC tests. The pore pressure generated is positive for both tests indicating contractive behavior during shear.

4.5.4. CI/ K_0 DC Triaxial Tests

Two drained triaxial tests were performed on RNSC in order to observe the shear stress response and friction angle. In a drained compression shear mode, the stress path for a soil in MIT p-q space extends at a 45 degree angle in increasing p values. TX1344 was isotropically consolidated to a maximum stress of 0.78 MPa prior to drained shearing. TX1345 was K_0 consolidated to a maximum stress of 0.15 MPa prior to drained shearing.

Figure 4-47 shows the stress strain curves for the drained triaxial tests. Figure 4-48 shows the normalized stress strain curves from the drained triaxial test where the shear stresses

are normalized to the consolidation stress. TX1344 has a very rounded stress strain curve. The stress strain curve for TX1345 has a small segment at low strains (<0.3%) that appears to be linear elastic. At higher strains, TX1345 has a rounded stress strain curve similar to TX1344 indicating both tests were strain hardening during shearing. The test indicates RNSC undergoes large strains in drained shear.

The friction angle at maximum shear stress for triaxial tests TX1344 and TX1345 was measured to be 22.27 degrees and 24.02 degrees respectively. The 24.02 degree friction angle measured in TX1345 is very similar to undrained friction angles measured in TX1283 and TX1379. TX1283 and TX1379 had undrained friction angles of 28.95 degrees and 25.39 degrees respectively. All three tests were consolidated to the same general stress level of 0.15 MPa.

Figure 4-49 shows the volumetric strain by axial strain from the shearing phase of the two drained triaxial tests (TX1344 and TX1345). The flat portion of the curve for TX1344 that starts around 9% strain indicates that the specimen may have been non-uniform as the shear stress continues to increase. When the volumetric strain by axial strain is constant one would expect the specimen to be at its critical state and the shear stress to also be constant. The continual rise in volumetric strain shown within the curve of TX1345 indicates that the sample has not yet reached its critical state yield point as well.

4.5.5. CK₀UE Triaxial Tests

Five NC CK₀UE triaxial tests were performed on RNSC as an exploration of the strength anisotropy within the soil. Strength anisotropy is the variation of strength parameters of the soil with the change of loading direction with respect to sedimentary layering. During the undrained shearing portion of a CK₀UE test, the specimen is unloaded in the axial direction until failure

occurs. Understanding the strength anisotropy within soil is important for the design and installation of soil retaining structures and geo-mechanical modeling.

Figure 4-47 shows the shear stress by axial strain for the NC CK₀UE tests performed on RNSC. For this research the axial stress will be presented as a negative value to indicate extension. The general trends observed are, that for each extension test, a significant amount of strain (>9%) is required before reaching the minimum shear stress. In general, the extension mode stress strain curves are very rounded Figure 4-48 shows the normalized shear stress by axial strain for NC CK₀UE. The normalized stress strain curves show a similar trend to the NC compression triaxial tests in which an increase in the consolidation stress leads to a decrease in the absolute value of the normalized maximum shear stress. However, the stress dependence is not as strong.

The friction angle of RNSC measured in the extension mode shows a trend of decreasing with an increase in consolidation stress on the sample. Figure 4-63 shows the variation in critical state friction angle by average stress at failure. Figure 4-63 shows that both the extension and compression mode critical failure envelope follows a clear trend of decreasing with increasing average stress at failure. This indicates that the failure envelopes for both extension and compression are likely curved.

Figure 4-52 shows the shear stress paths in MIT p-q space for the five NC CK₀UE tests. RNSC shows an increase in extension shear strength with an increase consolidation level. Figure 4-53 shows the normalized shear stress paths in MIT p-q space for the five NC CK₀UE tests.

A plot of the shear induced pore pressure normalized to the maximum confining stress by axial strain for the CK₀UE tests is presented in Figure 4-54. The generation of positive pore

pressures is observed through the entirety of the shear phase. This indicates that during extension tests RNSC has contractive tendencies.

4.5.6. High OCR Triaxial Tests

The Over Consolidation Ratio is defined as the soil's maximum past pressure by the current effective stress on the soil. The maximum past pressure is typically determined through a graphical construct on a consolidation curve. Where the maximum past pressure is the point of maximum curvature on a reloading to normally consolidated portion. Within triaxial testing the maximum past pressure can be set through consolidating the soil. Then the OCR can be set for a soil by swelling the soil (alleviating stress) to a desired stress state. This technique was used to measure, RNSC Stress History and Normalized Soil Engineering Parameters (SHANSEP). The SHANSEP method for fine grained soils is detailed within Ladd & Foote, (1974). In general the SHANSEP equation provides a methodology to relate the normally consolidated undrained shear strength to the shear strength of an over consolidated fine grained soil. The SHANSEP equation is shown as Equation 4-1.

$$\frac{S_u}{\sigma'_{vc}} = S (OCR)^m \quad \text{Equation 4-1}$$

Where S is the undrained strength ratio for normally consolidated clay and m is the power coefficient typically between 0.75 and 1. Within Abdulhadi (2009) the S parameter was found to be stress dependent for Boston Blue Clay. The stress dependence of S was further explored in Casey B. (2014) where it was found that S changes systematically but m does not.

For RNSC at a stress level of 280 KPa S=0.79 and m=0.71 can be used to fit Equation 4-1. This is based on test results from TX1326 and TX1332.

Two CK_0UC triaxial tests were performed at OCRs higher than 1. Both tests (TX1332 and TX1337) had an OCR around 2. The compression curves of the high OCR triaxial tests in strain space are presented in figure 4-55. The CR values ranged from 0.173 to 0.193 with an average value of 0.183. The consolidation curves in a void ratio space are presented in Figure 4-56. The two tests show a good correlation between stress and void ratio for the normally consolidated portion.

Shear stress by axial strain curves for the high OCR tests are presented in Figure 4-57. These curves have a similar trend to the normally consolidated test in which a higher vertical consolidation pressure correlates to higher maximum shear strength. This is expected as detailed within Ladd & Foote (1974). Both tests show consistent strain softening after maximum shear stress. The normalized shear stress by axial strain is presented in Figure 4-58. It is important to note that the shear stress is normalized to the pre-shear consolidation stress and not the maximum consolidation stress. Each specimen was held for a minimum of one log cycle of secondary compression (typically > 40 hours) at the pre-shear stress. TX1332 and TX1337 (OCRs of 2) had similar peak normalized shear stress but TX1337 was measured to have slightly higher shear strength which can be attributed to the higher pre-consolidation stress. The variation in stress level and OCR for RNSC can be observed by the shear stress paths in MIT p-q space shown in Figure 4-59. The stress paths within Figure 4-59 travel along the yield surface to higher p values which are characteristic of over consolidated clay soils as discussed within Ladd (1964). The normalized shear stress paths in MIT p-q space are presented in Figure 4-60. These stress paths are normalized to the pre-shear consolidation stress and not the maximum consolidation stress. Similar to the normalized stress strain curves, the normalized shear paths show that RNSC has sensitivity to both consolidation stress and OCR.

The shear induced pore pressure by axial strain from the high OCR triaxial tests is presented in Figure 4-61. TX1332 and TX1337 show a negative pore generated during shear for the first 1% of strain. This shows that the material had dilative behavior during the initiation of strain and this causes an increase in mean effective stress making the material stronger.

4.5.7. Critical State Friction Angle

The critical state friction angle for all compression tests performed at a stress level under 1 MPa was found to range between 22.3 degrees and 34.2 degrees. Figure 4-62 shows the variation in critical state friction angle over consolidation stress for all compression triaxial test types. The average of the compression test critical state angle was 26.0 which increase to 27.4 when TX1341 is not considered. As discussed within the Section 4.5.2 RNSC shows a consistent trend of decreasing effective friction angle with increasing maximum consolidation pressure.

Figure 4-63 shows the variation in critical state friction angle by average stress at failure for all triaxial test types. The extension tests were found to have a critical state friction angle ranging between 27.0 degrees and 55.6 degrees. The average critical state friction for RNSC in extension under a maximum consolidation stress was found to be 39.7 degrees. There is a trend of decreasing friction angle with increasing average stress at failure within the extension test data points.

4.5.8. Undrained Shear Strength

In both the extension and compression modes the undrained shear strength of RNSC was found to be very sensitive to the maximum consolidation stress. In compression the undrained shear strength ranged from 47 to 137 KPa for a range of maximum consolidation stress levels between 129 and 585 KPa. Figure 4-64 shows a plot of maximum shear stress by maximum consolidation stress for all triaxial tests.

In extension testing, the range of undrained shear strength was found to be between -37 and -164 KPa over a maximum consolidation pressure range of 142 to 931 KPa. There were no conclusive trends observed within the data for undrained shear strength by vertical consolidation stress from the extension tests performed on RNSC.

The variation in compression and extension strength was studied in RNSC through the compressive strength to tensile strength ratio (S_{UC}/S_{UT}). At a stress of around 150 KPa the compressive strength to tensile strength ratio was found to be 1.26. In order to illustrate the strength anisotropy within RNSC Figure 4-65 presents undrained extension and compression stress strain curves for RNSC at a consolidation stress of 150 kPa. At a stress of around 370 KPa the compressive strength to tensile strength ratio was found to be 1.46. The increase in the compressive strength to tensile strength ratio in conjunction with the data presented in Figure 4-64, indicates that the compressive strength of RNSC increase more rapidly than the tensile strength of RNSC with increases of consolidation stress.

4.5.9. Lateral Stress Coefficient K_0

The lateral stress coefficient of RNSC has been found to be sensitive to the maximum consolidation stress. K_0 measured within triaxial tests on RNSC has been found to range between 0.45 (TX1283) and 0.90 (TX1331). The variation in K_0 is likely due to the variation in maximum consolidation stress. Figure 4-66 shows the K_0 value versus maximum consolidation stress and there is a clear trend that as the consolidation stress increases the K_0 increase.

4.5.10. Undrained Secant Young's Modulus E_U

A general approximation of the stiffness of RNSC can be made through the slope of the stress strain curve during undrained shearing as an elastic parameter known as Young's modulus. Within the TAG lab the Young's modulus is calculated as the secant slope from the

initial data point to the current data point. Figure 4-67 shows an annotated example of the calculation. The low stress triaxial equipment used for the RNSC testing did not utilize the specialty setup required for a direct measurement of the undrained/drained Secant Young's Modulus ($E_{u/D}$). Where undrained/drained just denotes the method in which the soil was sheared. Also, there is some plastic deformation occurring during shearing which is incorporated in the calculation of the Secant Young's Modulus. All values $E_{u/D}$ reported herein are approximate and are being discussed in order to understand broader trends in RNSC's material behavior.

The Secant Young's Modulus for RNSC was calculated for the undrained/drained stress-strain curves during the shearing of each specimen. The Secant Young's Modulus was not evaluated in extension tests due to equipment limitations. $E_{u/D}$ was calculated at two different strains (0.01% and 0.1%) within each test to illustrate the change during shearing. Figure 4-68 shows the variation in the $E_{u/D}$ by maximum consolidation stress. At 0.01% strain E_u ranged from 19,064 KPa/ ϵ to 199,022 KPa/ ϵ , and E_D ranged between 79,009 KPa/ ϵ and 197,631 KPa/ ϵ . At 0.1% E_u ranged between 16,522 KPa/ ϵ and 72,475 KPa/ ϵ , and E_D ranged between 14,285 KPa/ ϵ and 23,595 KPa/ ϵ .

Figure 4-69 shows the variation in normalized $E_{u/D}$ by maximum consolidation stress. Initially the values are high at stresses less than 200 KPa. Normalized $E_{u/D}$ for RNSC at 0.01 % showed a general decrease in increasing consolidation stress. At 0.1% past a consolidation stress of 200 KPa, normalized $E_{u/D}$ is fairly constant around 100,000 with scatter of +/- 50,000. This may indicate that the Young's modulus of RNSC has a dependence on the confining stress. The three major trends observed within RNSC were

1. RNSC had a lower E at 0.1% strain than at 0.01% strain. This indicates the material softened with an increase in strain.
2. At both strain levels (0.1% and 0.01%) the Young's Modulus was found to increase with an increase in consolidation stress.
3. The Young's Modulus of RNSC may be dependent on the consolidation stress.

RNSC Series	Specific Gravity	Liquid Limit (%)	Plastic Limit (%)	Plasticity Index (%)	Calcite Equivalence (%)	Salt Concentration g/kg	Organic Content (%)	Comments
I	N/A	61.50	24.50	37.00	N/A	N/A	N/A	>#100 Sieve Sized Particles Removed
II	2.816	62.12	23.44	38.68	3.3	0.02	2	Full range of Soil Particles
III	N/A	66.28	29.66	36.62	N/A	N/A	N/A	>#200 Sieve Sized Particles Removed

Table 4- 1: Summary of RNSC Index Properties

Test No.	Resed No.	Series	Setup Conditions					Maximum Stress				Final W _c (%)	CR at		SR OCR = 4	RR (OCR=4) Stress Range Mpa		RR/CR Stress Range Mpa	
			W _i (%)	e _i	S _i (%)	γ _d (g/cm ³)	γ _t (g/cm ³)	σ' _{vm} (Mpa)	ε _a (%)	e _c	γ _t (g/cm ³)		(0.1-1 Mpa)	(1-10 Mpa)		(0.1-1 Mpa)	(1-10 Mpa)	(0.1-1 Mpa)	(1-10 Mpa)
			CRS 1493	RS470	I	43.99	1.230	102.47	1.262	1.826	9.149		36.349	0.3524		2.343	18.81	0.215	0.176
CRS 1494	RS470	I	48.45	1.400	98.83	1.180	1.753	9.626	35.817	0.3663	2.329	28.33	0.207	0.171	0.014	N/A	N/A	N/A	N/A
CRS 1504	RS504	II	44.25	1.163	107.15	1.302	1.878	7.783	35.208	0.3430	2.352	21.17	0.218	0.180	0.026	0.062	0.052	0.284	0.289

Table 4- 2: Summary of CRS Phase Relations and Compression Parameters

Test No.	Resed No.	Test Type	Series	Maximum Resedimentation stress MPa	Setup Conditions					Maximum Stress				Pre-Shear					CR ¹	
					W _i (%)	e _i	S _i (%)	γ _d (g/cm ³)	γ _t (g/cm ³)	σ' _{vm} (Mpa)	ε _a (%)	e _c	K _{0(NC)}	σ' _{vc} (Mpa)	ε _a (%)	e _c	γ _t (g/cm ³)	OCR		K _{0(NC)}
TX1283	RS470	CK ₀ UC	I	N/A	46.52	1.381	99.73	1.232	1.807	0.152	10.72	1.122	0.450	0.152	10.72	1.122	1.856	1.010	0.450	0.218
TX1316	RS513	CK ₀ UC	II	0.300	35.00	1.042	94.60	1.376	1.858	0.584	7.86	0.836	0.720	0.584	7.86	0.836	1.989	1.000	0.720	0.127
TX1326	RS534	CK ₀ UC	II	0.147	40.46	1.184	96.68	1.289	1.812	0.228	10.93	0.910	0.580	0.228	10.93	0.910	1.951	1.040	0.580	0.163
TX1327	RS527	CK ₀ UC	II	0.281	36.07	1.065	95.49	1.361	1.853	0.580	8.73	0.870	0.740	0.580	8.73	0.870	1.971	1.060	0.740	0.091
TX1329	RS537	CK ₀ UE	II	N/A	42.46	1.204	99.44	1.276	1.817	0.343	14.88	0.871	0.620	0.343	14.88	0.871	1.971	1.000	0.620	0.097
TX1330	RS540	CK ₀ UC	I	0.335	37.40	1.069	98.64	1.359	1.867	0.395	10.88	0.832	0.510	0.395	10.88	0.832	1.991	1.010	0.510	0.122
TX1331	RS536	CK ₀ UE	II	0.361	34.13	0.997	96.61	1.408	1.889	0.931	10.43	0.764	0.880	0.931	10.43	0.764	2.029	1.000	0.880	0.150
TX1332	RS543	CK ₀ UC	II	0.140	41.98	1.232	96.12	1.260	1.789	0.289	10.23	1.022	N/A	0.139	9.65	1.006	1.905	2.080	N/A	0.193
TX1333	RS544	CK ₀ UE	I	0.331	35.98	1.069	94.91	1.359	1.848	0.678	10.98	0.852	0.649	0.678	10.98	0.852	1.981	1.000	0.649	0.152
TX1337	RS549	CK ₀ UC	I	0.343	34.84	1.045	94.00	1.375	1.854	0.701	9.66	0.833	N/A	0.352	9.44	0.835	1.990	1.990	N/A	0.173
TX1338	RS553	CIUC	II	0.147	41.34	1.224	95.25	1.264	1.787	0.390	2.37	1.178	N/A	0.390	2.37	1.178	1.834	1.000	N/A	0.057
TX1343	RS560	CK ₀ UE	II	0.147	41.91	1.220	96.89	1.267	1.812	0.650	9.13	1.006	0.680	0.650	9.13	1.006	1.905	1.000	0.680	0.668
TX1344	RS479	CIDC	II	0.078	48.67	1.412	97.20	1.165	1.733	0.784	9.39	0.999	N/A	0.784	9.39	0.999	1.908	1.000	N/A	0.050
TX1345	RS559	CK ₀ DC	II	0.142	42.85	1.237	97.74	1.257	1.796	0.152	4.76	1.121	0.601	0.152	4.76	1.121	1.856	0.970	0.601	0.167
TX1346	RS478	CIUC	II	0.104	45.35	1.301	98.31	1.222	1.776	0.129	0.91	1.061	N/A	0.129	0.91	1.061	1.881	1.030	N/A	N/A
TX1375	RS564	CK ₀ UE	II	0.105	46.35	1.324	98.72	1.210	1.771	0.142	9.77	1.093	0.551	0.142	9.77	1.093	1.868	1.000	0.551	0.227
TX1379	RS563	CK ₀ UC	III	0.088	49.92	1.371	102.70	1.186	1.778	0.141	9.26	1.139	0.531	0.141	9.26	1.139	1.849	1.000	0.531	0.268

1. Consolidation Ratio (CR) is the slope of the virgin compression line in ε-LogP space, measured during the Consolidation phase of a triaxial test.

Table 4- 3: Summary of RNSC Triaxial Test Phase Relations and Consolidation Phase Compression Parameters

Test No.	Resed No. Test Type		Series	End of Consolidation Conditions						At Maximum Shear				At Maximum Obliquity				Stiffness	
				σ'_{vc} ¹	ϵ_a	e_c	Time of Secondary	Pre-Shear K	OCR	ϵ_a	q/σ'_{vc}	P/σ'_{vc}	ϕ'	ϵ_a	q/σ'_{vc}	P/σ'_{vc}	ϕ'	$E_{U/D}$ (Kpa/ $\epsilon X100$)	
				(Mpa)	(%)		(Hours)			(%)				(%)				$\epsilon_a=0.01\%$	$\epsilon_a=0.1\%$
TX1283	RS470	CK ₀ UC	I	0.152	10.72	1.122	14.1	0.45	1.01	0.30	0.36	0.73	28.95	8.60	0.30	0.55	33.86	48185	18696
TX1316	RS513	CK ₀ UC	II	0.584	7.86	0.836	113.5	0.72	1.00	0.56	0.23	0.80	16.84	9.04	0.21	0.55	22.52	175927	72475
TX1326	RS534	CK ₀ UC	II	0.228	10.93	0.91	26.4	0.58	1.04	0.24	0.28	0.76	21.35	5.63	0.25	0.56	27.02	54831	23206
TX1327	RS527	CK ₀ UC	II	0.580	8.73	0.87	22.4	0.74	1.06	3.81	0.21	0.56	22.04	7.11	0.20	0.52	23.13	87516	51002
TX1329	RS537	CK ₀ UE	II	0.343	14.88	0.871	26.0	0.62	1.00	-9.23	-0.24	0.35	42.34	-9.73	-0.24	0.35	42.47	N/A	N/A
TX1330	RS540	CK ₀ UC	I	0.395	10.88	0.832	130.0	0.51	1.01	0.28	0.35	0.77	26.75	8.21	0.30	0.55	33.59	93269	52167
TX1331	RS536	CK ₀ UE	II	0.931	10.43	0.764	23.3	0.88	1.00	-10.68	-0.18	0.39	26.98	-11.01	-0.18	0.39	27.03	N/A	N/A
TX1332	RS543	CK ₀ UC	II	0.139	9.65	1.006	37.8	N/A	2.08	0.97	0.51	1.16	25.96	0.69	0.50	1.13	26.23	N/A	N/A
TX1333	RS544	CK ₀ UE	I	0.678	10.98	0.852	64.5	0.65	1.00	-10.14	-0.21	0.36	35.39	-8.77	-0.21	0.36	35.49	N/A	N/A
TX1337	RS549	CK ₀ UC	I	0.352	9.44	0.835	92.9	N/A	1.99	1.27	0.55	1.25	26.18	6.87	0.52	1.12	27.90	N/A	N/A
TX1338	RS553	CIUC	II	0.390	2.37	1.178	60.7	N/A	1.00	11.38	0.22	0.57	23.39	11.38	0.22	0.57	23.39	61278	44885
TX1343	RS560	CK ₀ UE	II	0.289	9.26	0.996	66.5	0.68	1.00	-10.18	-0.24	0.40	37.91	-10.18	-0.24	0.40	37.91	N/A	N/A
TX1344	RS479	CIDC	II	0.779	9.39	0.999	0.3	N/A	1.00	15.26	0.54	1.44	22.27	15.23	0.54	1.44	22.27	197632	23595
TX1345	RS559	CK ₀ DC	II	0.147	4.76	1.121	56.3	0.60	0.97	14.86	0.43	1.05	24.02	14.86	0.43	1.05	24.02	79009	14285
TX1346	RS478	CIUC	II	0.129	0.91	1.061	60.5	N/A	1.03	7.20	0.42	0.74	34.20	7.20	0.42	0.74	34.20	63171	37410
TX1375	RS564	CK ₀ UE	II	0.142	9.77	1.093	39.8	0.55	1.00	-9.05	-0.26	0.32	55.80	-9.05	-0.26	0.32	55.80	N/A	N/A
TX1379	RS563	CK ₀ UC	III	0.141	9.26	1.139	32.8	0.53	1.00	0.31	0.33	0.77	25.39	8.29	0.28	0.54	30.78	19064	16522

1. σ'_{vc} is the stress at the end of consolidation prior to shearing.

Table 4- 4: Summary of RNSC Triaxial Test Shearing Phase Engineering Parameters

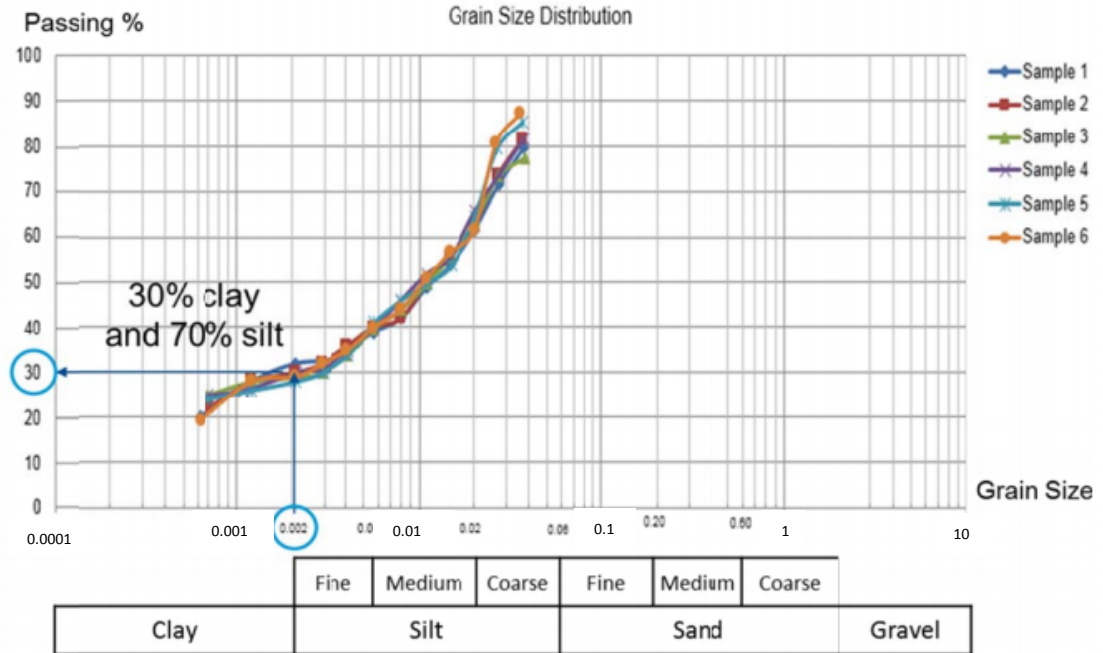


Figure 4- 1: Grain size Distribution from Sedimentation Testing on Series I

Courtesy of Dr. Sherif Akl University of Cairo

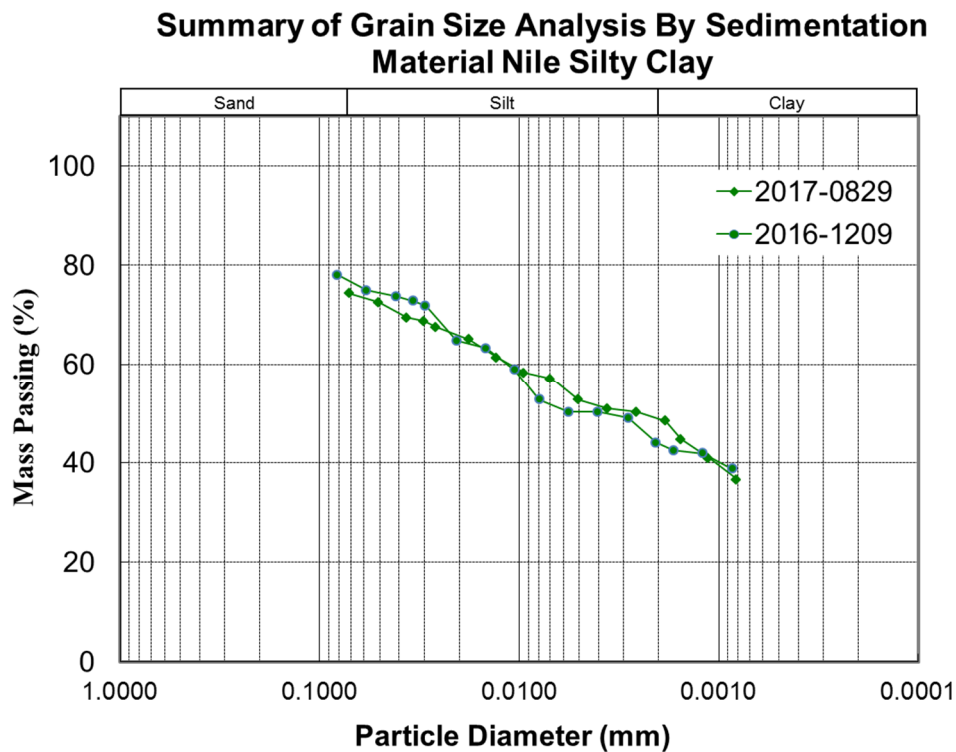


Figure 4- 2: Grain size Distribution from Sedimentation Testing on Series II

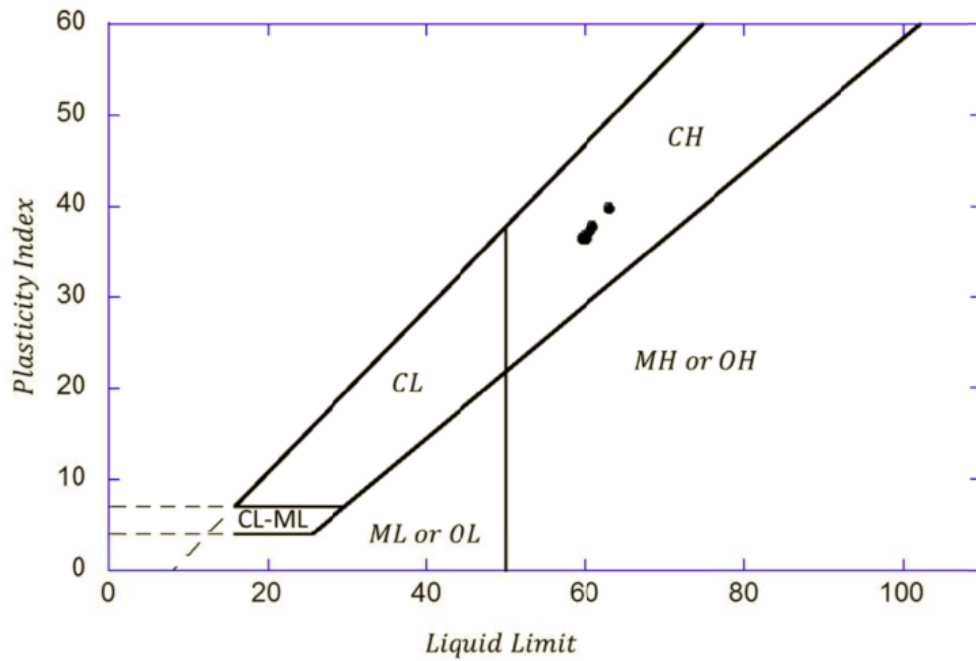


Figure 4- 3: Atterberg Limit Testing Performed on Series I Material

Courtesy of Dr. Sherif Akl University of Cairo

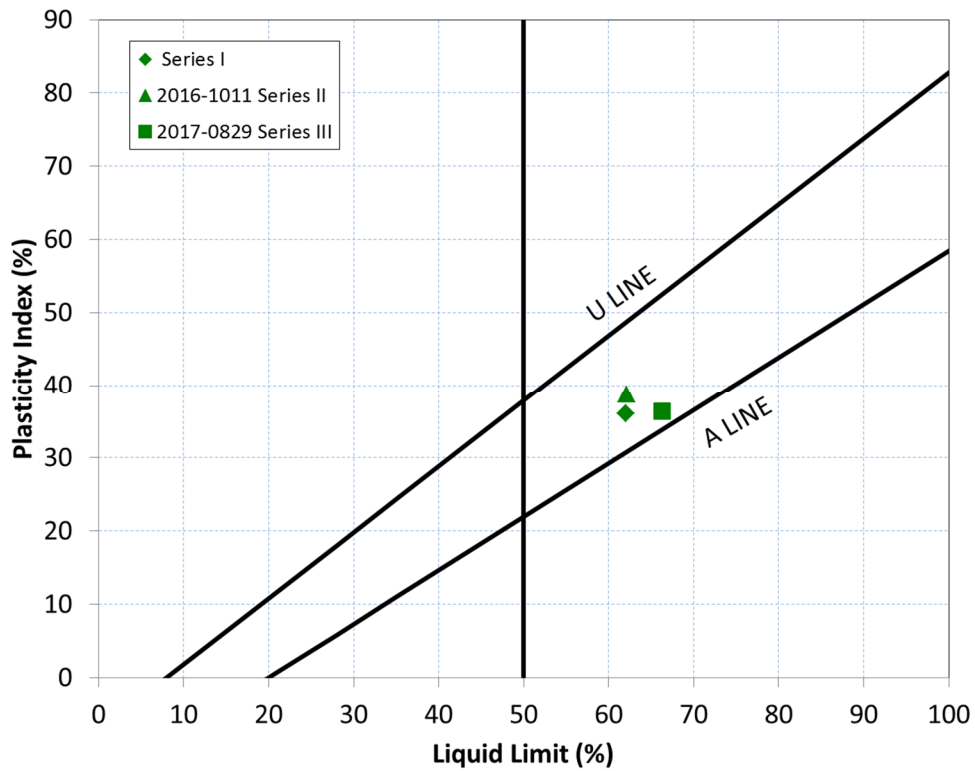


Figure 4- 4: Results of Atterberg Limit Testing on Series II and Series III Material

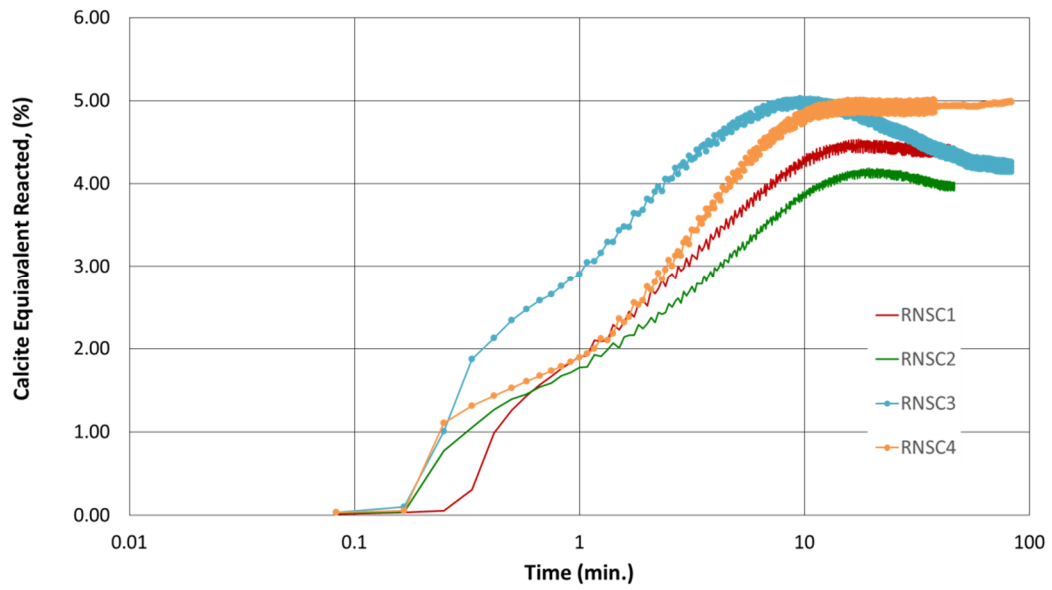


Figure 4- 5: Calcite Equivalency Pressure Curves (Series II)

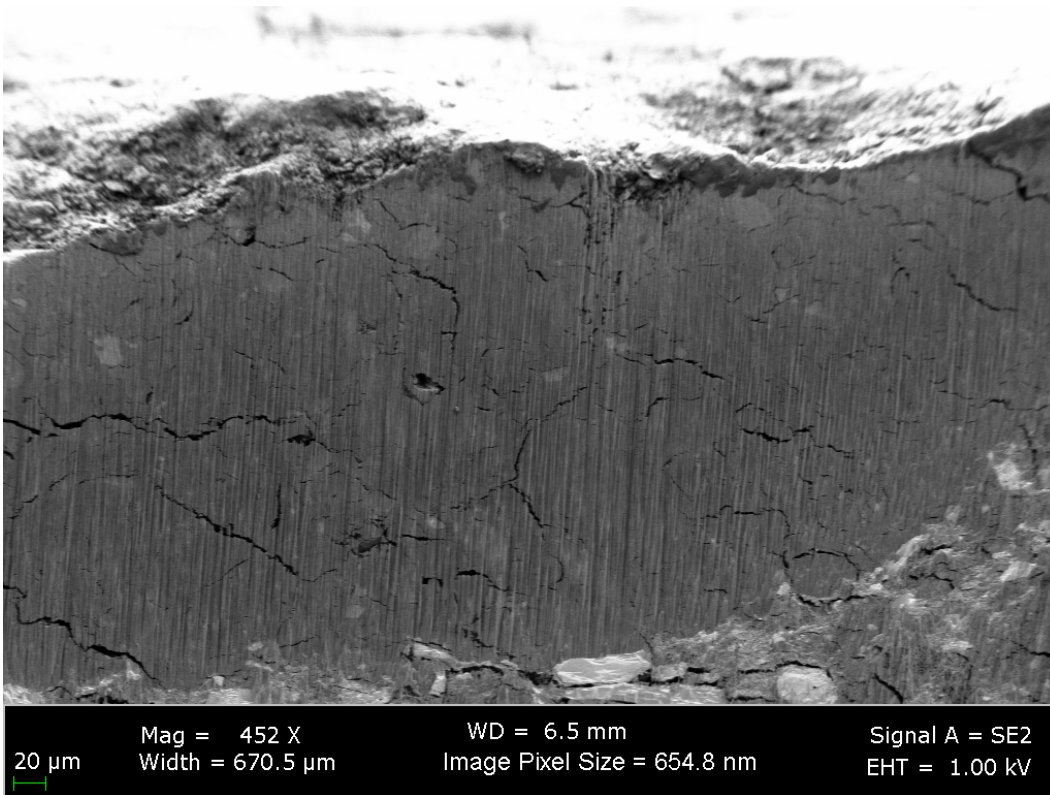


Figure 4- 6: Ion Milled Cross Section at Low Magnification in in TX1316 (Series II)

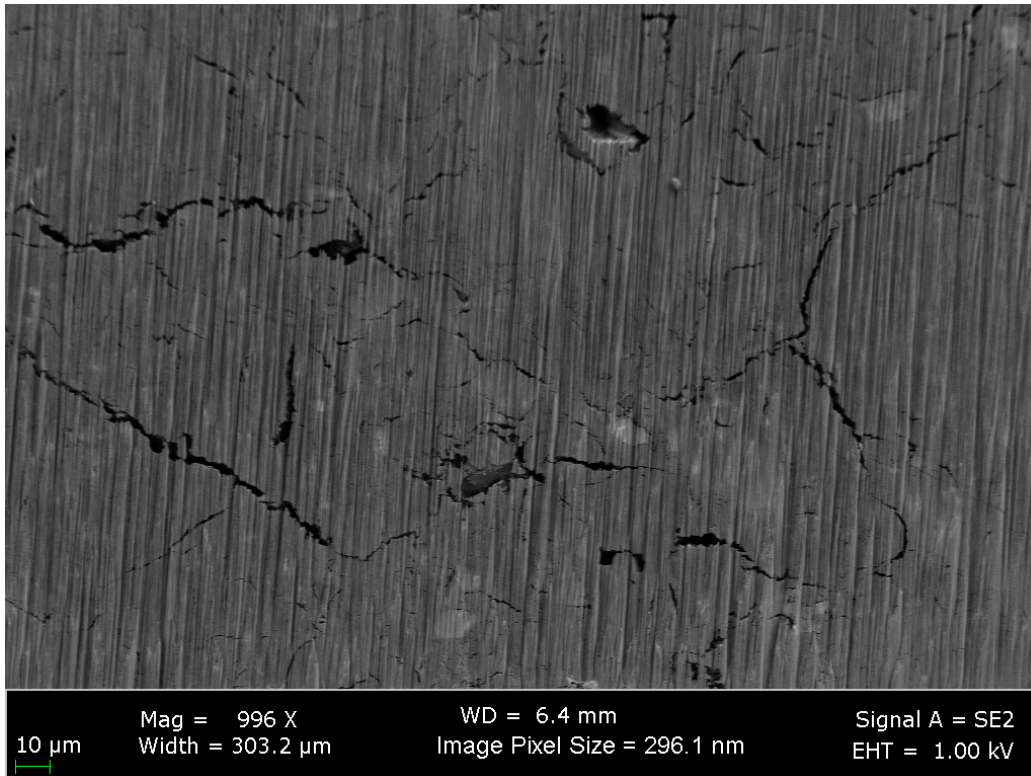


Figure 4- 7: Cracking in the fabric of TX1316 (Series II)

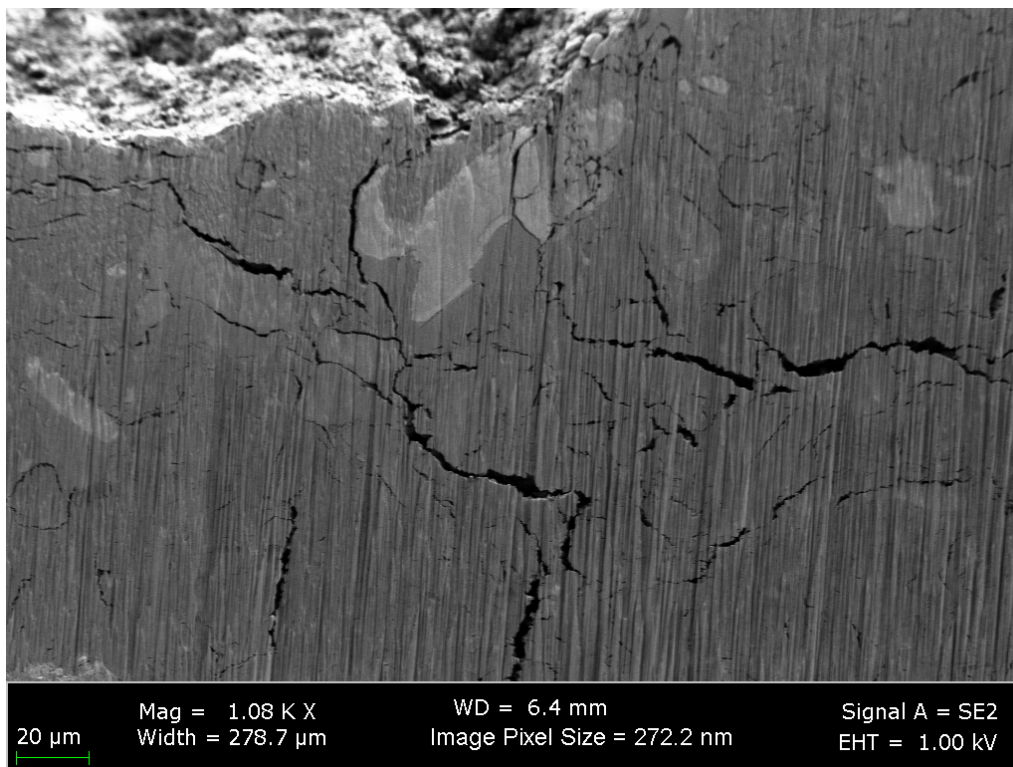


Figure 4- 8: Ion Milled Minerals within the Clay Matrix of TX1316 (Series II)

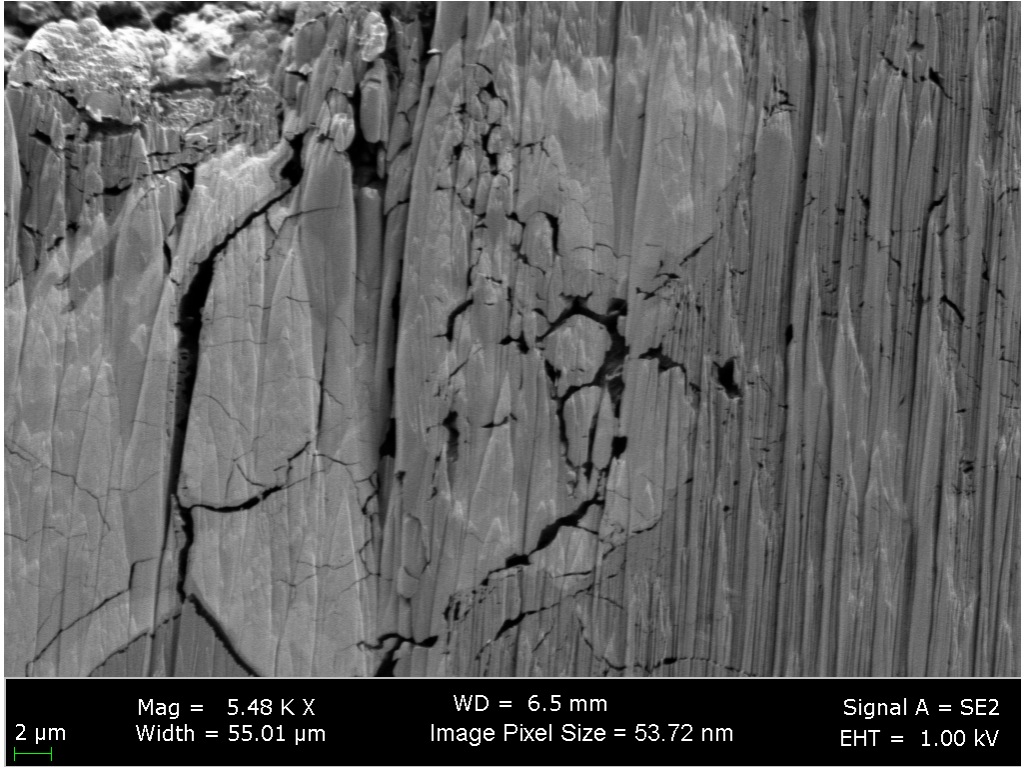


Figure 4- 9: Intra-particle Porosity within TX1316 (Series II)

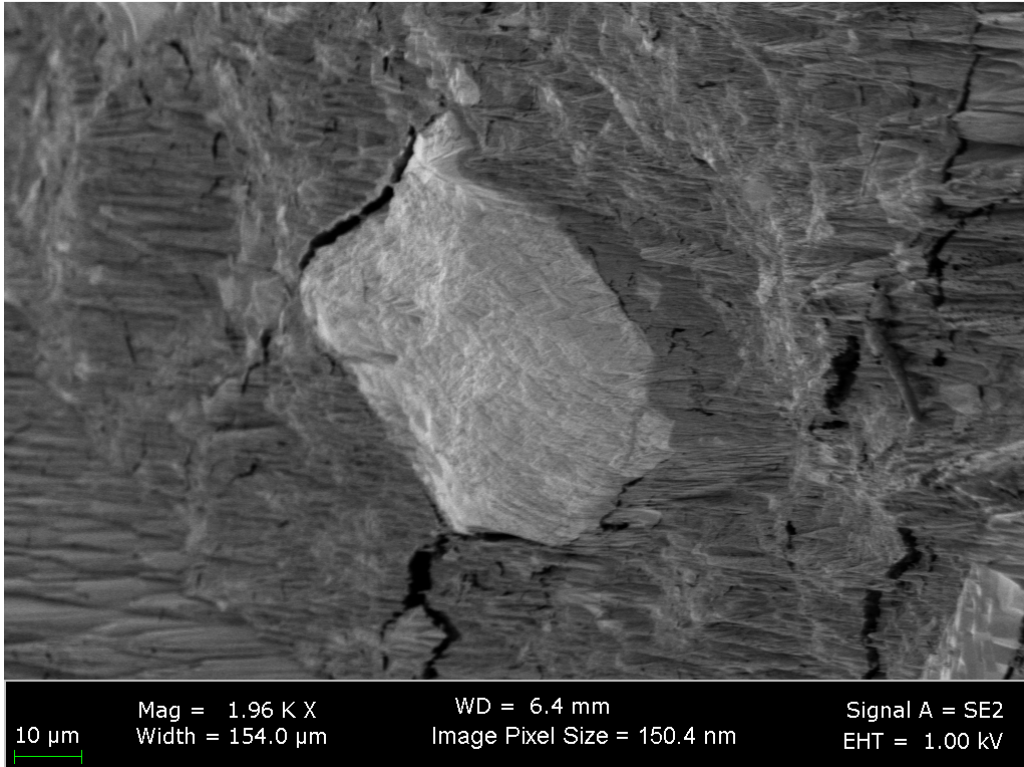


Figure 4- 10: Typical Mineral Grain within TX1316 (Series II)

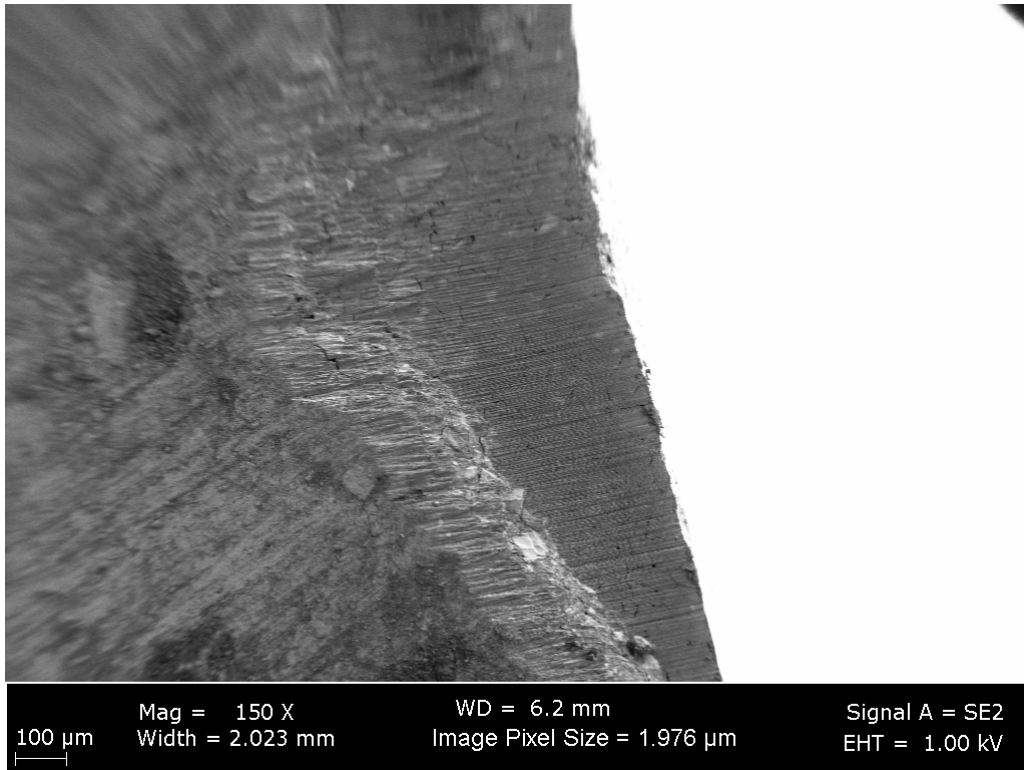


Figure 4- 11: Ion Milled Cross Section of TX1379 (Series III)

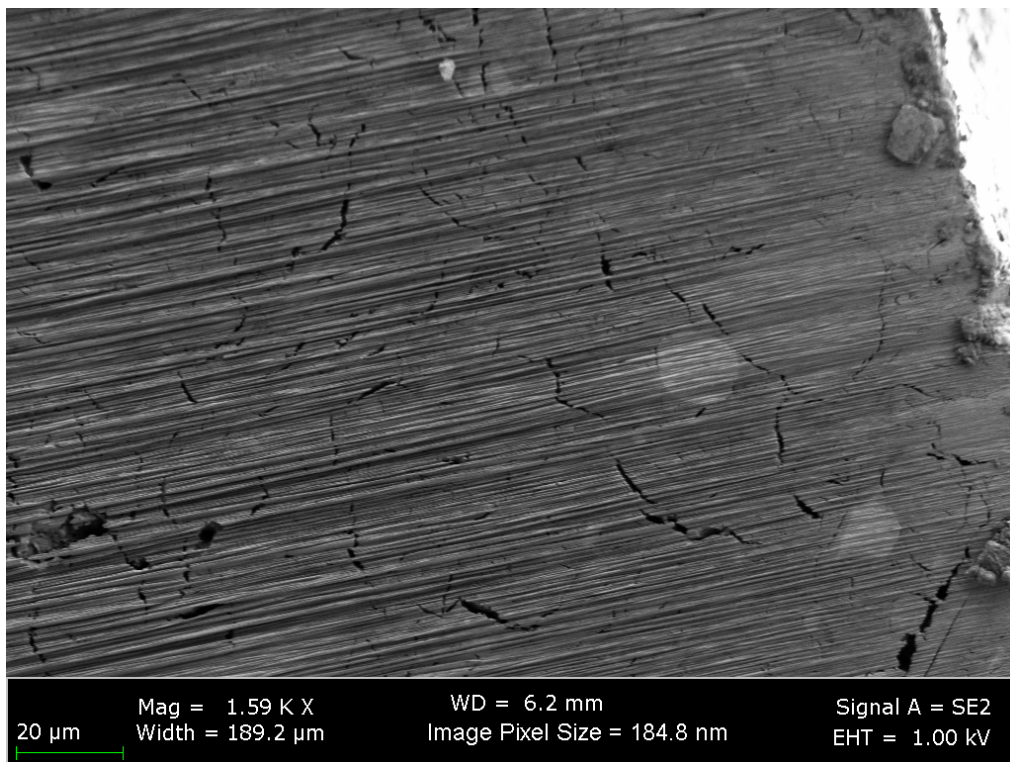


Figure 4- 12: Typical Crystalline Mineral Grains within TX1379 (Series III)

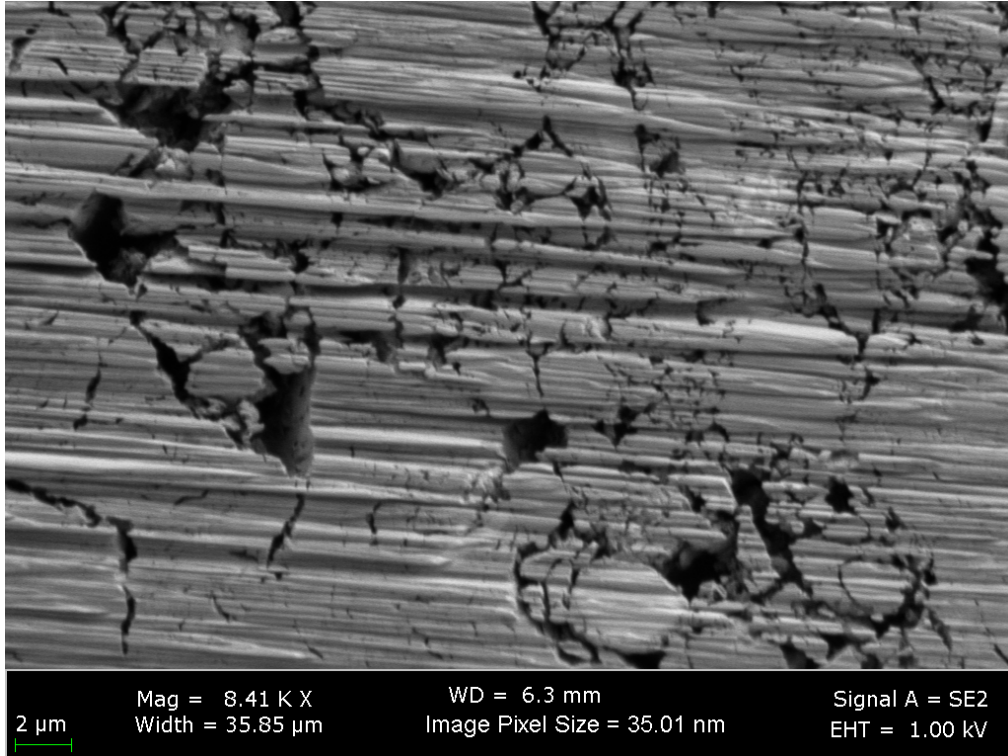


Figure 4- 13: Typical Pore Space Observed within TX1379 (Series III)

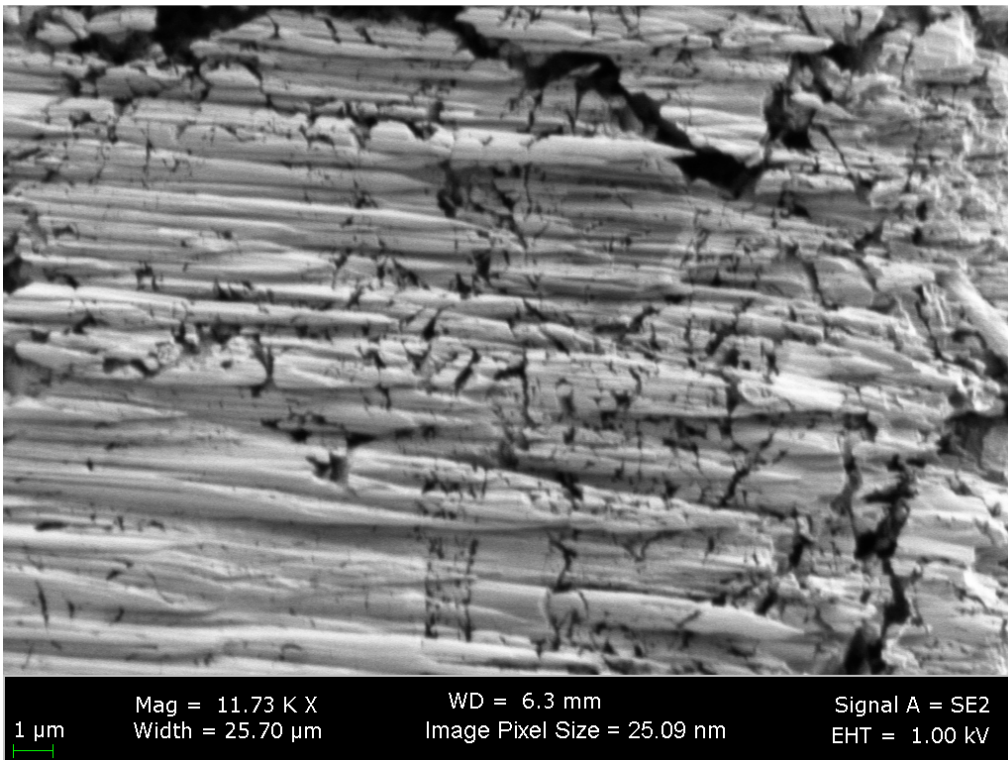


Figure 4- 14: Typical Microscopic Pore Space Observed within TX1379 (Series III)

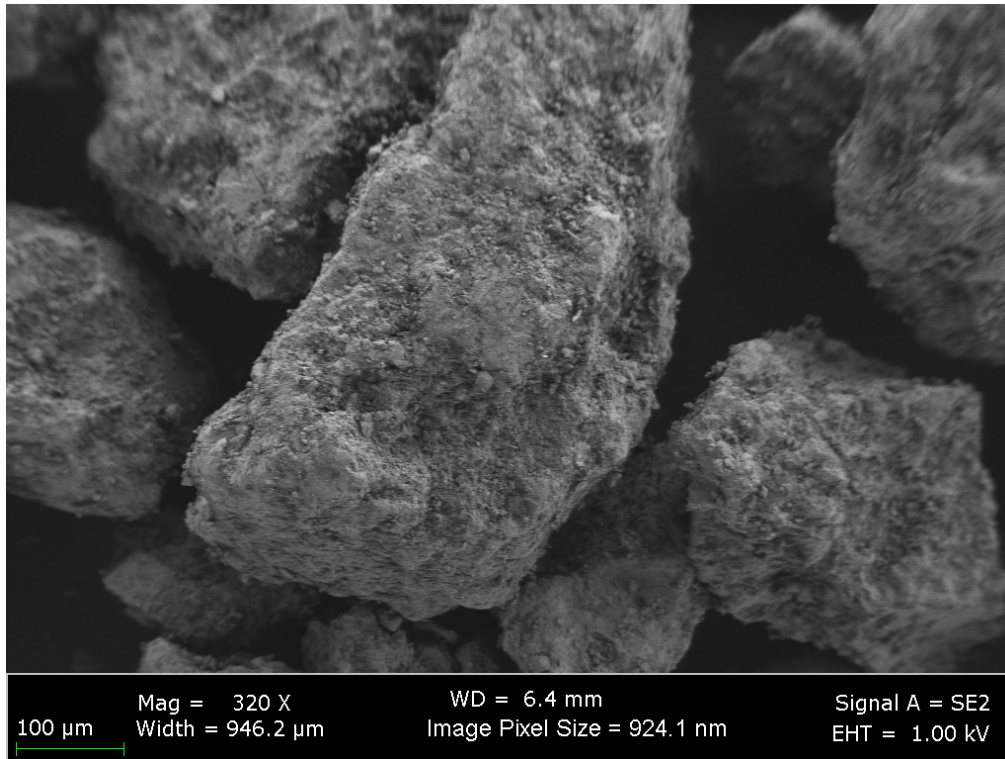


Figure 4- 15: >#200 Sieve Grains Potentially Clay Cemented Aggregates

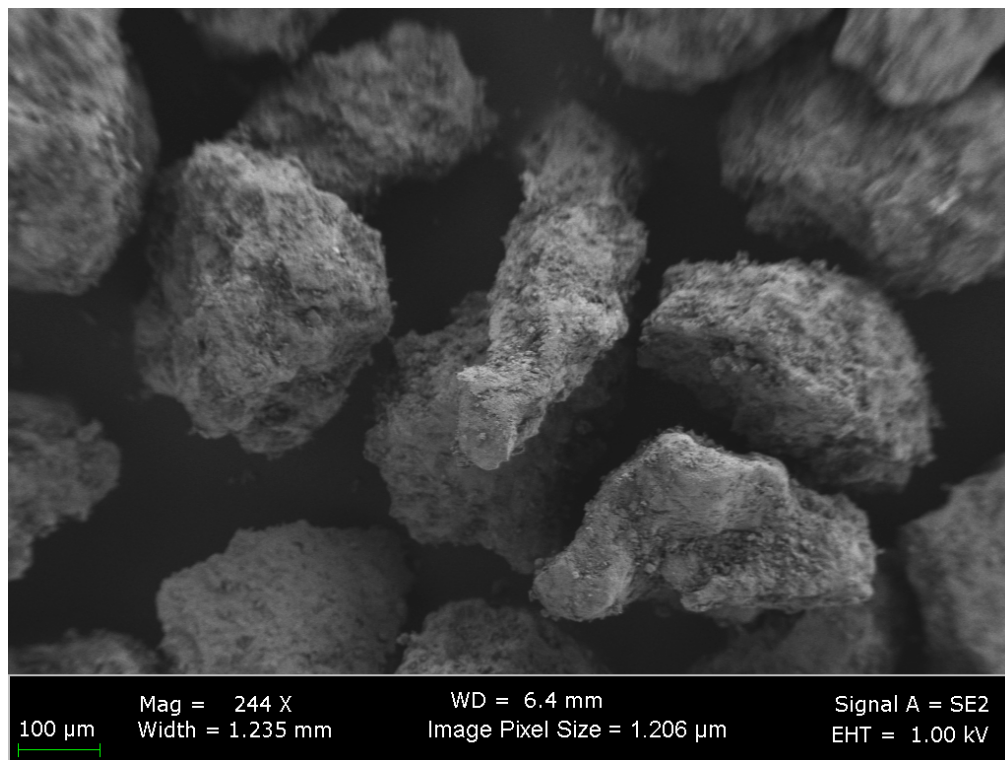


Figure 4- 16: >#200 Sieve Grains Potentially Clay Cemented Aggregates

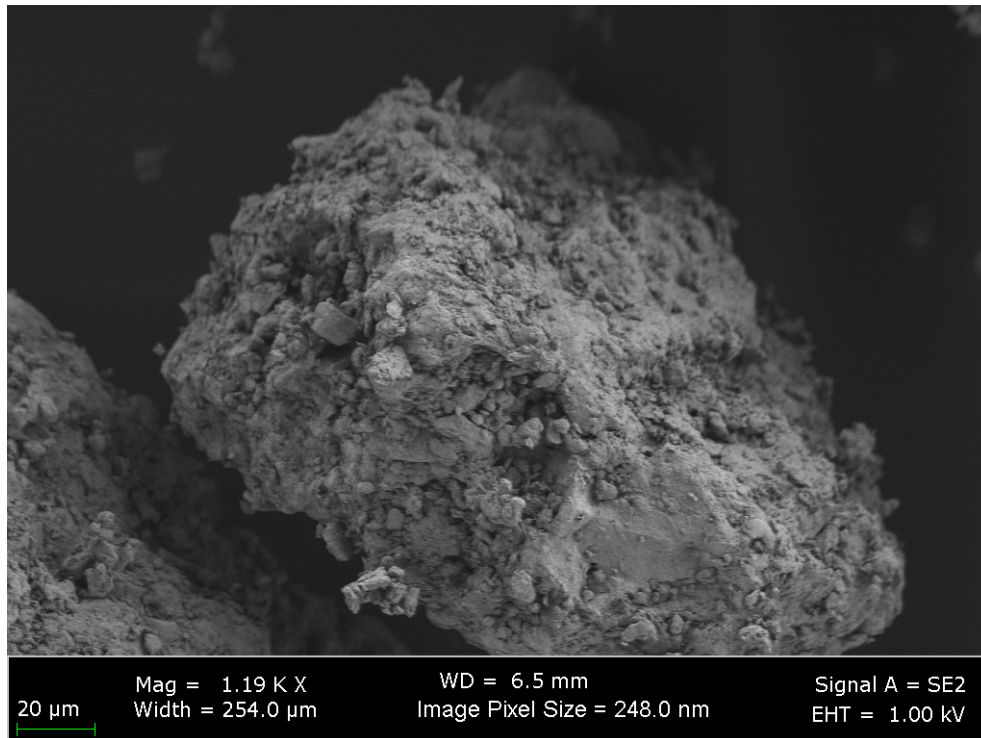


Figure 4- 17: >#200 Sieve Grain Potentially Clay Cemented Aggregates

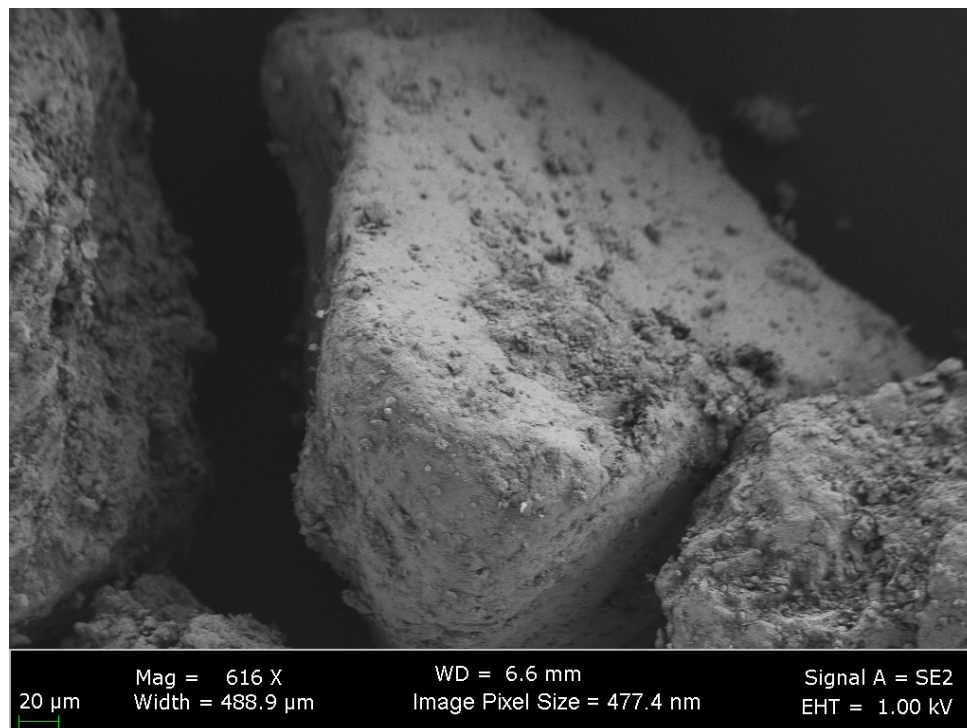


Figure 4- 18: >#200 Sieve Grain Crystalline Mineral

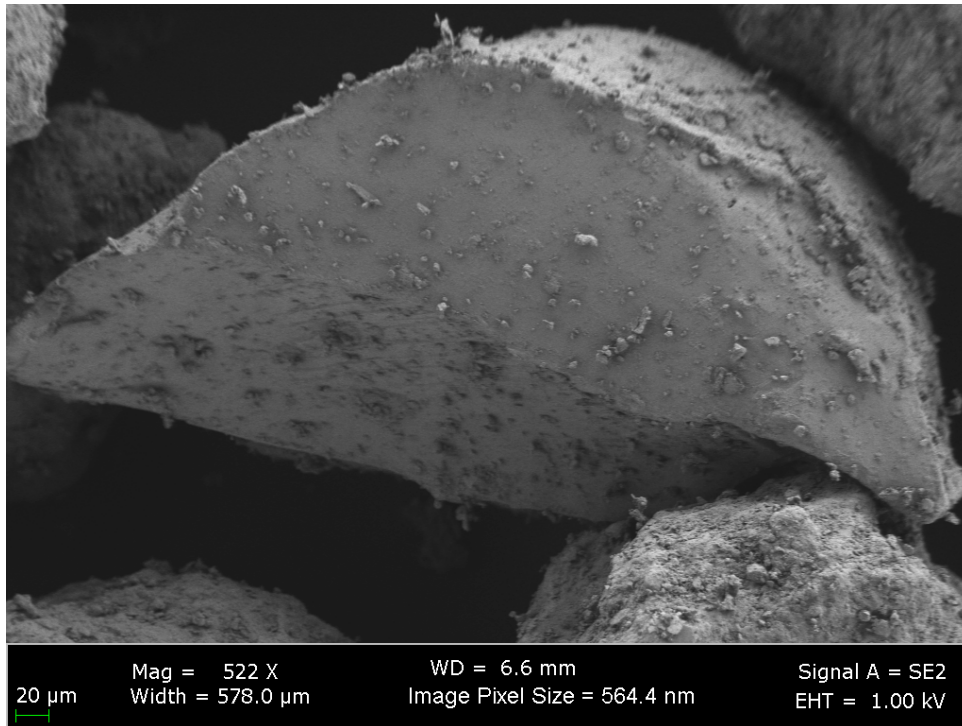


Figure 4- 19: >#200 Sieve Grain Crystalline Mineral

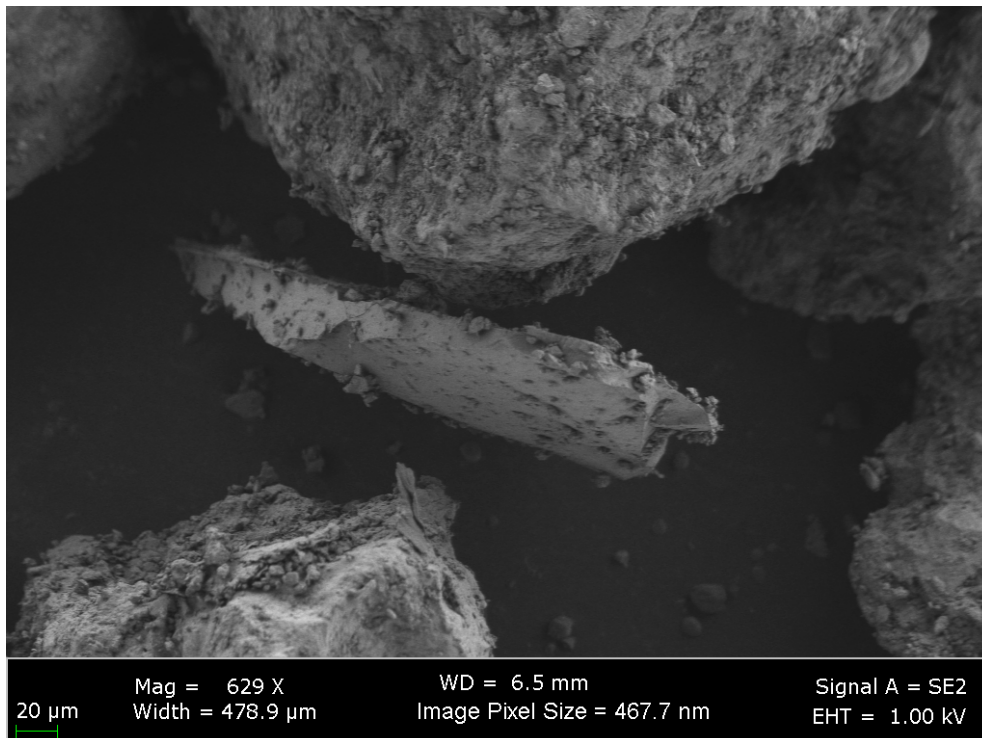


Figure 4- 20 >#200 Sieve Grain Crystalline Mineral

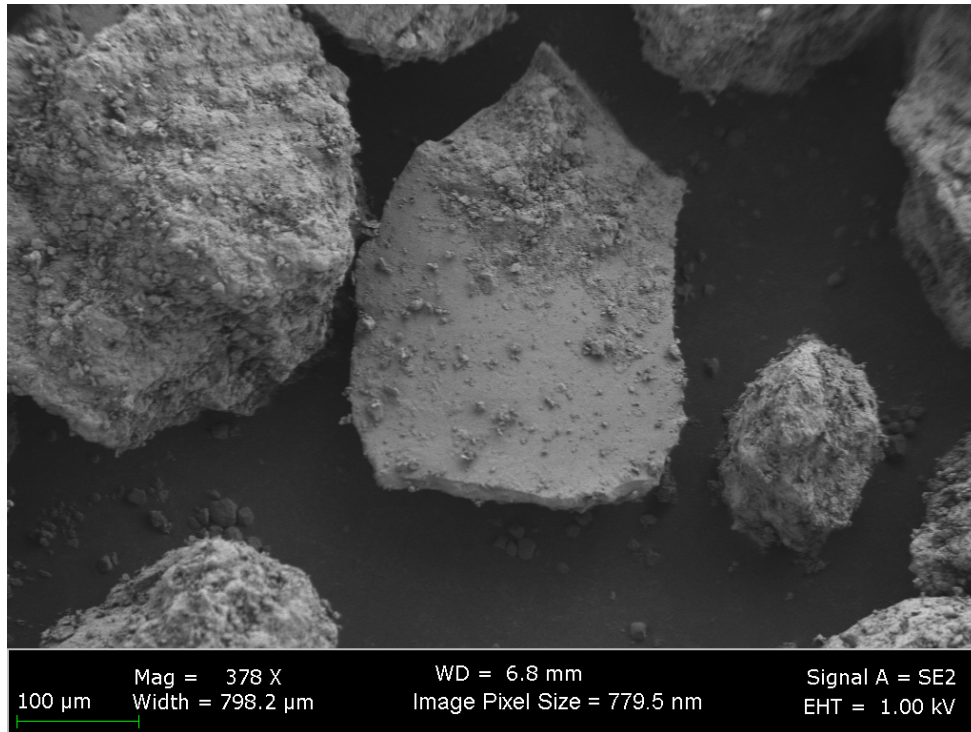


Figure 4- 21: >#200 Sieve Grain Crystalline Mineral

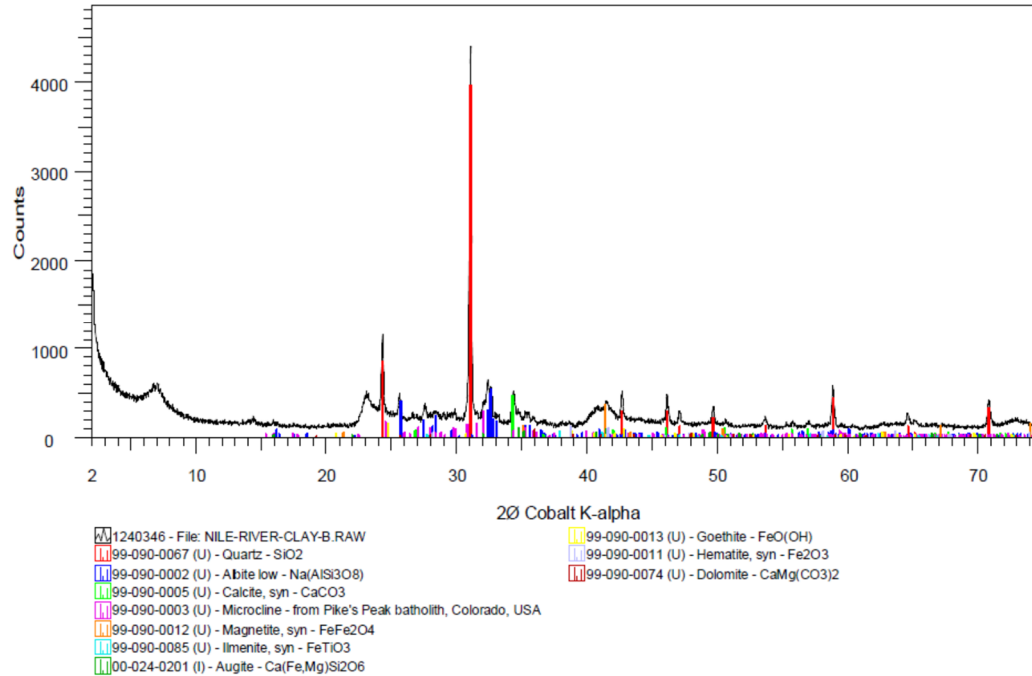


Figure 4- 22: Bulk XRPD Pattern with Main Non-Clay Phases

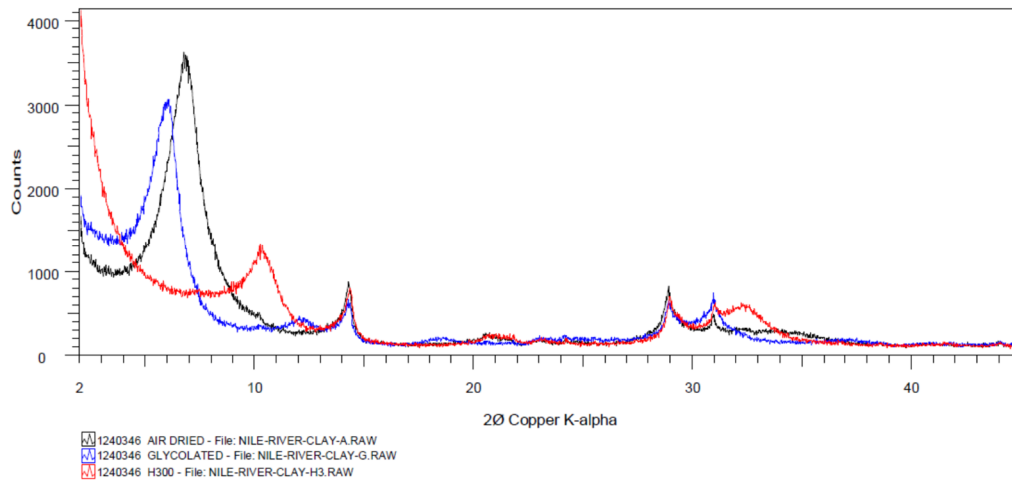


Figure 4- 23: XRPD Results of Clay Fraction (<2μm particle size) of RNSC

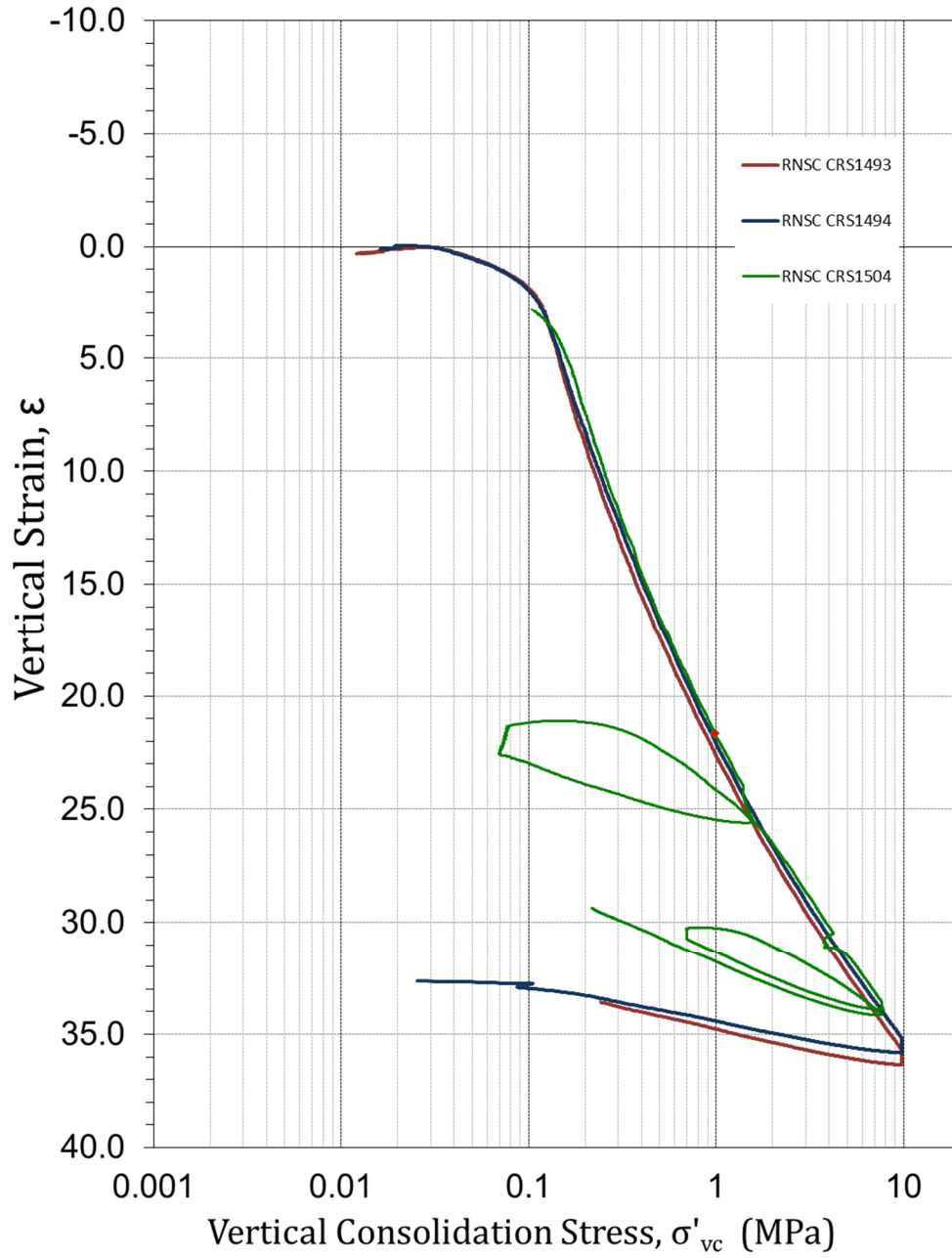


Figure 4- 24: CRS Test Results as plotting in Log Effective Stress by Axial Strain

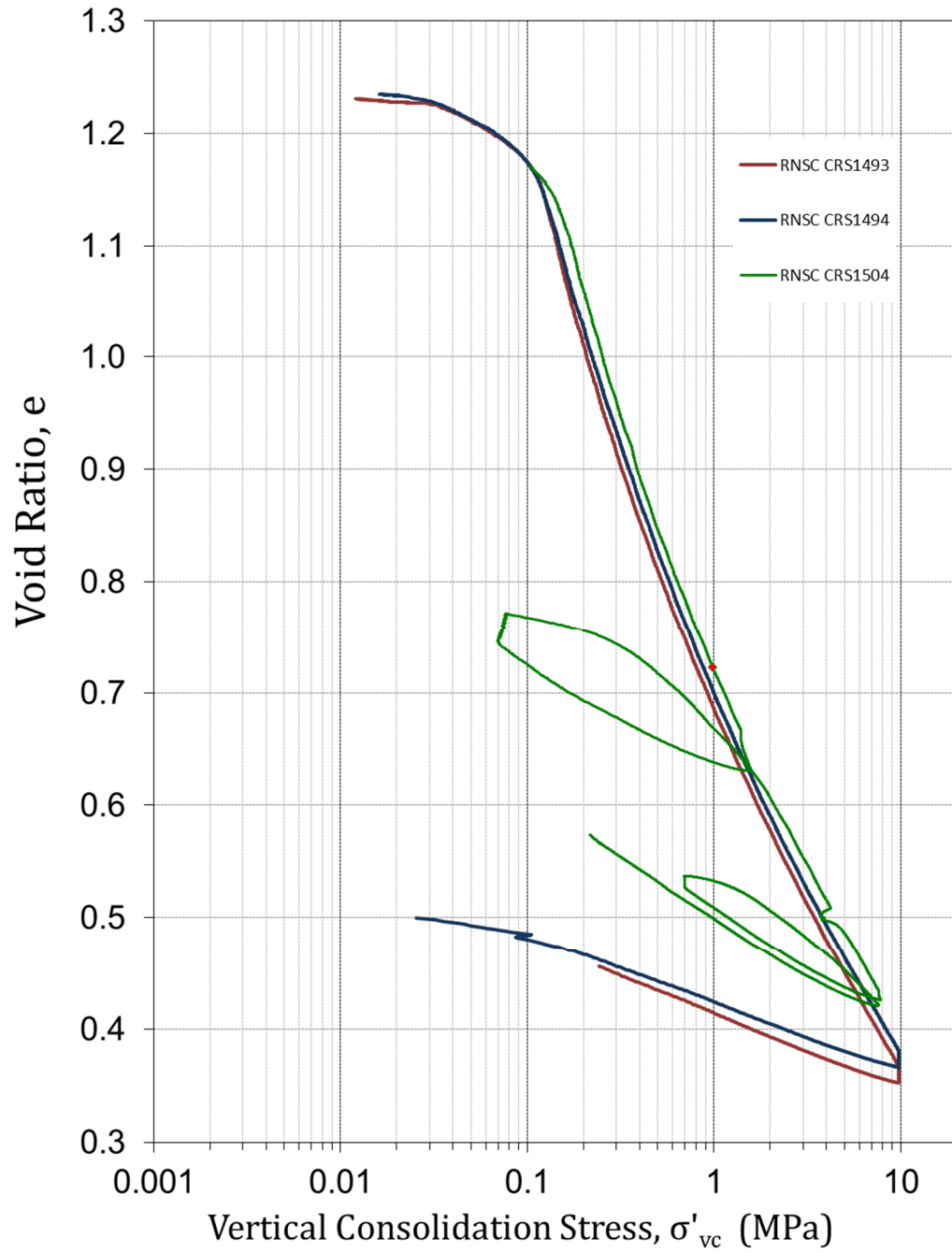


Figure 4- 25: CRS Test Results as plotting in Log Effective Stress by Void Ratio

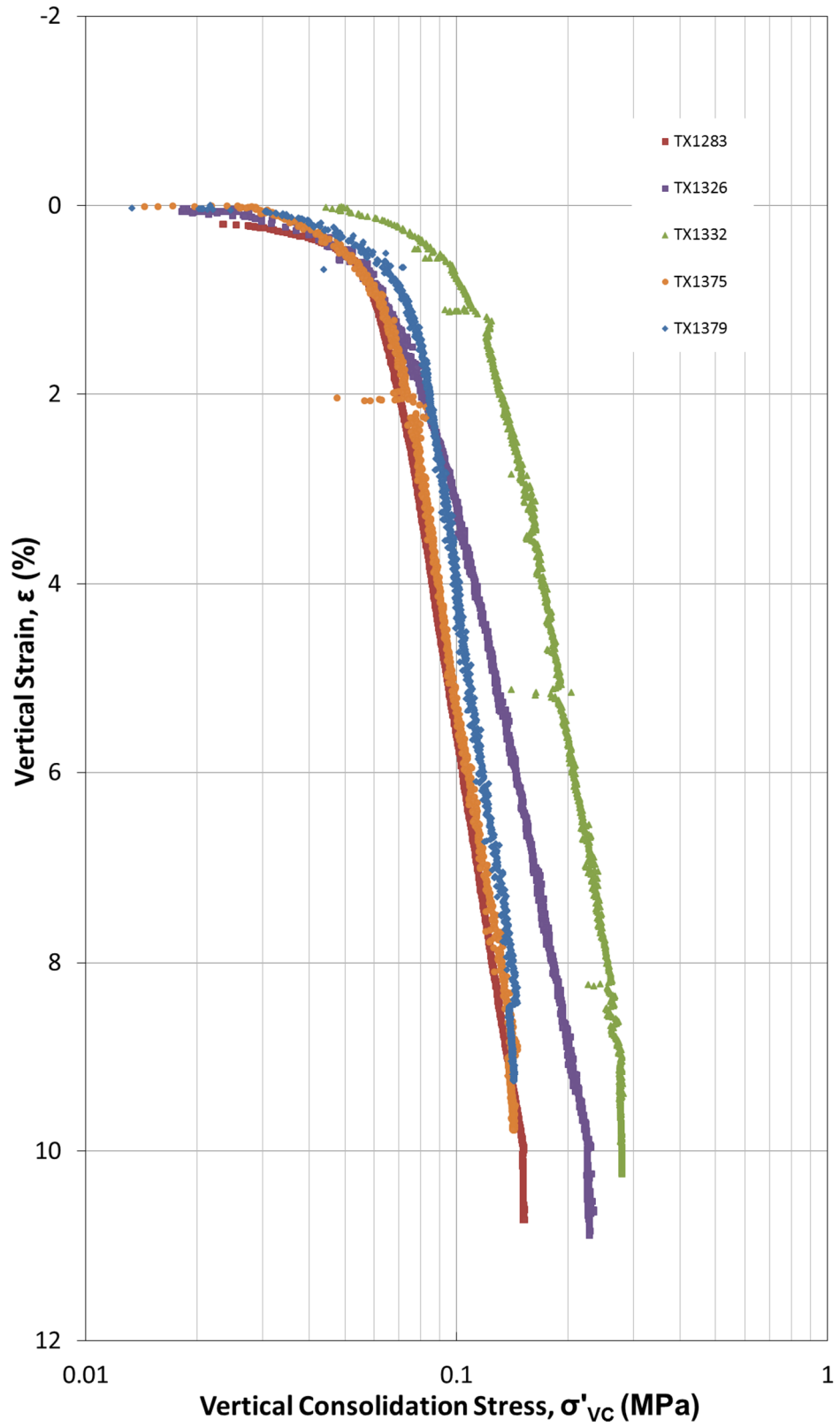


Figure 4- 26: ϵ - $\text{Log}\sigma$, Triaxial Consolidation Curves for Select RNSC Tests

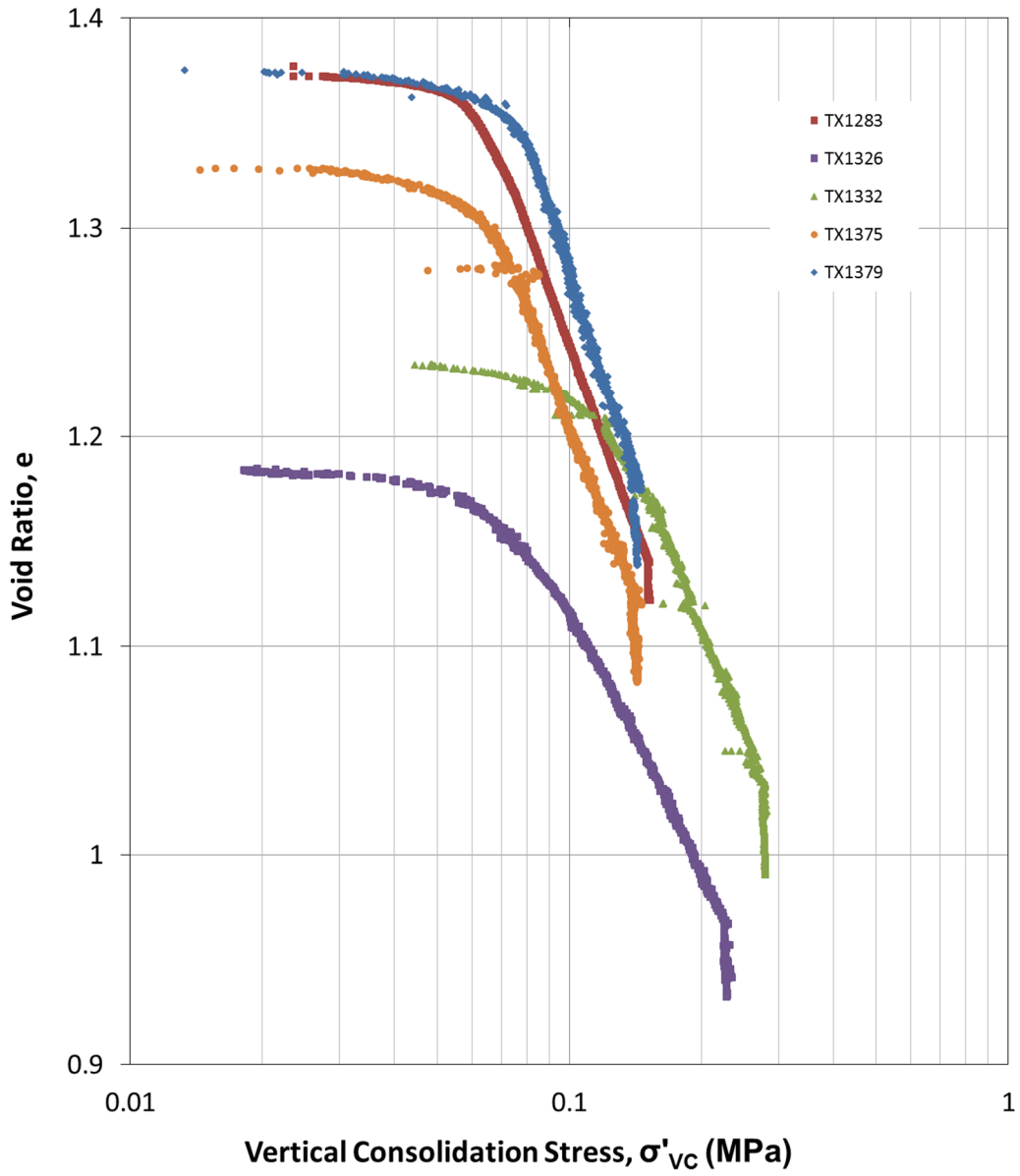


Figure 4- 27: e-Log σ , Triaxial Consolidation Curves for Select Tests

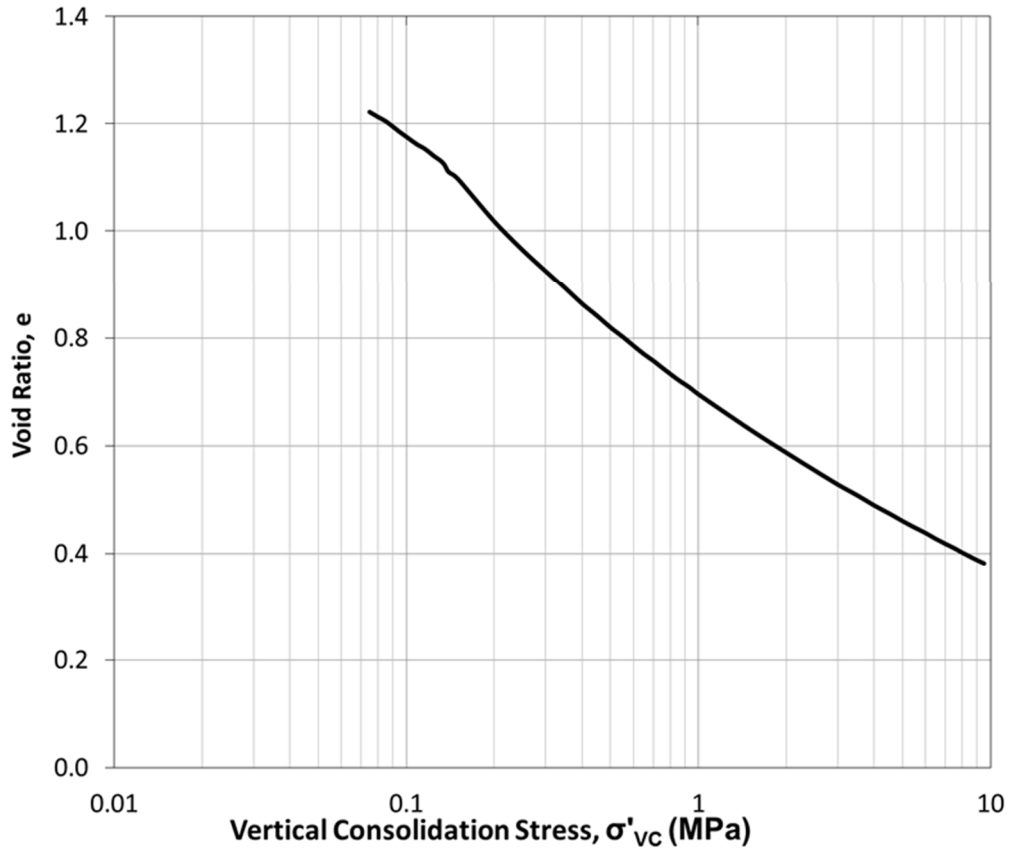


Figure 4- 28: e - $\text{Log}\sigma$, Average Compression Curve for RNSC

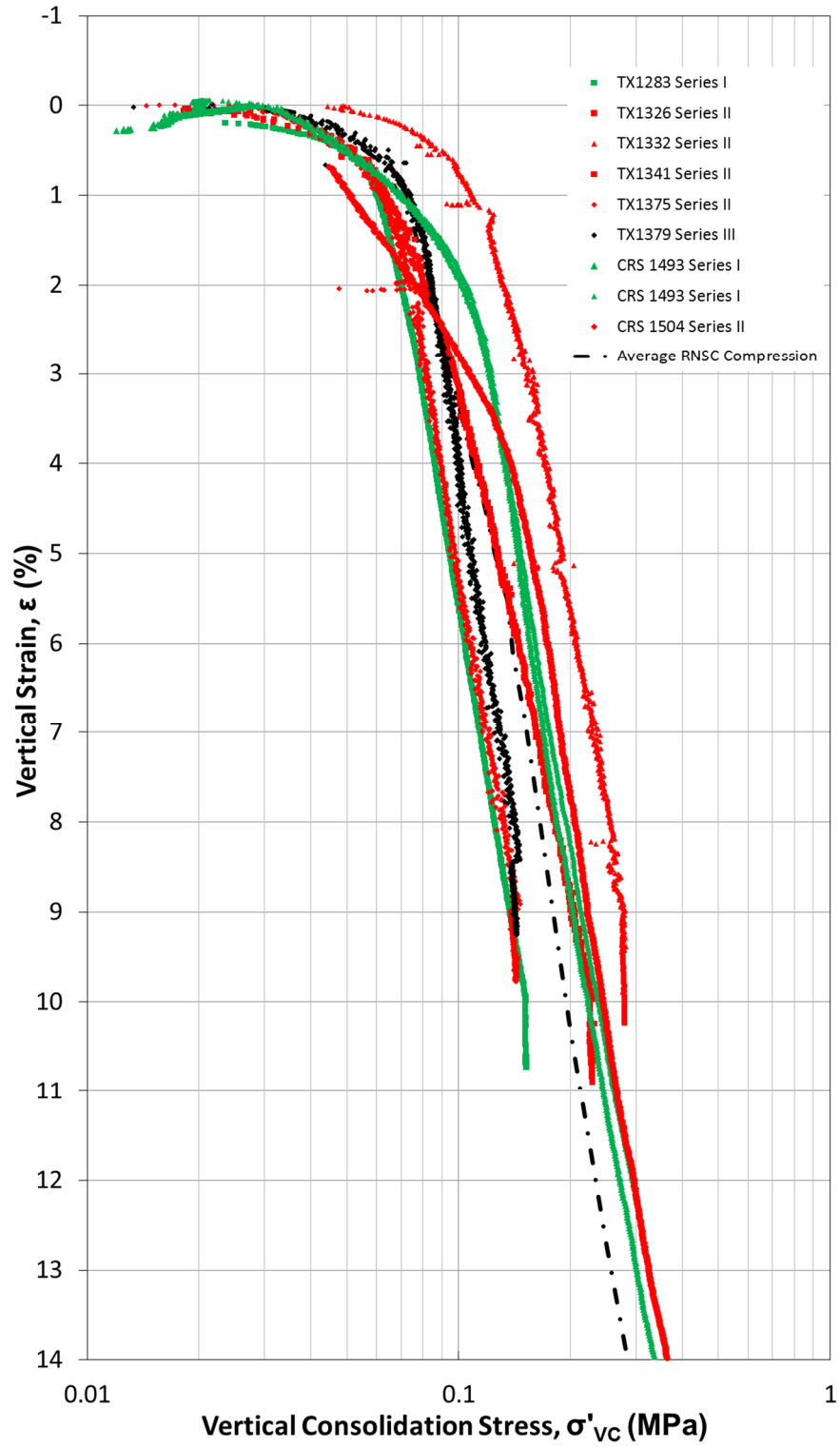


Figure 4- 29: ϵ -Log σ , Consolidation Curves by RNSC Series for triaxial and CRS Tests

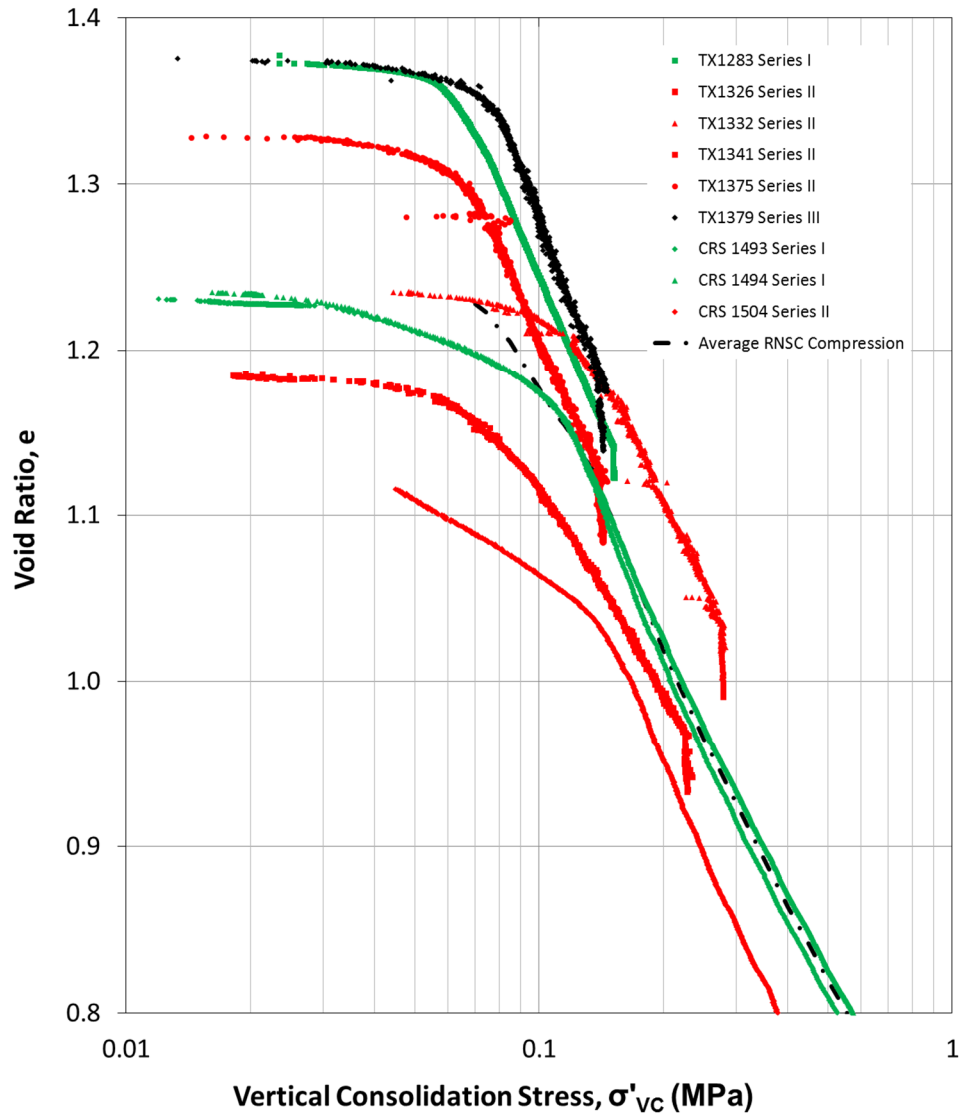


Figure 4- 30: e - $\text{Log}\sigma$, Consolidation Curves by RNSC Series for triaxial and CRS Tests

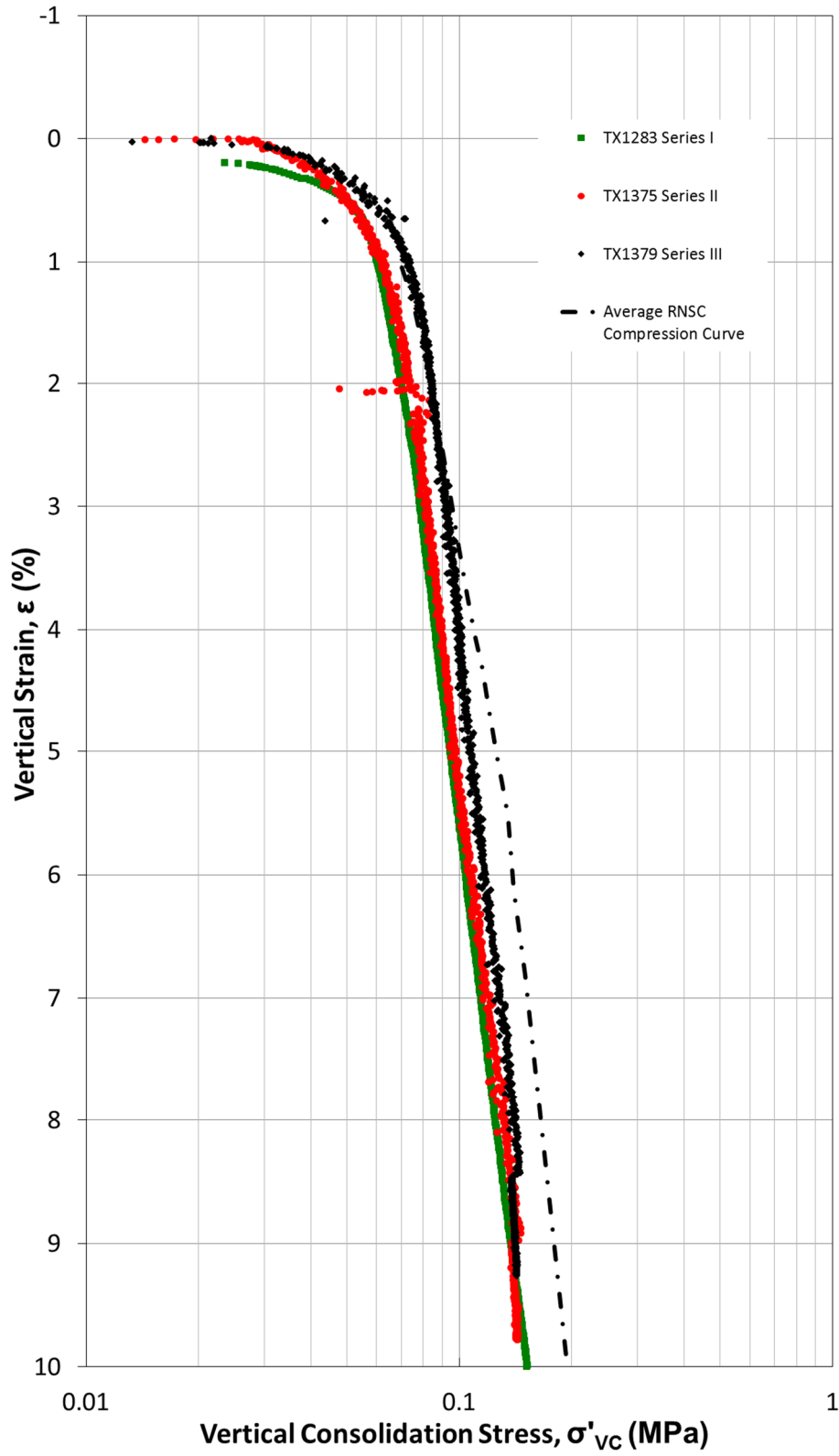


Figure 4- 31: ϵ - $\text{Log}\sigma$, Compression curves of the Three RNSC Series

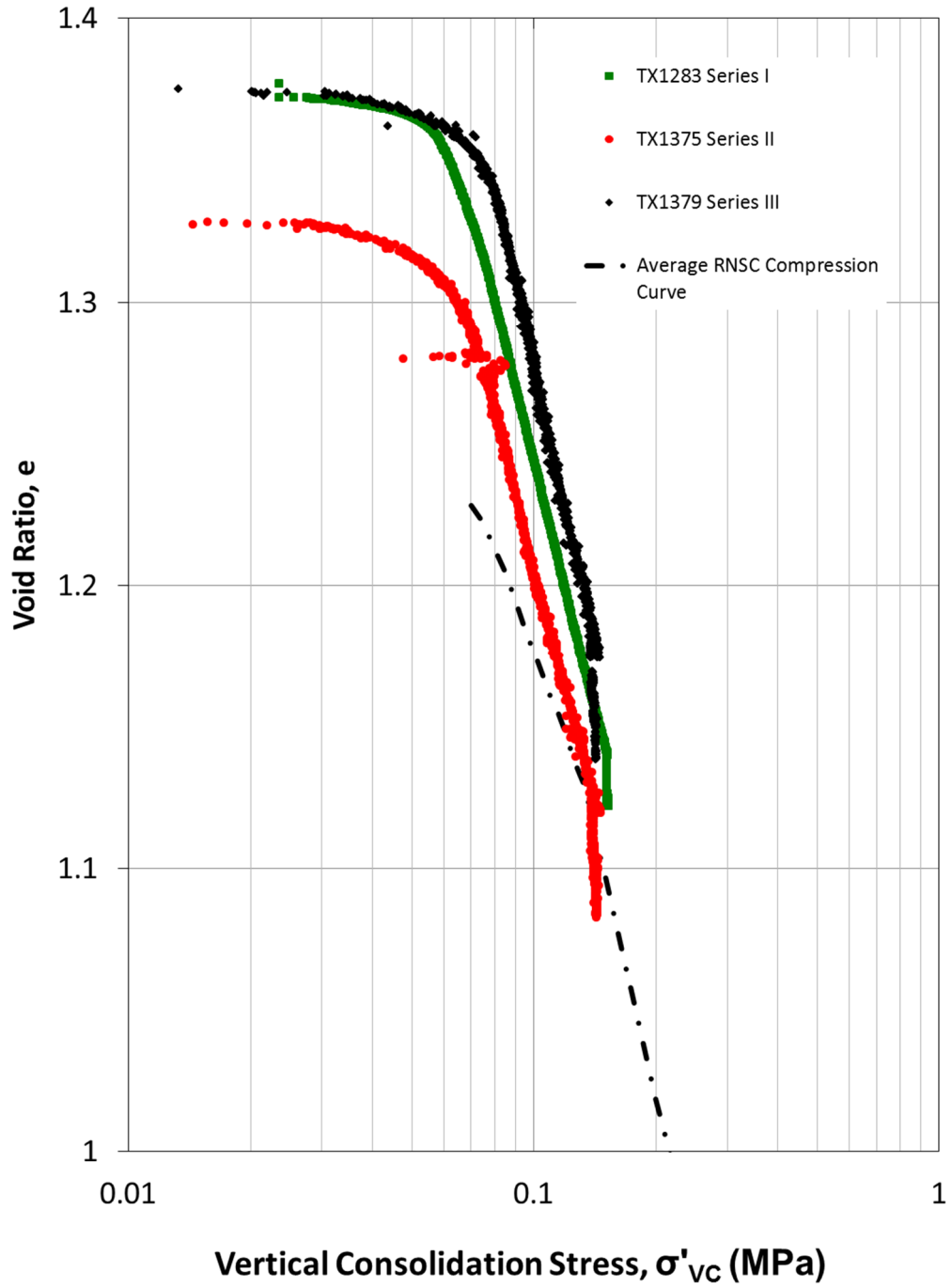


Figure 4- 32: e - $\text{Log}\sigma$, Compression Curves of the Three RNSC Series

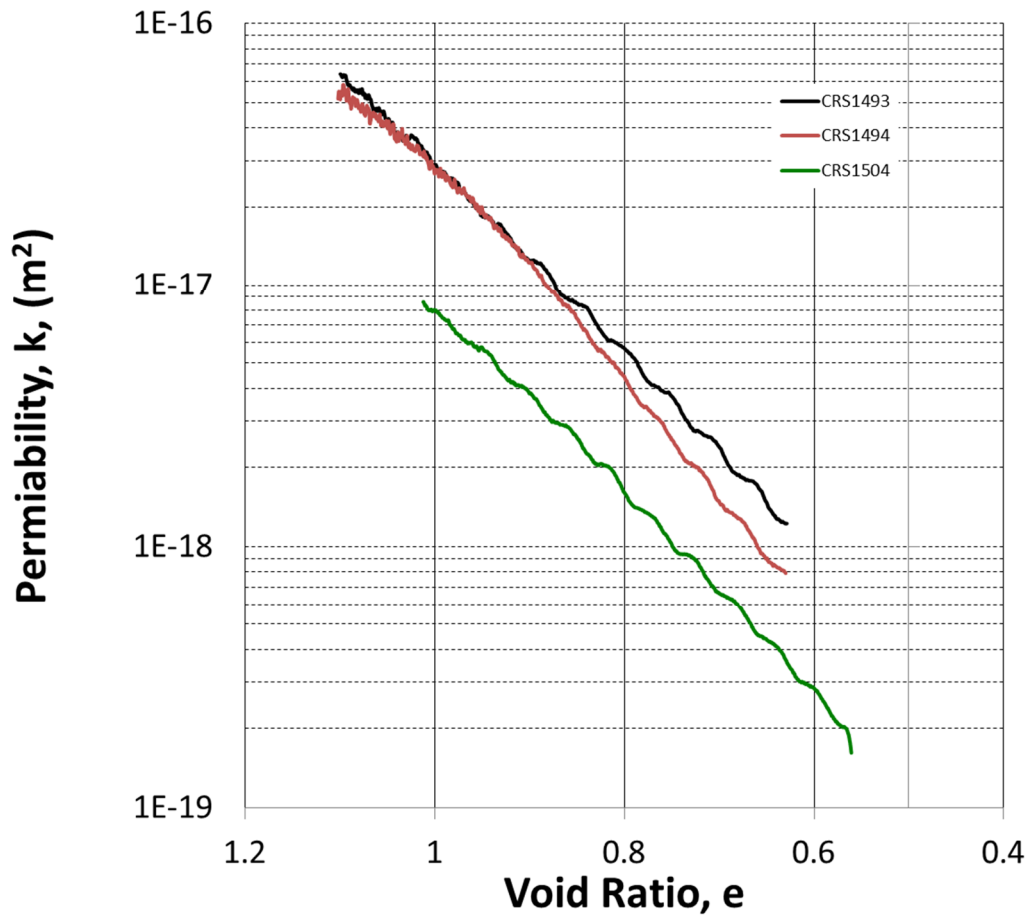


Figure 4- 33: Permeability by Void Ratio Calculated from RNSC CRS Tests

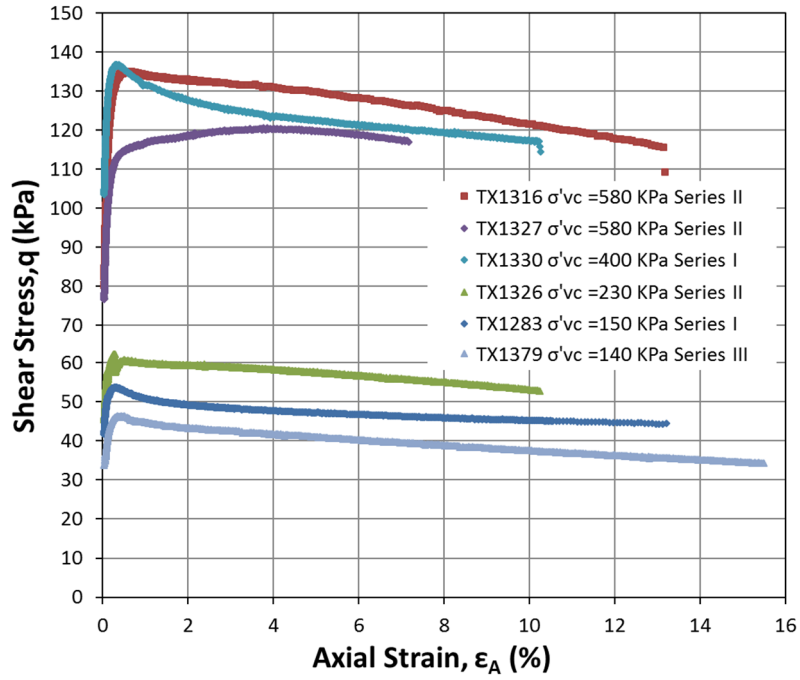


Figure 4- 34: Stress-Strain Curves from CK₀UC Triaxial Tests

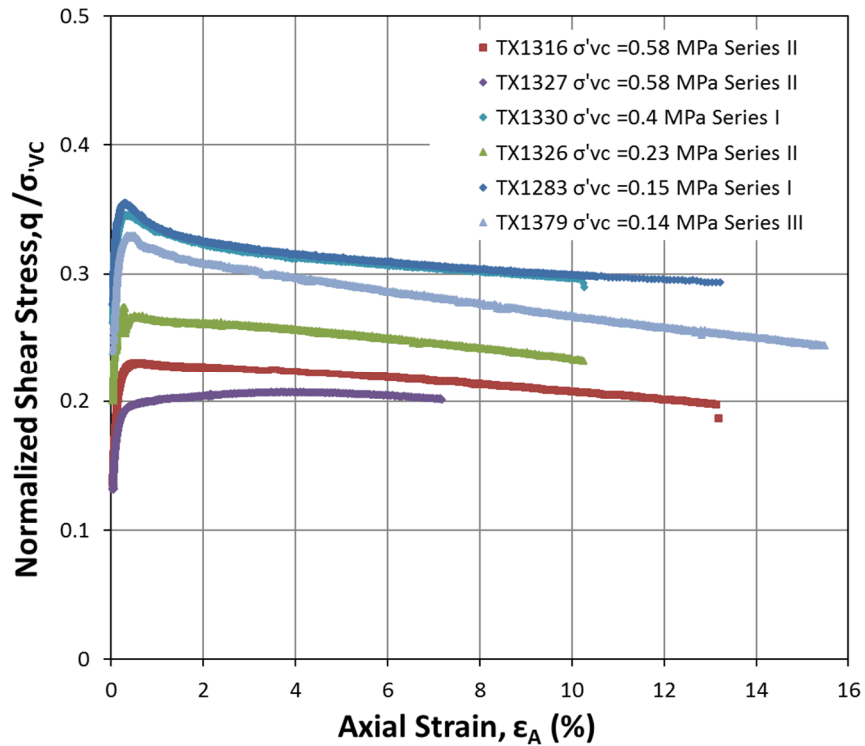


Figure 4- 35: Normalized Stress-Strain Curves from CK₀UC Triaxial Tests

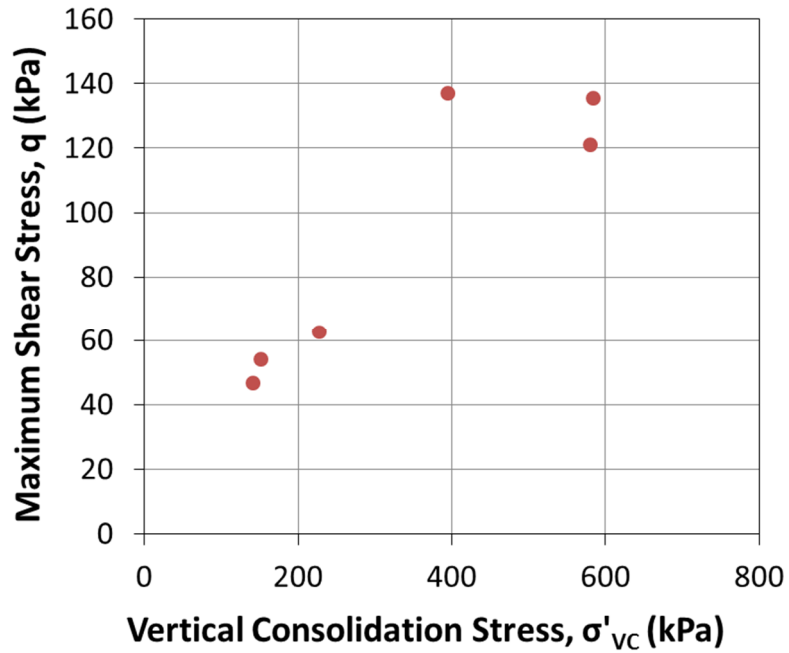


Figure 4- 36: Maximum Shear Stress by Consolidation Stress from NC CK₀UC Triaxial Tests

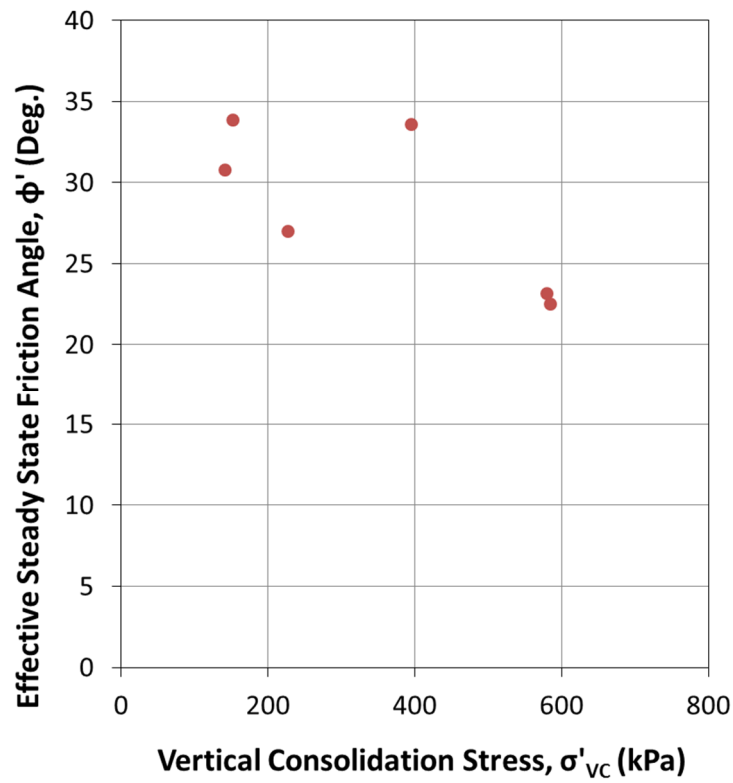


Figure 4- 37: Effective Steady State Friction Angle by Consolidation Stress from NC CK₀UC Triaxial Tests

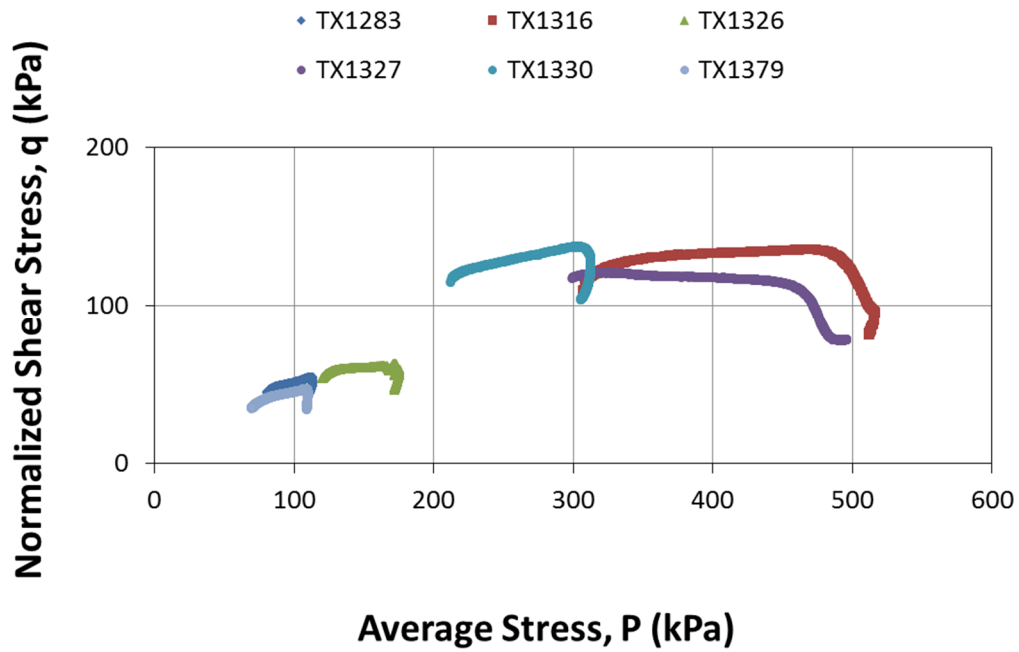


Figure 4- 38: Shearing Stress Paths from CK₀UC Triaxial Tests in MIT p-q Space

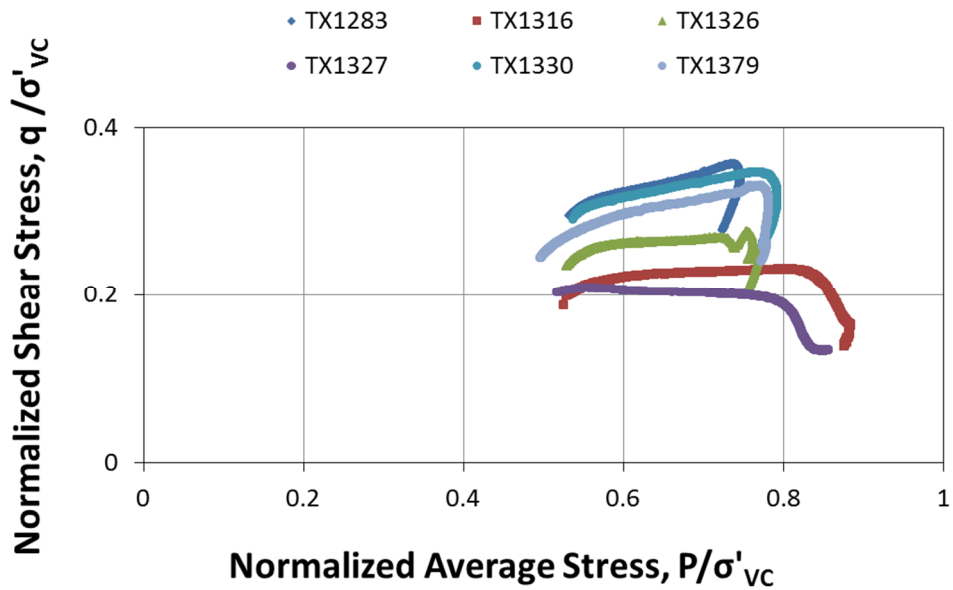


Figure 4- 39: Normalized Shearing Stress Paths from CK₀UC Triaxial Tests in MIT p-q Space

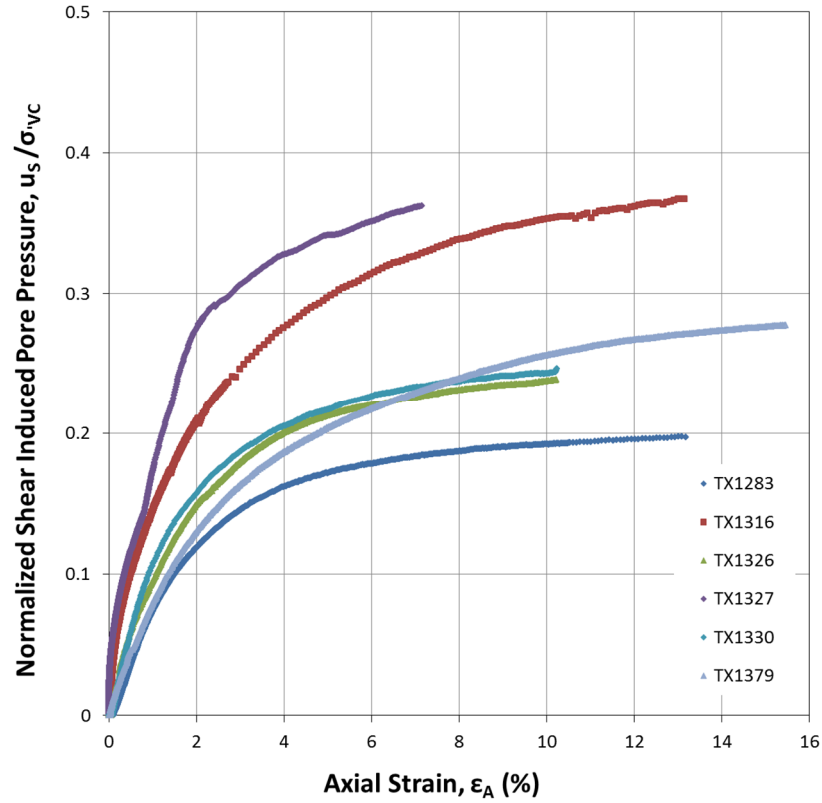


Figure 4- 40: Sheared Induced Pore Pressure by Axial Strain in CK_0UC Triaxial Tests

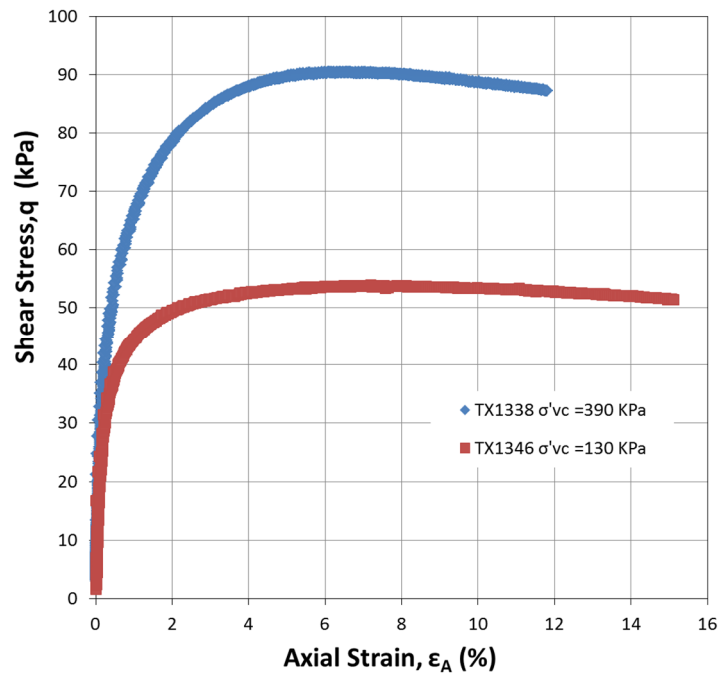


Figure 4- 41: Stress Strain Curves from CIUC Triaxial Tests

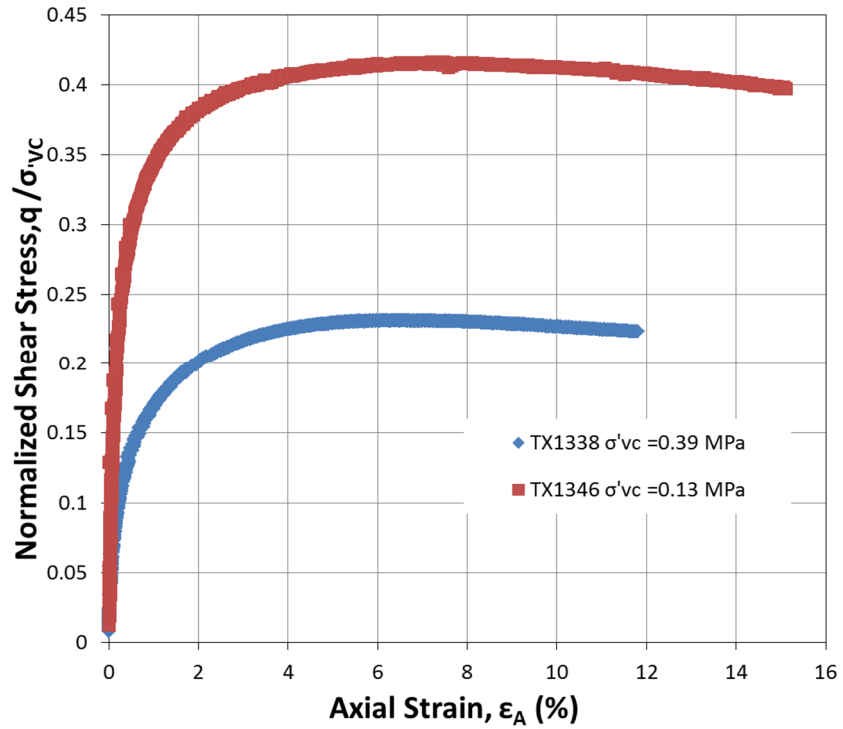


Figure 4- 42: Normalized Stress Strain Curves from CIUC Triaxial Tests

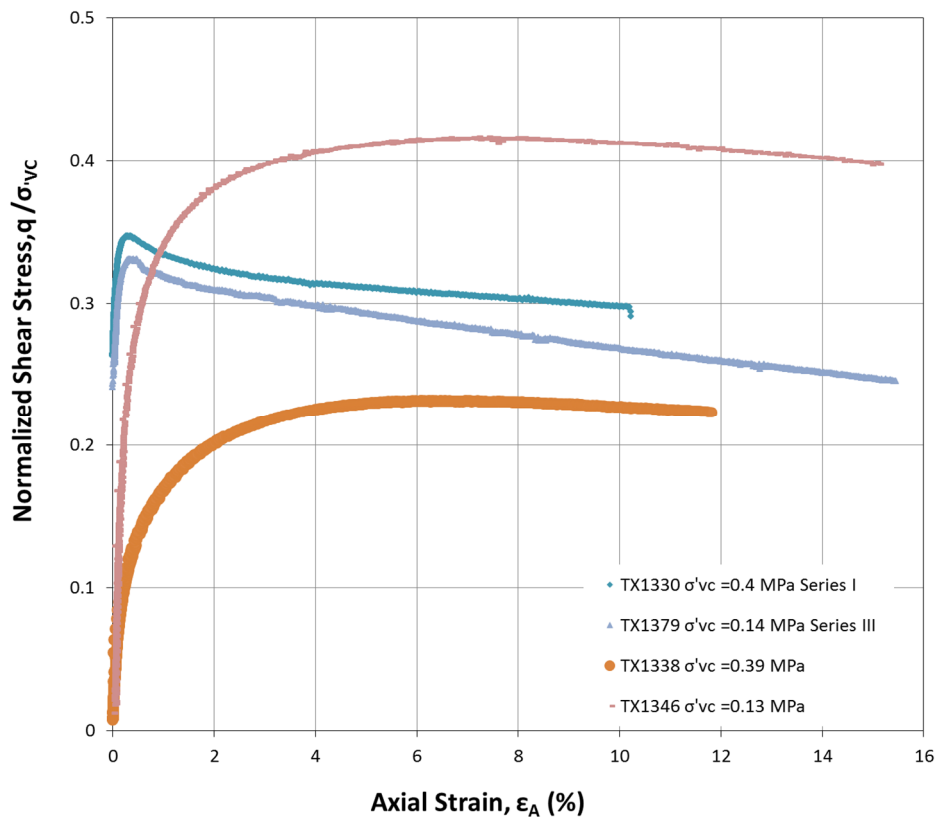


Figure 4- 43: Normalized Stress Strain Curves from CIUC and CK₀UC Triaxial Tests

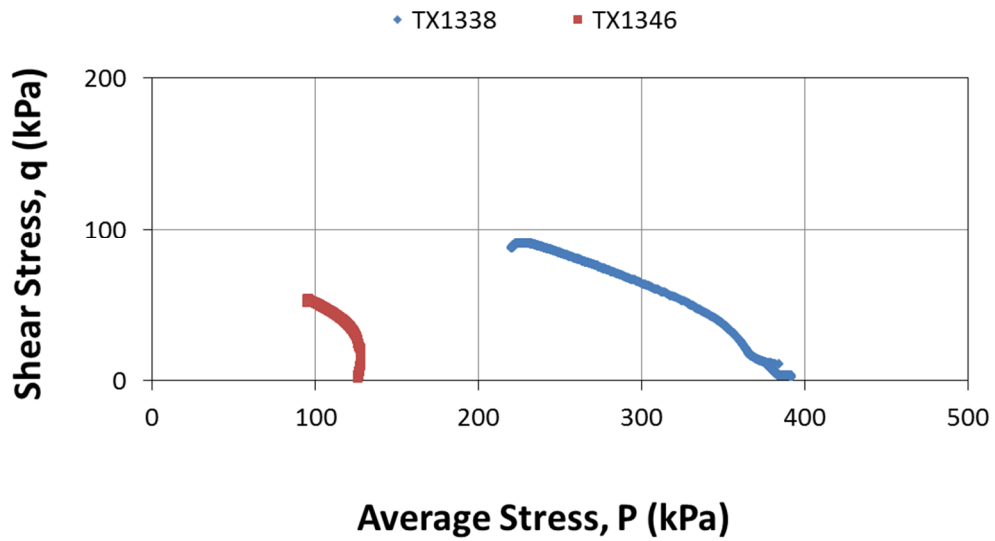


Figure 4- 44: CIUC Triaxial Test Shear Stress Paths in MIT p-q Space

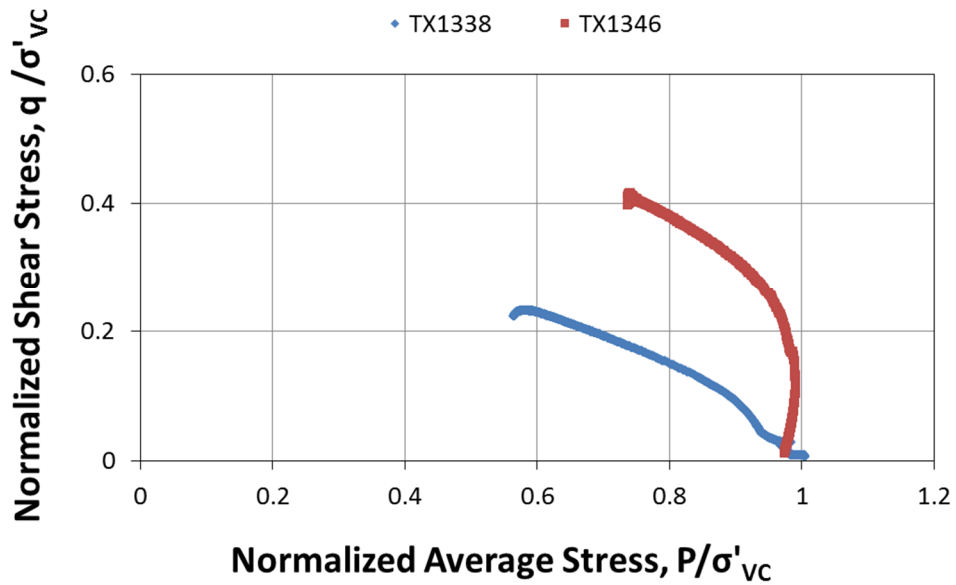


Figure 4- 45: Normalized Shear Stress Paths from CIUC Triaxial Tests

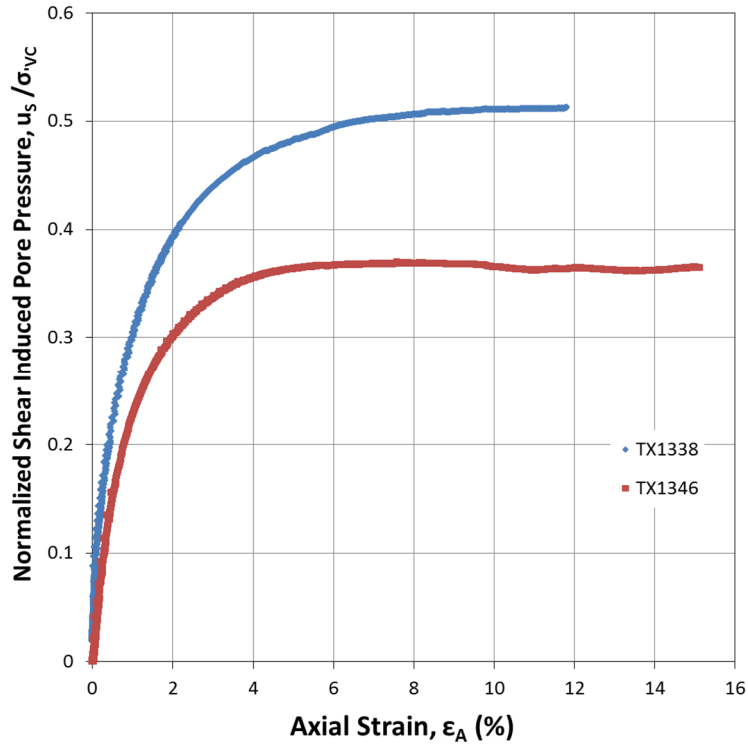


Figure 4- 46: Sheared Induced Pore Pressure by Axial Strain in CIUC Triaxial Tests

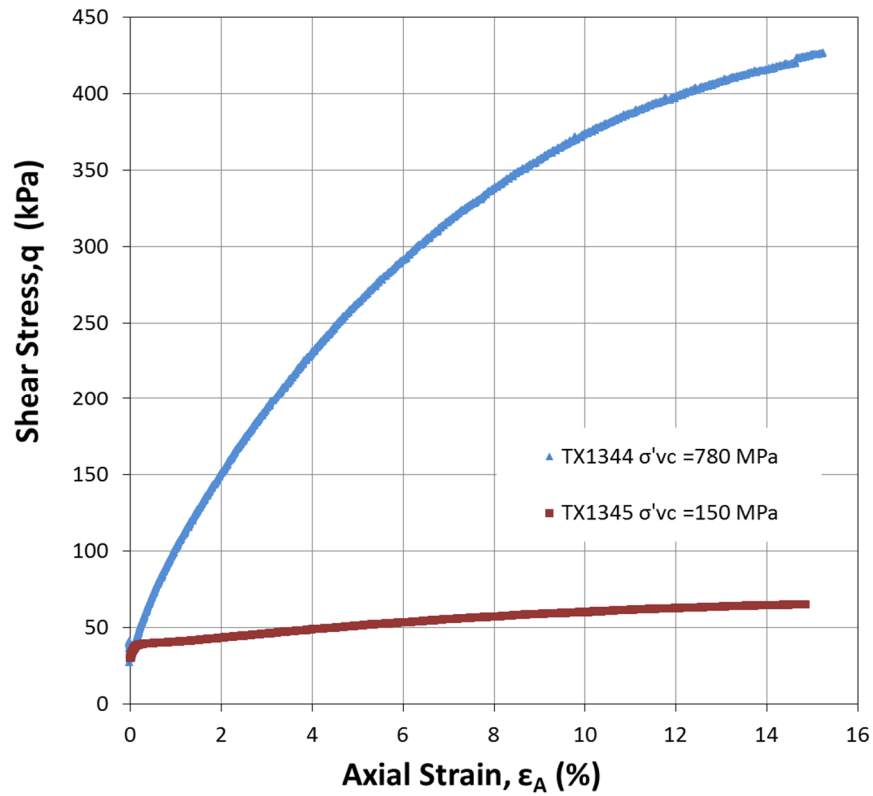


Figure 4- 47: Shear Stress by Axial Strain from Drained Triaxial Tests

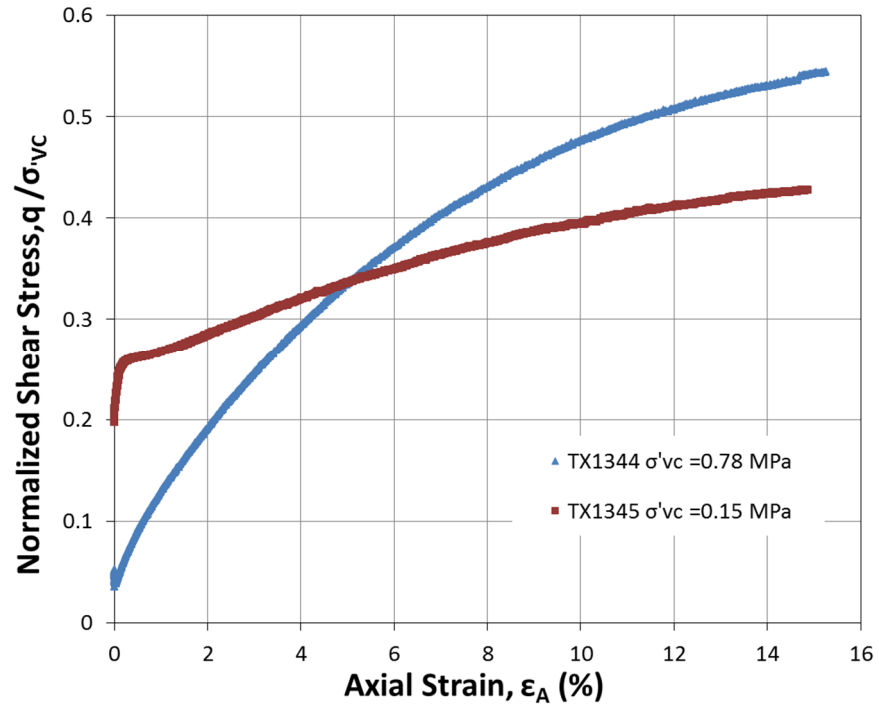


Figure 4- 48: Normalized Shear Stress by Axial Strain from Drained Triaxial Tests

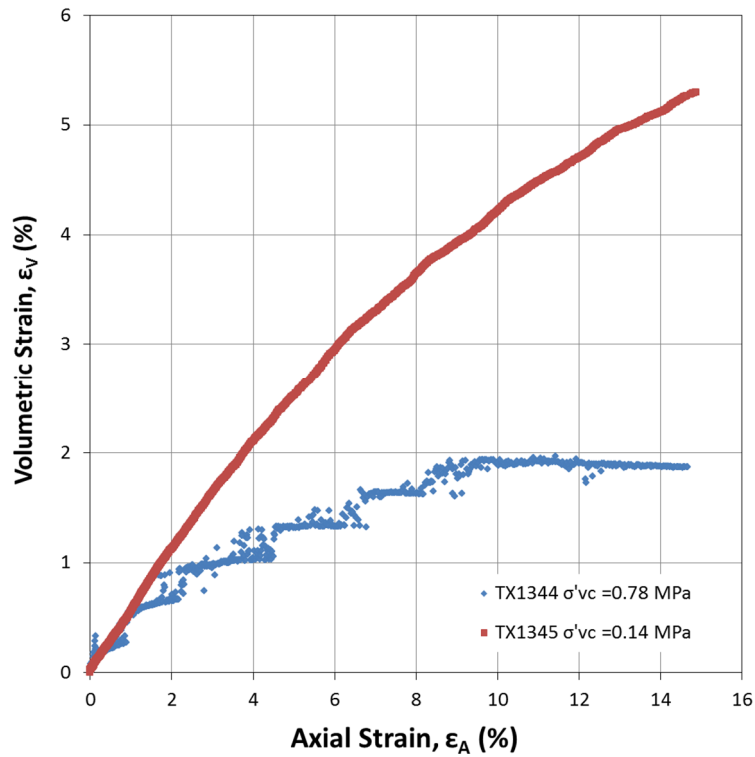


Figure 4- 49: Volumetric Strain by Axial Strain from Drained Triaxial Tests

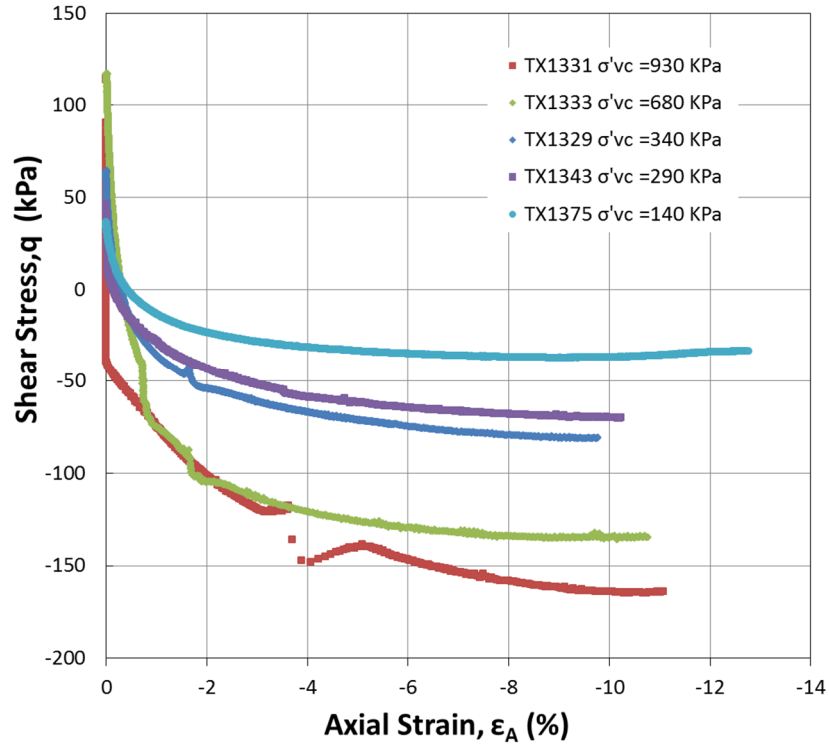


Figure 4- 50: Shear Stress by Axial Strain from Shear Phase of CK₀UE Triaxial Tests

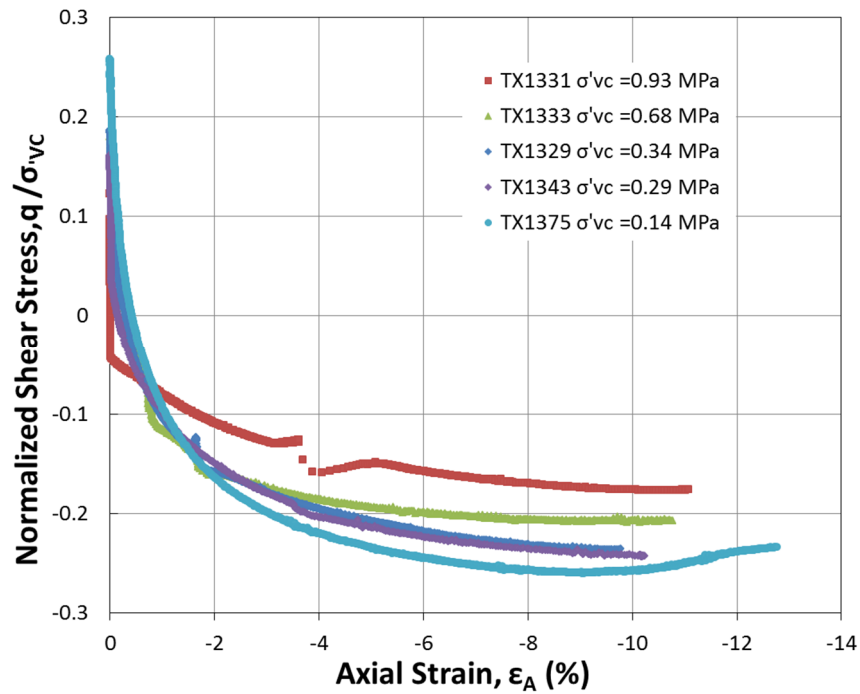


Figure 4- 51: Normalized Shear Stress by Axial Strain from Shear Phase of CK₀UE Triaxial Tests

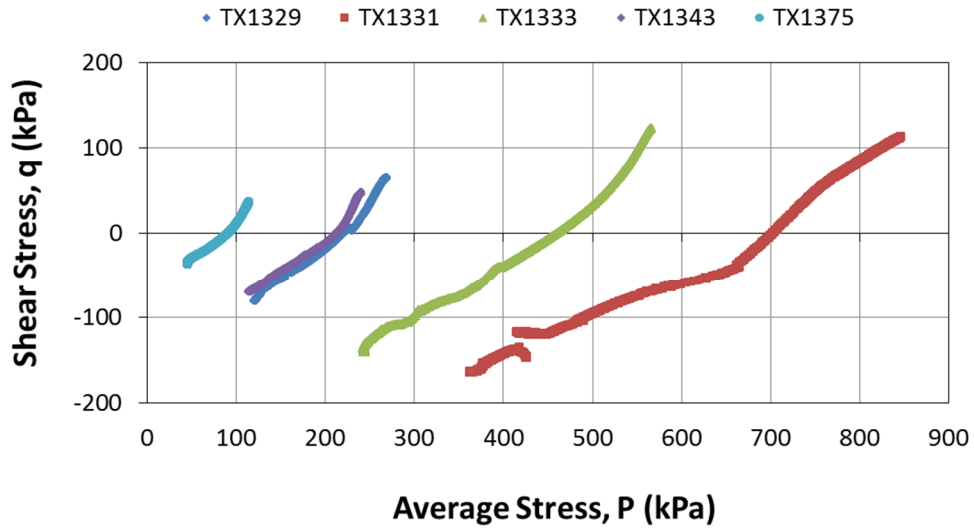


Figure 4- 52:CK₀UE Triaxial Test Shear Stress Paths in MIT p-q Space

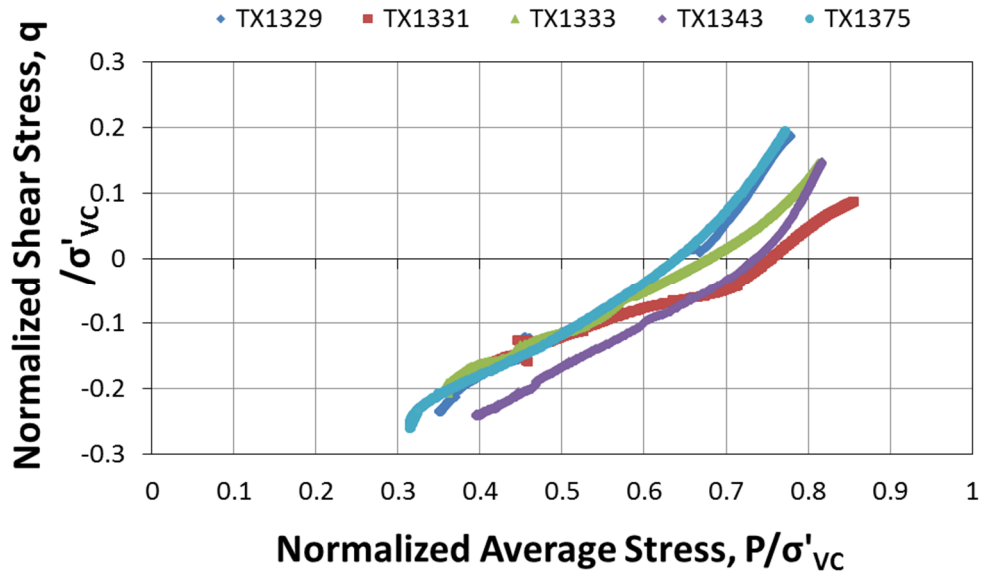


Figure 4- 53: Normalized Shear Stress Paths from CK₀UE Triaxial Tests

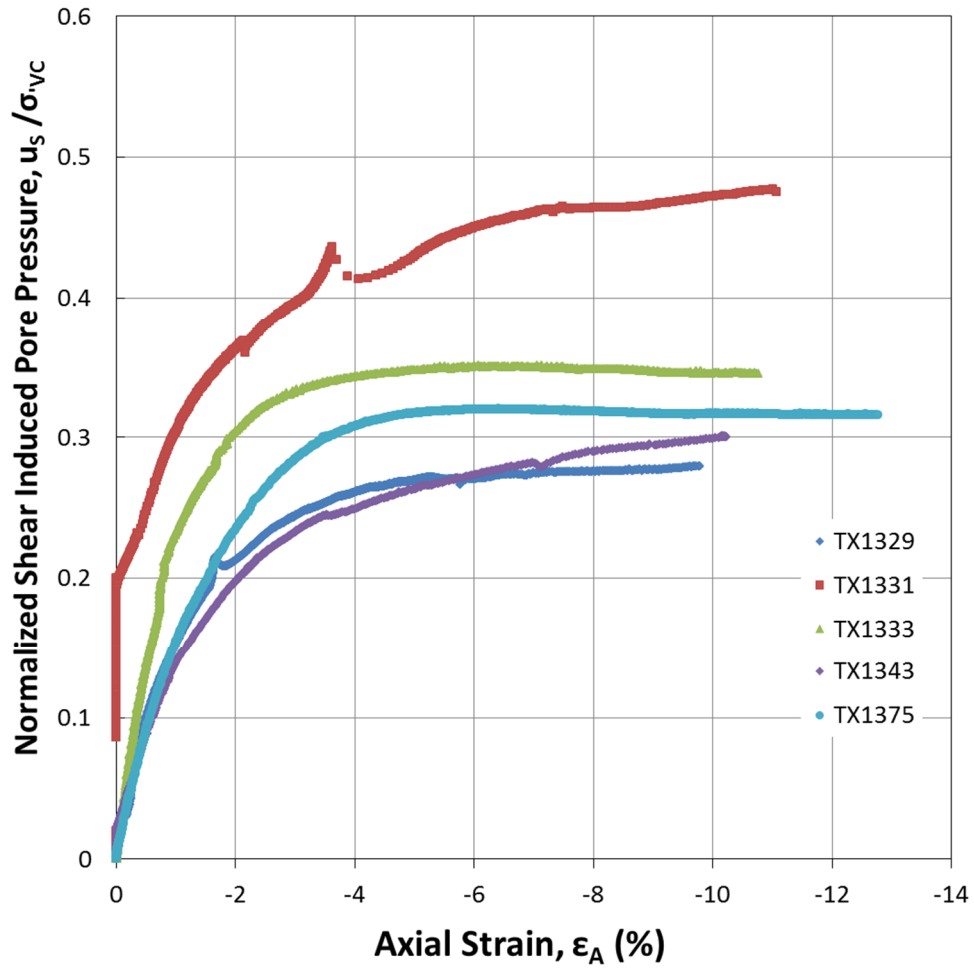


Figure 4- 54: Normalized Shear Induced Pore Pressure by Axial Strain from CK_0UE Triaxial Tests

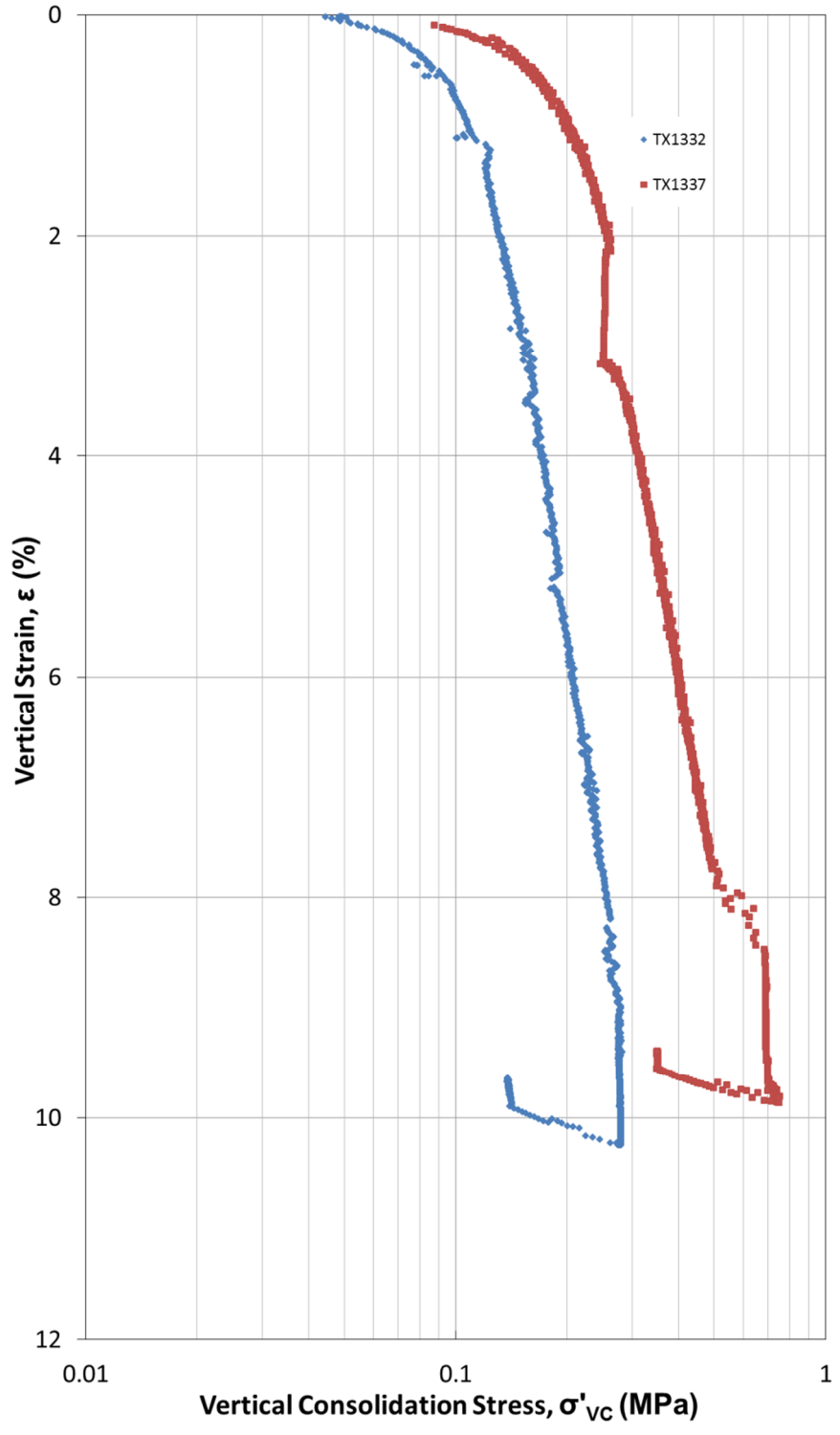


Figure 4- 55: ϵ - $\text{Log}\sigma$ Consolidation Curves for High OCR CK_0UC Triaxial Tests

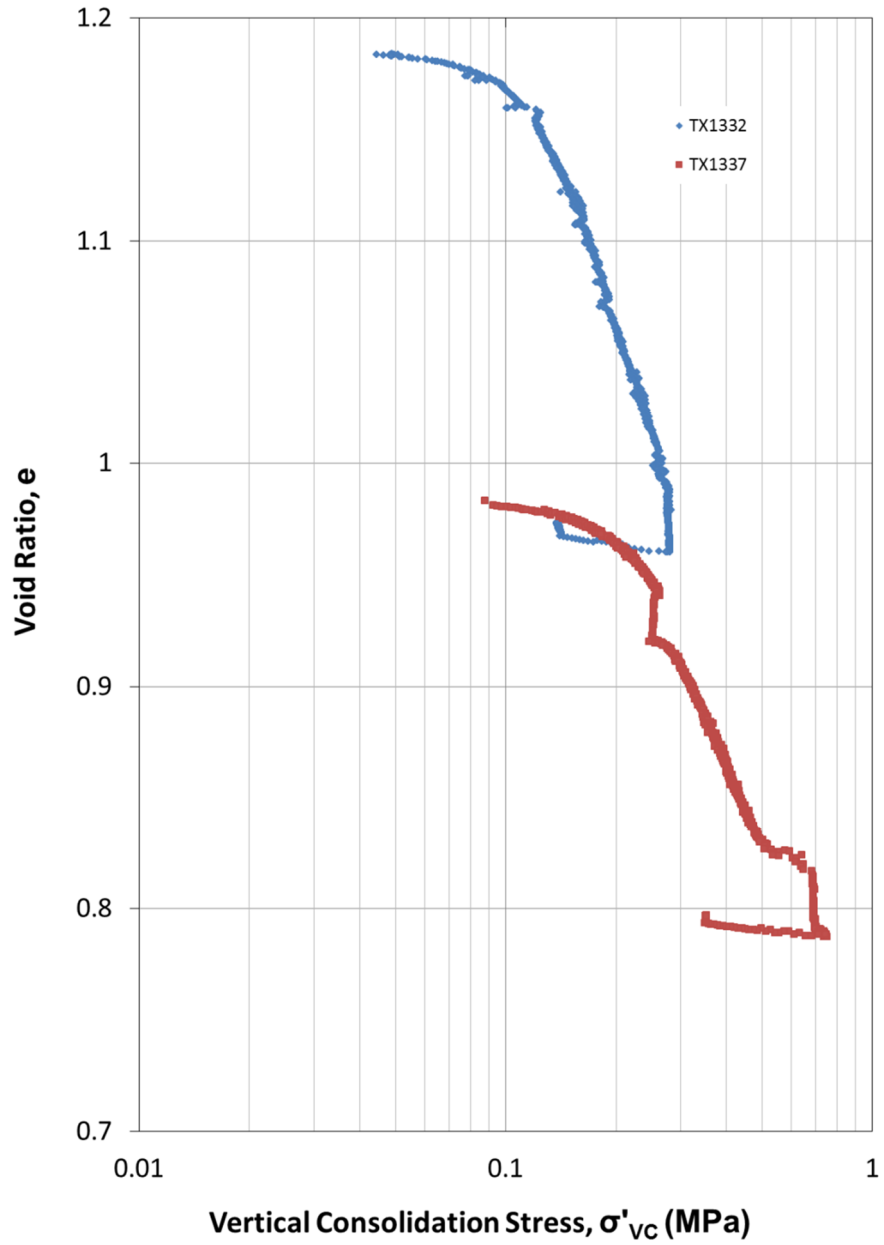


Figure 4- 56: e- Log σ Consolidation Curves for High OCR CKOUC Triaxial Tests

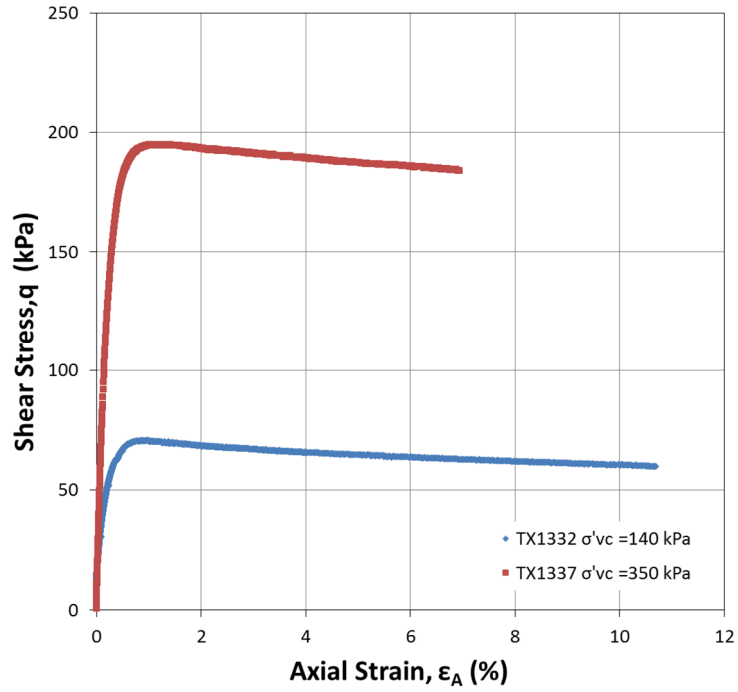


Figure 4- 57: Stress Strain Curves from High OCR CK₀UC Triaxial Tests

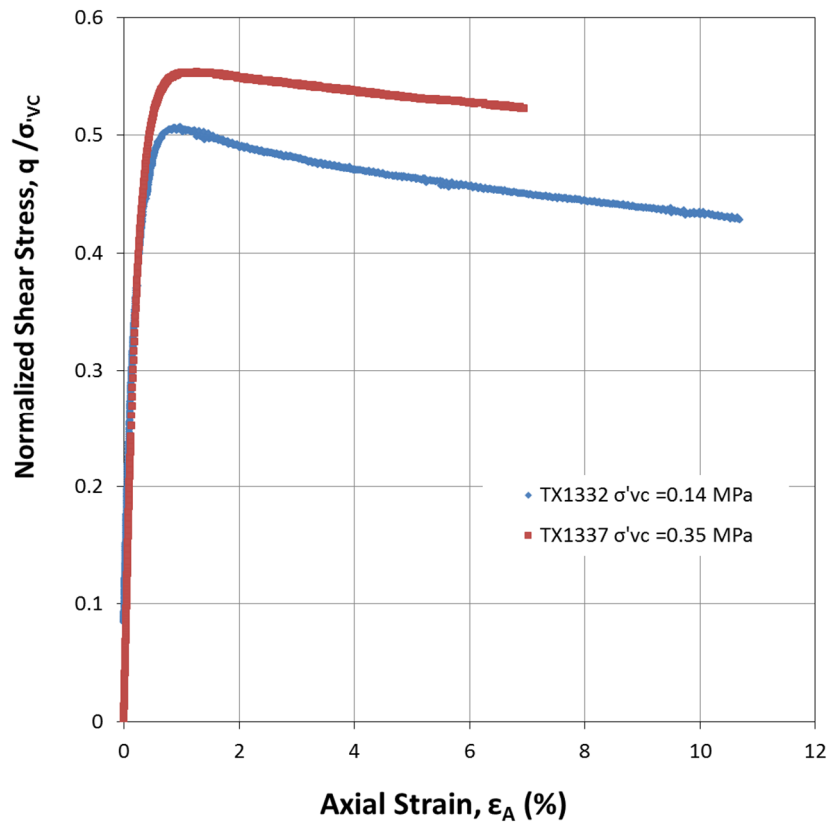


Figure 4- 58: Normalized Stress Strain Curves from High OCR CK₀UC Triaxial Tests

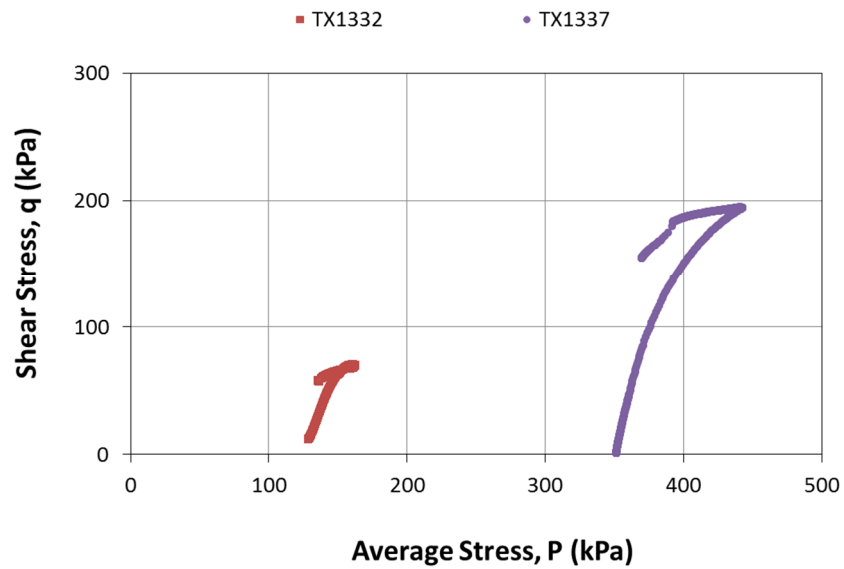


Figure 4- 59: Shear Stress Paths from *High OCR Triaxial Tests in MIT p-q Space*

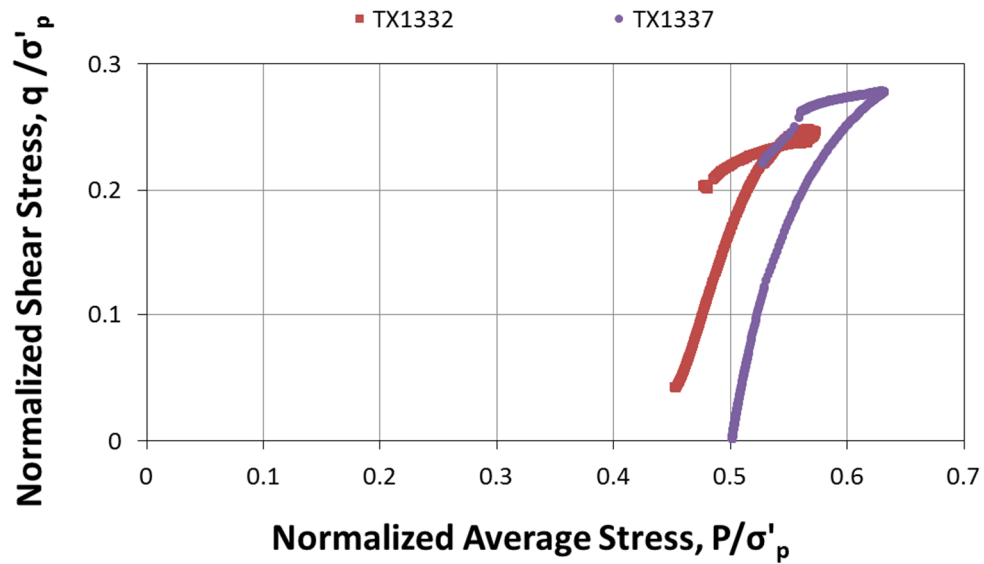


Figure 4- 60: Normalized Shear Stress Paths from High OCR Triaxial Tests in MIT p-q Space

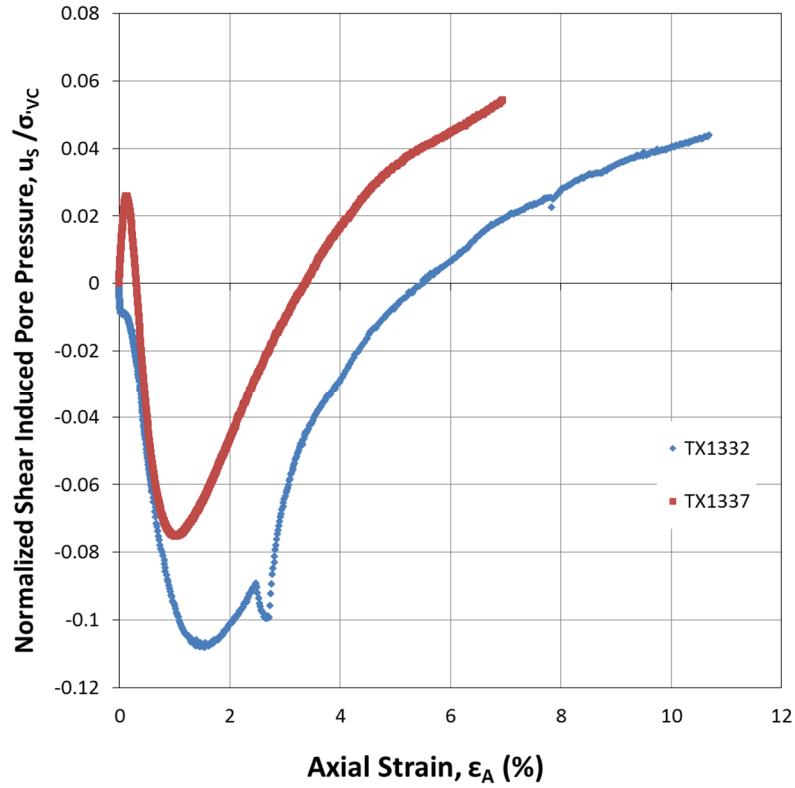


Figure 4- 61: Normalized Shear Induced Pore Pressure by Axial Strain from High OCR Triaxial Tests

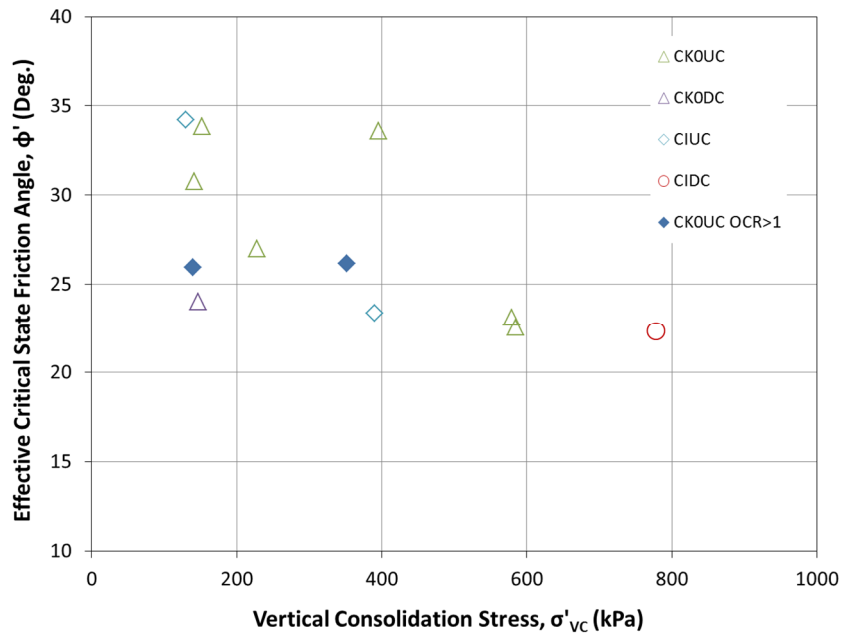


Figure 4- 62: Variation in Critical Friction Angle by Vertical Consolidation test for RNSC Triaxial Tests

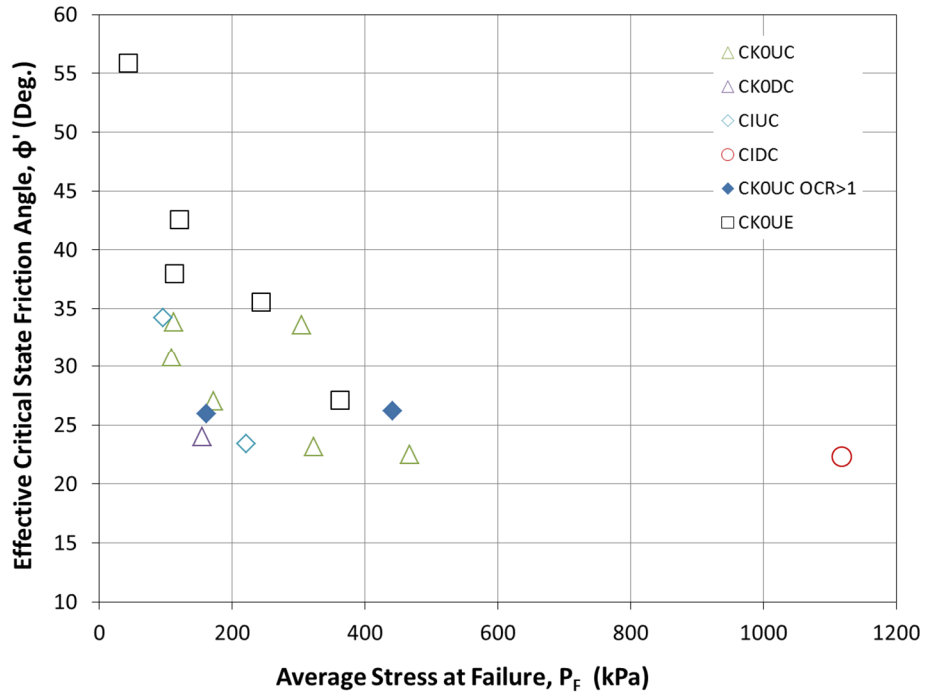


Figure 4- 63: Variation in Critical Friction Angle by Average Stress at Failure for RNSC Triaxial Extension Tests

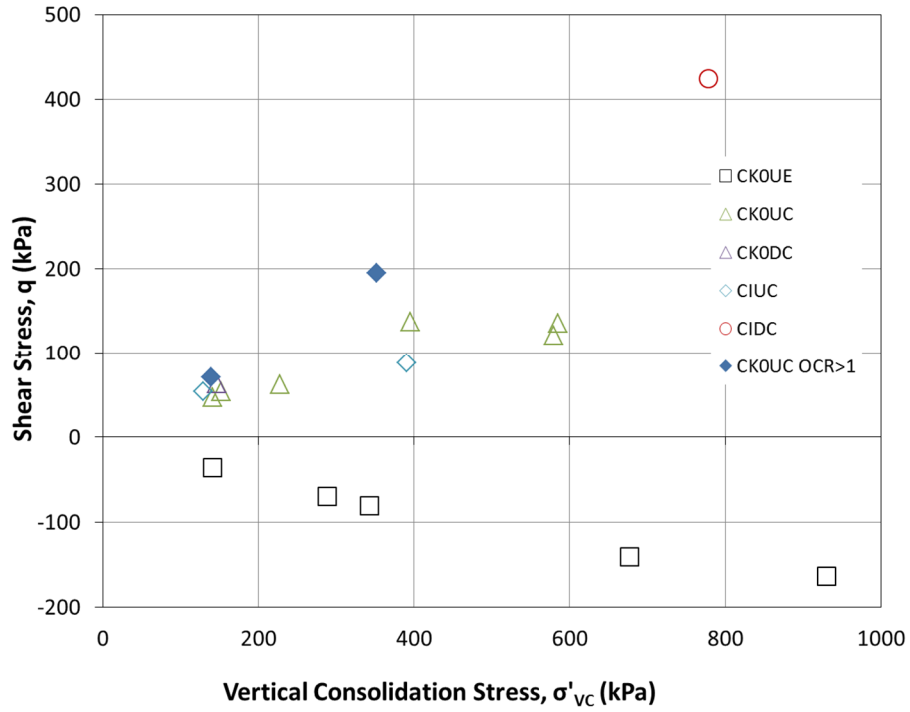


Figure 4- 64: Maximum Shear Stress by Maximum Consolidation Stress for Compression Triaxial Tests

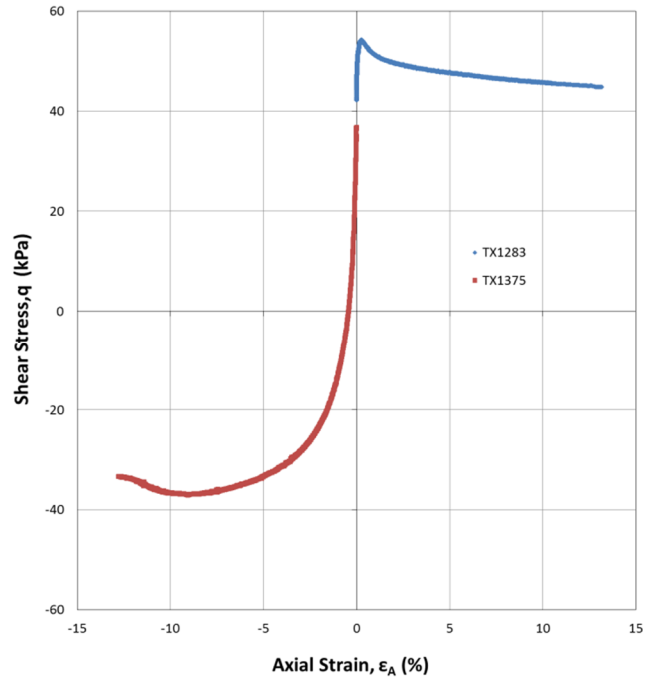


Figure 4- 65: Compression and Tension Stress Strain Curves at 150 KPa (TX1283 & TX1375)

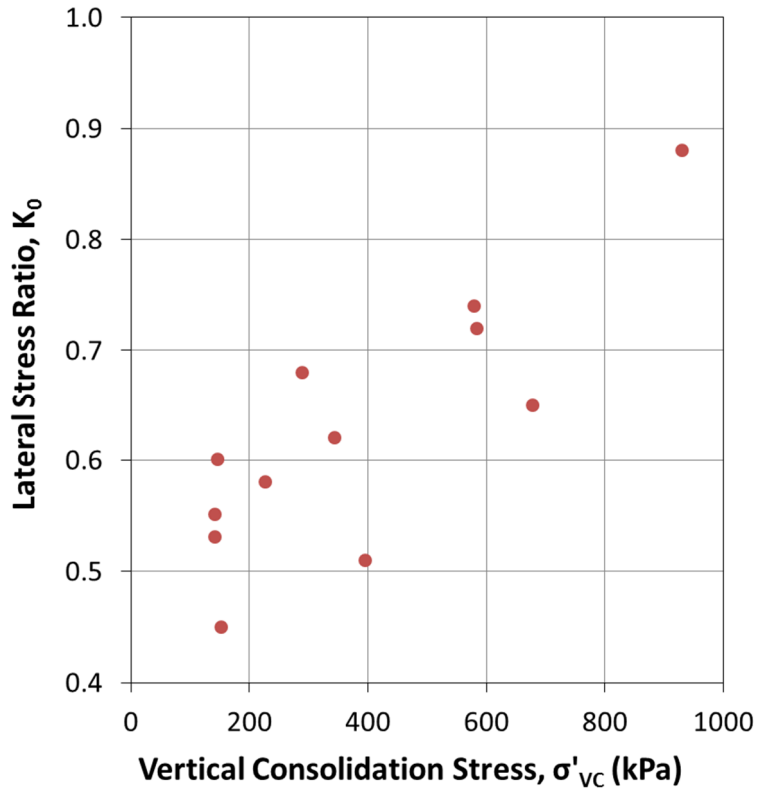


Figure 4- 66: K_0 by Maximum Vertical Consolidation Stress for K_0 Consolidated Triaxial Tests

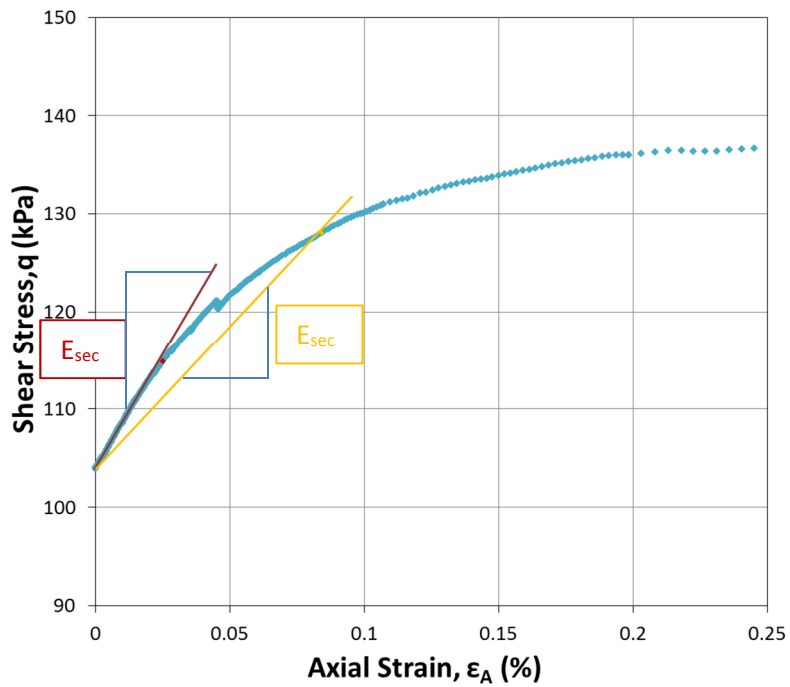


Figure 4- 67: Example Calculation of E_{sec} for Undrained Triaxial Tests

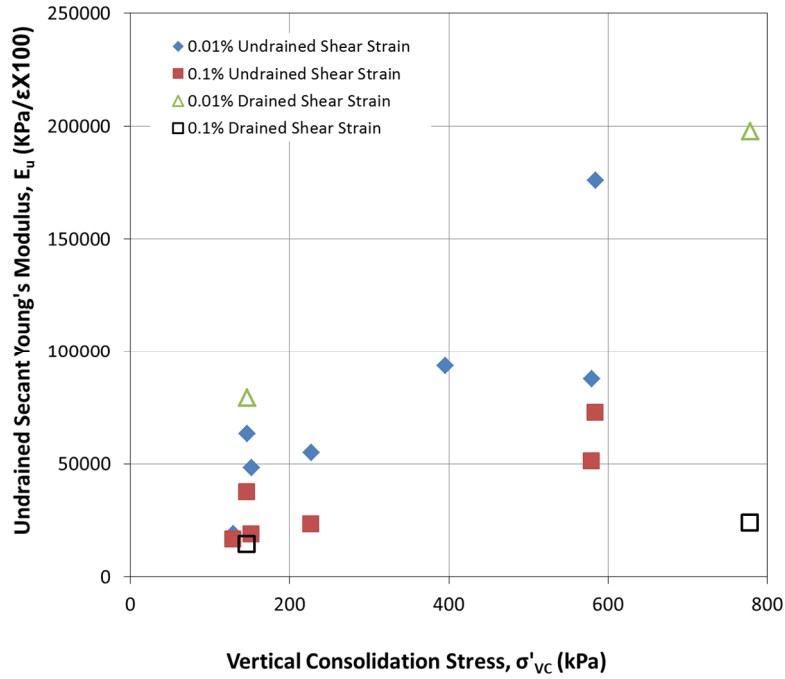


Figure 4- 68: Elastic Modulus by Maximum Consolidation Pressure at 0.01% and 0.1% Strain During Shearing of Normally Consolidated Triaxial Compression Tests

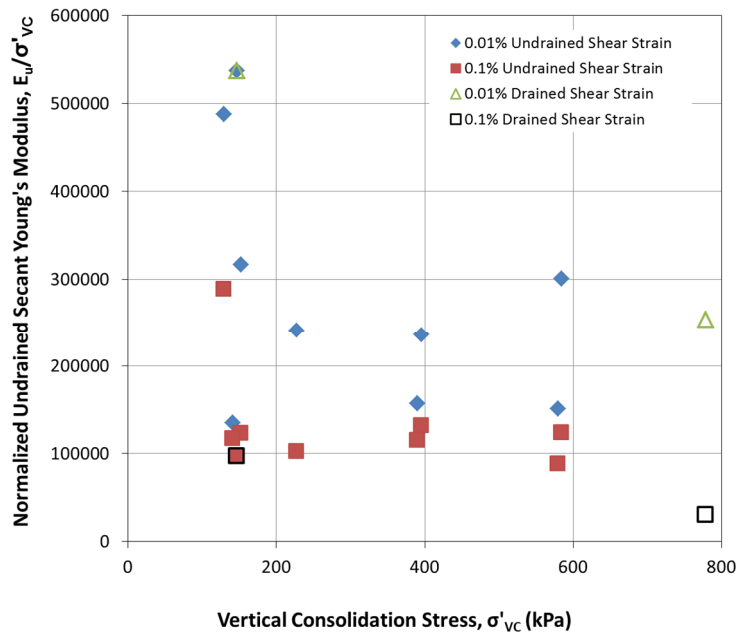


Figure 4- 69 Normalized Elastic Modulus by Maximum Consolidation Pressure at 0.01% and 0.1% Strain During Shearing of Normally Consolidated Triaxial Compression Tests

Chapter 5

RNSC Comparison to Established Clay Behaviors

5.1 INTRODUCTION

Geotechnical Engineering has been built on the basis of comparing observed material behaviors of new soils to the established behaviors of well researched soils. Variations in natural soils have infinite possibilities as such the variations of the engineering parameters have infinite possibilities. Thus by comparing new tested soils to established soils, general trends can be established and the soils can be partitioned into like behaviors. Boston Blue Clay was chosen as a well-studied material for its historic significance in the field of geotechnical engineering. Boston Blue Clay has long been the subject of study at the Massachusetts Institute of Technology. Several reports and theses have been published from test data on BBC and RBBC starting in the 1960's, a few notable reports are Varallyay (1964), Ladd & Luscher (1965), Ladd, Young, Kraemer, & Burke, 1999) (1999), House (2012) and Casey B. (2014). Boston Blue Clay is a non cemented soil found naturally in Boston, Massachusetts. Boston Blue Clay was deposited prior to glaciation. In addition to Boston Blue Clay, Gulf of Mexico Eugene Island clay will be compared to RNSC. Gulf of Mexico Eugene Island Clay (GoM_EI) and Resedimented Gulf of Mexico Eugene Island Clay (RGoM_EI) have been well studied over the last decade at MIT and TAG. A few notable theses with RGoM_EI data are Casey B. (2014), Fahy, (2014), Nordquist (2015) and Hanley (2017). Gulf of Mexico Eugene Island Clay is found in within the Eugene Island Block off the coast of Louisiana within the Gulf of Mexico and is found to have relatively high salt concentrations

(Stump, 1998). RGoM_EI was chosen as standard clay for comparison due to its high Smectite content and high liquid limit which are similar to RNSC.

Section 5.2 will provide a comparison of the mineralogy, index properties, specific gravity, and natural salt concentration of the three soils. Any expected behavior changes due to variations in the composition of these soils will be highlighted.

Section 5.3 will compare the compression behavior and permeability behavior measured with CRS tests performed on the three soils.

Section 5.3 will compare the stress-strength-strain behavior of RNSC to the stress-strength-strain behavior of the other two soils. This section will explore the links to strength parameters and plasticity presented in Casey B (2014).

5.2 INDEX PROPERTY AND CHARACTERISATION TESTS

3.2.11 Introduction

Characteristic and index property tests are used to classify a soil for field identification, but index properties can also be used to provide clues on material behavior. This section will compare the index property and classification tests of RNSC to RBBC and RGoM_EI in order to highlight variations in the materials.

3.2.12 Grain Size Distribution and Specific Gravity

The grain size distribution of RNSC, RBBC and RGoM_EI was measured by the sedimentation method. Figure 5-3 shows the grain size distribution curves in particle size (mm) by percent finer. RNSC has the largest sand fraction at 24% but the smallest silt fraction at 30% and the smallest clay fraction at 46%. RBBC was found to have a silt fraction of 45% and a clay fraction of 55%. RGoM_EI was found to have a silt content of

36% and a clay content of 64%. The variation in particle size affects the compressibility behavior of the soil as documented in Mitchell (1976), Lupini (1982), and Yang & Aplin (2010).

The specific gravity of a soil largely depends on the density of its constituent minerals. The specific gravity of RNSC, RBBC, and RGoM_EI was 2.816, 2.778, and 2.775 respectively.

3.2.13 Atterberg Limits

Variations in the Atterberg limits can be used to index the soil behavior. The connection to plasticity and variations in material behavior was extensively studied and detailed over a wide range of clays soils in Casey B. (2014).

Figure 5-2 shows the Atterberg limits for NSC, BBC, and GoM_EI. GOM_EI has the highest plasticity index at 62.9% and liquid limit at 85.8%. NSC was found to have the second highest plasticity index at 38.7% and the second highest liquid limit at 62.1%. BBC was found to have the lowest plasticity index at 22.7% and the lowest liquid limit at 46.5%. Surprisingly the plastic limit for all three soils was in a fairly tight window ranging from 22.9% to 23.8%. Based on the high Smectite content in the mineralogical clay fraction one would expect NSC to have a higher plasticity than GoM_EI. It is not known why NSC does not have a higher liquid limit.

3.2.14 Bulk Mineralogy an Mineralogy of Clay Fraction

The bulk mineralogy of the three soils was determined through XRPD on powder samples of all three materials at the James Hutton Limited Institute. The bulk mineralogy of RNSC is comprised predominantly of Smectite (36.8%), Quartz (23.9%), Plagioclase (13.9%), Kaolinite (7.2%), and K-Feldspar (5.4%). RNSC contains trace (<5%)

Pyroxene, Calcite, dolomite, Hematite, Geothite, Magnetite, Anatase, and Ilmenite. The bulk mineralogy of RGoM_EI is comprised predominantly of Illite (44.4%), Quartz (27.8%), Kaolinite (9.1%), and Plagioclase (5.3%). RGoM_EI contains trace (<5%) K-Feldspar, Calcite, dolomite, Siderite, Pyrite, Barite, Anatase, Muscovite, Halite, and Ilmenite. The bulk mineralogy of RBBC is comprised predominantly of Quartz (21.3%), Plagioclase (20.5%), Muscovite (13.8%), Tri-Mica (9.2), K-Feldspar (8.2%), Illite/Illite-Smectite (7.3%), Chlorite (6.2%), and Hydrobiotite (5.4%). RBBC contains trace (<5%) Calcite, Dolomite, Amphiole, Halite, and Kaolinite.

The mineralogical clay fraction of the three soils was determined through X-Ray scanning of the <2 μm fraction of the soil, oriented on a glass slide, obtained through timed sedimentation, glycolated, and oven dried to 300° C. The mineralogical clay fraction of RNSC was found to be 93% Smectite, 1% is Illite, and various clay minerals constitute the remaining 6%. The mineralogical clay fraction of BBC was found to be 91.6% Illite, 1.4% Smectite, and the remaining 7% was various minerals. The mineralogical clay fraction of GoM_EI was found to be 65.3% Smectite, 29.8% Illite and the remaining 4.9% was found to be other various minerals. Figure 5-1 shows a series of pie charts that illustrate the mineralogical clay fraction of the three soils of comparison. RNSC has a much higher Smectite content than both BBC and GoM_EI. From Casey B. (2014) this would imply that the RNSC would likely have a larger liquid limit, larger void ratios at low stresses and larger compressibility.

5.3 COMPRESSION AND PERMEABILITY BEHAVIOR

5.3.1. Introduction

Compressibility has been found to vary with mean particle size as detailed within Yang & Aplin (2010) as well as plasticity as detailed within Casey B. (2014). Permeability is intrinsically connected to compressibility through the restriction of the pore space caused by change in stress level. Soils with a high Smectite content have been found to have larger pore spaces at low stress and to have a high compressibility when loaded. Illite dominated soils have been found to have smaller void spaces at low stresses and to be less compressible. A noted observation within Casey B. (2014) was that soil compression behavior for a wide variety of soils converged to a narrow characteristic band at high effective stress levels (>10 MPa).

Section 5.3.2 will discuss the variation of compressibility within the three materials by comparing the Compression Ratio (CR) and the stress dependence of CR at medium stresses (<10 MPa). The changes in density will be compared for the normally consolidated soils with a change in stress.

Section 5.3.3 will discuss the variations in permeability for the soils as calculated from the normally consolidated hydraulic conductivity measurements from CRS testing. A correlation between the liquid limit and permeability was presented within Casey B. (2014) this correlation will be used to estimate the permeability of RNSC. The estimation will be compared to the measured permeability.

5.3.2. Compressibility

Compressibility comparisons for this research are from CRS testing of RBBC, RGoM_EI, and RNSC. The RNSC CRS testing was performed within the TAG laboratory

and the RBBC and RGoM_EI CRST testing was performed by others as listed in Table 5-1. The data for the RBBC CRS testing is from (GeoFluids, Boston Blue Clay, 2018), and the data for RGoM_EI is from (GeoFluids, Gulf of Mexico Eugene Island, 2016). Figure 5-4 presents the normally consolidated compression curves of the three soils in ϵ -Log σ space. Table 5-2 summarizes the average CR values at two stress levels and the Swelling Ratio (SR) value for the three soils. RGoM_EI was found to be the most compressible soil with a CR of 0.255 (between 0.1 and 1 MPa) and a CR of 0.220 (between 1 and 10 MPa). RNSC was the second most compressible soil with a CR of 0.213 (between 0.1 and 1 MPa) and a CR of 0.176 (between 1 and 10 MPa). RBBC was found to be the least compressible soil with a CR of 0.151 (between 0.1 and 1 MPa) and a CR of 0.144 (between 1 and 10 MPa). RNSC was found to have the largest reduction in compressibility with change in stress level. There was a 17% decrease in CR from the CR calculated between 0.1 and 1 MPa and 1 to 10 MPa. Between these same stress levels RBBC and RGoM_EI had reductions in CR of 5% and 14% respectively. The SR of RGoM_EI was the highest measured at 0.035, which is nearly double the SR of RNSC 0.018 and nearly triple the SR of RBBC 0.012.

Figure 5-5 shows the normally consolidated one dimensional compression curves for the three soils in e -log σ space. This can be compared to Figure 5-6 which shows the normally consolidated one dimensional compression curves for three Smectitic mixtures as published within Marcial, Delage, & Yu Jun (2001). Between stress levels of 0.1 MPa to 10 MPa, the average void ratio of the three smectitic mixtures reduces from approximately 6.0 to 1.0. Over the same stress range RGoM_EI shows a reduction in void ratio from approximately 1.4 to 0.4. RBBC shows a reduction in void ratio from approximately 1.2 to 0.52. RNSC shows a reduction of void ratio from approximately

1.19 to 0.36. This indicates Smectite concentration is a factor in the compressibility of clays as the larger changes in void ratio over the same stress level were observed in the clays with higher Smectite concentration. This reasoning would also imply that RNSC would likely be more compressible than RGoM_EI. This might not be the case due to the larger sand concentration of RNSC as compared to RGoM_EI.

Figure 5-7 shows a family of normally consolidated one dimensional compression curves for Resedimented Boston Blue Clay at various clay particle concentrations from Schneider (2011). Within Figure 5-7 there is a clear trend that as the clay concentration decreases the compressibility of the soil decreases. As shown in Table 5-1, RGoM_EI has approximately 18% more clays sized particles than RNSC. This may account for the higher compressibility observed within RGoM_EI as compared to RNSC, even though RNSC has a significantly higher Smectitic mineralogical clay fraction.

5.3.3. Permeability

Permeability has been found to correlate with plasticity Casey B. (2014) as an index of clay mineralogy content Van Olphen (1963), and by particle size distribution Schneider (2011) and Yang & Aplin (2010). Figure 5-8 presents the permeability of the three soils by porosity. The predominantly illitic RBBC was found to be the most permeable soil at a given stress. RNSC was found to be the second most permeable soil and RGoM_EI was the least permeable soil. The three materials compared within this study are only ordered appropriately in decreasing permeability with the correlation to plasticity index presented within Casey B. (2014). The plasticity index is an indirect measure of both the clay mineralogy and particle size distribution.

5.4 STRESS-STRENGTH-STRAIN

5.4.1. Introduction

A comparison of the Stress-Strength-Strain properties of RNSC, RBBC and SGoM_Ei will be provided in this section. From Casey B. (2014) soil plasticity is linked to higher shear stresses (shear strength) at lower consolidation stresses, a rapid reduction in peak shear strength, a greater sensitivity to normalized maximum shear stress to consolidation level, a rapid reduction in friction angle with increase in consolidation stress, and a greater sensitivity of friction angle to consolidation stress level.

Strength is the maximum shear stress sustained by the sample given its pre-consolidation stress. Section 5.4.2 will present a comparison of the undrained maximum shear stress for the three soils. Section 5.4.3 will present a comparison of the effective friction angle for the three soils. Section 5.4.4 will present a comparison of the lateral stress ratio K_0 for the three soils.

Due to equipment limitations during the laboratory testing program performed on RNSC these comparisons will be limited to a low stress range of <1 MPa. Table 5-3 summarizes the triaxial tests used for comparison.

5.4.2. Undrained Shear Strength

Triaxial compression testing was performed on Normally Consolidated RNSC, RBBC and RGoM_Ei. From those tests the peak shear stress (i.e. shear strength) was measured for each soil. Figure 5-9 shows the maximum shear stress by horizontal confining stress of each of the triaxial tests for the study soils. Horizontal confining stress is defined as the triaxial cell fluid pressure minus the back pressure during the shearing portion of the test. At very low stresses (<0.1 MPa) the maximum shear

stresses of the three soils are generally the same. As the confining stress increases the shear strength of the three soils starts to diverge. In general RBBC has the highest shear strength, followed by RGoM_EI and the weakest is RNSC.

Figure 5-10 presents the normalized maximum shear stress by maximum consolidation stress in a low stress range (<1 MPa) for the three soils. The shear stress was normalized by the maximum consolidation stress for the plot (for each specimen). RNSC was found to have the highest normalized shear strength at lowest consolidation stress and the most drastic reduction in shear strength with increase in consolidation stress level. At a maximum consolidation stress level around 0.14 MPa RNSC had an average normalized peak shear stress of 0.37 while at the same consolidation stress, RBBC and RGoM_EI had a normalized shear strength of 0.33 and 0.28 respectively. At a consolidation stress around 0.6 MPa RNSC had average normalized peak shear strength of 0.22. This shows RNSC has a reduction in normalized peak shear stress of 0.15 over an increase of consolidation stress by 0.45 MPa. For comparison RBBC shows a reduction in normalized shear stress of 0.02 over a .48 MPa increase in consolidation stress and RGoM_EI shows a reduction in normalized shear stress of .02 in a 0.51 MPa increase in consolidation stress. Variations in peak shear stress are expected due to the sand content of RNSC compared to RBBC and RGoM_EI (Das, 2010) and due to the high plasticity of RNSC and RGoM_EI (Casey B., 2014).

As shown in Figure 5-10, RNSC has the most sensitive shear strength to consolidation pressure. This is likely not caused by the clays plasticity as RGoM_EI has a higher plasticity and higher clay content than RNSC. The trend in the RNSC data shows a very steep increase in shear strength with a decrease in consolidation pressure which

indicates the sand content in RNSC may be controlling the strength at low stresses. At higher stresses the clay content of RNSC might be lubricating the sand particles which could account for the weaker shear strengths as compare to RBBC and RGoM_EI.

5.4.3. Effective Friction Angle

The critical state friction angle is a major component in determining soil strength behavior. The critical state friction angle was chosen for comparison as oftentimes the friction angle at peak shear has a significant variation from the critical state friction angle. For this research the critical state friction angle is taken as the angle of maximum obliquity measured during the shearing portion of the triaxial test. The friction angle at peak shear is the friction angle measured at maximum shear stress during the shearing portion of the triaxial test.

Figure 5-11 presents the effective friction angle by maximum consolidation stress for normally consolidated RNSC, RBBC and RGoM_EI. All three soils displayed a trend of decreasing friction angle with an increase of consolidation stress. RBBC within the 0.1 to 1 MPa stress range had the consistently highest critical state friction angle which ranged from 39.4 degrees at a consolidation stress of .14 MPa to 31 degrees at a consolidation stress of 0.97 MPa. RNSC initially has the second highest critical state friction angle of 34.2 at consolidation stress of 0.13 MPa. RNSC quickly falls into a similar friction angle range of RGoM_EI with a friction angle of 22.5 at a consolidation stress of 0.58 MPa. RGoM_EI had the consistently lowest critical state friction angle of 26.8 degrees at a consolidation stress of 0.13 MPa and decreasing to 22.8 degrees at a consolidation stress of 0.88 MPa.

Similar trends of decreasing friction angle with increase in consolidation stress level were observed for 8 study soils within Casey B. (2014). Within this study two clear trends were observed, the critical state friction angle decreases with an increase in consolidation stress for all of the studied soils. Critical state friction angle is related to plasticity behaviors. For the 8 studied soils within Casey B. (2014) the low plasticity soils had higher critical state friction angles for a given consolidation stress and smaller changes in friction angle with an increase in consolidation stress. The high plasticity soils had lower critical state friction angles for a given consolidation stress and larger changes in friction angle with an increase in consolidation stress. These same trends are generally observed within the research herein.

RBBC has the lowest plastic limit and has the highest critical state friction angle at low stress. RBBC also has the smallest change in critical state friction angle from consolidation stress of 0 to 1MPa. RNSC has a higher critical state friction angle than RGoM_EI at low stress, but as the consolidation stress increases the critical state friction angle for RNSC quickly decreases to be roughly the same as RGoM_EI. The High friction angle of RNSC at low stress could be caused by free movement of the sand and silt grains through the clay particles, making grain to grain contacts. At higher stresses the clay particles could potentially be too dense for free movement of the sand silt particles limiting the grain to grain contact. This would be observed within RNSC due to the appreciable sand content.

5.4.4. Lateral Stress Ratio, K_0

The lateral stress ratio, K_0 , is the effective horizontal stress divided by the effective vertical stress prior to shearing. To measure K_0 in a triaxial cell, the cell needs to be

designed and programmed to perform K_0 consolidation. Figure 5-12 presents the lateral stress ratio by maximum consolidation stress for the three normally consolidated comparison soils at a low stress range <1 MPa. RBBC shows a very consistent increase of K_0 with increase of consolidation stress. With a K_0 of 0.518 at a consolidation stress of 0.14 MPa rising to a K_0 of 0.55 at a consolidation stress of 0.96 MPa. RGoM_EI has a more significant rise in K_0 with an increase in consolidation stress. With a K_0 of 0.62 measured at a consolidation stress of 0.13 MPa rising to a K_0 of 0.655 at a consolidation stress of 0.88 MPa. RNSC shows the most drastic rise in K_0 ; with a K_0 of 0.45 at a confining stress of 0.15 MPa to a K_0 of 0.74 at a confining stress of 0.58 MPa. RNSC does have a lot of scatter associated with its K_0 measurements, the reason for this scatter is unknown but possible sources are; stress sensitivity due to the expansion of the double layer in a low saline pore fluid solution, and a stress sensitivity caused by the expansive Smectite particles. In Casey B. (2014) a trend is noted that K_0 increases with increasing consolidation stress for all of the studied soils with the increase being most rapid in high plasticity clays. This same trend is generally observed within Figure 5-12.

Figure 5-13 presents the Lateral stress Ratio by the normalized undrained shear strength for each of the three study soils. This figure shows that an increase in K_0 corresponds to a decrease in normalized shear strength. This trend was previously presented within Casey B. (2014). The trend is shear strength varies with the lateral stress ratio K , but there is a unique relationship between K_0 , shear strength, and critical state friction angle. Regardless of the K value a specimen is consolidated to the critical state friction angle will always be the same for the same consolidation stress. Figure 5-14 presents the friction angle by lateral stress ratio of the three study soils. This includes a line representing the 1948 Jaky equation which correlates the at rest earth

pressure (lateral stress ratio, K_0) to the friction angle of the soil (Jaky, 1948). This correlation originally used for granular soils has been found to agree with cohesive soils as detailed within Casey B. (2014). For the three studied soils, there is a clear trend that as the friction angle of the soil decreases the lateral stress ratio increases. The Jaky curve also provides a lower bound for the friction angle of clay soils.

The behavior of RNSCs lateral stress ratio provides that at low stress levels RNSCs sand content may control the behavior of the soil through grain to grain contacts. It is hypothesized that at higher stresses the clay particles start inhibiting the sand particles thus changing the behavior of the material into a more fine grained response. This is thought to be the case, due to the rapid increase of K_0 with an increase of consolidation stress as shown in Figure 5-12. This illustrates that RNSC behaves as a high plasticity soil as the consolidation stress increases indicating that the clay structure may be controlling the behavior at higher stress levels. The normalized undrained shear strength decreases with an increase of K_0 . This indicates at higher consolidation stress levels (as indicated by higher K_0 values) RNSC has a more ductile response to shear stress and cannot support the same equivalent magnitude of stress that low stress RNSC can. This potentially indicates grain to grain contacts within RNSC at low stresses provide internal stress resistance not observed at higher stress. The 1948 Jaky equation was developed from normally consolidated sands back filled into a silo. The silo prohibits the soils lateral deformation leading to the K_0 condition. At low K_0 values (low consolidation stress) RNSC has a strong agreement with the Jaky equation. As K_0 increases (consolidation stress increases) RNSC begins to diverge from the Jaky equation. Again indicating that at low stresses the sand particles may be dominating the RNSC rheology.

Origin	Nile Silty Clay Cairo, Egypt	Boston Blue Clay Boston, Massachusetts	Gulf of Mexico Eugene Island Eugene Island, Gulf of Mexico
Contributing Researchers	Author	Walbaum (1988), Ahmed (1990), Seah (1990), Sheahan (1991), Santagata (1994), Santagata (1998) Abdulhadi (2009), Moniz (2009), Horan (2012), Casey (2014)	Betts (2014) Fahy (2014)
Liquid Limit, WL %	62.1	46.5	85.8 ^F
Plastic Limit, PL %	23.4	23.8	22.9
Plasticity Index, PI %	38.7	22.7	62.9
Activity	0.84	0.41	0.98
Sand Fraction %	24	0	0
Silt Fraction %	30	45	36
Clay Fraction %	46	55	64
USCS Classification	CH	CL	CH
Specific Gravity	2.816	2.778	2.775
Clay Mineralogy (< 2 µm Particle Size)			
Illite %	1.0	91.6	29.8
Smectite %	93.0	1.4	65.3
Other %	6.0	7.0	4.9

F- For RGoM_EI the fall cone method was used to determine the Liquid Limit. The Cassagrande Cup method was used for RNSC and RBBC

Table 5- 1: Index Properties of RNSC, RBBC, and RGoM_EI

		Nile Silty Clay	Boston Blue Clay	Gulf of Mexico Eugene Island
CR	0.1-1 (Mpa)	0.213	0.151	0.255
	1-10 (Mpa)	0.176	0.144	0.220
SR	(OCR=4)	0.018	0.012	0.035

Table 5- 2: Compression Properties of RNSC, RBBC, and RGoM_EI

Nile Silty Clay								Boston Blue Clay						Gulf of Mexico Eugene Island									
Test No.	Test Type	Source	σ'_{vc} (Mpa)	ϵ_a (%)	q/σ'_{vc}	K_0 Pre-Shear	ϕ'_{cs}	Test No.	Test Type	Source	σ'_{vc} (Mpa)	ϵ_a (%)	q/σ'_{vc}	K_0 Pre-Shear	ϕ'	Test No.	Test Type	Source	σ'_{vc} (Mpa)	ϵ_a (%)	q/σ'_{vc}	K_0 Pre-Shear	ϕ'
TX1283	CK ₀ UC	Author	0.15	0.30	0.36	0.45	33.860	TX724	CK ₀ UC	Abdulhadi (2009)	0.333	0.178	0.31	0.528	35.5	TX1175	CK ₀ UC	Fahy (2014)	0.878	1.91	0.238	0.655	22.76
TX1316	CK ₀ UC	Author	0.58	0.56	0.23	0.72	22.520	TX727	CK ₀ UC	Abdulhadi (2009)	0.964	0.335	0.288	0.546	32.1	TX1180	CK ₀ UC	Fahy (2014)	0.126	0.34	0.276	0.619	26.85
TX1326	CK ₀ UC	Author	0.23	0.24	0.28	0.58	27.016	TX732	CK ₀ UC	Abdulhadi (2009)	0.142	0.165	0.326	0.518	39.4	TX1182	CK ₀ UC	Fahy (2014)	0.379	0.39	0.263	0.626	23.87
TX1327	CK ₀ UC	Author	0.58	3.81	0.21	0.74	23.130	TX741	CK ₀ UC	Abdulhadi (2009)	0.478	0.252	0.297	0.536	33.5	TX1214	CK ₀ UC	Fahy (2014)	0.38	0.48	0.27	0.595	26.1
TX1338	CIUC	Author	0.39	11.38	0.22	1.00	23.390	TX748	CK ₀ UC	Abdulhadi (2009)	0.817	0.284	0.292	0.542	32.4	TX1199	CK ₀ UC	Fahy (2014)	0.333	0.45	0.236	0.68	26.7
TX1346	CIUC	Author	0.13	7.20	0.42	0.98	34.200	TX757	CK ₀ UC	Abdulhadi (2009)	0.67	0.223	0.292	0.542	32.4	TX1201	CK ₀ UC	Fahy (2014)	0.372	0.36	0.237	0.649	23.2
TX1379	CK ₀ UC	Author	0.14	0.31	0.33	0.53	30.778	TX762	CK ₀ UC	Abdulhadi (2009)	0.189	0.154	0.313	0.523	36.4								
								TX787	CK ₀ UC	Abdulhadi (2009)	0.332	0.158	0.305	0.538	34.2								
								TX788	CK ₀ UC	Abdulhadi (2009)	0.972	0.367	0.289	0.542	31								
								TX1036	CK ₀ UC	Casey (2014)	0.557	0.11	0.31	0.493	31.7								
								TX1070	CK ₀ UC	Casey (2014)	0.555	0.3	0.316	0.517	34.8								
								TX1073	CK ₀ UC	Casey (2014)	0.563	0.15	0.324	0.492	34.8								

Table 5- 3: Summary of Triaxial Tests Used to Compare RNSC, RBBC, and RGoM_EI

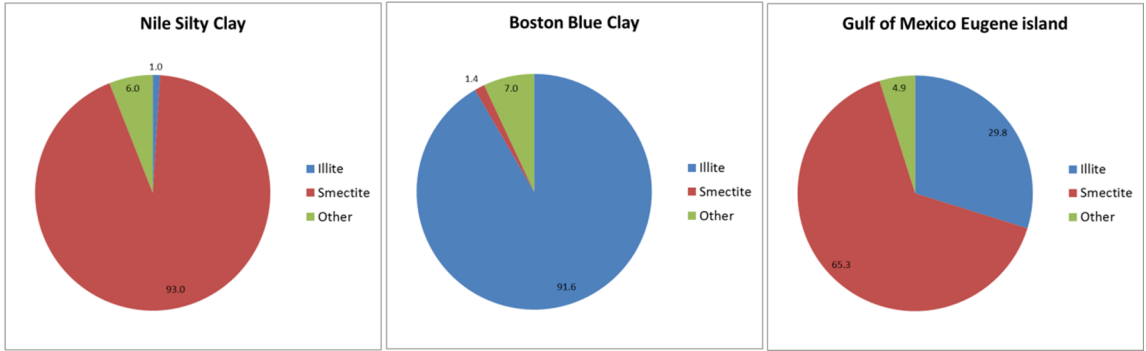


Figure 5- 1: Constituent Minerals of Clay Fraction (<math><2\mu\text{m}</math>) of NSC, BBC and GoM_EI

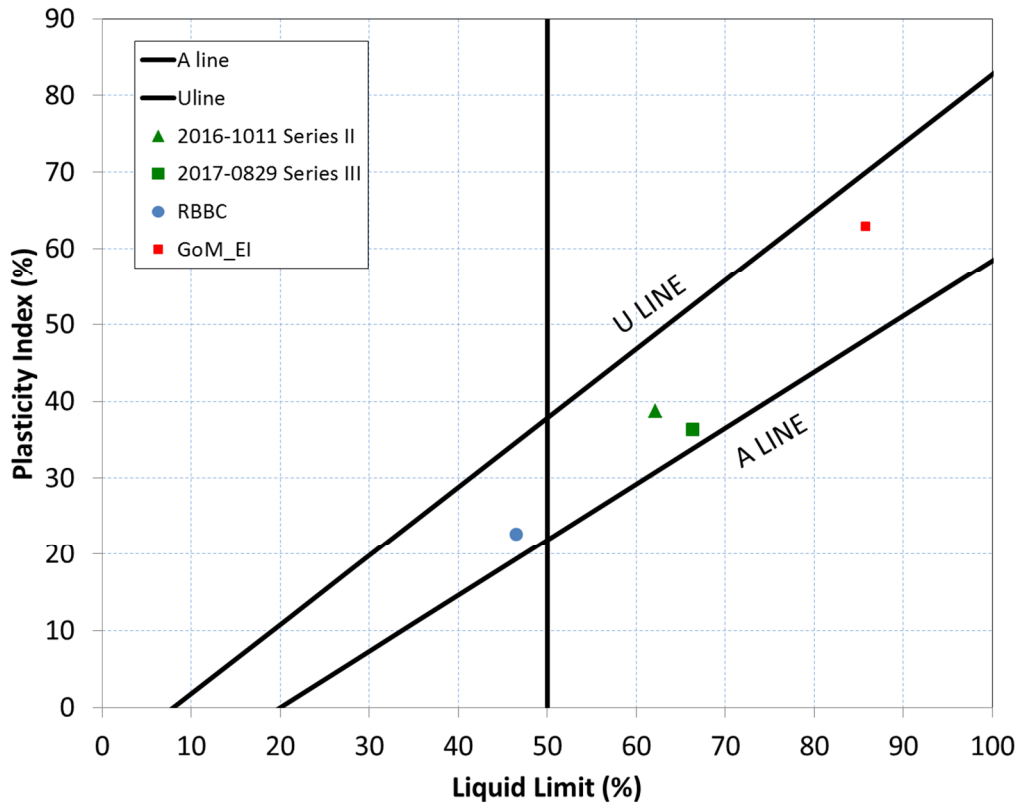


Figure 5- 2: Atterberg Limits of RNSC, RBBC and RGoM_EI

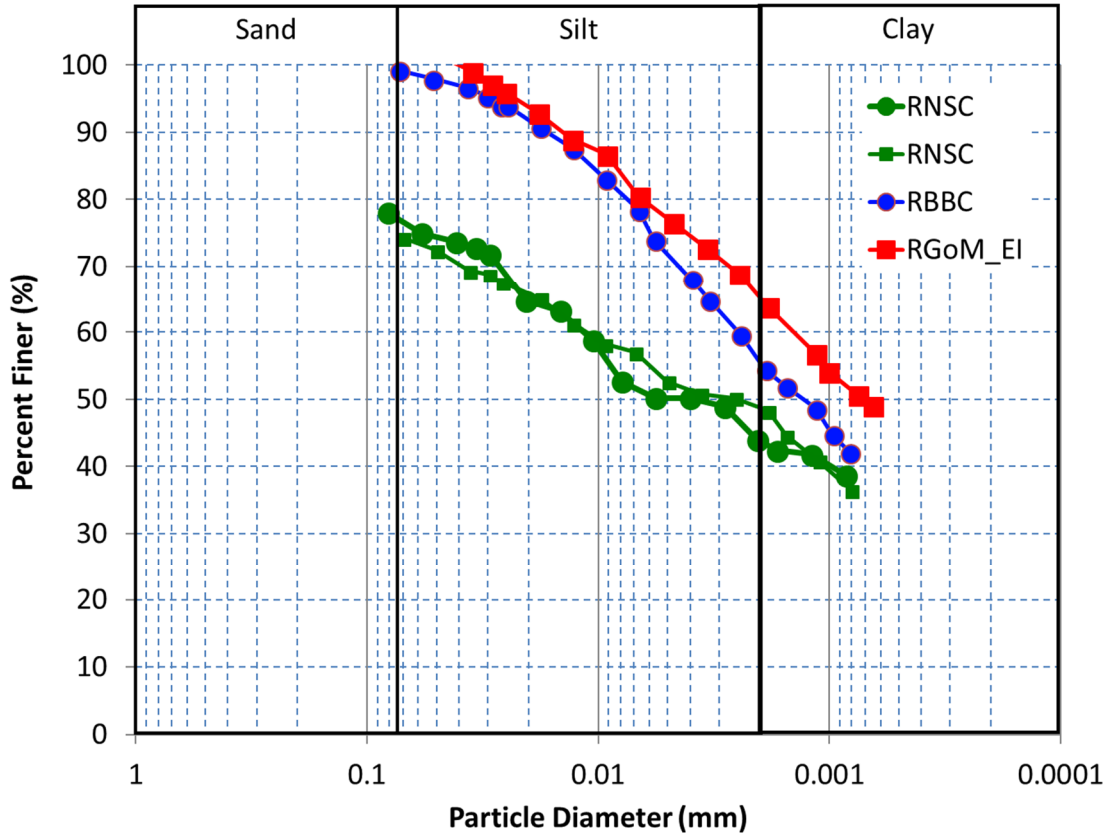


Figure 5- 3: Particle Size Distribution by Sedimentation Testing for RSC, RBBC and RGoM_EI

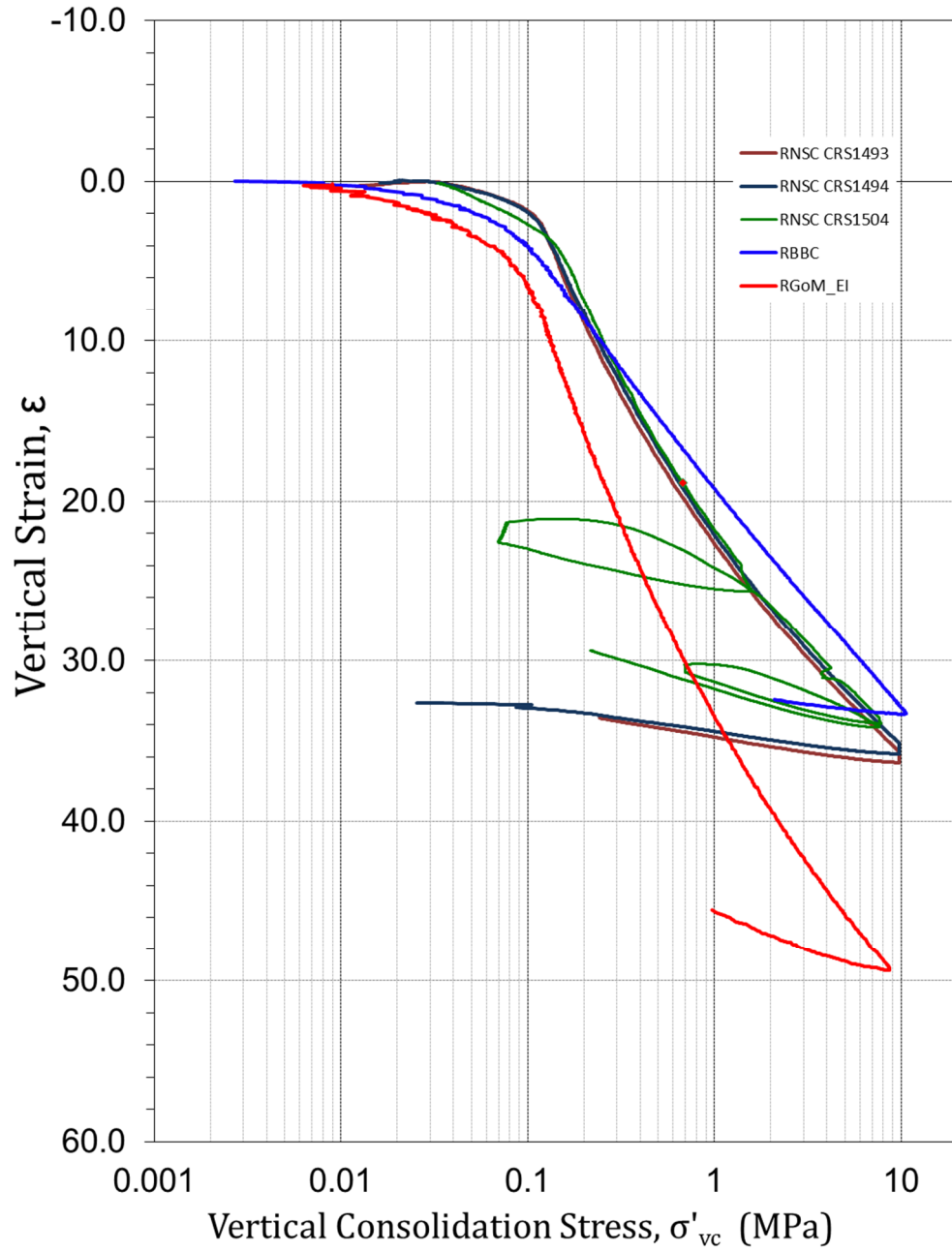


Figure 5- 4: Virgin Compression Behavior from CRS tests for RNSC, RBBC and RGoM_EI in ϵ - $\log\sigma'_{vc}$ space

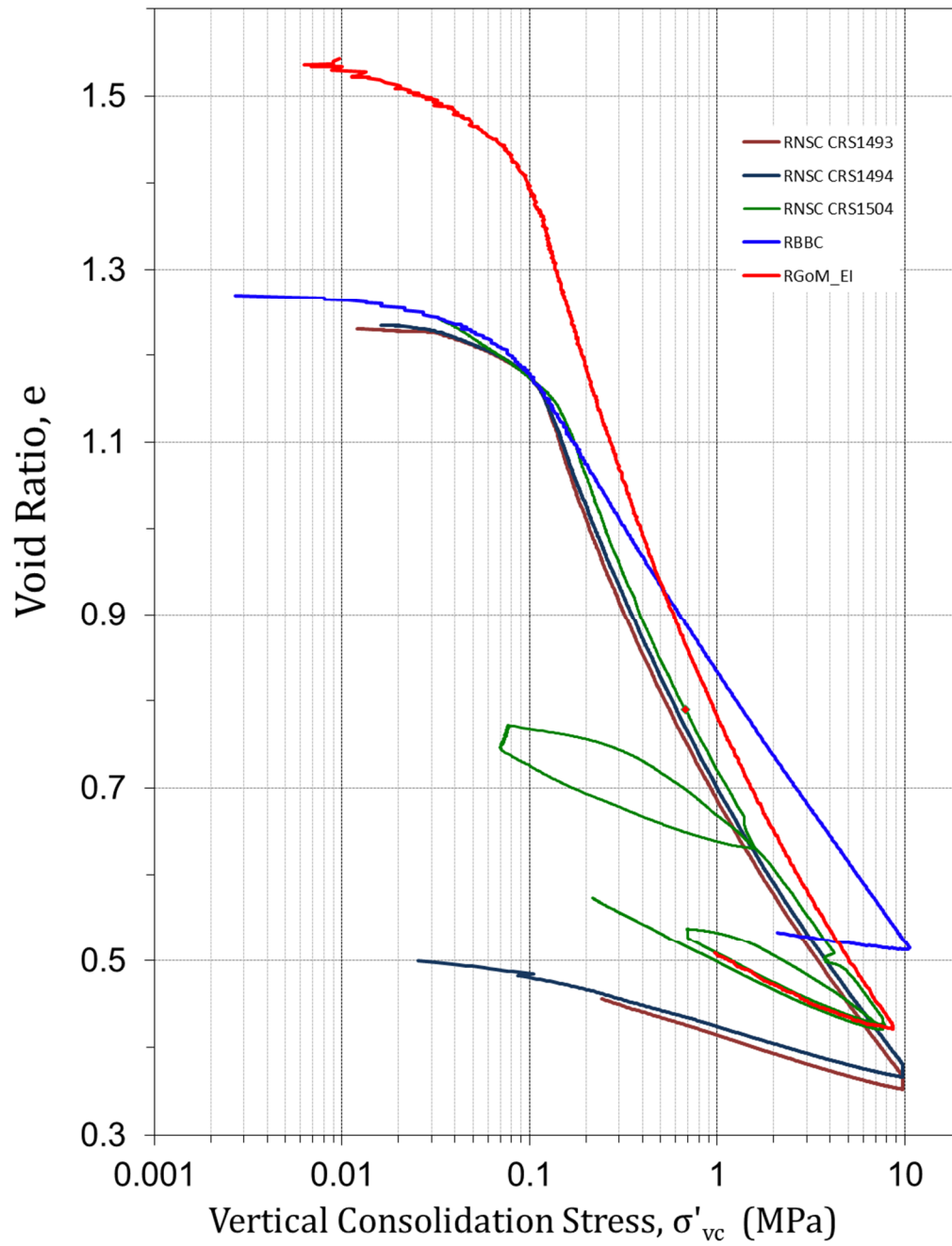


Figure 5- 5: Virgin Compression Behavior from CRS tests for RNSC, RBBC and RGoM_EI in e - $\log\sigma'_{vc}$ space

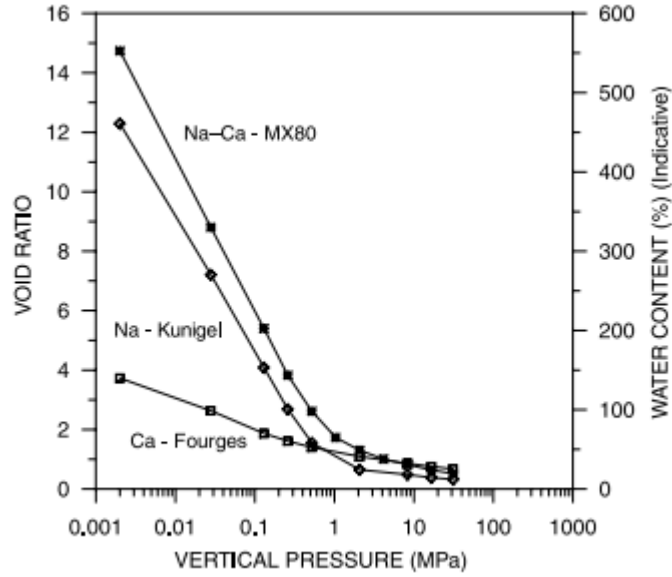


Figure 5- 6: Consolidation Curves of Bentonite Mixtures from (Marcial, Delage, & Yu Jun, 2001)

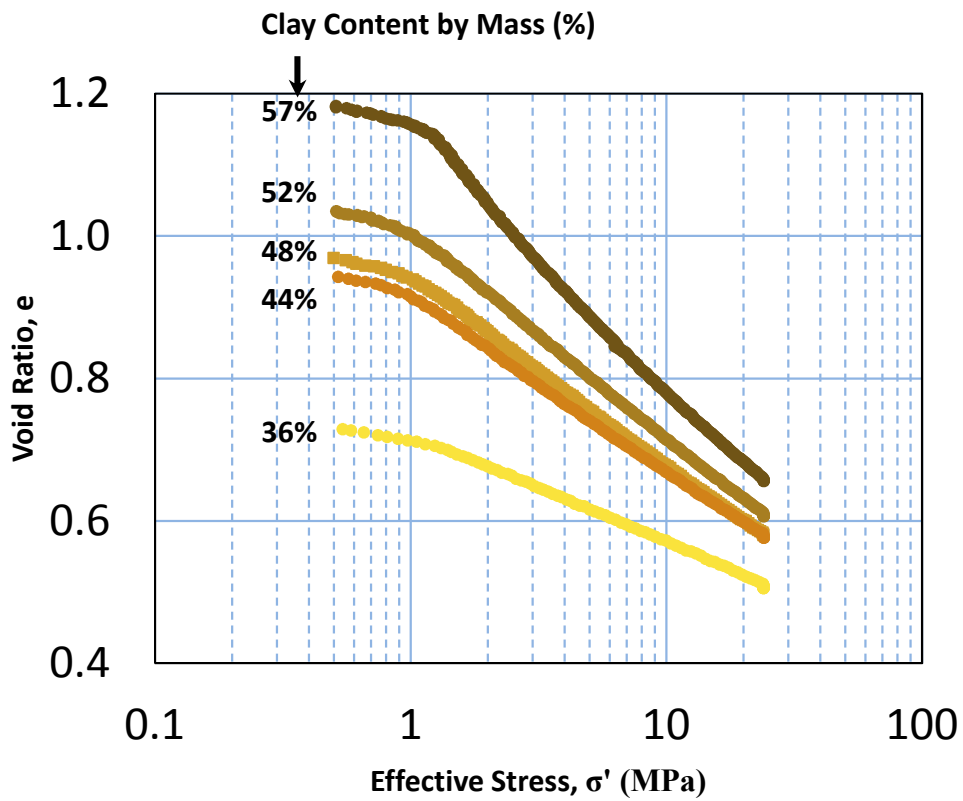


Figure 5- 7: Variations in RBBC Consolidation with Variations of Clay Concentration from (Schneider, 2011)

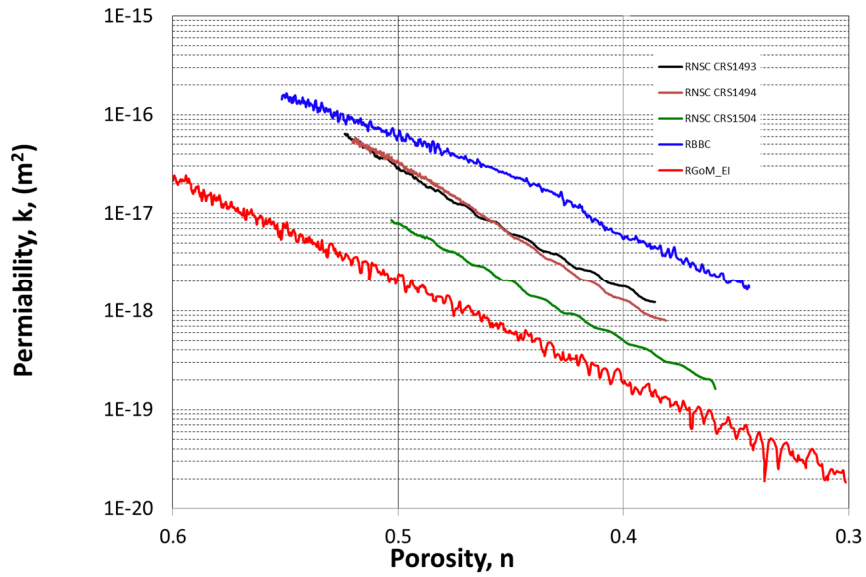


Figure 5- 8: Change in Permeability by Porosity for RNSC, RBBC and RGoM_EI from CRS Testing

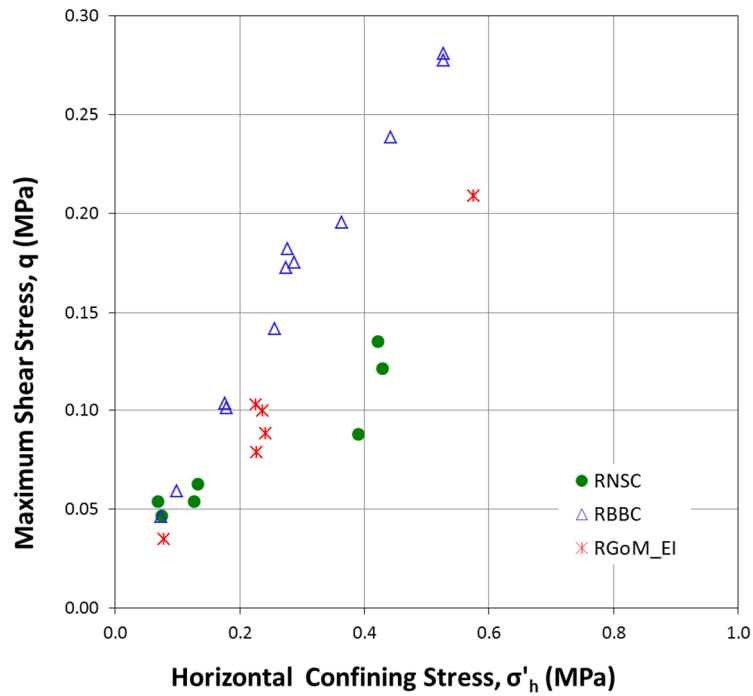


Figure 5- 9: Maximum Shear Stress by Horizontal Confining Stress of the Three study Soils

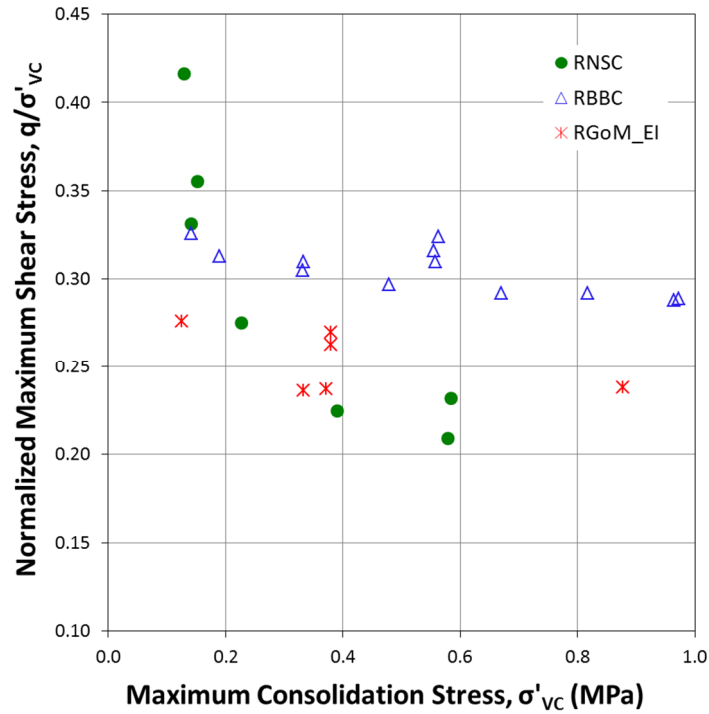


Figure 5- 10: Normalized Maximum Shear Stress by Maximum Consolidation Stress for RNSC, RBBC and RGoM_EI

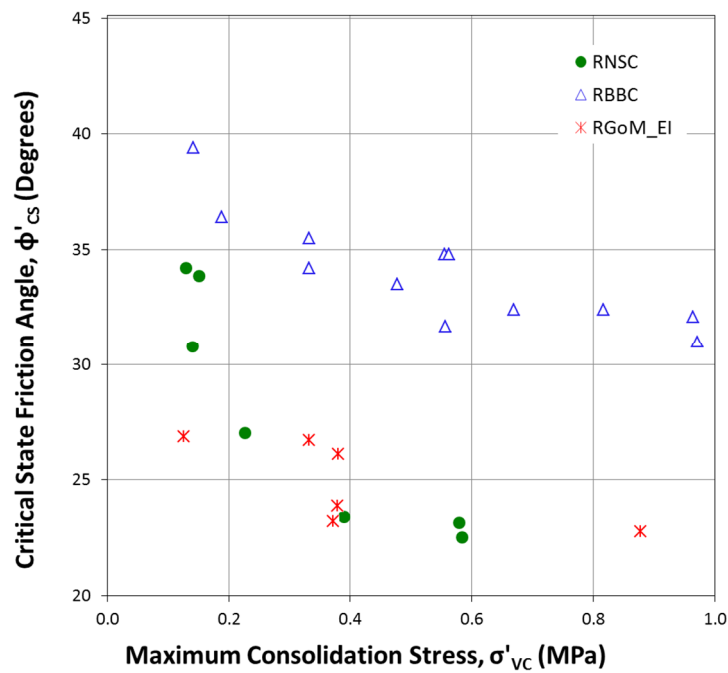


Figure 5- 11: Critical State Friction Angle by Maximum Consolidation Stress for RNSC, RBBC and RGoM_EI

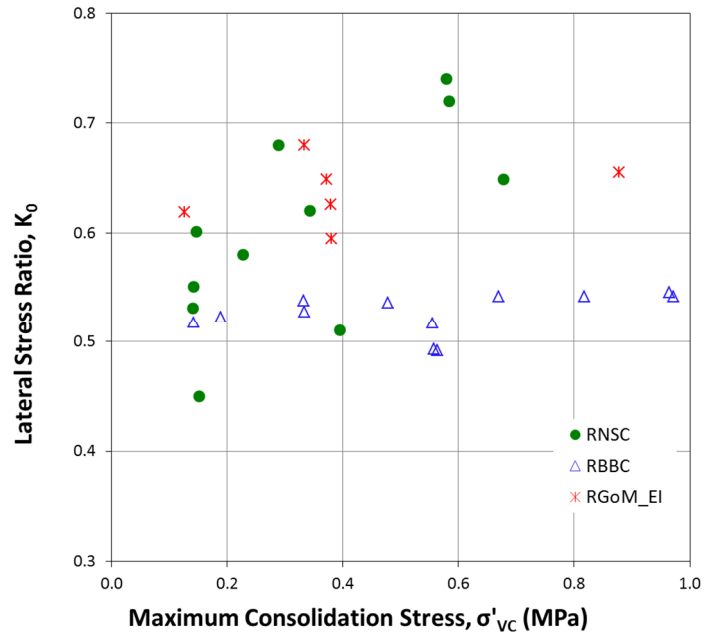


Figure 5- 12: Coefficient of Lateral Earth Pressure K_0 by Maximum Consolidation Stress for RNSC, RBBC, and RGoM_EI

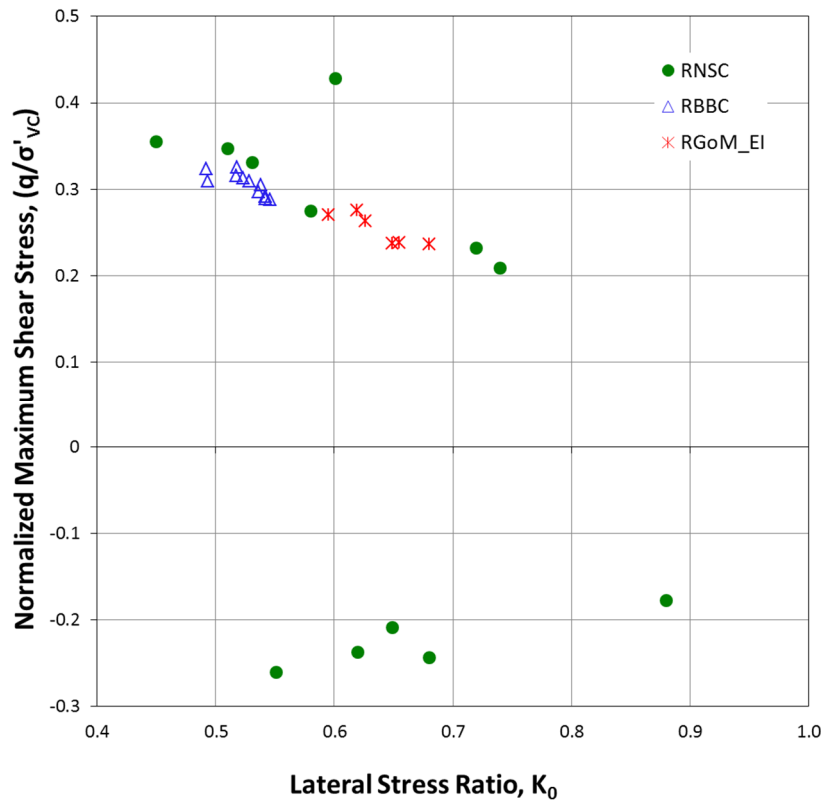


Figure 5- 13: K_0 by Normalized Shear Strength for RNSC, RBBC, and RGoM_EI

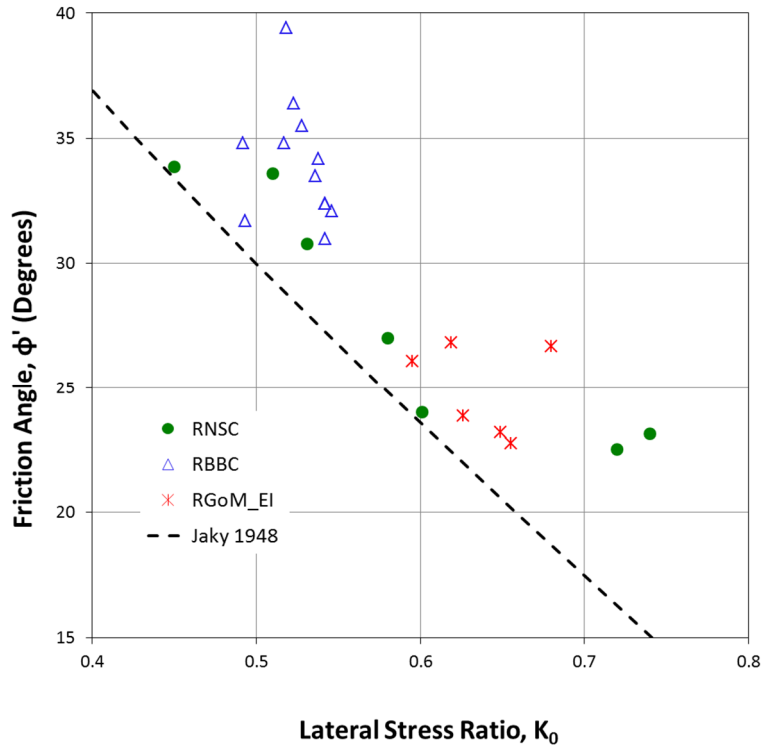


Figure 5- 14: Critical state Friction Angle by Lateral Stress Ratio with Comparison to Jaky1948 for RNSC, RBBC, and RGoM_EI

Chapter 6

CONCLUSIONS AND RECOMMENDATIONS

6.1 CONCLUSIONS

6.1.1 Introduction

An extensive experimental testing program was undertaken to characterize Nile Silty Clay. Initial identification of the index properties, grain size distribution, natural salinity and specific gravity was determined for field identification and to support a laboratory testing program of the material. The testing program made use of consolidation and triaxial shear devices to provide the engineering parameters. The results and conclusions are included in this section.

6.1.2 Nile Silty Clay

Nile Silty clay is a Brown clay found within Egypt along the banks of the Nile River. Nile Silty Clay is a geologically young Alluvial sediment, with deposition starting an estimated 8000 years before present. The material is deposited during floods from the Nile River. The base minerals for Nile Silty Clay come from four major contributing sources, weathered rocks from the Ethiopian highlands carried from the Blue Nile, historic wadis in Egypt, hard crystalline sediments from the White Nile, and Aeolian dusts from the Sahara Desert. The sample for this research was collected from a construction site in Cairo at an estimated depth of 10 to 15 feet. It was provided to Tufts University by Dr. Sherif Akl of the University of Cairo.

6.1.3 Resedimentation

The resedimentation technique as detailed within sections 3.3.2 and 3.3.3 herein provided a high quality specimen for laboratory testing. At the start of the testing program it was unknown whether resedimentation would be an acceptable form of specimen reconstitution for RNSC. The water content for stable slurry and the natural salt content of RNSC needed to be determined to support the resedimentation procedure. It is possible that there are deviations in the material fabric between the reconstituted specimens and naturally occurring RNSC. These variations exist for all reconstitution techniques and the specimens created from resedimentation are thought to be of high quality and repeatability.

6.1.4 Successful Testing Procedures

RNSC was found to be a suitable material for all standard test methods. No special exceptions or deviations were required to execute the laboratory program.

6.1.5 Laboratory Testing

This section includes, results of the series I and Series II materials for index property tests, compressibility testing, permeability testing, and triaxial shear testing. This section does not include data on Series III, due to the limited amount of tests performed on series III.

6.1.5.1 Index Properties and Characterization Tests

Series I RNSC was found to be 70% silt and 30% clay by particle size. Series II RNSC was found to be 24% sand, 30% silt and 46% clay by particle size. The average liquid limit for Series I was found to be 61.5% and the plastic limit was found to be 24.5%. For Series II the liquid limit was found to be 62.1% and the plastic limit was found to be

23.4%. The organic content of the Series II bulk NSC powder was found to be a maximum of 2% by mass. The specific gravity of Series II RNSC was found to be 2.816. The natural salt content of Series II was found to be 0.02 grams of salt per kilograms of soil.

XRPD testing determined bulk RNSC to be predominantly Quartz (24%), Plagioclase (14%) and K-feldspar (5%) with some calcium cementation in the form of Calcite (3.3%) and Dolomite (0.3%). The clay fraction of RNSC (<2 μ m particle size) was found to consist of Smectite (93%), Kaolinite (4%) and trace Chlorite and Illite.

SEM imaging was used to view the crystalline mineral and clay aggregates that compose the greater than #200 sieve sized particles found within series II RNSC. SEM imaging was also used to look at the microstructure of oven dried series II triaxial specimens as reported within section 4.2.5.

6.1.5.2. Compressibility

Both Constant Rate of Strain (CRS) and triaxial consolidation tests were used to characterize the compressibility of RNSC. From the CRS testing, at low stresses (0.1 to 1 MPa) RNSC has an average Compression Ratio (CR) of 0.213. At higher stresses (1 to 10 MPa) RNSC has an average CR of 0.176. RNSC had an average Swelling Ratio (SR) 0.054 as determined at the end of a CRS test. CRS1504 had two unload/reload cycles to explore the recompression behavior of RNSC. The first one was at a stress range of .07 to 1.5 MPa. This unload reload cycle was found to have a RR of 0.062. The second unload and reload cycle was performed at a stress range of 0.7 to 8 MPa. This unload/reload cycle was found to have a RR of 0.052.

A total of 17 consolidated triaxial tests were performed on RNSC, of which 4 of the tests were performed on Series I material and 13 of the tests performed on Series II material. From select K_0 consolidated tests the Compression Ratio of RNSC, within the stress range of 0.1 To 0.35 MPa is 0.218. The average CR for a stress range of 0.1 to 1 MPa from all consolidation testing was 0.190.

6.1.5.3. Permeability

The normally consolidated permeability results measured from CRS testing shows a log linear trend of decreasing permeability with decreasing void ratio. The RNSC Series II material was observed to be less permeable than RNSC Series I for a given porosity. This is though to be caused by the clay particles expanding into the pore spaces between the sand particles sealing the available pore space for flow (Mollins, Stewart, & Cousens, 1995).

6.1.5.4. Stress-Strength Response

All aspects of the rheology of RNSC were observed to be very sensitive to the consolidation stress applied to the soil during triaxial testing. The material strength behavior indicates that the sand-silt fraction is affecting the strength. At higher stress the material behaves mechanically like a traditional fine grained soil.

6.1.6 Comparison to Other Soils

A comparison of Resedimented Nile Silty Clay, to Resedimented Boston Blue Clay, and Resedimented Gulf of Mexico Eugene Island Clay was presented in Chapter 5 herein. The three materials in general exhibited similar underlying mechanical behaviors. RNSC exhibited some behaviors typically at lower consolidation stress not observed within the other two materials.

In general the behaviors of RNSC, RBBC and RGoM_EI were ordered best by the correlations on behavior with Atterberg Limits presented within Casey B. (2014), specifically the correlations on compressibility, and permeability.

RNSC showed a much higher sensitivity to consolidation stress than RBBC or RGoM_EI, this is shown in the strength properties. The changes in shear strength, critical state friction angle and lateral stress ratio are more varied and occur more rapidly in RNSC than RBBC or RGoM_EI.

6.2 Recommendations for Future Research

6.2.1 Introduction

Despite the extensive testing program that was undertaken in this research, there are still many unknowns about the material. To further advance knowledge on the subject of Nile Silty Clays recommendations for future research are provided in the following sections.

6.2.2 Triaxial Testing

The triaxial testing reported herein was limited to a maximum stress level of 1 MPa. Future considerations should be given to triaxial testing at higher stress levels. Also the testing performed on over-consolidated RNSC was limited to two tests at OCRS of 2. RNSC should be tested at higher OCRS to observe the behavior of the soil within the SHANSEP framework.

6.2.3 CRS Testing

The CRS testing reported herein was limited to a maximum effective stress of 10 MPa. Future consideration should be made for CRS testing to higher stress levels.

Future considerations should also be made for CRS testing of Series III RNSC for both determining the effects of the sand content on compressibility and permeability.

6.2.4 Salinity

The natural salt concentration of RNSC was measured to be fairly low. Since the clay mineralogy was dominated by Smectitic clays which have large double layers, RNSC is likely to be very sensitive to salinity effects. Future consideration should be given to exploring the effect of pore salinity on RNSC.

6.2.5 Liquefaction

Due the relatively high plasticity liquefaction is not expected to be a concern within RNSC. To ensure this is the case, cyclic triaxial tests should be performed on the material to determine its susceptibility to liquefaction.

6.2.6 Evolution of Microstructure

As suggested by (Mollins, Stewart, & Cousens, 1995) the clay fraction of a Smectitic soil swells to a stress dependent void ratio independent of silt and sand grains at low stresses. As the consolidation stress increases the Smectitic clays are no longer able to move the silt and sand grains and the clays do not reach the same clay void ratio. Future research should consider determine the stress threshold at which the silt and sand will effect the microstructure of the soil.

APPENDIX A

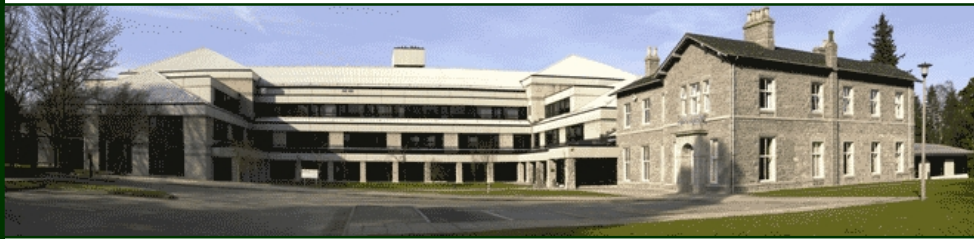
RNSC XRPD REPORT



**Report on the Mineralogy of a Single Sample
by X-Ray Powder Diffraction (XRPD)**

FOR:

Mark Zablocki
TUFTS CEE
113 Anderson Hall
200 College Ave
Medford
MA 02155
USA



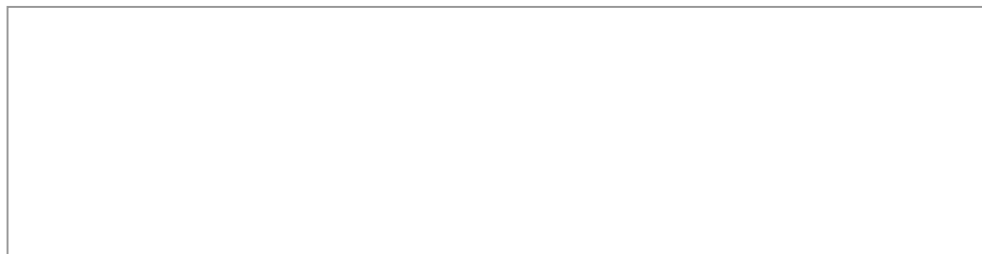
REPORT AUTHORS:



INVESTORS IN PEOPLE

Ian M Phillips BSc, PhD (Senior Analyst)

(e-mail: ian.phillips@hutton.ac.uk T: 01224 395356)



Tests marked "N/A" are not covered by the UKAS Schedule for this laboratory.
Opinions and interpretations expressed herein are outside the scope of UKAS Accreditation.
This report shall not be reproduced, except in full, without written approval of the laboratory.

Job and Sample Information:	
Job No(s):	2016-24155
Client Order No/Reference:	Credit card
Date Sample(s) Received:	17-October-2016
Lab Code	Client Code
1240346	Green Nile River Clay

Introduction

A single sample was forwarded for bulk and clay size fraction mineralogical analysis by X-ray powder diffraction (XRPD).

Methods

Methods	Accreditation Reference
Identification and Quantification of Polycrystalline Material by XRPD	GM003 and GM004
Identification and Semi-Quantification of Clay Minerals	GM001 and GM002

XRPD

The bulk sample was wet ground (in ethanol) in a McCrone mill and spray dried to produce a random powder. The X-ray powder diffraction (XRPD) pattern was recorded from 2-75°2θ using Cobalt Kα radiation. Quantitative analysis was done by a normalised full pattern reference intensity ratio (RIR) method. Unless stated otherwise, expanded uncertainty using a coverage factor of 2, i.e. 95% confidence, is given by $\pm X^{0.35}$, where X = concentration in wt.%, e.g. 30 wt.% ± 3.3 . Note also that for phases present at the trace level (<1%) there may also be uncertainty as to whether or not the phase is truly present in the sample. This is both phase and sample dependent. It arises because at trace concentrations identification is often based on the presence of a single peak and the judgement of the analyst in assigning that peak to a likely mineral.

The clay fraction of <2µm was obtained by timed sedimentation, prepared as an oriented mount using the filter peel transfer technique and scanned from 2-45°2θ in the air-dried state, after glycolation, and after heating to 300°C for one hour. Clay minerals identified were quantified using a mineral intensity factor approach based on calculated XRPD patterns. Unless otherwise stated, for clay minerals present in amounts >10wt.% uncertainty is estimated as better than ± 5 wt.% at the 95% confidence level.

The XRPD patterns are identified by a labcode and by a name based on customer supplied identifiers, plus the suffix 'A' for air-dried, 'G' for glycolated, 'H3' for heated to 300°C and 'B' for bulk sample.

Results

The bulk XRPD results are presented in Table 1 and clay fraction results in Table 2. The XRPD pattern, with the main non-clay phases identified in the bulk samples by reference to patterns from the International Centre for Diffraction Database (ICDD), is provided for reference.

Comments and opinions

Mineral phases identified and quantified in the whole rock include quartz, plagioclase, K-feldspar, pyroxene, calcite, dolomite, hematite, goethite, magnetite, ilmenite, anatase, dioctahedral smectite and kaolinite. The smectite appears somewhat iron-rich. Note also that goethite may be overestimated, and we are not absolutely certain of the presence of pyroxene, although the full pattern fitting is improved and some minor peaks explained by its inclusion.

The <2 micron clay size fraction is dominated by smectite (possibly with some mixed-layering) along with small amounts of kaolinite, and traces of chlorite and illite.

Note:

Samples will be stored for a period of eight weeks following completion of analysis and acceptance of analytical report(s) at no extra cost after which samples will be disposed of unless a specific instruction is given (with the sample analysis request/order) to store the sample beyond this period. Extended storage charges will apply.

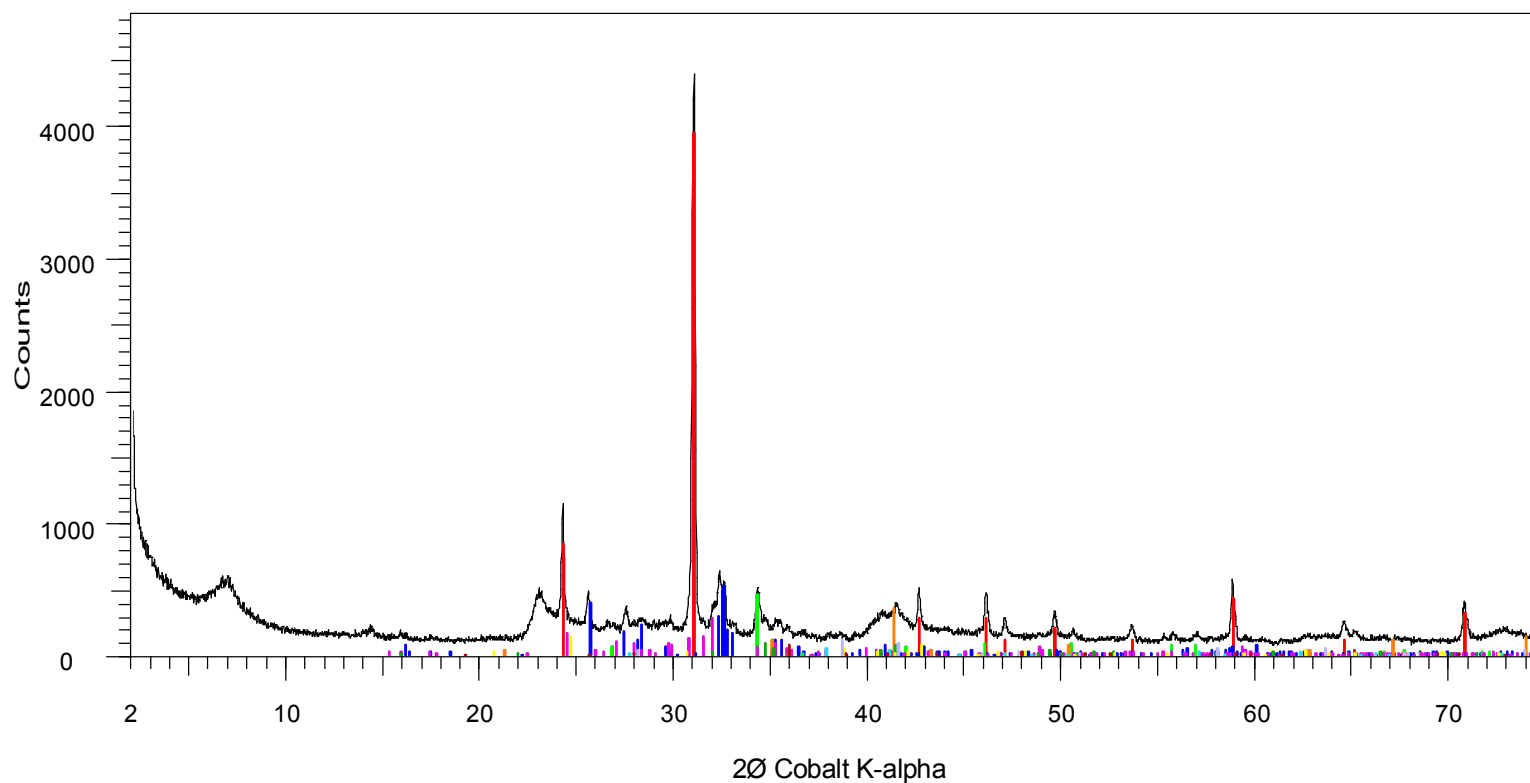
Table 1: XRPD Bulk Mineralogy (weight %) RIR Method

Labcode	Sample ID	Quartz	Plagioclase	K-feldspar	Pyroxene	Calcite	Dolomite	Hematite	Goethite	Magnetite	Ilmenite	Anatase	Smectite(Di)	Kaolinite	TOTAL
1240346	NILE-RIVER-CLAY	23.9	13.9	5.4	2.8	3.3	0.3	0.5	3.6	0.9	0.9	0.3	36.9	7.2	100.0

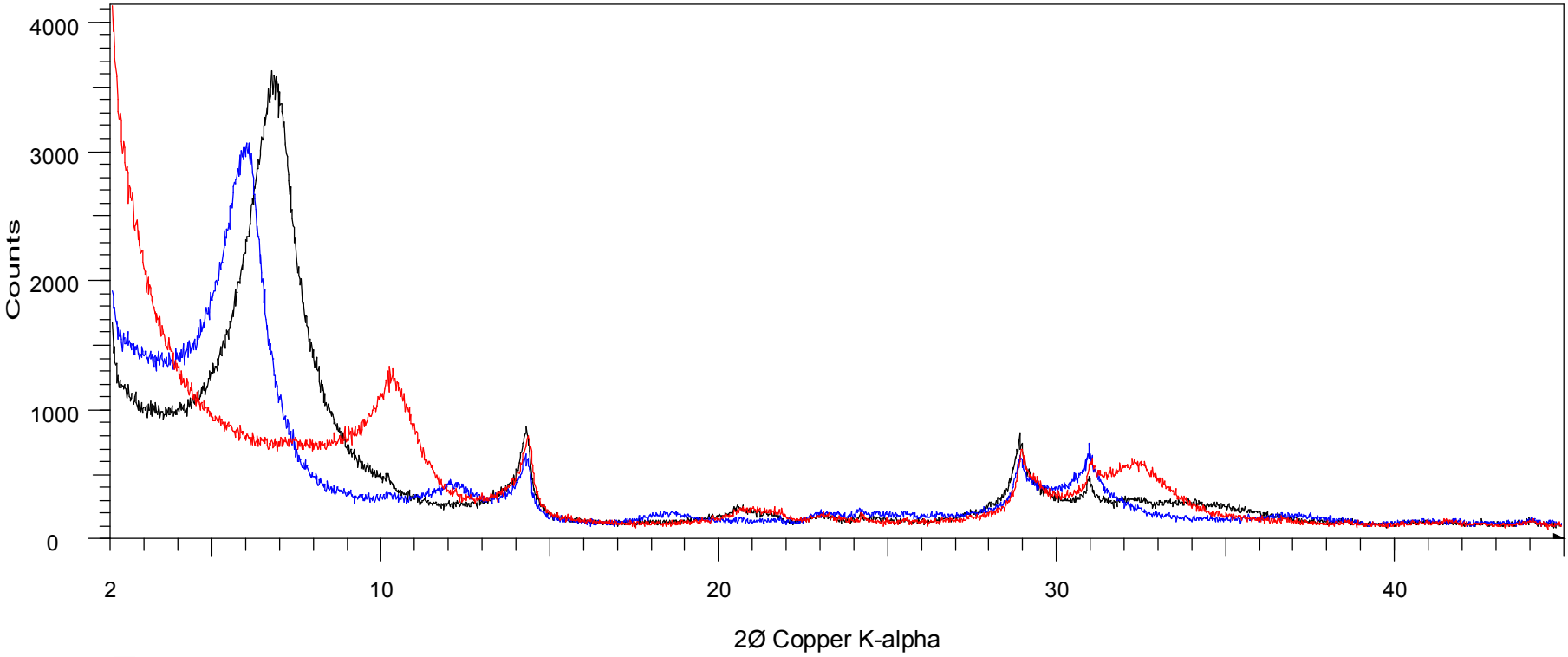
Smectite(Di) = Dioctahedral smectite

Table 2: Relative percentage of clay minerals in the <2µm clay size fraction

Labcode	Sample ID	Chlorite(Tri)©	Kaolinite©	Illite©	Smectite(Di)©
1240346	NILE RIVER CLAY	2	4	1	93



- | | |
|--|--|
| <ul style="list-style-type: none"> 1240346 - File: NILE-RIVER-CLAY-B.RAW 99-090-0067 (U) - Quartz - SiO₂ 99-090-0002 (U) - Albite low - Na(AlSi₃O₈) 99-090-0005 (U) - Calcite, syn - CaCO₃ 99-090-0003 (U) - Microcline - from Pike's Peak batholith, Colorado, USA 99-090-0012 (U) - Magnetite, syn - FeFe₂O₄ 99-090-0085 (U) - Ilmenite, syn - FeTiO₃ 00-024-0201 (I) - Augite - Ca(Fe,Mg)Si₂O₆ | <ul style="list-style-type: none"> 99-090-0013 (U) - Goethite - FeO(OH) 99-090-0011 (U) - Hematite, syn - Fe₂O₃ 99-090-0074 (U) - Dolomite - CaMg(CO₃)₂ |
|--|--|



1240346 AIR DRIED - File: NILE-RIVER-CLAY-A.RAW
1240346 GLYCOLATED - File: NILE-RIVER-CLAY-G.RAW
1240346 H300 - File: NILE-RIVER-CLAY-H3.RAW

Bibliography

- Abdulhadi, N. O. (2009). *An Experimental Investigation into the Stress-Dependant Mechanical Behavior of Cohesive Soil with Application to Wellbore Instability*. Cambridge, Massachusetts: MIT University.
- Abu-Lughod, J. (1965). *Tale of Two Cities: The Origins of Modern Cairo*. (C. S. History, Ed.) Cambridge, United Kingdom: Cambridge University Press.
- Abuo El-Ela, A., El-Hadidy, M., Deif, M., & Abou Elenean, K. (2012). Seismic Hazard Studies in Egypt. *NRIAG Journal of Astronomy and Geophysics*, 119-140.
- Aggour, T. A., Korany, E. A., Mosaad, S., & Kehew, A. E. (2012). Geological conditions and characteristics of the Nubia Sandstone aquifer system and their hydrogeological impacts, Tushka area, South western Desert, Egypt. *Egyptian Journal of Pure and Applied Science*, 27-37.
- Ahmed, I. (1990). *Investigation of Normalized Behaviour of Resedimented Boston Blue Clay using Geonor Direct Simple Shear*. Cambridge, Massachusetts: MIT, S.M. Thesis.
- Amy, A. L. (2011). *Laboratory Evaluation of the Constant Rate of Strain and Constant Head Techniques for Measurement of the Hydraulic Conductivity of Fine Grained Soils* (Vol. MS Thesis). Cambridge, Massachusetts: Massachusetts Institute of Technology.
- ASTM. (2014). *Rapid determination of Carbonate Content of Soils*.
- ASTM. (2014). *Standard Test Methods for Moisture, Ash, and Organic Matter of Peat and Other Organic soils*.
- ASTM. (2014). *Standard Test Methods for Specific Gravity of Soil Solids by Water Pycnometer*.
- ASTM. (2017). *Standard Test Method for Particle-Size Distribution (Gradation) of fine-Grained Soils Using the Sedimentation (Hydrometer) Analysis*.
- ASTM. (2017). *Standard Test Methods for Liquid Limit, Plastic Limit, and Plasticity Index of Soils*.
- Becker, R., & Sultan, M. (2009). *Land Subsidence in the Nile Delta: Inferences from Radar Interferometry*. Kalamazoo, MI: The Holocene.
- Betts, W. (2014). *Compression and Permeability Behavior of Gulf of Mexico Mudrocks, Resedimented and In-situ*. Austin, Texas: University of Texas at Austin, M.S. Thesis.

- Casey, B. (2014). *The Consolidation and Strength Behavior of Mechanically Compressed Fine-Grained Sediments* (Vol. Phd Thesis). Cambridge, Massachusetts: MIT.
- Casey, B., Germaine, J., Flemings, P., Reece, J., Gao, B., & Betts, W. (2013). Liquid limit as a predictor of mudrock permeability. *Marine and Petroleum Geology*, 256-263.
- CIA. (2017, July). *Central Intelligence Agency*. Retrieved January 2018, from World Factbook: <https://www.cia.gov/library/publications/the-world-factbook/geos/eg.html>
- Das, B. M. (2010). *Principles of Geotechnical Engineering*. Stamford, CT: Cengage Learning.
- Dawood, Y., & Abd El-Naby, H. (2012). Distribution of Uranium and Thorium Radioelements in Subsurface Pleistocene-Holocene Sediments of the Nile Delta, Egypt. *Earth Science*, Vol. 23 PP 149-169.
- DeGroot, D., & Ladd, C. (2015). Site Characterization for Cohesive Soil Deposits Using Combined In Situ and Laboratory Testing. *Geotechnical engineering and state of practice*, 565-607.
- Derieh, A. (2016). *From Clay Slurries to Mudrocks: A Cryo-SEM Investigation of the Development of the Porosity and Microstructure*. Cambridge, MA: MIT.
- Eggleton, R., Foudoulis, C., & Varkevisser, D. (1987). Weathering of Basalt: Changes in Rock Chemistry and Mineralogy. *Clays and Clay Minerals*, Vol. 35 PP 161-169.
- El-sherbiny, S., & Amin, S. (2012). *Characterization and Use of Nubian Sandstone in the Ceramic Tile Industry*. *Journal of Material Science and Engineering*.
- Embabi, N. (2018). *Landscapes and Landforms of Egypt*. Springer International Publishing.
- Fahy, B. (2014). *The Influence of Salinity on the Mechanical Behavior of High Plasticity*. Cambridge, Massachusetts: Massachusetts Institute of Technology, S.M. Thesis.
- Foott, R., & Ladd, C. (1981). Undrained Settlement of Plastic and Organic Clays. *Journal of the Geotechnical Engineering Division, ASCE*, 107 (8), 1079-1094 .
- Gani, N., Adbelsalam, M., Gera, S., & Gani, M. (2009). Stratigraphic and structural evolution of the Blue Nile Basin, Northwestern Ethiopian Plateau. *Geological Journal*, Vol 44 PP 30-56.
- Garzanti, E., Ando, S., Vezzoli, G., Megid, A., & El Kammar, A. (2006). *Petrology of Nile River sands (Ethiopian)*. Earth Planetary Science Laboratory.
- GeoFluids, U. (2016). *Gulf of Mexico Eugene Island*. Austin, Texas: University of Texas.

- GeoFluids, U. (2018). *Boston Blue Clay*. Austin, Texas: University of Texas.
- Germaine, J. (1982). "Development of the Directional Shear Cell for Measuring Cross-Anisotropic Clay Properties". Cambridge, MA: ScD Thesis, MIT.
- Germaine, J., & Germaine, A. (2009). *Geotechnical Laboratory Measurements for Engineers*. John Wiley & Sons, Inc.
- Germaine, J., & Ladd, C. (1988). Triaxial Testing of Saturated Cohesive Soils: State of the Art Paper. *Advanced Triaxial Testing of Soil and Rock*, pp. ASTM STP 977, pp. 421 – 459.
- Hanley, A. (2017). *The Characterization of the Yield Surface for Fine-Grained Sediments*. Medford, Massachusetts: Tufts University, M.S. Thesis.
- Hoeg, K., Dyvik, R., & Sanbaekken, G. (2000 July). Strength of Undisturbed versus Reconstituted Silt and Silty Sand Specimens. *Journal of Geotechnical and Geoenvironmental Engineering*.
- Horan, A. (2012). *The Mechanical Behavior of Normally Consolidated Soils as a Function of Pore Fluid Salinity*. Cambridge, Massachusetts: S.M Thesis, Massachusetts Institute of Technology.
- House, R. (2012). *A Comparison of the Intact Behavior and Resedimented Boston Blue Clay (BBC)*. Cambridge, Massachusetts: Massachusetts Institute of Technology, M.E. Thesis.
- Jaky, J. (1948). Pressure in Silos. *Proc., 2nd Int. Conf. on soil Mech. and Found.* (p. Vol. I 103 to 107). Rotterdam, Netherlands: A. A. Balkema.
- Kieffer, B., Arndt, N., Lapierre, H., Bastien, F., Bosch, D., Pecher, A., . . . Meugniot, C. (2004). Flood and Shield Basalts from Ethiopia: Magmas from the African Superswell. *Journal of Petrology*, 793-834.
- Ladd, C. (1964). *Stress-Strain Behavior of Saturated Clay and Basic Strength Principles*. Cambridge, Massachusetts: Massachusetts Institute of Technology.
- Ladd, C., & Foote, R. (1974). A new design procedure for stability of soft clays. *Journal of the Geotechnical Engineering Division*, 763-786.
- Ladd, C., & Foote, R. (1974). New Design Procedure for Stability of Soft Clays. *Journal of the Geotechnical Engineering Division, ASCE*, 763-786.
- Ladd, C., & Luscher, U. (1965). *Engineering Properties of the Soils Underlying the MIT Campus*. Rept. R65-58: MIT Dept. of Civil Engineering Res.

- Ladd, C., & Varrallyay, J. (1965). *"The Influence of Stress System on the Behavior of of Saturated Clays During Undrained Shear," Research Report R65-11, Soil Publication No. 177.* Cambridge, MA: Department of Civil Engineering, MIT.
- Ladd, C., & Varrallyay, J. (1965). *The Influence of Stress System on the Behavior of of Saturated Clays During Undrained Shear.* Department of Civil Engineering,. Cambridge, MA: MIT.
- Ladd, C., Young, G., Kraemer, S., & Burke, D. (1999). *Engineering properties of Boston Blue Clay from special testing program.* Boston, Massachusetts: Special Geotechnical Testing: Central Artery/Tunnel Project, ASCE GSP 91, pg 1-24.
- Lupini, J. (1982). *The Residual Strength of Soils.* London: PhD Thesis, London University.
- Marcial, D., Delage, P., & Yu Jun, C. (2001). *On the high stress compression of bentonites.* Caracas, Venezuela: NRC Research Press .
- Martin, R. (1982). *Suggested Method of Test for Determination of Soluble Salts in Soil.* ASTM STP 476, 288-290.
- McGregor, A. J. (2006). *A Military History of Modern Egypt: From the Ottoman Conquest to the Ramadan War.* Westport, Connecticut, USA: Greenwood Publishing Group. doi:ISBN 0-275-98601-2
- Mitchell, J. (1976). *Fundamentals of Soil Behavior.* University of California, Berkeley: John Wiley & Sons, Inc.
- Mogessie, A., Krenn, K., Schaflechner, J., Koch, U., Egger, T., Goritchnig, B., . . . Demessie, M. (2002). *A Geological Excursion to the Mesozoic Sediments of the Abay Basin (Blue Nile), Recent Volcanics of the Ethiopian Main Rift and Basement Rocks of the Adola Rea, Ethiopia.* Institute of Mineralogy and Petrology University of Graz, Austria.
- Mollins, L., Stewart, D., & Cousens, T. (1995). Predicting the Properties of Bentonite-Sand Mixtures. *Clay Minerals*, 243-252.
- Moniz, S. (2009). *The Influence of Effective Consolidation Stress on the Normalized Extension Strength Properties of Resedimented Boston Blue Clay.* Cambridge, Massachusetts: MIT, M.Eng. Thesis.
- Nordquist, T. (2015). *Permeability anisotropy of resedimented mudrocks.* Cambridge, Massachusetts: Massachusetts Institute of Tehnology, S.M. Thesis.
- Said, R. (1981). *The Geological Evolution of the River Nile.* New York, New York: Springer-Verlag New York Inc.

- Said, R. (1990). *The Geology of Egypt*. Rotterdam, Netherlands: A.A.Balkema .
- Said, R. (1993). *The River Nile Geology, Hydrology and Utilization*. Tarrytown, New York: Pergamon Press.
- Santagata, M. (1994). *Investigation in Soft Clays Using Triaxial Element Tests* (Vol. SM Thesis). Cambridge, Massachusetts: MIT.
- Santagata, M. (1998). *Factors Affecting the Initial Stiffness Degradation of Cohesive Soils*. Cambridge Massachusetts: MIT.
- Schenk, C. J., Kirshbaum, M. A., Charpentier, R. R., Klett, T. R., Brownfield, M. E., Pitman, J. K., . . . Tennyson, M. E. (2010). *Assessment of Undiscovered Oil and Gas Resources of the*. USGS.
- Schneider, J. (2011). *Compression and Permeability Behavior of Natural Mudstones*. Austin, Texas: Ph.D Thesis, University of Texas at Austin.
- Seah, T. (1990). *Anisotropy of Resedimented Boston Blue Clay*. Cambridge, MA: MIT, ScD Thesis.
- Shata, A. (n.d.). Geology of Cairo, Egypt. *Environmental and Engineering Geoscience*, xxv (2), 149–183. Retrieved from <https://doi.org/10.2113/gseegeosci.xxv.2.149>
- Sheahan, T. (1991). *An Experimental Study of the Time-Dependent Undrained Shear Behavior of Resedimented Clay Using Automated Stress-Path Triaxial Equipment* (Vol. ScD Thesis). Cambridge, MA: MIT.
- Sheahan, T., & Germaine, J. (1992). Computer Automation of Conventional Triaxial Equipment. *Geotechnical Testing Journal*, 15(4), 311-322.
- Skempton, A. (1954). The Pore Pressure Coefficients A and B. *Geotechnique*, 143-147.
- Smith, R., & Wahls, H. (1969). Consolidation Under Constant Rates of Strain. *Journal of Soil Mechanics and Foundations Division, ASCE*.
- Stump, B. B. (1998). *Illuminating Basinal Fluid Flow in Eugen Islan 330 (Gulf of Mexico) Through In Situ Observations, Deformation Experiments and Hydrodynamic Modeling*. State College, PA: Penn State University MS.
- Terzaghi, K. (1943). *Theoretical Soil Mechanics*. New York: John Wiley and Sons.
- USGS. (2014, September 15). *Understanding Plate Motions*. Retrieved from USGS Publications: <https://pubs.usgs.gov/publications/text/understanding.html>

- va der Does, M., Korte, L., Munday, C., Brummer, G.-J., & Stut, J.-B. (2016). Particle size traces modern Saharan dust transport and deposition across the equatorial North Atlantic. *Atmospheric Chemistry and Physics*.
- Van Olphen, H. (1963). *An Introduction to Colloid Chemistry*. New York: John Wiley and Sons Inc.
- Varallyay, J. (1964). *The Influence of Stress System Variables on The Undrained Strength of Boston Blue Clay*. Cambridge, Massachusetts: Massachusetts Institute of Technology, M.S. Thesis.
- Walbaum, M. (1988). *Procedure for Investigation of Sample Disturbance using the Direct Simple Shear Apparatus*. Cambridge, Massachusetts: MIT, S.M. Thesis.
- Weir, A., Ormerod, E., & El Mansey, I. (1975). *Clay Mineralogy of Sediments of the Western Nile Delta*. Cairo, Egypt: Rothamsted Experimental Station.
- Wissa, A., Christian, J., Davis, E., & Heiberg, S. (1971). Consolidation at Constant Rate of Strain. *Journal of Soil Mechanics and Foundation*, Vol. 97(SM10), 1393-1412.
- Woodward, J., Macklin, M., Fielding, L., Millar, I., Spencer, N., Welsby, D., & Williams, M. (2015). Shifting sediment sources in the world's longest river: A strontium. *Quaternary Science Reviews*, 124-140.
- Yang, Y., & Aplin, A. (2010). A Permeability-Porosity Relationship for Mudstones. *Marine and Petroleum Geology*, 163-175.